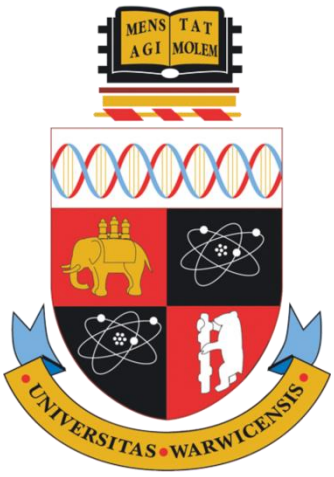

Low Temperature Epitaxy of Germanium-Tin Semiconductor Heterostructures on Silicon

by

Pedram Jahandar

Thesis

submitted to the University of Warwick

for the degree of Doctor of Philosophy

Department of Physics

August 2022

Table of Contents

List of Figures

List of Tables

Acknowledgements

I would like to express my deepest appreciation to my mother, father and brother for giving me the opportunity to develop my interest in scientific research and also to my partner for her understanding and encouragement. I could not have undertaken this journey without their endless support.

I would also like to thank my supervisor Prof Maksym Myronov for his guidance and expertise in semiconductor epitaxy, which led to the design and epitaxial growth of all the materials presented in this work. Last but not least, I would like to sincerely thank all the researchers and professionals who helped me and shared their knowledge and experience with me throughout the research: Dr Gerard Colston, Dr Alan Burton, Dr Elnaz Shabani, Ms Susan Tatlock, Dr Marc Walker, Ms Rosalind Johnstone, Dr Simone Rossi, Dr David Walker, Ms Maxine Little and Dr Alireza Garmabi.

Declaration

This thesis is submitted to the University of Warwick in support of my application for the degree of Doctor of Philosophy. It has been composed by myself and has not been submitted in any previous application for any degree. Except where specifically stated, all experimental measurements were carried out by the author or by specialists under his direction.

Publications & Presentations

The following publications and presentations are either from research done within this thesis or other research I was involved in, during the time of my studies at the University of Warwick.

Journal Publications

1. **P. Jahandar**, E. Shabani, A. Burton, M. Myronov, "Very low-temperature heteroepitaxy of $Ge_{1-y}Sn_y$ binary alloy using chemical vapour deposition" to be published.

2. S. De Cesari, A. Balocchi, E. Vitiello, **P. Jahandar**, E. Grilli, T. Amand, X. Marie, M. Myronov, and F. Pezzoli, Physical Review B 99, 9, 035202 (2019).

3. **P. Jahandar**, D. Weisshaupt, G. Colston, P. Allred, J. Schulze, and M. Myronov, Semiconductor Science and Technology 33, 6, 034003 (2018).

4. D. Weisshaupt, **P. Jahandar**, G. Colston, P. Allred, J. Schulze, and M. Myronov, 2017 40th International Convention on Information and Communication Technology, Electronics and Microelectronics (Mipro), 43 (2017).

5. R. W. Millar, D. C. S. Dumas, K. F. Gallacher, **P. Jahandar**, C. MacGregor, M. Myronov, and D. J. Paul, Optics Express 25, 25374 (2017).

Conference Presentations

1. **P. Jahandar**, M. Myronov "Very Low-Temperature Heteroepitaxy of $Ge_{1-y}Sn_y$ Binary Alloy using Chemical Vapour Deposition" Global Summit on Condensed Matter Physics (CONMAT 2021), Valencia, Spain, 18th October – 20th October 2021.

2. S. De Cesari, A. Balocchi, E. Vitiello, **P. Jahandar**, T. Aman, X. Marie, M. Myronov, F. Pezzoli "Carrier and Spin Coherent Dynamics in Strained Germanium-Tin Semiconductor on Silicon" ICSI-ISTDM 2019 conference, Madison, USA, 2nd June – 6th June 2019.

3. F. Pezzoli, S. de Cesari, A. Balocchi, E. Vitiello, **P. Jahandar**, E. Grilli, T. Amand, X. Marie, M. Myronov "Carrier and Spin Coherent Dynamics in Strained Germanium-Tin Semiconductor on Silicon" 34th International Conference on the Physics of Semiconductors (ICPS 2018), Montpellier, France, 29th July – 3rd August 2018.

4. R.W. Millar, D.C.S. Dumas, K. Gallacher, **P. Jahandar**, M. Myronov and D. J. Paul "Tensile strained GeSn mid-infrared light emitters" 2017 IEEE 14th International Conference on Group IV Photonics, Berlin, Germany, 23rd August – 25th August 2017.

5. D. Weisshaupt, **P. Jahandar**, G. Colston, P. Allred, J. Schulze and M. Myronov "Impact of Sn segregation on GeSn epi-layers growth by RP-CVD" 2017 40th International Convention on Information and Communication Technology, Electronics and Microelectronics (MIPRO) Opatija, Croatia, 22nd May – 26th May 2017.

6. **P. Jahandar**, D. Weisshaupt, G. Colston, P. Allred, J. Schulze, and M. Myronov, "Effect of Ge precursor on heteroepitaxy of Ge1-xSnx on Si substrate" The 10th International Conference on Silicon Epitaxy and heterostructures (ICSI-10), Coventry, UK, 14th May – 19th May 2017.

Abstract

$Ge_{1-y}Sn_y$ binary alloy is an intriguing group IV semiconducting material which offers energy bandgap engineering by modifying its Sn concentration, indirect-to-direct bandgap transition with Sn concentration of 6–11 at.%, strain engineering by controlling its thickness and Sn concentration, interface improvement, defect prevention, and temperature reduction in the process of epitaxial growth. There have been several achievements in the development of $Ge_{1-y}Sn_y$ optoelectronic devices, such as IR LEDs, IR LASER, and IR photodetectors with high efficiency. There are other exciting potential $Ge_{1-y}Sn_y$ electronic and quantum applications, such as MOSFET with high mobility, TFET with low energy consumption and high performance, IR wave guides, and spintronics. However, to further develop $Ge_{1-y}Sn_y$ applications and devices, it is essential to fully understand the epitaxy and material properties. In this research, the heteroepitaxial growth of $Ge_{1-y}Sn_y$ on a Si (001) substrate via a relaxed Ge virtual substrate using CVD with either of GeH_4 or Ge_2H_6, in combination with $SnCl_4$. It is demonstrated that Sn segregation and precipitation are controlled when GeH_4 is used over Ge_2H_6, under very similar growth conditions, which is crucial for the growth of monocrystalline $Ge_{1-y}Sn_y$ thin films. Contrary to previously reported results, the GeH_4 could indeed be a viable Ge precursor for epitaxy of superior quality $Ge_{1-y}Sn_y$ epilayers at very low cost. In addition, the growth of fully strained $Ge_{1-y}Sn_y$ epilayers with a Sn concentration of over 13 at.% at a very low growth temperature when using GeH_4 and $SnCl_4$, which was previously assumed to be impossible, is successfully achieved. The lowest temperature at which epitaxial growth of $Ge_{1-y}Sn_y$ can take place is estimated at ~231 °C, which is very close to the melting point of Sn. Moreover, since strain relaxation in $Ge_{1-y}Sn_y$ epilayers affects their electrical and physical properties, it is therefore essential to investigate the mechanism of strain relaxation in $Ge_{1-y}Sn_y$ epilayers. The effect of strain relaxation of compressive strained $Ge_{1-y}Sn_y$ epilayers as a function of growth rate and Sn concentration is investigated. Additionally, a grading technique, in which the $SnCl_4/GeH_4$ ratio is tuned during the growth of $Ge_{1-y}Sn_y$ epilayers, is demonstrated. It is shown how the grading technique can enable the growth of thick $Ge_{1-y}Sn_y$ epilayers by suppressing Sn segregation. As a result, a relaxed $Ge_{1-y}Sn_y$ epilayer with a higher quality and smoother surface is achieved. Furthermore, since doped $Ge_{1-y}Sn_y$ epilayers could offer more flexibility to control physical, electrical, and optical properties over undoped ones, it is crucial to discover mechanisms that can control the incorporation of dopants into $Ge_{1-y}Sn_y$ epilayers. The attempt of heteroepitaxial growth of both p- and n-type $Ge_{1-y}Sn_y$ epilayers is examined. It is demonstrated that such attempt does not affect the quality of epilayers but influences their Sn concentration and growth rate. The attempt of incorporation of Si into $Ge_{1-y}Sn_y$ (as known as $Ge_{1-x-y}Si_xSn_y$) is also investigated. The incorporation of Si up to ~3 at.% into $Ge_{1-x-y}Si_xSn_y$ with a Sn concentration of ~9 at.% is successfully achieved. Finally, epitaxial growth of $Ge\backslash Ge_{1-y}Sn_y\backslash Ge$ quantum well, $Ge_{1-y}Sn_y\backslash Ge$ multilayers, and $Ge_{1-y}Sn_y\backslash Ge_{1-z}Sn_z$ (in which $y \neq z$) is achieved. Epitaxial growth of the corresponding heterostructures, the investigation of the growth mechanisms, and the impact of CVD growth conditions on the quality of epilayers have been extensively carried out. These heterostructures could potentially offer greater flexibility in controlling the physical, electrical, and optical properties of $Ge_{1-y}Sn_y$ related materials for device fabrication.

Abbreviations

ADC	Analog to Digital Converter
AFM	Atomic Force Microscopy
AP-CVD	Atmospheric Pressure Chemical Vapour Deposition
B	Boron
B_2H_6	Diborane
BF	Bright Field
b^{GeSn}	Bowing parameter for GeSn
CCD	Charge-Coupled Device
CVD	Chemical Vapour Deposition
DF	Dark Field
EDS	Energy Dispersive X-ray Spectroscopy
EL	Electroluminescence
FCC	Face Centred Cubic
FEG	Field-Emission Electron Gun
FTIRS	Fourier Transform Infrared Spectroscopy
FWHM	Full Width at Half Maximum
Ge	Germanium
Ge-VS	Germanium Virtual Substrate
GeH_4	Germane
Ge_2H_6	Digermane
$Ge_{1-y}Sn_y$	Germanium-Tin binary alloy
$Ge_{1-x-y}Si_xSn_y$	Silicon-Germanium-Tin ternary alloy
h_c	Critical thickness at which $Ge_{1-y}Sn_y$ growing layers begin to relax
HR-XRD	High Resolution X-ray Diffraction
IR	Infrared
LASER	Light Amplification by Stimulated Emission of Radiation
LED	Light Emitting Diode
MBE	Molecular Beam Epitaxy
MO-CVD	Metal Organic Chemical Vapour Deposition
MOSFET	Metal Oxide Semiconductor Field Effect Transistor
NMOS	N-type Metal Oxide Semiconductor
P	Phosphorus
PH_3	Phosphine

PIPS	Precision Ion Polishing System
PL	Photoluminescence
PMOS	P-type Metal Oxide Semiconductor
RMS	Root Mean Squared
RP-CVD	Reduced Pressure Chemical Vapour Deposition
RSM	Reciprocal Space Map
RTA	Rapid Thermal Annealing
SEM	Scanning Electron Microscopy
Si	Silicon
SiC	Silicon-Carbide
$Si_{1-x}Ge_x$	Silicon-Germanium binary alloy
Si_2H_6	Disilane, DS
Si_3N_4	Silicon-Nitride
Sn	Tin
$SnCl_4$	Tin Tetrachloride
SnD_4	Tin Deuteride
ST	Straight Through
STP	Standard Temperature and Pressure
TEM	Transmission Electron Microscopy
TFET	Tunnel Field Effect Transistor
UHV-CVD	Ultra-High Vacuum Chemical Vapour Deposition
UHV	Ultra High Vacuum
ULSI	Ultra Large Scale Integrated
UV	Ultraviolet
VS	Virtual substrate
XPS	X-ray Photoelectron Spectroscopy
XRD	X-ray Diffraction
X-TEM	Cross Sectional Transmission Electron Microscopy
α-Sn	Non-metallic phase of Tin (Sn), also known as grey Sn
β-Sn	Metallic phase of Tin (Sn), also known as white Sn

Chapter 1

Introduction

1.1 Group IV Semiconductors

The most critical parameter of a semiconductor, which other electronic and optical properties sensitively depend on, is its fundamental electronic bandgap. To optimise performance of semiconductor devices, it is crucial to be able to carefully control its bandgap. Bandgap engineering can be achieved by changing compositions in semiconductor alloy systems [1]. The field of bandgap engineering was then significantly expanded soon after epitaxial growth technique was introduced [2]. Epitaxy refers to growth of crystalline layer, known as epitaxial layer, on top of a crystalline substrate with same orientation. In this technique, large stresses in epitaxial layers are generated because of lattice constant mismatch between epitaxial layer and substrate [3]. The strain in epitaxial layer provides an additional design flexibility for electronic band structure engineering. However, such flexibility is limited to critical thickness, h_c, of epitaxial layer, where strain starts to relieve due to formed dislocations as a consequence of strain relaxation [3]. For example, if lattice constant of epitaxial layer significantly depends on its composition, appropriate composition could lead to significant strain energy and so large reduction in h_c into an undesirable value. To overcome this, decoupling of the band structure and strain is required which can be done by increasing the alloy system's complexity, such as $Ge_{1-y}Sn_y$ which is a binary semiconductor alloy for group IV semiconductors [4].

Since initial development of Si nanoelectronics, the performance of Si ULSI circuits has improved year after year with more elementary devices integration with downscaling their sizes; For example, MOSFETs scaling, which has been such a driving force to keep up Moore's law. However, in more recent developments, the device performance has not been improved with scaling technology, suggesting that to follow Moore's law, some other technologies, other than scaling, should be introduced to develop novel materials with high dielectric insulators, high mobility channels, low resistance semiconductor or metal contacts

[5]. To commercialise new functional devices, such as spintronics, power generation, and optoelectronics devices, they are required to be integrated into Si ULSI devices [6]. Furthermore, group IV semiconductors with direct bandgaps can have many applications in integrated photonics technologies. But epitaxial growth of these materials with high quality has been challenging as it requires to understand fundamental surface and interfaces associate with them.

1.1.1 $Ge_{1-y}Sn_y$

The exploration of eutectic Ge-Sn system was done for the first time in 1939 when it was shown, and later confirmed by solidus curves study [7,8], that solid solubility of Sn in Ge is less than 0.6 at.% [9,10]. A few decades later, we see discovery of α-Sn (non-metallic form of Sn, also known as grey Sn) semiconducting properties [10,11] as well as single crystal growth from a mercury solution [12]. After investigation of α-Sn single crystal electronic properties [13], the possibility of indirect-to-direct transition in binary $Ge_{1-y}Sn_y$ alloys with high carrier mobilities was shown in 1982 [14].

Due to low solid solubility of Sn in Ge and their large lattice mismatch, $Ge_{1-y}Sn_y$ alloys with Sn concentrations exceeding 0.6 at.% were considered as hypothetical alloys by 1980s [10]. However, this thought was changed soon after the first successful growth of α-Sn films on InSb and CdTe substrates at temperature of 25 °C by metal beam epitaxy [15]. The first formation of microcrystalline $Ge_{1-y}Sn_y$ using crystallisation of amorphous sputtered films by means of UV excimer LASER radiation on ZnSe and InP crystalline substrates was done in 1983 [16]. After that, the first monocrystalline $Ge_{1-y}Sn_y$ epilayers, with Sn concentration of up to 8 at.%, were grown on GaAs and Ge substrates using bias-sputter deposition [17]. Soon after this achievement, many researchers focus on epitaxial growth of $Ge_{1-y}Sn_y$ using MBE [18-23].

Despite all challenges in growth of $Ge_{1-y}Sn_y$ binary alloys, researchers have succeeded in growing these epilayers using various techniques such as sputtering [17,24-27], ion-assisted MBE [28,29], pulsed LASER deposition [30], and solid phase epitaxy [31,32]. Nevertheless, MBE [18-21,33-36] and CVD [37-49] that is most important growth technique in terms of applicability and practicability. More recent development on growth of $Ge_{1-y}Sn_y$ will be discussed later.

1.1.2 Motivation

There are several potential optoelectronic, electronic and quantum applications for $Ge_{1-y}Sn_y$ binary alloy. In the next chapter, these applications and recent developments are discussed in more detail. To commercialise $Ge_{1-y}Sn_y$ applications, it is essential to consider the practicality of its growth procedure. In this work, all growth has been achieved by industrial epitaxial growth, CVD. It is also very important to understand the mechanism of how to engineer $Ge_{1-y}Sn_y$ epilayers on conventional substrates (Si or Ge) and how to control the primary characteristics of $Ge_{1-y}Sn_y$ epilayers such as Sn concentration and strain within crystalline structure. It was shown later how these two primary characteristics affect the electrical and physical properties of $Ge_{1-y}Sn_y$ epilayers. In this study, two of widely commercially available precursors, GeH_4 and $SnCl_4$, are used to reduce cost and practicality of $Ge_{1-y}Sn_y$ growth process. Growth of $Ge\backslash Ge_{1-y}Sn_y$ multilayers are studied which is important for device fabrication. Moreover, doping $Ge_{1-y}Sn_y$ are studied as well as growth of $Ge_{1-x-y}Si_xSn_y$. These epilayers offer more flexibility to control physical, electrical, and optical properties of $Ge_{1-y}Sn_y$. In all these research studies, quality of grown structures is carefully investigated and presented.

1.2 Dissertation Outline

In chapter 2, some of the most important electrical and physical properties of crystalline Si, Ge and Sn as well as $Ge_{1-y}Sn_y$ related background such as Vegard's law and bowing parameter, low Sn solubility into Ge, strain relaxation within the epilayers, band structures, and concept of Sn segregations are presented. Epitaxial growth methods such as MBE and CVD are reviewed in more details. Finally, potential applications and recent developments in $Ge_{1-y}Sn_y$ epitaxy and device fabrications as well as challenges that should be overcome are discussed. In this chapter 3, experimental techniques, including epitaxial growth and material characterisation methods used in this research, are explained. The history and recent development in the used growth method, RP-CVD, is explain in detail.

In chapter 4, the heteroepitaxial growth of $Ge_{1-y}Sn_y$ on a Si (001) substrate via a relaxed Ge buffer using commonly available commercial Ge precursors, GeH_4, in combination with $SnCl_4$ precursors, using RP-CVD is comprehensively investigated. Since Ge_2H_6 is much more expensive, difficult to handle and store than GeH_4, it is of great interest to develop high quality $Ge_{1-y}Sn_y$ epilayers with high Sn concentration using the latter precursor. The effects of Ge precursors (Ge_2H_6 and GeH_4) on the heteroepitaxy of $Ge_{1-y}Sn_y$ epilayers is extensively discussed in chapter 5. After that, in chapter 6, the chemical mechanisms accountable for the CVD growth of $Ge_{1-y}Sn_y$ binary alloys using $SnCl_4$ and GeH_4 precursors at very low temperature are discussed. The effects of growth temperature and $SnCl_4/GeH_4$ ratio on growth rate and layer composition are examined. After that, thermochemical analyses, which show possible reaction pathways, are proposed. In this work, heteroepitaxy of $Ge_{1-y}Sn_y$ is achieved at a very low temperature which has previously been thought to be an impossible task.

The physical, optical, and electrical properties of $Ge_{1-y}Sn_y$, depends on strain relaxation in its crystalline layers. For example, it has been suggested that tensile and compressive strain reduce and increase the required Sn concentration to achieve indirect-to-direct bandgap transition [50]. Therefore, it is essential to fully understand the strain relaxation of $Ge_{1-y}Sn_y$ epilayers, which is done in chapter 7.

The impact of grading the $SnCl_4/GeH_4$ ratio during epitaxial growth of $Ge_{1-y}Sn_y$ epilayers on their growth and quality is examined in chapter 8. Here, the grading means that the $SnCl_4$ flow rate is tuned at a constant rate from a very low level to an appropriate level during growth. This technique was not tested for epitaxial growth of $Ge_{1-y}Sn_y$ binary alloys. This method is

proposed to achieve a high Sn concentration $Ge_{1-y}Sn_y$ using $Ge_{1-y}Sn_y$ with lower Sn concentration as an intermediate epilayer (similar to a VS) to minimise the effective lattice mismatch.

Doped $Ge_{1-y}Sn_y$ epilayers offer more flexibility to control physical, electrical, and optical properties over ordinary $Ge_{1-y}Sn_y$ binary alloys. The ability to carefully control the incorporation of dopant into $Ge_{1-y}Sn_y$ binary alloys is essential for the development of efficient and effective nanoelectronic devices, such as TFETs and MOSFETs, as well as optoelectronic devices, such as LASER diodes and LEDs. In chapter 9, attempt of Attempt of heteroepitaxial growth of p-type (B) and n-type (P) $Ge_{1-y}Sn_y$ binary alloys is done. Furthermore, epitaxial growth of $Ge_{1-x-y}Si_xSn_y$ ternary alloys was investigated. Incorporation of Si into $Ge_{1-y}Sn_y$ epilayers not only improves the physical properties of the epilayers, but also influences their optical and electrical properties, which can be beneficial for device fabrications. As incorporation of Si into $Ge_{1-y}Sn_y$ epilayers leads to a faster increase in bandgap at the Γ-point compared to that at the L-point, the indirect-to-direct bandgap transition in $Ge_{1-x-y}Si_xSn_y$ mostly depends on the concentration of Si rather than Sn. For device fabrication and commercialisation of $Ge_{1-y}Sn_y$ devices, it is essential to develop appropriate techniques for growth of $Ge_{1-y}Sn_y$\Ge multilayers, Ge\$Ge_{1-y}Sn_y$\Ge quantum wells and $Ge_{1-y}Sn_y$\$Ge_{1-z}Sn_z$ in which $y \neq z$. These techniques are developed, examined, and presented in chapter 10.

Chapter 2

Theoretical Background

2.1 Introduction

In this chapter, the crystalline, physical and electrical properties such as the band structure of bulk crystalline Si, Ge, Sn are initially reviewed. Then, the low Sn solubility in Ge, as well as the lattice and band structure of $Ge_{1-y}Sn_y$ binary alloys, are discussed. Some important $Ge_{1-y}Sn_y$ related background and concepts, such as Sn segregation, Sn precipitation, possible defects and strain relaxation, are also described and discussed. After that, epitaxial growth techniques such as MBE, sputtering epitaxy, CVD and challenges for epitaxial growth of $Ge_{1-y}Sn_y$ related materials are reviewed in more detail. Finally, recent progress in $Ge_{1-y}Sn_y$ application and device fabrication in electronics, optoelectronics and quantum devices is presented.

2.2 $Ge_{1-y}Sn_y$

To understand the physical and electrical properties of $Ge_{1-y}Sn_y$, it is essential to first fully understand its elements. As (usually) Si is the best substrate in terms of practicability and applicability, it is important to also investigate its properties carefully. In this section, properties of Si, Ge, and Sn as well as their band structures will be addressed. After that, properties, and possible band structure of $Ge_{1-y}Sn_y$ binary alloy will be discussed, both theoretical and experimental. Finally, some of the most important possible occurrence of defects in $Ge_{1-y}Sn_y$ binary alloys and interfaces will be shown.

2.2.1 Physical Properties of Si, Ge, & Sn

Crystalline Si and Ge are both group IV semiconductors having diamond cubic lattice structure, as known as FCC, with strong covalent bonds. On the other hand, another element of this group, Sn, has two allotropes with the occurrence of phase transition at a temperature of 13.2 ℃. The semiconducting phase with diamond cubic lattice is called α-Sn, also known as grey Sn due to its colour. The metallic phase, β-Sn (or white Sn), has a body centred tetragonal structure [9,10]. Some of their primary properties can be found in Table 1. Moreover, bonds in crystalline Sn are "borderline" between metallic and covalent [51]. Crystal structures of both Sn allotropes, including their temperature ranges, are shown in Figure 2.1. It should be noted that there is large change in volume, about 26 %, during allotropic transformation [52]. Due to these properties of crystalline Sn, the synthesis of Sn and thus the discovery of its electronic properties were challenging tasks [9,10].

Phase	**Crystal Structure**	**Lattice Constant (Å)**	**Cell Volume ($Å^3$)**	**Density (gcm^{-3})**	**Stable at Temperature (℃)**
α-Sn	Diamond cubic	6.493	273.233	5.771	≤ 13.2
β-Sn	Body centered tetragonal	a: 5.831 c: 3.182	108.190	7.288	≥ 13.2

Table 1 Properties of two allotropes of Sn.

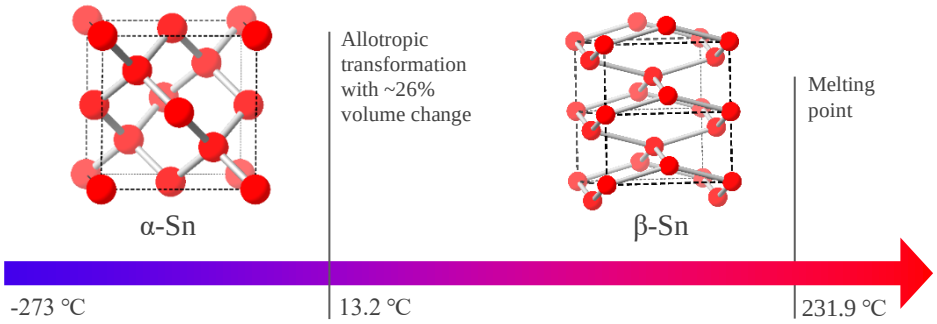

Figure 2.1 Crystalline lattice structures of both Sn phases, β Sn (a: 5.831 Å, c: 3.182 Å) and α-Sn (6.493 Å).

Diamond cubic lattice structures of Si (5.431 Å), Ge (5.658 Å), and α-Sn (6.493 Å) [10] with relative proportional lattice constant are all given in Figure 2.2, where large lattice mismatch can be seen visually. These crystal structures are modelled using CrystalMaker software and relative differences between their lattice constants are considered.

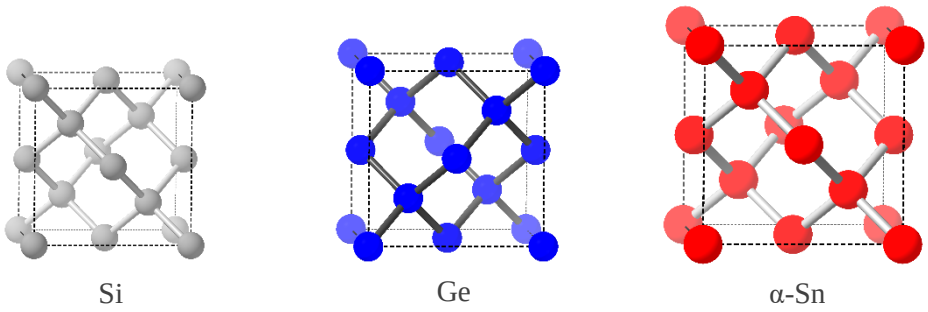

Figure 2.2 Diamond cubic lattice structures (FCC) of Si (5.431 Å), Ge (5.658 Å), and α-Sn (6.493 Å) presented with relative proportional lattice constants.

2.2.2 Band Structure of Si, Ge, & α-Sn

The band structure of α-Sn was studied using photoemission spectroscopy on α-Sn films on CdTe and InSb substrates [52], that were grown using a MBE technique developed at that time [10,15]. In 1963, a model for the band structure of α-Sn was proposed, in which α-Sn is considered as a semimetal with an inverted band structure [53]. Valence and conduction bands in the band structure of α-Sn are bent upwards and downwards, respectively, which creates a negative bandgap of $E_{g\Gamma}$ = -0.41 eV [10]. It is possible to compare the band structure of α-Sn with that of bulk Si and Ge, both of which have an indirect bandgap, as shown in Figure 2.3. All three bulk Si, Ge and α-Sn do have a diamond cubic (or FCC) lattice structure as seen in Figure 2.2.

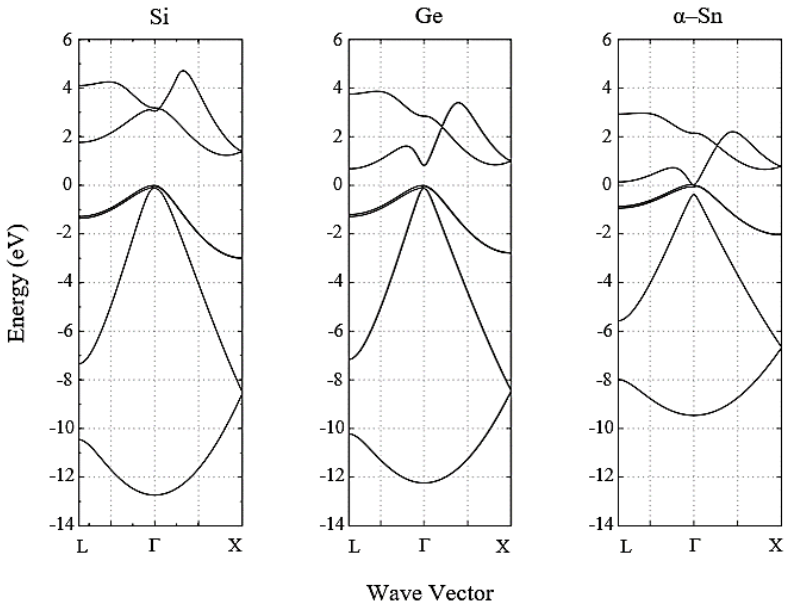

Figure 2.3 Electronic band structure of bulk Si (1.12 eV), Ge (0.66 eV) and α-Sn (-0.41 eV) at ambient temperature [54].

2.2.3 Sn Solubility in Ge

Due to the large covalent radius of α-Sn (1.431 Å) compared to Ge (5.658 Å) [10], that is 14.7% to Ge as shown in Figure 2.2, the solid solubility of α-Sn in Ge is extremely low.

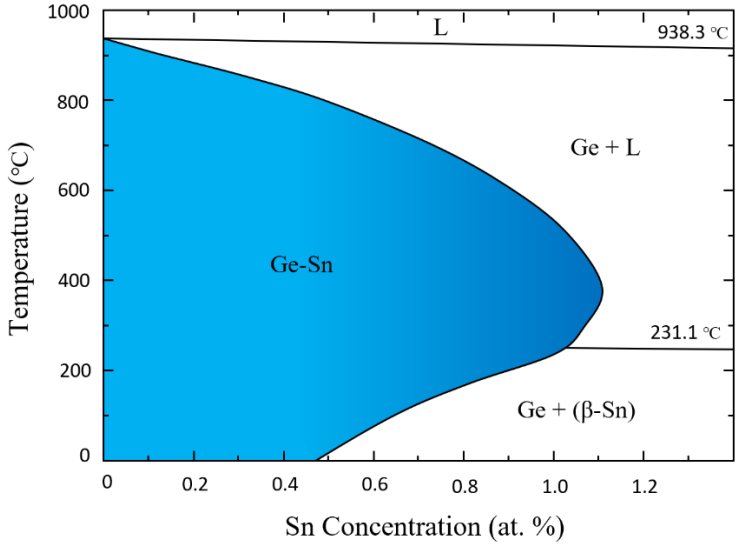

Figure 2.4 Phase diagrams of the Ge-Sn system reproduced after reference [55]. The melting temperature for Sn is 231.1 °C.

The maximum Sn solubility in Ge is 1.1 at.%, approximately [55]. The solid solubility of α-Sn in Si is even lower, less than 0.1 at.%, because of greater lattice mismatch between α-Sn and

Si. It should be noted as Si concentration in Ge increases, the solid solubility of α-Sn decreases significantly [56]. As shown in Figure 2.4 (marked blue), there is a single phase region $Ge_{1-y}Sn_y$ with y < 1.1 at.% in equilibrium. However, the Ge-Sn phase diagram is dominated by other two phase mixtures (both with y < 0.01) of Ge+β-Sn, that is solid Ge with solid β-Sn, and Ge+L, that is solid Ge with liquid β-Sn, below and above Sn melting temperature of 231.1°C [55]. This is the reason why non-equilibrium growth conditions for growth of $Ge_{1-y}Sn_y$ are required to go beyond Sn concentration of 1.1 at.%. It is also necessary to take such growth conditions into account in order to avoid phase separation as a result of bulk Sn precipitation or surface segregation.

2.2.4 Strain-Relaxation of $Ge_{1-y}Sn_y$ & h_c

Cross sectional schematic of Ge and $Ge_{1-y}Sn_y$ lattices are given in Figure 2.5. It is not surprising that $Ge_{1-y}Sn_y$ lattice constant is larger than that of Ge, however, such lattice constant depends closely on Sn concentration in $Ge_{1-y}Sn_y$. As the Sn concentration (y) in $Ge_{1-y}Sn_y$ binary alloy increases, we expect its lattice constant increases.

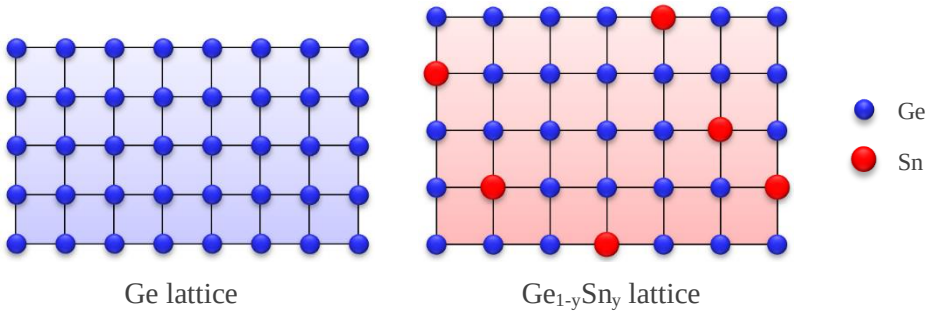

Figure 2.5 Two dimensional schematic of Left: diamond cubic (FCC) structure of Ge lattice, and Right: diamond cubic (FCC) structure of $Ge_{1-y}Sn_y$ lattice. Exaggerated differences for both lattice constants and atom sizes are considered for a better representation.

Later, it will be shown how such a relationship between Sn concentration and lattice constant can be used to estimate Sn concentration in $Ge_{1-y}Sn_y$ epilayer with high accuracy. Before this, however, it is necessary to understand how the large lattice mismatch between $Ge_{1-y}Sn_y$ and Ge (or Si) can influence the epitaxial growth of $Ge_{1-y}Sn_y$ epilayers on Ge-VS (or Si substrate). Here, Ge-VS is a substrate that consists of Ge layer, which is epitaxially grown on an Si substrate.

When growing a material with the same crystal structure with a different lattice constant from the substrate or buffer layer (as a VS), the grown material either has a tensile strain or a

compressive strain. In the case of $Ge_{1-y}Sn_y$ grown on Ge-VS (or Si substrate), the grown $Ge_{1-y}Sn_y$ epilayer will have a tensile strain because its lattice constant is larger than that of Ge-VS (or Si substrate). If the grown $Ge_{1-y}Sn_y$ has exactly the same inner plane (in-plane) lattice parameter as its Ge-VS (or Si substrate), but larger outer plane (out-of-plane) lattice parameter, we call it a fully strained $Ge_{1-y}Sn_y$ as seen in Figure 2.6 (left). Fully strained $Ge_{1-y}Sn_y$ can be grown up to a certain thickness, so called critical thickness h_c, which mainly depends on Sn concentration (y). Above h_c, $Ge_{1-y}Sn_y$ epilayer gradually begins to relax the tensile strain by forming misfit dislocations.

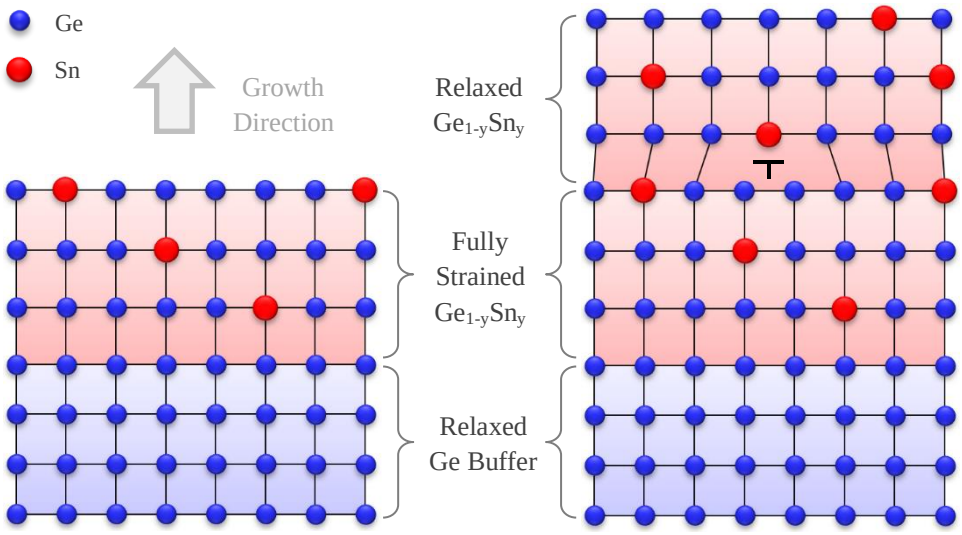

Figure 2.6 Two dimensional schematic presentation of the strain relaxation of fully strained $Ge_{1-y}Sn_y$ grown on Ge-VS. Left: Fully strained $Ge_{1-y}Sn_y$ epilayer grown on a relaxed Ge buffer layer. Right: Strain relaxation of $Ge_{1-y}Sn_y$ is achieved after growing over h_c, and as a result, a misfit dislocation is formed (shown with ⊤ symbol). Exaggerated differences for both lattice constants and atom sizes are considered for a better presentation.

Theoretical calculations of h_c for $Ge_{1-y}Sn_y$ films grown on Si substrate via a relaxed Ge-VS, as shown in Figure 2.7, were done using the People Bean (P-B) model and the Matthew Blakeslee (M-B) model.

The growth of high quality $Ge_{1-y}Sn_y$ directly on Si substrate using CVD is very challenging due to their large lattice mismatch. To overcome this challenge, a high quality relaxed Ge buffer, which has a smaller lattice constant than Si, can be grown on Si substrate and used as an intermediate layer (VS) to reduce the effective lattice mismatch. The strain is a key parameter that influences the physical, optical, and electrical properties of the $Ge_{1-y}Sn_y$ epilayer. In addition to Sn concentration, it is possible to adjust carrier mobility [57,58] and

band structure [50,59] of the epilayer by modifying the strain in the $Ge_{1-y}Sn_y$ epilayer, which will be discussed later.

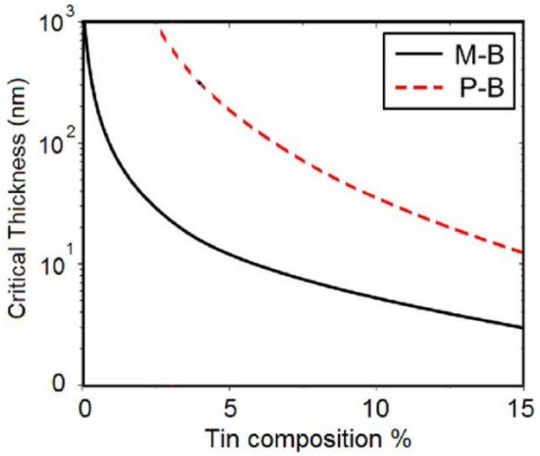

Figure 2.7 Theoretical calculations of h_c for $Ge_{1-y}Sn_y$ films grown on Si substrate via a relaxed Ge-VS using the People Bean (P-B) model and the Matthew Blakeslee (M-B) model.

2.2.5 Band Structure $Ge_{1-y}Sn_y$

Theoretically, it is possible to tune the energy bandgap of $Ge_{1-y}Sn_y$ alloy from 0.66 eV down to 0.0 eV by modifying the Sn concentration in $Ge_{1-y}Sn_y$ [16,60]. Ge is a group IV semiconductor with an indirect bandgap and an energy difference of 0.66 eV between the lowest conduction band minimum, L-point, and the highest valence band maximum, Γ-point, at ambient temperature [10]. As y increases in $Ge_{1-y}Sn_y$, the L-valleys diminishes slower than the Γ-valley as a consequence of $E_{g\Gamma,Ge} - E_{g\Gamma,\alpha\text{-}Sn} > E_{gL,Ge} - E_{gL,\alpha\text{-}Sn}$, suggesting an indirect-to-direct bandgap transition for a certain y [10]. It has been shown that bandgap energy decreases as a result of tensile biaxial strain in $Ge_{1-y}Sn_y$, as the effect of strain is significantly higher in direct gap than indirect [61,62]. The achievement of direct bandgap $Ge_{1-y}Sn_y$ depends strongly on its strain relaxation, for instance, for compressive strained $Ge_{1-y}Sn_y$, higher Sn concentration is required for an indirect-to-direct bandgap transition than tensile strained $Ge_{1-y}Sn_y$ [10].

The effect of biaxial strain on the bandgap structure of $Ge_{1-y}Sn_y$ was theoretically investigated. It was suggested that tensile and compressive strain will respectively lower and raise the required Sn concentration in order to achieve indirect-to-direct bandgap transition in $Ge_{1-y}Sn_y$ [50]. Tensile strained $Ge_{1-y}Sn_y$ could be grown on partially or fully relaxed $Ge_{1-y}Sn_y$ [63-66] while compressive strained $Ge_{1-y}Sn_y$ could be grown on Si via Ge-VS [67,68]. Recent

predictions show that indirect-to-direct bandgap transition in $Ge_{1-y}Sn_y$ could be achieved with Sn concentration of 6–11 at.% [50,69-73].

2.2.6 Bandgap Energy as a Function of Crystal Lattice

The range of bandgap energy, a function of lattice constant for $Ge_{1-y}Sn_y$, as well as those of other III-V semiconductor alloys, is shown in Figure 2.8 [74]. As can be seen, the unique range of bandgap energy and lattice constant of $Ge_{1-y}Sn_y$ could expand the horizon of possible applications in electronic and optoelectronic devices. It should be noted that there is a transition in the rate of reduction of bandgap energy at the lattice constant of ~0.58 nm for $Ge_{1-y}Sn_y$, as seen in Figure 2.8.

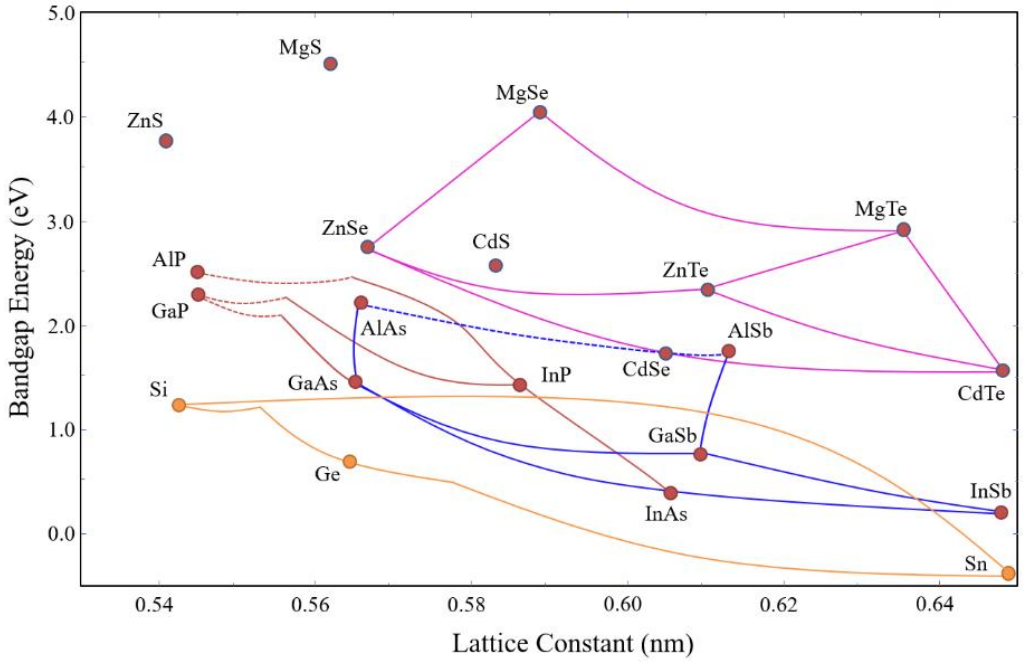

Figure 2.8 The range of bandgap and lattice parameters of Si, Ge and α-Sn with comparison to those of other III-V semiconductor alloys, reproduced after reference [74].

2.3 $Ge_{1-y}Sn_y$ Epitaxy

2.3.1 Introduction

$Ge_{1-y}Sn_y$ alloys as a new group IV material have received great attention in recent years. Many epitaxial growth techniques have been used to grow high quality $Ge_{1-y}Sn_y$ alloys on Si substrates. In general, epitaxy describes a single crystalline film growth on a substrate in which grown layers have the same orientation as their substrate [75]. Epitaxial growth proceeds when atoms are attached to the appropriate position of the corresponding lattice. The formation of crystals by atoms from the vapour phase generally involves three steps of adsorption, diffusion and incorporation into the surface, as shown in Figure 2.9.

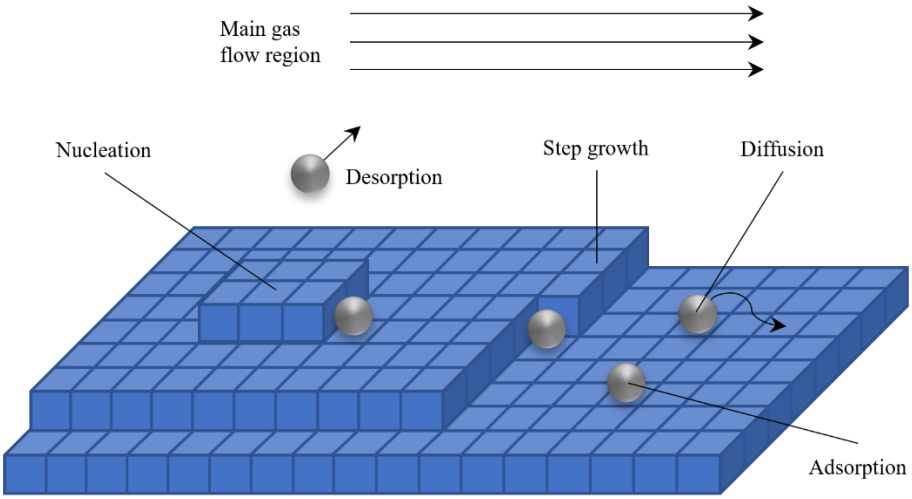

Figure 2.9 Overview of the steps in the epitaxial growth of a layer from the vapour phase.

2.3.2 Challenges

Epitaxy is a form of material deposition and crystal growth in which new crystalline layers are formed with one or more orientations regarding the crystalline substrate layer. When growing high quality crystal, the energy is minimised, which is a necessary driving force of epitaxial growth. A clean surface of the substrate, which yields information about orientation, is a primary requirement for epitaxial growth. If the surface is rough or not clean, the epitaxial grown layers will have crystal defects or be amorphous or polycrystalline. Considering this, it could be useful to have a vapour or chemical wet and appropriate annealing process before epitaxial growth to remove carbon residues and oxides. The epitaxial growth occurs layer by layer on top of the substrate when atoms are placed and attached appropriately within the given

lattice appropriately. Epitaxial growth could be homoepitaxy and heteroepitaxy. Homoepitaxy is when the substrate and grown material on it have the same material. This could be used to grow doped layers of the same material as the substrate. On the other hand, heteroepitaxy is a variety of epitaxy, in which an epitaxial layer is deposited on a substrate with a different material. This type of epitaxial growth could be used for the growth of virtual substrates, intermediate layers, heterojunction devices, source-drain engineering, quantum wells growth, and selective epitaxial growth [10].

There are also three growth modes: Volmer Weber (island formation), Frank van der Merwe (layer-by-layer), and Stranski Krastanov (layer-plus-island). These modes depend closely on differences in chemical and structural properties of substrate and epilayer(s). Lattice constant and thermal expansion mismatch between substrate and epilayer, as well as solubility of materials (for example Sn solubility into Ge) are just a few examples of these chemical and structural properties. In this respect, the free energies at the interface between the substrate and the growing layer are an important parameter. Such energies can be defined by considering excess energies compared to the bulk of:

- A thin epilayer at the interface
- A distorted layer with thickness of 1-2 monolayer(s) at the growing epilayer surface
- A distorted layer with thickness of 1-2 monolayer(s) at the substrate surface [76,77]

The transition of the growth mode from a 2D growth mode (Frank-van der Merwe mode) [78], in which growth is done layer by layer, to 3D growth mode (Volmer-Weber mode) [10,79], which is island based growth, occurs when the sum of the free energies of the epilayer-substrate interface and the growing epilayer is greater than the free energy of the substrate. However, if the lattice mismatch between substrate and growing epilayer is large, in which strained epilayers with low free energies of the substrate and epilayer–substrate interface. In such a case, a 2D wetting layer may be grown (Stranski–Krastanov mode) [10,80] before the growth of the islands. The formation of these islands occurs after exceeding the corresponding h_c to elastically release the strain within the epilayer lattice. As the thickness of the epilayer continues to increase, the relaxation of the epilayer begins via phase separation or plastically [10]. While grown epilayers have the same orientation as their substrate, their lattice constant could be changed as they become thicker, known as strain relaxation, as previously explained. Although Ge-VS and Si (001) are mostly used substrates for recent $Ge_{1-y}Sn_y$ growth, most researchers preferred other substrates than these two at the beginning

of $Ge_{1-y}Sn_y$ discovery [10]. The technique, so called substrate stabilised metastable epitaxy, in which metastable growth could be achieved by using substrate materials with the minimum possible lattice mismatch compared to $Ge_{1-y}Sn_y$ to prevent Sn segregation and avoid surface kinetic roughening [28].

Although $Ge_{1-y}Sn_y$ binary alloy holds promises in optoelectronics, electronics and quantum devices applications, the epitaxial growth of high quality $Ge_{1-y}Sn_y$ binary alloys on Si substrate, with various Sn concentrations, has remained the main technical challenge. The covalent radius of α-Sn (1.405 Å) is 14.7% greater than Ge (1.225 Å) [81,82]. Keeping this in mind, it is foreseeable that the solid solubility of α-Sn into Ge or Si is relatively low. Figure 2.4 shows that the maximum bulk solubility of Sn into Ge is ~1.1 at.% and decreases when it approaches the eutectic temperature of Sn (231.1 °C) [55]. Therefore, in order to synthesise metastable $Ge_{1-y}Sn_y$ binary alloys with Sn concentration over bulk solubility of Sn in Ge, it is essential to consider thermodynamic non-equilibrium growth conditions. Moreover, the large lattice mismatch between α-Sn and Si (with the covalent radius of 1.173 Å) is 19.7% [81,82] leading to formation of defects, especially at interfaces, during $Ge_{1-y}Sn_y$ heteroepitaxy on Si substrate. Furthermore, during heteroepitaxy of $Ge_{1-y}Sn_y$ epilayer on its corresponding substrate (for example Ge-VS), built-in strains of grown layers of $Ge_{1-y}Sn_y$ epilayer can be used for bandgap engineering. It should also be noted that these built-in strains within grown layers of $Ge_{1-y}Sn_y$ epilayer can probably influence $Ge_{1-y}Sn_y$ binary alloy phase breakdown and plastic relaxation processes. Moreover, if the thickness of $Ge_{1-y}Sn_y$ epilayer is greater than the h_c dislocations can form at the two ends of the misfit [83]. These dislocations could create a loop so that the two ends can join or thread onto the surface, which could potentially restrict $Ge_{1-y}Sn_y$ applications [84,85]. Considering this, it is essential to explore and fully understand the strain relaxation mechanism and h_c in $Ge_{1-y}Sn_y$ epilayers which closely depend on their Sn concentrations.

It should be noted that careful consideration should be taken to appropriately adjust growth temperature as the most important growth condition and understand its impact on growth rate and Sn concentration of $Ge_{1-y}Sn_y$ epilayers [10]. Since the melting temperature and surface energy of Sn are lower than those of Ge, Sn segregation can occur during $Ge_{1-y}Sn_y$ binary alloy epitaxy at a temperature range of about 140 ℃ to 250 ℃ [60]. As shown in Figure 2.10, Figure 2.11 and Figure 2.12, the main challenge is to prevent phase separation through Sn precipitation or segregation, which results due to comparably low free surface energy of

Sn [10]. In order to epitaxially grow crystalline single phase $Ge_{1-y}Sn_y$ without Sn segregation, low growth temperatures (< 475 °C) should be used. In modern epitaxy methods, very low growth temperatures are used, in which lattice diffusion is minimised and h_c is increased [75]. However, as the growth rate usually decreases with regard to the reduction of growth temperature, the suppression of segregation necessary for successful growth becomes a challenging task.

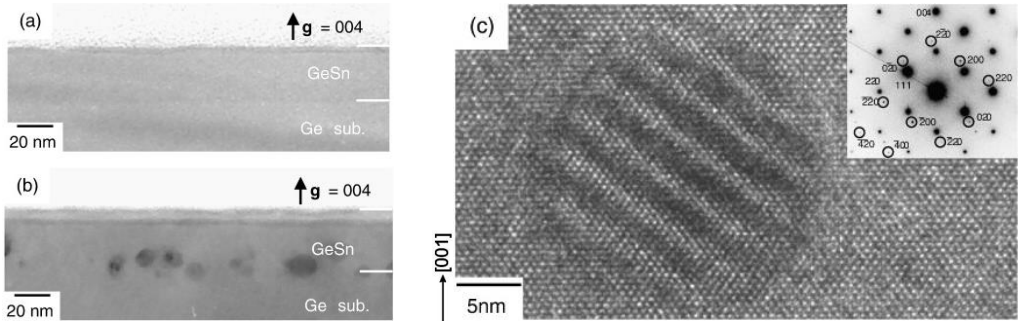

Figure 2.10 a) $Ge_{0.92}Sn_{0.08}$ epilayer grown on Ge-VS [65]. b) Precipitation of Sn within $Ge_{0.92}Sn_{0.08}$ epilayer grown on Ge-VS as a result of annealing process [65]. c) Lattice resolution of Sn precipitation within $Ge_{0.92}Sn_{0.08}$ epilayer [65].

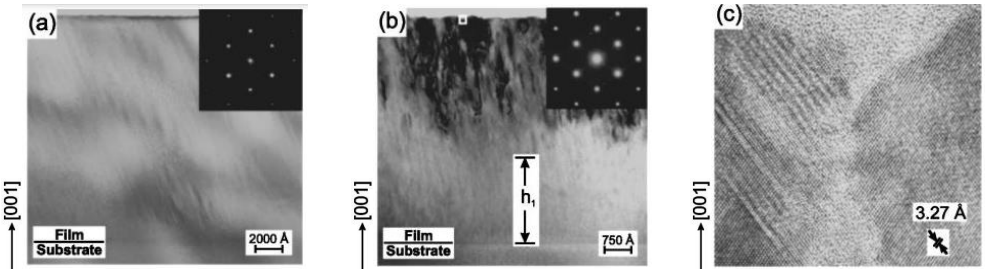

Figure 2.11 a) X-TEM micrograph of 630 nm thick $Ge_{0.945}Sn_{0.055}$ epilayer grown on the substrate from [86]. b) X-TEM micrograph of the $Ge_{0.945}Sn_{0.055}$ epilayer in DF showing effect of strain relaxation when growing over h_c from [86]. c) Lattice resolution of Sn precipitation within the $Ge_{0.945}Sn_{0.055}$ epilayer from [86].

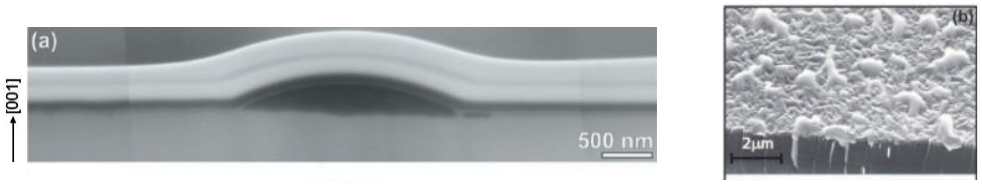

Figure 2.12 a) X-TEM micrograph of a Sn droplet that is formed on the surface of the $Ge_{1-y}Sn_y$ epilayer grown on Ge-VS from [87]. b) Scanning electron micrograph of segregation of Sn on the surface of $Ge_{1-y}Sn_y$ during epitaxial growth at relatively high temperature of 475 °C from [45].

In addition, since Sn has relatively low solid solubility in Ge [7,8] and Si [88], as well as low surface energy compared to Ge [89,90]. Consequently, during growth or annealing processes of $Ge_{1-y}Sn_y$ binary alloy, precipitation of Sn atoms may lead to Sn segregation on the surface of $Ge_{1-y}Sn_y$ epilayer [91-93]. Additionally, the desorption of Sn from the surface of the $Ge_{1-y}Sn_y$ epilayer may be caused by deposition or annealing processes at high temperatures [91,92,94]. These indicate that the fabrication of Sn based devices (such as MOSFET) is challenging, as it is difficult to carefully maintain or manipulate behaviour of Sn atoms in $Ge_{1-y}Sn_y$ epilayer, either during growth or annealing processes. To address these challenges, it is necessary to control the interface structures of MOSFETs by using surface oxidation, capping layers and epitaxial growth techniques [6].

A linear segregation model can illustrate approximation of exchange of adatom (Ge) with surface dopant atom (Sn) [35,95] as following:

$$n_s = n\Delta_s \qquad (2.1)$$

Here n_s is the surface adatoms concentration, n is the bulk Sn concentration, and Δ_s is the length of segregation. In order to avoid Sn segregation on the surface of the $Ge_{1-y}Sn_y$ epilayer, the growth temperature should be kept at its lowest possible level. It should be noted that at low growth temperatures, the exchange rate between adatoms (Ge) and surface dopant atoms (Sn) is reduced. Moreover, increasing growth rates, which can reduce the required time slot for exchange, can lead to suppression of Sn segregation. However, Sn precipitation, as shown in Figure 2.10 and Figure 2.11, is usually due to post growth processes such as annealing processes [10,65].

It is interesting to look closely at the SEM image in Figure 2.13, where a large Sn-rich micro-island with a diameter of ~10μm moved on the surface and absorbed the smaller Sn-rich islands. Looking at Ge and Sn images in Figure 2.13, which were obtained using the EDAX EDS, it becomes clear that these micro-islands are Sn-based. It should also be noted that the surface roughness in areas of the $Ge_{1-y}Sn_y$ epilayer where none of these noticeable Sn-rich islands is less than ~3 nm.

In general, if the growth rate in relation to the available amount of Sn atoms on the surface is not sufficient, then the Sn atoms on the surface can form these Sn-rich islands, which can effectively terminate $Ge_{1-y}Sn_y$ growth. Furthermore, there may be other factors that can prevent Sn from segregating on the surface. One could be the flow of carrier gas H_2, which

can remove some extra Sn atoms on the growing layers. Another factor could be the effect of produced HCl, which could potentially etch and remove these Sn structures from the surface of growing layers during the $Ge_{1-y}Sn_y$ growth. This later factor is discussed in more detail in chapter 6.

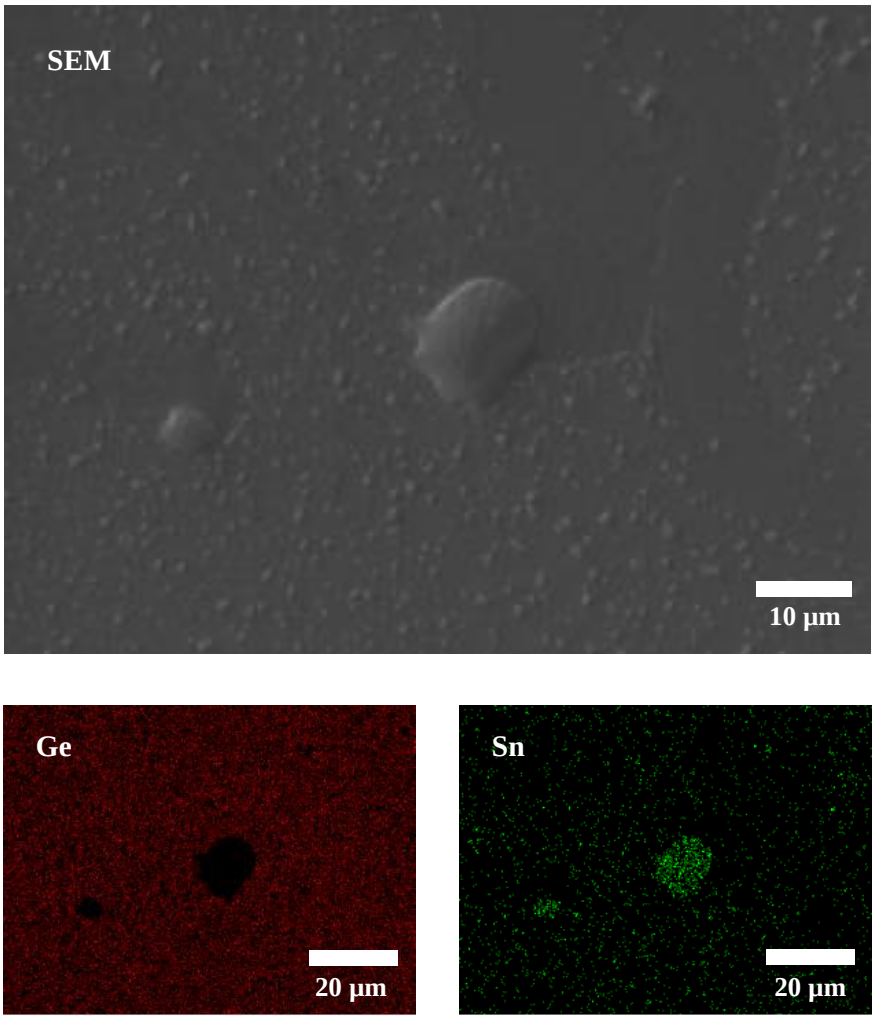

Figure 2.13 Top: SEM image of $Ge_{0.894}Sn_{0.106}$ grown on Si (001) via Ge-VS with growth temperature of 270 °C and growth pressure of 500 Torr and growth time of 20:00 min using 2.6×10^{-3} $SnCl_4/GeH_4$ partial pressure ratio. Left: Same area analysis of Ge detected. Right: Same area analysis of Sn detected.

Many efforts have been made to research and develop epitaxial $Ge_{1-y}Sn_y$ growth methods using various growth techniques, such as MBE [17,21,96], MO-CVD [97], UHV-CVD [47,98] and RP-CVD [39,49,99]. In the following sections, some of the most promising epitaxial growth techniques are presented in more detail.

2.3.3 CVD

Growth of $Ge_{1-y}Sn_y$ binary alloy on Si (100) by UHV-CVD at 350 °C with $C_6H_5SnD_3$ (replacement of one D by Ph = C_6H_5 in SnD_4 for stability enhancement) and Ge_2H_6 as Sn and Ge precursors, respectively, was first introduced in 2001 [47]. In the same year, it was also shown H_2 diluted SnD_4 could be used to grow high quality $Ge_{1-y}Sn_y$ due to its high stability [46]. It was later reported that it is also possible to grow $Ge_{1-y}Sn_y$ on Si (100) using SnD_4 and Ge_3H_8 precursors at lower growth temperatures [100].

It was previously suggested that due to concomitant surface roughening and Sn precipitation, it is not possible to grow $Ge_{1-y}Sn_y$ alloys at temperature above 350 °C [48]. As SnD_4 synthesis is not easy, widely commercially available Sn precursor, $SnCl_4$, which is also more stable and commercially available than SnD_4 [60], and Ge_2H_6 were then successfully used to grow $Ge_{1-y}Sn_y$ with 8% Sn concentration on Ge(001) substrate in AP-CVD [39]. Total absence of instability issues was mentioned as the main advantage of $SnCl_4$ over SnD_4; But more importantly, the growth temperature was reported as low as 320 °C when using Ge_2H_6 and $SnCl_4$ [39]. Since then, to keep the growth temperature in such range, Ge_2H_6 has been preferred over other Ge precursors, even when using $SnCl_4$ [39,40]. The main reason for this is that Ge_2H_6 is more reactive than the other commercially available Ge precursor, GeH_4, at temperature lower than 350 °C [101]. It has also been believed that Ge_2H_6 has two order of magnitude higher growth rate than GeH_4 when growing Ge under similar growth conditions [101].

Nevertheless, it should also be noted in order to increase Sn concentration in $Ge_{1-y}Sn_y$, it is necessary to reduce growth temperature [102], which means we cannot simply compare growth rate of $Ge_{1-y}Sn_y$ at very similar growth temperature when using either of GeH_4 or Ge_2H_6. Instead, we need to compare growth rate of similar grown $Ge_{1-y}Sn_y$ when using one of these Ge precursors. More recent research achieved successfully grown $Ge_{1-y}Sn_y$ binary alloys using GeH_4 and $SnCl_4$ [49,68,103]. Today not only it is possible to grow high quality $Ge_{1-y}Sn_y$ with relatively high Sn concentration using $SnCl_4$ and GeH_4, but also it is possible to do it at temperature lower than 350 °C [68]. It should also be noted that commercially available GeH_4 is much more cost effective than Ge_2H_6 [60,103] and therefore it is more favourable in commercialisation of $Ge_{1-y}Sn_y$ optoelectronic devices. However, there are some studies on technical advantages of using GeH_4 over Ge_2H_6 in terms of epitaxial growth of high quality $Ge_{1-y}Sn_y$ [68,103].

One of the main challenges in the development of epitaxial growth of $Ge_{1-y}Sn_y$ binary alloys (as well as $Ge_{1-x-y}Si_xSn_y$) using CVD techniques is the lack of stable Sn precursors. At ambient temperature, Sn hydrides are extremely unstable and thus immediately dissociate because of the low bond energy of SnH [10]. The initial successful growth of monocrystalline $Ge_{1-y}Sn_y$ epilayers, by means of UHV-CVD, was achieved using Ge_2H_6 and $C_6H_5SnD_3$ precursors at the growth temperature of 350 °C. These $Ge_{1-y}Sn_y$ epilayers with Sn concentrations of 5 at.% to 12 at.% were grown directly on Si (001) with a growth rate of 1 nm/min, approximately [46,47,104].

Later, another Sn precursor, SnD_4, was introduced, which extended the permitted growth temperature window to 250 °C to 350 °C when used alongside Ge_2H_6 [37,105,106]. Nevertheless, it has been unclear how adequate reactivity can be achieved for corresponding chemical precursors during epitaxial growth [102]. It has been shown that the incorporation of Sn into $Ge_{1-y}Sn_y$ epilayers can increase due to a reduction in growth temperature. However, it is not practical to grow $Ge_{1-y}Sn_y$ epilayers with relatively significant thickness using SnD_4 and Ge_2H_6 precursors due to a very limited growth rate at lower growth temperatures, where a high Sn concentration is achieved, which is necessary for optoelectronic applications [10].

In addition to Ge_2H_6 precursor, higher order Ge hydride precursor, Ge_3H_8, was used in combination with SnD_4 to enhance growth rate of $Ge_{1-y}Sn_y$ at reduced growth temperature to achieve thick $Ge_{1-y}Sn_y$ epilayers with high Sn concentration (up to 9 at.%) [100]. This is due to higher elevated reactivity and lower decomposition temperature of Ge_3H_8 [10].

2.3.4 Other Epitaxial Techniques: MBE, Sputtering

MBE is a widely used growing technique for the growth of high quality $Ge_{1-y}Sn_y$ binary alloys on Si, Ge, or other substrates. There have been several reports of successful growth of $Ge_{1-y}Sn_y$ epilayers on Ge or Si substrates, in which Sn and Ge were typically deposited in an UHV chamber with Knudsen cells [20,21,23,29,107,108]. The estimated equilibrium vapour pressure of Sn is at 9.8×10^{-10} Torr and 4.5×10^{-7} Torr at 500 °C and 800 °C, respectively [109], while the melting point of Sn is relatively low at 231.1 °C. Therefore, a relatively high crucible temperature of up to 800 °C may be required to achieve a sufficient growth rate, which is necessary to suppress Sn segregation [6]. To successfully grow high quality $Ge_{1-y}Sn_y$ without the appearance of Sn precipitation using MBE, it is necessary to carefully select an appropriate substrate temperature. A common temperature, which is normally used for epitaxial growth

of Ge (>400 °C), cannot be used for epitaxial growth of $Ge_{1-y}Sn_y$, since Sn precipitation occurs at this temperature. Therefore, a lower growth temperature, down to the eutectic temperature of 231.1 °C, must be used to minimise Sn precipitation [6].

Even though the growth of high quality $Ge_{1-y}Sn_y$ binary alloys has been reported using MBE and CVD, additional research has been carried out to develop alternative $Ge_{1-y}Sn_y$ growth approaches, such as metal-induced crystallisation, solid phase epitaxy and sputtering. Among these methods, it seems that sputtering is the most promising, which could potentially provide an opportunity to achieve an economical mass production of $Ge_{1-y}Sn_y$. The first successful growth of crystalline $Ge_{1-y}Sn_y$ binary alloys on Ge substrates with sputtering was reported in 2002 [25]. It has also been established that it is possible to grow high quality $Ge_{1-y}Sn_y$ with low defect density directly on Si (001) substrate at low temperatures by means of radio frequency sputtering epitaxy [26], which is a method with practical applications in the production of IR optoelectronics [60].

2.3.5 Advantages of CVD

Since CVD offers uniform and homogenous formation of $Ge_{1-y}Sn_y$ on large substrates, it is most important epitaxial growth technique for mass production of $Ge_{1-y}Sn_y$ applications, especially for development of Si ultra-large-scale integrated devices [6]. In this work, we tend to fully understand the effects of CVD growth conditions such as pressure and temperature on $Ge_{1-y}Sn_y$ epilayers when using $SnCl_4$ and GeH_4 as Sn and Ge precursors, respectively. It will be presented how it could be possible to grow high quality $Ge_{1-y}Sn_y$ with high Sn concentration at a very low temperature, which has not been reported before, and explore techniques we have used to achieve growth rates at a temperature that has not been reported by any other research groups to grow $Ge_{1-y}Sn_y$. The $SnCl_4/GeH_4$ ratio is considered as a primary CVD condition to understand the effect of precursors on epitaxial growth of $Ge_{1-y}Sn_y$ epilayers.

2.3.6 Importance of Quality of $Ge_{1-y}Sn_y$ Related Materials on Applications

The lowest activation energies of growth rate for grown $Ge_{1-y}Sn_y$ using CVD were recorded at 0.26 eV. Nevertheless, a rapid thermal annealing for $Ge_{1-y}Sn_y$ should be carried out after its growth to observe photoluminescence (PL) spectra, which depends on Sn concentration, at ambient temperature. The rapid thermal annealing could greatly improve the crystalline quality of the $Ge_{1-y}Sn_y$ epilayer. Since thermal annealing can diminish defects, the non-radiative recombination paths can also be reduced. Thus, the FWHM of the XRD peak

can be reduced. It should also be noted that there may be a red shift in PL peaks due to the decreased bandgap of $Ge_{1-y}Sn_y$, as a consequence of an increase in Sn concentration [10].

The development and use of high quality Ge-VS has been one of the most prominent achievements, leading to the development and epitaxial growth of high quality $Ge_{1-y}Sn_y$ binary alloys with Sn concentration exceeding the bulk solubility of Sn into Ge [110-114]. Ge (001) substrate is a more appropriate alternative to Si (001) substrate due to a significantly lower lattice constant mismatch between substrate and $Ge_{1-y}Sn_y$ epilayer. A reduction in the lattice mismatch between substrate and epilayer leads to an improvement in the optical and crystalline quality of $Ge_{1-y}Sn_y$ binary alloys, which can lead to substantial improvement in PL signals. $Ge_{1-y}Sn_y$ binary alloy with a Sn concentration of ~10 at.% and thickness of ~0.6 μm was grown on Ge-VS using UHV-CVD method with SnD and Ge_3H_8 precursors [43,115,116]. The degree of strain relaxation of the grown $Ge_{1-y}Sn_y$ epilayers was ~80 %, while the highest achieved growth rate was ~9 nm/min [115].

PL analysis for $Ge_{1-y}Sn_y$ epilayers with Sn concentration of over 7 at.%, in which XRD FWHM exceeds 0.18° [43], becomes possible without considering any post growth thermal annealing. As Sn concentration in $Ge_{1-y}Sn_y$ increases, the PL peaks increase and redshift, demonstrating that the offset between L- and Γ-valleys is reduced in the bandgap of the binary alloy. In addition, further PL analysis brought the following assumptions for the bowing parameters b_0 and b_{ind} [116], which depend on Sn concentration, for the direct and indirect conduction band valleys:

$$b_0(y_{Sn}) = (2.66 \pm 0.09)eV - (5.4 \pm 1.1) \cdot y_{Sn}eV \quad (2.2)$$

$$b_{ind}(y_{Sn}) = (1.11 \pm 0.07)eV - (0.78 \pm 0.05) \cdot y_{Sn}eV \quad (2.3)$$

By using these equations, it was predicted that to achieve indirect-to-direct transition, Sn concentration of 8.7 at.% is required [10].

Another Sn precursor, $SnCl_4$, which is a more stable and commercially available precursor, was later introduced in combination with Ge_2H_6 to grow $Ge_{1-y}Sn_y$ binary alloys under atmospheric pressure [39]. High quality fully strained $Ge_{1-y}Sn_y$ with Sn concentration of 8 at.% was grown on Ge-VS at growth temperature of 320 °C using $SnCl_4$ precursor [40]. In further research, $Ge_{1-y}Sn_y$ epilayers with thickness above the strain relaxation h_c, with Sn concentration above 12 at.%, were successfully grown using the same Sn precursor [41,117].

It was confirmed that the lattice constant deviated from Vegard's law with a bowing parameter of 0.041 Å is reasonably close enough to theoretical predictions [118].

It is worth noting that the growth rate itself also depends on the thickness of the $Ge_{1-y}Sn_y$ epilayer. As the thickness of the $Ge_{1-y}Sn_y$ epilayer increases, the more strain relaxation is achieved, and the $Ge_{1-y}Sn_y$ growth rate increases coherently. The mechanism of strain relaxation, which is accompanied by the formation of amorphous $Ge_{1-y}Sn_y$ islands, depends not only on the thickness of the $Ge_{1-y}Sn_y$ epilayer, but also on its Sn composition [117]. These sorts of islands have also been observed for Ge homoepitaxy at atmospheric pressure when using Ge_2H_6 precursor, suggesting that the formation of these islands does not depend solely on the mechanism of strain relaxation, but is also attributed to Ge_2H_6 precursor. Furthermore, it was previously shown that the density of diffused Sn from the formed islands increases with the thickness of $Ge_{1-y}Sn_y$ epilayer and when carrier gas changes from N_2 to H_2 [10,117].

It is assumed that the formation of clusters made of contaminant atoms or hydrogen could suppress available lattice sites on the surface of the wafer during epitaxial growth. To address this problem, epitaxial growth of $Ge_{1-y}Sn_y$ is proposed at higher pressure and reduced pressure, making the appearance of these types of amorphous islands on the surface of grown $Ge_{1-y}Sn_y$ less likely [45]. In addition, X-ray absorption revealed that Sn atoms in $Ge_{1-y}Sn_y$ epilayers, grown in CVD at atmospheric pressure, are covalently bonded in a tetrahedral configuration to Ge atoms without making Sn clusters [119].

Furthermore, several successful epitaxial growths of $Ge_{1-y}Sn_y$ in the reduced pressure regime using different growth conditions and precursor combination were reported by several research teams [42,44,45,49,120]. Without taking into account any thermal treatment process, these grown $Ge_{1-y}Sn_y$ epilayers have shown strong PL signals at ambient temperature. However, the intensity of PL reduces as a function of rapid thermal annealing (RTA). Applying high annealing temperature (above 450 °C) may lead to Sn segregation, and formation of Sn micro-scale structures on the surface of the epilayer [10].

The growth of $Ge_{1-y}Sn_y$ directly on Si (001) substrate at reduced pressure with $SnCl_4$ in combination with Ge_2H_6 was investigated in 2013 [45]. Later, the first attempt to grow $Ge_{1-y}Sn_y$ epilayers with $SnCl_4$ in combination with GeH_4, which is a more conventional and cheaper Ge precursor, was carried out in 2014 [49,120]. The incorporation of Sn into $Ge_{1-y}Sn_y$

has been shown to increase with decreasing growth temperature in reduced pressure condition [10].

The $Ge_{1-y}Sn_y$ growth rate activation energy for ultra-high vacuum CVD epitaxy with Ge_3H_8 in combination with SnD_4 [100] is significantly larger than for AP-CVD epitaxy with Ge_2H_6 [40]. Further study has been carried out to investigate RP-CVD $Ge_{1-y}Sn_y$ epitaxy [44,66,121] on Si (001) substrate via Ge-VS [112,114]. Growth of thick (over 1 µm) $Ge_{1-y}Sn_y$ with high quality crystalline and smooth surface on Ge-VS has been successfully achieved, in which the $Ge_{1-y}Sn_y$ epilayer is partially strain relaxed and has a Sn concentration of over 15 at.% [44]. Such $Ge_{1-y}Sn_y$ epilayers, which exhibit direct bandgap without considering any post growth thermal annealing, could be the final step towards initial development of direct bandgap group IV LASERs [122].

It should be noted that it is possible to extend the growth temperature window by considering Ge-VS over Si (001) substrate [10]. This is mainly due to the smaller lattice mismatch between $Ge_{1-y}Sn_y$ and Ge-VS. As previously explained, sufficient Sn concentrations in strain relaxed $Ge_{1-y}Sn_y$ binary alloys may lead to the indirect-to-direct bandgap transition; thus, converting them into increasing gain material for LASER applications or NMOS [10]. Another way to take advantage of these layers is to consider them as strain relaxed buffer to enable tensile strain overgrown elemental $Ge_{1-y}Sn_y$ layers. Tensile strain of 0.4% in $Ge_{1-y}Sn_y$ was achieved by considering such an epitaxial strain method [121]. Additionally, fully compressive strained $Ge_{1-y}Sn_y$ grown on Si (001) via Ge-VS could be an excellent option for channel material for PMOS [10].

2.4 Progress in $Ge_{1-y}Sn_y$ Devices & Applications

There are many achievements in development of $Ge_{1-y}Sn_y$ binary alloy optoelectronic devices such as IR LEDs [123-127], IR LASER [122,128,129], and IR photodetectors with high efficiency [130-138] and spintronics [102,139]. Group IV LASERs are the best chance for development of monolithic integration of LASERs with Si optoelectronics which could bring many applications in optical communication and sensing [140,141]. However, as both Si and Ge have indirect bandgaps, we cannot expect efficient light emission from them [142-148]. By α-Sn incorporation into Ge lattice, $\Delta E_{\Gamma\text{-}L}$ decreases as y in $Ge_{1-y}Sn_y$ increases. It is not only possible to modify Ge bandgap, but also SiGe by Sn incorporation. It is theoretically possible to tune the energy bandgap of $Ge_{1-y}Sn_y$ alloy from 0.66 eV down to 0.0 eV [16,60]. This means photodetectors with active layer of $Ge_{1-y}Sn_y$ could easily expand the range of Si photonics to mid-IR region. Moreover, as $Ge_{1-y}Sn_y$ undergoes an indirect-to-direct energy bandgap transition for predicted value of 6-11 at.% for Sn concentration, there could be promising applications in highly efficient group IV light sources [50,69].

There are some other potential applications for $Ge_{1-y}Sn_y$ binary alloy, such as MOSFET with high mobility, TFET with low energy consumption and high performance, and IR wave guides [6]. Unlike other group IV semiconductors such as SiGe, in $Ge_{1-y}Sn_y$ binary alloy electrons begin to populate the Γ-valley. This is because the Γ-valley in $Ge_{1-y}Sn_y$ binary alloy with low effective mass in centre of Brillouin zone is below the fourfold degenerated L-valleys energetically. As a result, the electron mobility increases significantly [149], which makes $Ge_{1-y}Sn_y$ a considerable candidate as a channel material with high mobility to be used in n-MOSFETs [10]. Another advantage of $Ge_{1-y}Sn_y$ binary alloy is its possibility of indirect-to-direct bandgap which can have applications for electronics such as tunnel FETs [72]. It has been demonstrated that tunnelling probability can be increased in fundamental direct bandgap semiconductors [73,150] and $Ge_{1-y}Sn_y$ tunnel diodes with negative differential resistance has been achieved [10,151].

Controlling the energy band structure as well as effective mass of $Ge_{1-y}Sn_y$ binary alloy can be done by tuning Sn concentration, y, enables the fabrication of high performance MOSFETs and devices with low power consumption. Operation of p-channel and n-channel $Ge_{1-y}Sn_y$ has not been demonstrated yet with satisfactory performances as expected theoretically [69,149]. It has shown MOSFETs with higher performance could be achieved when considering

p-channel $Ge_{1-y}Sn_y$ MOSFETs over Ge one [6,152,153]. The mobility can be enhanced when Sn concentration in $Ge_{1-y}Sn_y$ increases which could be used for improvement of performance of MOSFETs. However, it is necessary to develop new technologies and optimised fabrication processes in order to make high performance devices. Many optoelectronic applications of $Ge_{1-y}Sn_y$ have been published, including LEDs, LASERs, photovoltaic cells, and photodiodes. In these studies, the properties of $Ge_{1-y}Sn_y$ were employed for the purpose of energy band engineering [122,125,130,154-156]. For example, the narrowing of the energy band can be achieved by increasing the Sn concentration in $Ge_{1-y}Sn_y$. This can extend the available wavelength to a longer range than that of Ge photoelectronic devices. Furthermore, the indirect-to-direct cross over in $Ge_{1-y}Sn_y$ with a Sn concentration of ~8% can substantially improve the performance of photoresponse and photoabsorbance devices. Moreover, $Ge_{1-x-y}Si_xSn_y$ ternary alloys offer many more possibilities for energy band engineering and lattice control technology, like the group III–V compound semiconductors [6]. Furthermore, theoretical estimations for $Ge_{1-y}Sn_y$ LASER applications were reported by several research teams [157-162]. An experimental investigation of lasing in direct bandgap $Ge_{1-y}Sn_y$ grown on a Ge-VS was carried out. The lasing was detected at low temperatures below ~200 °C under optical pumping in a cavity of $Ge_{1-y}Sn_y$ [6,122].

$Ge_{1-y}Sn_y$ photodetectors with high Sn concentration can offer a robust photoresponse at longer IR wavelengths [130,154,155]. In addition, $Ge_{1-y}Sn_y$ heterojunction LED was shown with $Ge_{1-y}Sn_y$ grown on Si substrate, using low-temperature MBE [125]. The $Ge_{1-y}Sn_y$ LED demonstrates a direct bandgap EL at RT, in which its intensity increases as the Sn concentration in $Ge_{1-y}Sn_y$ epilayer increases [6,60]. Ge direct bandgap of 0.800 eV means low responsivities of Ge films for wavelength of over 1550 nm. Here, responsivity, R (W/A), is calculated from ratio of photocurrent (electric current) to input optical power. Such detection spectrum was extended to 1800 nm with effective responsivity by fabricating p-i-n photodetectors out of $Ge_{0.97}Sn_{0.03}$\Ge\Si (001) grown by MBE [130]. In later years, this detection spectrum was tuned and extended up to 2100 nm by mainly modifying $Ge_{1-y}Sn_y$ epilayer [131-135]. Moreover, there have also been some developments on $Ge_{1-y}Sn_y$ based photoconductors (material that its conductivity tuned when exposed to photon) [136,137], however, due to Sn segregation for high Sn concentration $Ge_{1-y}Sn_y$, which is highly related to temperature, low thermal detector fabrication could be a promising approach [60].

Chapter 3

Experimental Techniques

3.1 Introduction

In this chapter, experimental techniques, including epitaxial growth and material characterisation methods used in this research, are given, and explained. The used growth method which is the RP-CVD is explained in the first section of this chapter. In the second section of this chapter, various material characterisation techniques have been used to analyse the quality and characteristics of grown epilayers, such as FTIRS, HR-XRD, AFM, TEM, XPS, SEM and EDS. I ensured that the all characterisation techniques are consistent to confirm that we receive a standardised result and analysis from all grown materials during the research. Different characterisation techniques are required not only to study and examine epitaxially grown materials in different ways, but also to confirm and verify the analyses and results obtained from each of these different techniques. For example, FTIRS, thickness fringes from HR-XRD $\omega - 2\theta$ coupled scans and X-TEM were used to measure the thickness of the epilayers.

3.2 Epitaxial Growth

3.2.1 RP-CVD

In the CVD technique, chemical reactions between gaseous reactants (known as precursors) initiate and drive material deposition (for example $Ge_{1-y}Sn_y$) on the substrate (for instance Ge-VS). Such a deposition method offers low costs and large growth of amorphous, polycrystalline, and monocrystalline layers, but its process development and optimisation may not be simple and requires thorough research and understanding. However, CVD has several advantages compared to other physical vapour deposition techniques, such as MBE. For instance, the possibility of selective growth, high growth rates, uniform and conformal depositions throughout the wafer area, and the ease of quality control in mass production [10]. The method of CVD is based on the thermal decomposition of precursors (gaseous reactants), which can be explained in the following steps:

1. Gaseous precursors are injected into the reactor chamber by carrier gases such as H_2, He, N_2, Ar.
2. Gaseous precursors diffuse towards the surface of the substrate, and initial chemical reactions between them are started.
3. Precursors are completely decomposed due to further chemical reactions between them.
4. Molecules of precursors and products of chemical reactions are adsorbed on the surface of the substrate.
5. Adatom surface are diffused and incorporated into a solid film, which results in material deposition on the surface.
6. Undecomposed molecules of precursors and by-products are desorbed and evacuated from the reactor.

Because of flexibility in considering growth conditions (such as temperature, chamber pressure, and partial pressure of precursors), there are three CVD growth regimes that can be used. Mass flow regime is when a relatively lower growth temperature is taken into account, in which the growth rate depends closely on and is limited by mass flow of precursors. While the growth rate is almost independent of the temperature in the mass flow regime, the distribution of gas flows of precursors over the entire wafer is the factor that indicates the uniformity of the thickness of the growing layers. Nevertheless, for the growth of $Ge_{1-y}Sn_y$

binary alloys, the growth temperature should be kept very low, in which the growth rate is controlled by chemical reactions on the substrate surface. Consequently, such a growth regime is called kinetic growth regime [10].

In the kinetic growth regime, the growth rate and uniformity of thickness depend strongly on the growth temperature. Hence, for the growth of $Ge_{1-y}Sn_y$ binary alloy, it is necessary to consider higher order hydrides, which have a lower composition temperature, in order to achieve a sufficient growth rate at low growth temperatures. In addition, in the kinetic growth regime, those chemical reactions that limit the growth rate are usually Cl or H temperature dependent desorption due to restriction made on open lattice sites on the surface [10]. However, it has previously been demonstrated that we may not need these available lattice sites on the surface when growing $Ge_{1-y}Sn_y$ using higher order hydrides precursors such as Ge_2H_6 [163]. The reason for this is that the surface reaction, as shown below [40], could form these available lattice sites:

$$Ge_2H_6 + H \rightarrow GeH_4 + GeH_3$$

The desorption of H from the surface could also be accelerated by the formation of GeH_4 from GeH_3 [10].

The epitaxial growth of $Ge_{1-y}Sn_y$ can also depend on the design of the CVD machine, such as its wafer transfer system, gas delivery system, and reactor module. The mechanical wafer transfer system is responsible for loading, unloading of wafer, as well as improving temperature uniformity over the area of the wafer by rotating it. The gas delivery system is responsible for distribution and transport of precursors using appropriate carrier gasses. The reactor module includes wafer heating with IR lamps, temperature detector and control system, and the reactor chamber with graphite susceptor coated with SiC. There are primarily four types of reactors used for epitaxial growth of $Ge_{1-y}Sn_y$, which are highly dependent on growth temperature and pressure. Reduced and atmospheric pressure systems, such as ASM's Epsilon reactors [39,49], Aixtron Tricent showerhead reactors [44,45,164], Centura reactors [42], and UHV-CVD systems [165]. In particular, in view of the heating approach and the chamber design, CVD systems from different suppliers differ greatly. For example, if the wafer is heated from both sides in a horizontal reactor [39] or only from underneath of the wafer [10,45]. Figure 3.1 shows a schematic configuration of a typical CVD with a horizontal flow reactor [166].

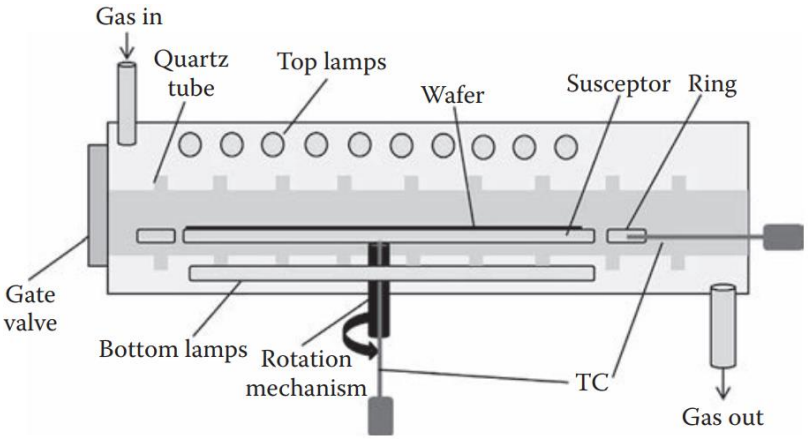

Figure 3.1 Schematic set up of a typical CVD with a horizontal flow reactor [166].

The growth of metastable, intrinsic, and doped $Ge_{1-y}Sn_y$ binary alloys on Si (001) and Ge (001) substrates and Ge-VSs by precisely selecting the appropriate growth conditions in each of the mentioned CVD reactors has been reported by several research teams. In the research of these teams, depending on the growth tool used, the selected growth temperature is from ~250 °C to ~475 °C, while the chosen reactor pressure is from ~10^{-4}mbar to ~10^{3} mbar [10]. It should also be noted that it is important to take into account the effects of precursors used during epitaxial growth of $Ge_{1-y}Sn_y$ in order to discover and determine the most appropriate combinations with regard to growth kinetics, such as activation energy, growth rate, strain relaxation and doping, to optimise crystalline quality, morphology of the epilayer and Sn concentration in $Ge_{1-y}Sn_y$ epilayer.

In this research, all crystalline materials were grown within ASM Epsilon 2000 (as shown in Figure 3.2); the system has been one of the most fundamental epitaxy tools in semiconductor manufacturing for more than two decades. The ASM Epsilon 2000 reactor is a horizontal flow, load-locked and a single wafer RP-CVD tool developed for high volume semiconductor production for various epitaxy applications. The wafer is mounted on a graphite susceptor coated with SiC, which is located in a quartz chamber with a cold wall. During the process, two lamps, which are placed on the bottom and top of the quartz chamber, are responsible for heating the reactor. To control growth at low temperatures, thermocouples embedded in the susceptor are used. For epitaxial growth of $Ge_{1-y}Sn_y$ binary alloys, $SnCl_4$ was used in combination with either GeH_6 or Ge_2H_6. Furthermore, H_2 was used as a carrier gas and chamber pressure controller. Growth was carried out at low temperatures between 240 °C and 350 °C and reduced pressures.

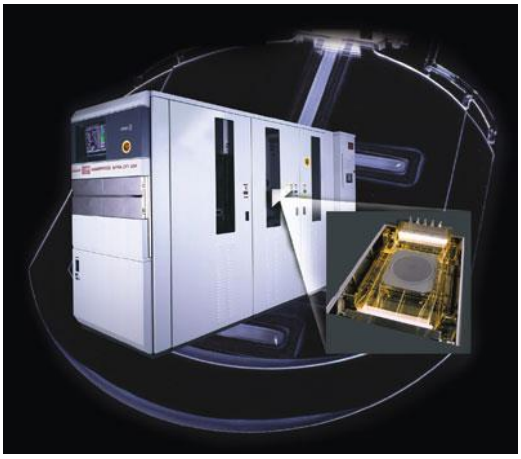

Figure 3.2 ASM Epsilon 2000 single wafer epitaxy CVD system.

Finding number of molecules from flow rate for each precursor depends on reference conditions, known as standard temperature and pressure (STP). In our set up, $P_{standard}$ = ~760 Torr (1 atm) and $T_{standard}$ = ~21.1 °C (294.25 K). Considering these numbers, from the equation given below, n in unit of moles (molecules) per minute can be calculated:

$$n = \frac{P_{standard} \times Flow\ Rate}{T_{standard} \times R} \qquad (3.1)$$

Where *Flow Rate* is flow of precursor in standard cubic centimetre per minute (sccm) which is cm^3min^{-1} in standard conditions of $P_{standard}$ and $T_{standard}$, and R is the universal gas constant, which is 82.057366 $cm^3atmK^{-1}mole^{-1}$ Estimation of n for each used precursor can provide us with molar $SnCl_4/GeH_4$ ratio which can be a very useful parameter to consider and compare all our grown $Ge_{1-y}Sn_y$.

There have been a limited number of published analyses aimed at understanding the fundamental surface chemical reactions and gas phases that lead to the growth of $Ge_{1-y}Sn_y$ binary alloys. The reason $Ge_{1-y}Sn_y$ grows at temperatures in the < 300 °C range and at higher growth rates than when growing Ge, is probably the most ambiguous. Studies on thermochemical values for the homogeneous decomposition of the precursors indicate that introducing $SnCl_4$ into GeH_4 may actually prevent the growth [16,17].

$$SnCl_4\ (g) \rightarrow SnCl_2\ (g) + Cl_2\ (g) \qquad \Delta H_r = 362\ kJ/mol$$

$$GeH_4\ (g) \rightarrow GeH_2\ (g) + H_2\ (g) \qquad \Delta H_r = 235\ kJ/mol$$

In some previous studies, the surface Sn catalytic effect on Cl and H desorption was given as an explanation for the increase in the growth rate of $Ge_{1-y}Sn_y$ [167,168]. Nevertheless, such an explanation does not take into account the low reactivity of $SnCl_4$ at typical growth temperatures, and only justifies how $Ge_{1-y}Sn_y$ growth proceeds after incorporation of Sn into growing layers. It has already been shown that $SnCl_4$ itself requires the presence of GeH_4 to react at typical $Ge_{1-y}Sn_y$ growth temperatures [167]. This was presumed to be due to a direct reduction of $SnCl_m$ by GeH_n producing HCl and $Ge_{1-y}Sn_y$ on the surface of the growing layers. Moreover, it was suggested that Ge_2H_6 and $SnCl_4$, which may have similar behaviours to GeH_4 and $SnCl_4$, react in the gas phase to form chlorogermane ($Cl_qGe_2H_{6-q}$) and chlorostannane (H_qSnCl_{4-q}) intermediates [169]. The H_qSnCl_{4-q} molecule can allow low temperature deposition due to its lower thermal stability compared to $SnCl_4$. It should also be noted that the gas phase reactions become more probable as growth pressure increases in CVD.

In summary, GeH_4 causes the formation of gas phase intermediates, which are more reactive and leads to the following reactions to completion on the surface through direct reduction [102]. More detailed explanations are given in Chapter 6, in which the mechanism of $Ge_{1-y}Sn_y$ CVD growth is investigated by observing experimental data with additional thermochemical and kinetic analyses. In this chapter, we focus more on the effects of growth conditions on epitaxial growth of $Ge_{1-y}Sn_y$ binary alloys. Figure 4.4 shows how a monolayer of $Ge_{1-y}Sn_y$ is deposited on a monolayer of Ge-VS. Here the growth is carried out with GeH_4 in combination with $SnCl_4$ with H_2 as a carrier gas, which also controls the pressure of the CVD chamber.

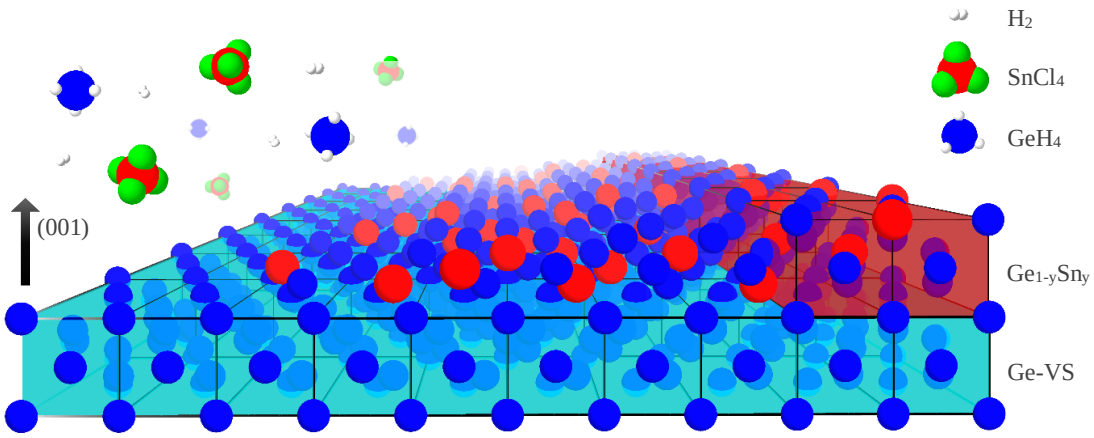

Figure 3.3 CVD growth schematics of $Ge_{1-y}Sn_y$ epitaxy on Ge buffer using H_2 as carrier gas, GeH_4 and $SnCl_4$ as Ge and Sn precursors, respectively. Here blue crystal lattice represents Ge buffer and red crystal lattice represents epitaxial $Ge_{1-y}Sn_y$ epilayer. For simplicity, Si (001) substrate is not shown.

3.3 Material Characterisation Techniques

The film properties, such as thickness, thickness uniformity, surface morphology, crystal quality, Sn concentration and elemental composition of all epitaxially grown heterostructures were performed by various characterisation techniques, including FTIRS, HR-XRD, AFM, X-TEM, XPS, SEM and EDS. These characterisation techniques are briefly described in this section.

3.3.1 HR-XRD

HR-XRD is one of the most important characterisation techniques for crystalline materials. It is not only possible to understand the crystallographic structure, but also the chemical composition of the epitaxial layers by means of this non-destructive material characterisation technique. XRD is based on Bragg's law:

$$n\lambda = 2d\sin(\Theta) \qquad (3.2)$$

Here n is order of diffraction, λ is X-ray wavelength, d is separation distance between crystal lattice planes, and Θ is the angle between incident X-ray with and surface of crystal plane, as shown in Figure 3.4.

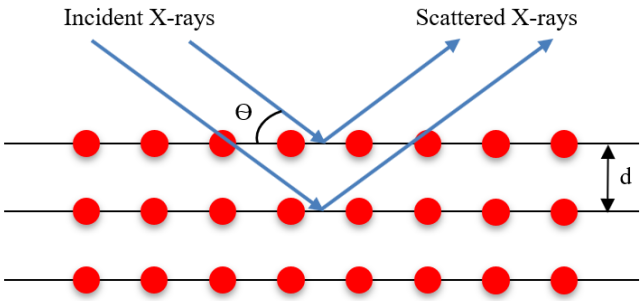

Figure 3.4 Schematic XRD measurement that leads to Bragg's law. Here we can see incident X-rays, with angle of Θ with respect to the surface of crystal lattice, are scattered from crystal planes that are separated by distance of d from each other.

HR-XRD ω–2θ coupled scans could be used to analyse the quality, strain state and composition of crystalline materials. In this research, ω–2θ coupled scans were performed for the (004) planes for fully strained $Ge_{1-y}Sn_y$ epilayers. For those $Ge_{1-y}Sn_y$ epilayers that are not fully strained, however, symmetric and asymmetric reciprocal space maps (RSMs), as shown in Figure 3.5, are required. These RSMs could provide further information on the position of

Bragg peaks and crystalline strain tilt and (in-plane and out-of-plane lattice parameters) which could be used to measure Sn concentration using Vegard's law.

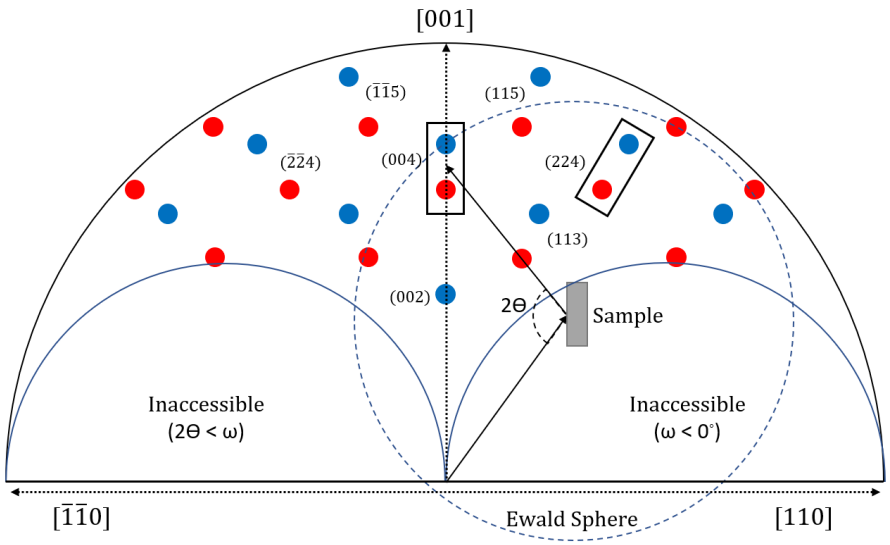

Figure 3.5 Two dimensional cross section of reciprocal space for $Ge_{1-y}Sn_y$\Ge-VS\Si (001). The red and blue circles represent the approximate position of $Ge_{1-y}Sn_y$ and Ge Bragg peaks, respectively. For simplicity, Bragg peaks of Si is not shown.

RSMs are formed by obtaining multiple coupled scans, each of which gives a slightly different offset to the ω-2θ angle, which is the angle between the incoming X-ray beam and the plane of the diffracted X-rays. By combining the scans, specific regions of reciprocal space could be mapped, enabling the determination of the positions of specific Bragg peaks in both the in-plane and out-of-plane directions, which then provide in-plane ($q_{\parallel}$) and out-of-plane ($q_{\perp}$) reciprocal lattice vectors:

$$q_{\parallel} = \frac{2\pi}{\lambda}\sin(\theta)\sin(\omega - \theta) \tag{3.3}$$

$$q_{\perp} = \frac{2\pi}{\lambda}\sin(\theta)\cos(\omega - \theta) \tag{3.4}$$

and therefore, the in-plane ($a_{\parallel}$) and out-of-plane ($a_{\perp}$) lattice parameters could be derived from following equations:

$$a_{\parallel} = \frac{\sqrt{h^2+k^2}}{q_{\parallel}} \tag{3.5}$$

$$a_{\perp} = \frac{\sqrt{l^2}}{q_{\perp}} \tag{3.6}$$

After determining $a_{\parallel}$ and $a_{\perp}$ lattice parameters, the strain in $Ge_{1-y}Sn_y$ epilayer, which is defined as the variation of its crystal structure from its relaxed structure of the $Ge_{1-y}Sn_y$ epilayer compared with its substrate (Ge-VS) could be measured. The in-plane ($\varepsilon_{\parallel}$) and out-of-plane ($\varepsilon_{\perp}$) strain relaxation are given by:

$$\varepsilon_{\parallel} = \frac{a_{\parallel} - a_0}{a_{Ge}} \quad (3.7)$$

$$\varepsilon_{\perp} = \frac{a_{\perp} - a_0}{a_{Ge}} \quad (3.8)$$

here, a_0 is the relaxed lattice constant of the $Ge_{1-y}Sn_y$ epilayer and a_{Ge} is the lattice constant of the Ge-VS. It is important to note that to determine a_0, the volume of the lattice is initially calculated directly from $a_{\parallel}$ and $a_{\perp}$ which are measured experimentally, and by considering that the volume to be constant regardless of the strain relaxation state, a_0 can be estimated.

Finally, to determine the Sn concentration in $Ge_{1-y}Sn_y$ epilayer from HR-XRD symmetric and asymmetric RSMs according to Vegard's law, the following steps were taken:

1. Correct the XRD intensities for any sample related or instrumental effects that could potentially influence peak intensity, such as peak broadening.
2. Identify the peaks that correspond to the Sn and Ge phases.
3. Calculate the lattice parameters for the Sn and Ge phases by fitting the peaks to a model that includes the relevant crystal structures.
4. Then Vegards's law is used to measure the $Ge_{1-y}Sn_y$ lattice parameter for a particular Sn concentration. The Vegard's law indicates that the lattice parameter of $Ge_{1-y}Sn_y$ is proportional to the weighted average of lattice parameters of its individual phases.
5. The estimated $Ge_{1-y}Sn_y$ lattice parameter could then be compared with the value derived experimentally from HR-XRD RSMs.
6. Finally, by repeating the last two steps for different values of Sn concentrations, the best fit between the estimated and experimental lattice parameters for a given Sn concentration was achieved. Such a Sn concentration which provides the best fit is the Sn concentration of the $Ge_{1-y}Sn_y$ epilayer.

It should be noted that Vegard's law suggests a linear relationship between alloy composition and lattice parameter. Nevertheless, this relationship can differ from linearity in some conditions, for example when the Sn concentration is high or there are lattice distortions or

phase transitions. Under these conditions, some other models, such as first principle calculations or coherent potential approximation. In this research, the Sn concentration of $Ge_{1-y}Sn_y$ binary alloys were calculated using the following modified Vegard's law:

$$a_0^{Ge_{1-y}Sn_y} = (1-y).a_0^{Ge} + y.a_0^{Sn} + y(1-y).b^{GeSn} \quad (3.9)$$

where a_0 is the relaxed lattice constant of each crystal, and b^{GeSn} is the bowing parameter. The bowing parameter (b^{GeSn}) used in this research is 0.041 Å [41] according to the latest agreed studies and relaxed lattice constant, a_0, is 5.6579 Å and 6.4892 Å for Ge and Sn, respectively [10]. The lattice constant of each epilayer was calculated from the in and out of plane lattice parameters obtained from RSMs.

The error in measuring Sn concentration in $Ge_{1-y}Sn_y$ depends on various factors such as the quality of the collected XRD data, the accuracy of the instrument, the accuracy of estimating lattice parameters and other systematic or random errors in the data. For $Ge_{1-y}Sn_y$ binary alloy, the error as a result of Vegard's law is the greatest. The error in Sn concentration for fully strained $Ge_{1-y}Sn_y$ is 1-2%, while due to strain relaxation in $Ge_{1-y}Sn_y$, it goes up to 5% for those $Ge_{1-y}Sn_y$ epilayers that are not fully strained. In this research, the highest possible errors for both fully strained (2%) and partially relaxed (5%) $Ge_{1-y}Sn_y$ are considered.

For all $\omega-2\theta$ coupled scans, symmetric and asymmetric RSMs, a Panalytical X'Pert Pro MRD using CuKα1 source was used for measurements. To form a quasi-parallel X-ray beam with a CuKα1 radiation of 1.54056 Å, the incident beam passes through a hybrid monochromator. Then an analyser crystal that is placed before the detector collects the diffracted beam to narrow the acceptance angle to 12 arc sec. Such a high resolution can provide XRD RSMs which can be used to estimate element compositions in crystalline binary alloys such as $Ge_{1-y}Sn_y$.

3.3.2 FTIRS

FTIRS is a non-destructive characterisation technique that can be used in transmittance and reflectance mode. In this research, only reflectance mode, in which the interference of light is used to measure the thickness of thin films ($Ge_{1-y}Sn_y$ epilayers) and thickness uniformity across wafers. The core of the FTIRS is the Michelson interferometer. A typical Michelson interferometer consists of a beam splitter and a couple of perpendicular mirrors, one of which is at a fixed distance from the beam splitter, and the other moves towards and away from the

beam splitter. As shown in Figure 3.6, the beam splitter initially splits the beam emitted from a source into two beams. Each beam is then reflected from each mirror and then recombined into a single beam, so called recombined beam, at the position of the beam splitter. The interference of the two beams leads to a unique light spectrum, which depends on the position of the moving mirror.

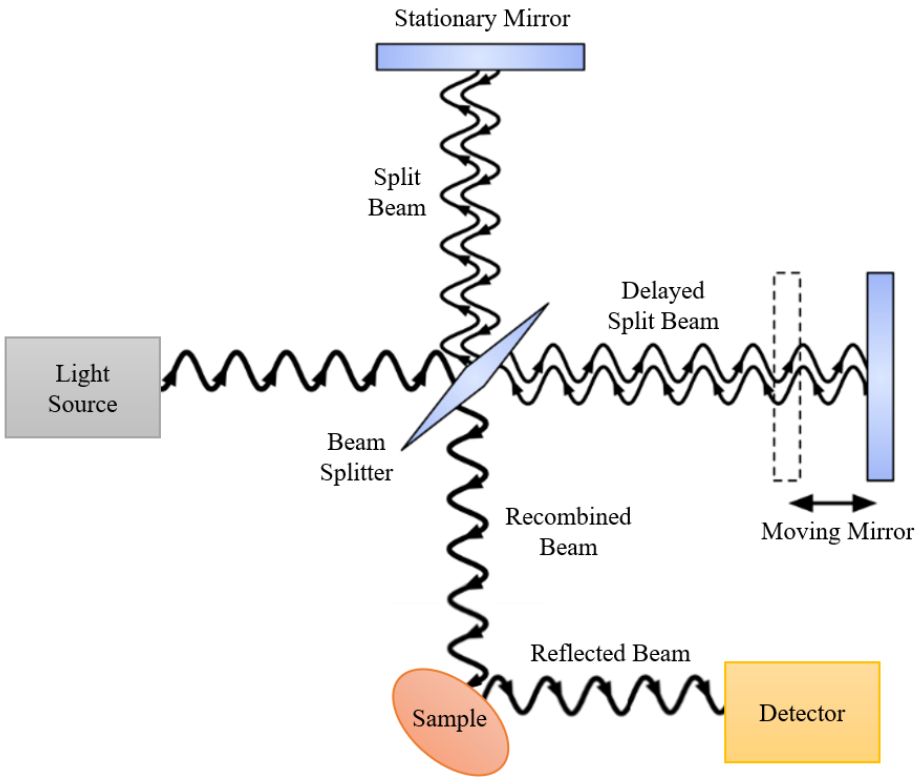

Figure 3.6 Schematic of a typical Michelson interferometer in reflectance mode. The beam splitter initially splits the light beam emitted from the source into two, then these two beams are reflected from two mirrors. The moving mirror is used to manipulate the phase of the beam to produce delayed split beam, which interferes with the split beam from stationary mirror. The resulted beams are combined and redirected towards sample. After that, the recombined beam is reflected from the surface and subsequent interfaces in the sample and recorded by the detector.

After that, as shown in Figure 3.7, the recombined beam is redirected towards the sample, and in the reflectance mode, the reflected light from the surface of the sample and other subsequent interfaces in the sample is recorded by the detector. Constructive interference is resulted when $m\lambda = 2dn_1$, in which m is an integer, λ is the wavelength, d and n_1 are the thickness and refractive index of the epilayer ($Ge_{1-y}Sn_y$), respectively and n_0 (refractive index of air) is 1. By obtaining a series of intensity measurements at each beam (with different phases) generated by the Michelson interferometer, FTIRS produces a wavelength dependent spectrum.

Therefore, a large intensity of light can be measured over a range of wavelengths, which greatly increases the signal to noise ration. In this study, the thickness uniformity of the $Ge_{1-y}Sn_y$ epilayers across the wafers was mapped using FTIRS reflectance measurements. This was done within a Bruker Vertex v70 FTIRS with a MappIR accessory that can be used to map wafers up to 200 mm in diameter.

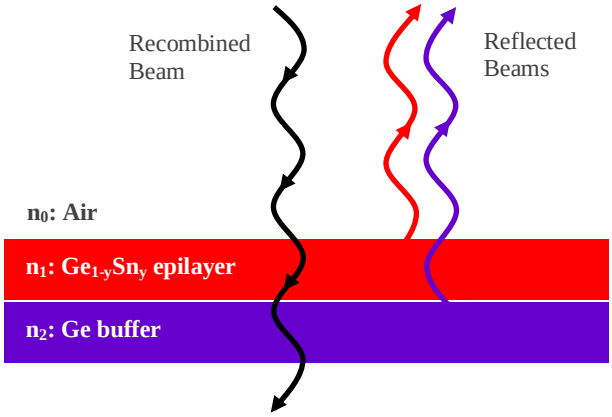

Figure 3.7 Representation the reflected light from the surface of the sample and other subsequent interfaces in the sample. Here, there are two layers: $Ge_{1-y}Sn_y$ epilayer and Ge buffer with refractive index of n_1 and n_2, respectively.

3.3.3 AFM

AFM is an advanced surface characterisation technique, which provides great information about surface roughness and surface morphology of materials with outstanding resolution. In the AFM technique, the surface of a solid material is scanned with a sharp probe (tip), which interacts with repulsive and attractive forces. Then the force response curve, as a function of distance between probe (tip) and the surface, is the total forces which include attractive force (van der Waals) and repulsive force (short range coulomb). The AFM scanning can be performed in a few modes, depending on the interaction between the probe and the surface of the sample: contact mode, non-contact mode and tapping mode. In this study, only tapping mode is used to study surface morphology and roughness of samples. The surface roughness of samples is calculated using the equation below:

$$RMS = \sqrt{\frac{\sum(h_i - h_m)^2}{n}} \qquad (3.10)$$

where h_i is the height of each measurement of the AFM scan, h_m is the mean height for the entire scan and n is the number of measurements. RMS provides a numerical representation

of the average deviation of the surface from its mean height and considers both the height and spatial distribution of surface features. In general, the scan area should be large enough to ensure that rare features are included. The choice of the right scan area depends on many factors. In this research, 20μm×20μm was found to be an appropriate scan area for RMS calculation.

In tapping mode, direct force is not measured. The sharp probe oscillates up and down as a result of vibration of the cantilever close to its resonant frequency. This enables the probe at the end of each oscillation cycle to touch the surface of the sample. This means the probe gets into intermittent contact with the surface. With a feedback loop, the position of the AFM probe and its distance from the surface are adjusted to preserve either the oscillation amplitude or the phase of the oscillating cantilever. In tapping mode, the probe is not in constant contact with the sample, which can therefore reduce damage to both the probe and the sample. Since lateral probe-sample forces are avoided in tapping mode, the resolution is normally higher than in the classical contact mode, in which the probe and the sample are in direct contact.

The surface morphology of the heterostructures (for instance grown $Ge_{1-y}Sn_y$) was mapped using an Asylum Research MFP-3D stand-alone AFM. The surface topology and roughness were captured using Si_3N_4 probes on the AFM operating in tapping mode.

3.3.4 X-TEM

TEM is a destructive high resolution imaging technique in which a high energy beam of electrons passes through an electron transparent sample. Due to interactions between electrons and atoms of the samples, transmitted electrons, affected by the thickness, composition, density and crystallinity of the sample, can form an image. The resolution in TEM is limited by the wavelength of each electron (which is much smaller than that of light) and the quality of the electron optics, which enables imaging at sub nanometre scale (lattice resolution). TEM could be used to observe the crystal structures of the grown layers, to analyse their elemental compositions, and to investigate features such as grain boundaries, dislocations, and defects.

As shown in Figure 3.8, the electron beam emitted from the electron gun is initially turned into a small coherent beam by condenser lenses, which is then limited by a condenser aperture that blocks any electron with high angles. When the electron beam hits the sample, depending on the electron transparency and thickness of the sample, some electrons (parts of the beam) are transmitted through it. The objective lens then focuses the transmitted beam to form an

image on the fluorescent screen or to be captured with a charge-coupled device (CCD). The objective aperture could also be employed to improve contrast by excluding diffracted electrons with high angles. Intermediate and projective lenses could additionally be used to enlarge the image before reaching the fluorescent screen or the CCD. When looking at a TEM image, the lighter areas represent the areas of the samples which more electrons could be transmitted, while the darker areas represent the areas of the sample which less electrons could be transmitted.

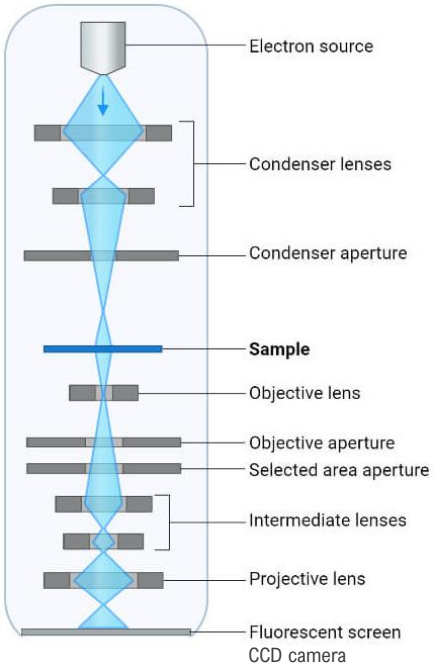

Figure 3.8 Schematic illustration of TEM [170]. The electron beam emitted from the electron gun is focused into a small coherent beam by condenser lenses and then is transmitted through an electron transparent sample. Transmitted electrons are then captured by CCD image capturing device for image formation and further analysis.

A TEM sample should be thin enough to transmit sufficient electrons to form an image with minimal energy loss. Therefore, the preparation of TEM samples is a crucial step that needs to be taken into account in order to achieve valuable images and analyses. The TEM sample preparation technique used in this research is the one in which the sample is initially glued appropriately, then thinned and polished as much as possible with grinding pads on a circular mechanical grinder. After that, the Cu rings are glued to the cross section of the thinned sample, which is now ready for ion milling. In the final step of this process, a PIPS is used, in which beams of Ar^+ ions with high energies and shallow angles thin the sample until electron-transparent regions suitable for TEM imaging are achieved. This TEM preparation

method is the most appropriate for thin epilayers and soft semiconductor materials such as $Ge_{1-y}Sn_y$, but the process is very time consuming. In this research, a Jeol JEM-2100 transmission electron microscope (TEM) was used to obtain high resolution cross sectional micrographs of heterostructures. X-TEM imaging allows direct observation of crystalline quality (defect imaging) and precise thickness measurement for epilayers.

Bright field (BF) and dark field (DF) are two distinct X-TEM imaging modes. In summary, BF X-TEM is sensitive to the electron absorption properties of the sample, while DF X-TEM is sensitive to the electron scattering characteristics of the sample. Both X-TEM imaging modes could be used to gain a comprehensive understanding of the quality and properties of materials.

In BF mode, all transmitted electrons through the sample, whether scattered or not, are detected. The resulting image may have a bright background and dark contrasts are proportional to electron absorption in the sample. BF X-TEM images provide information on the structure of the materials, such as the lattice spacing, orientation and crystalline structure. For example, the identification of the type of crystal structure and the determination of whether the material is crystalline, polycrystalline or amorphous can be carried out in this imaging mode. BF X-TEM images could also be used to investigate the microstructure of the material, including shape, grain size and distribution.

In DF mode, on the other hand, the electrons transmitted through the sample are detected, but the electrons scattered in the sample plane are disregarded. Therefore, the resulting image may have a dark background and bright contrasts proportional to the intensity of electron scattering in the sample. Since the scattered electrons are more sensitive to the presence of defects than the transmitted electrons, DF X-TEM images can be used to identify defects in materials such as inclusions, grain boundaries and dislocations. Furthermore, this X-TEM imaging mode could be used to investigate interfaces in materials, for example the interface between different epilayers.

3.3.5 SEM

Largely magnified images with very high resolution (~1 nm) can be produced using SEM, in which electrons with very short wavelengths are used instead of light to form an image. A beam of electrons emitted from an electron gun follows a vertical path through the microscope and is directed to the surface of the sample under vacuum condition. The beam is focused on

the surface of the sample by electromagnetic fields. After the beam hits the surface of the sample, X-rays, secondary electrons, Auger electrons and backscattered electrons are ejected from the sample and collected by the detectors and then converted into signals to produce the final image. In this research, Zeiss SUPRA 55-VP scanning electron microscope with a field emission electron gun (FEG).

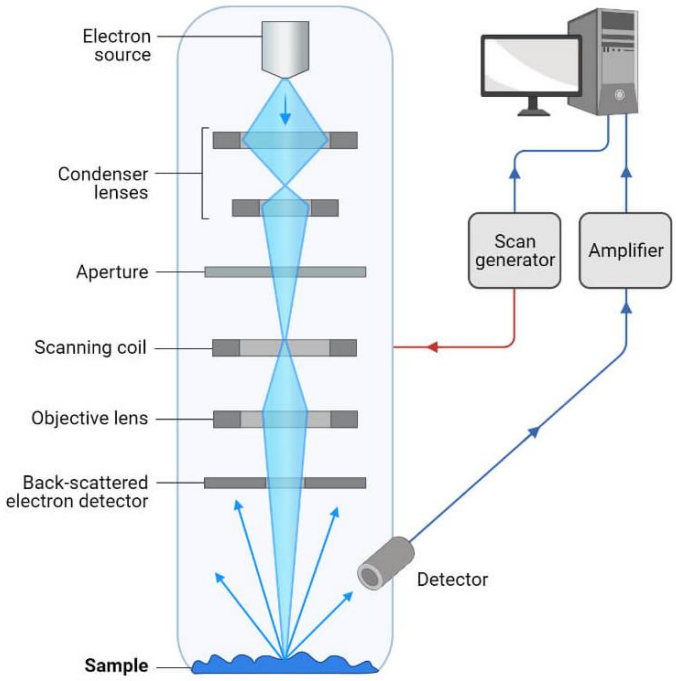

Figure 3.9 Schematic illustration of SEM [170]. The electron beam emitted from the electron gun is focused, directed toward the sample. Ejected secondary electrons are collected by the detectors and form the final image.

3.3.6 EDS

In the SEM technique, the electron beam that hits the surface of the sample can potentially excite electrons in the inner shells of atoms, creating holes that can then be filled by electrons from outer shells. In EDS, elemental compositions on the surface of the sample can be mapped by collecting X-rays emitted as a result of the transition of electrons from higher energy shells to lower energy shells [171]. The SEM system, Zeiss SUPRA 55-VP, is equipped with an EDAX energy dispersive X-ray spectrometer which could be used to obtain elemental composition analysis with a detection limit of approximately 0.5 at%. With this, Sn precipitants and Sn rich micro islands which could be formed because of Sn segregation on the surface of the $Ge_{1-y}Sn_y$ were analysed.

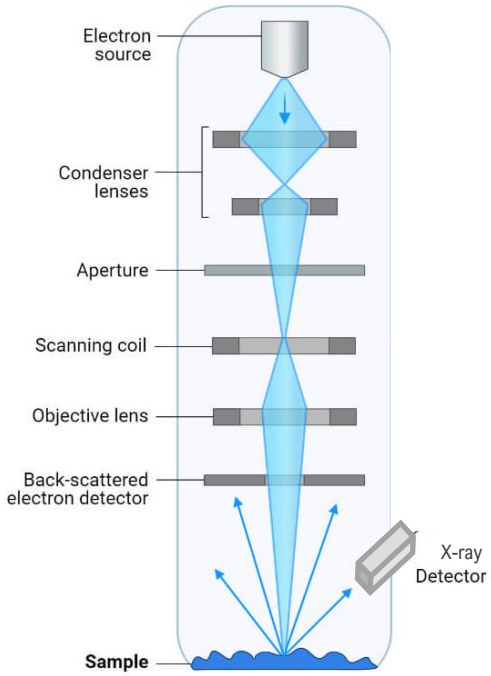

Figure 3.10 Schematic illustration of EDS [170]. The electron beam emitted from the electron gun is focused, directed toward the sample. Ejected X-rays from the sample are collected by the detectors for elemental composition analysis.

3.3.7 XPS

XPS is a non-destructive material characterisation technique used to measure elemental (and molecules) composition on the surface of doped $Ge_{1-y}Sn_y$ or $Ge_{1-x-y}Si_xSn_y$ ternary alloys. The XPS spectra are achieved by irradiating the surface of the solid material with an X-ray beam under high vacuum condition of ~10^{-8} Torr and measuring the kinetic energy of the electrons emitted from the top 1 nm to 10 nm of the material. A photoelectron spectrum is simply generated by measuring the number of ejected electrons over a range of kinetic energies. It is then possible to identify and quantify (measuring elemental composition) all elements on the surface of the solid material (except hydrogen) by investigating the kinetic energies and intensities of the photoelectron peaks.

Considering the energy of the monochromatic X-ray source, it is possible to determine the kinetic and binding energy of the emitted electrons. In this research, the monochromate Al Kα XPS was to perform on samples. The emitted electrons from the same element can have different energies, as there are several orbital shells. Thus, in XPS measurements, orbitals that provide stronger emission signals are usually investigated. Table 2 shows photoelectron lines

(in eV) with the strongest emission signals for elements studied in this research. It should be noted that the binding energy of the elements varies slightly due to the binding state of the element. For instance, the 2p electrons in Si in Si-O_2 have a binding energy of ~103 eV, while the 2p electrons in Si in Si-Si have a binding energy of ~99 eV. It is therefore possible to map the binding state of the compounds and their relative concentrations using XPS measurements [172].

Element	Atomic Number	Photoelectron Lines with the Strongest Emission
C	6	1s: 284.5 eV
O	8	1s: 531.0 eV
Si	14	2p: 99.3 eV
Ge	32	3d: 29.4 eV
Sn	50	$3d_{5/2}$: 485.0 eV $3d_{3/2}$: 493.4 eV

Table 2 List of photoelectron lines with the strongest emission of elements that are studied in research, when using monochromate Al Kα XPS.

Chapter 4

Heteroepitaxy of $Ge_{1-y}Sn_y$ Epilayers Using GeH_4 Precursor

4.1 Introduction

The first attempt to grow $Ge_{1-y}Sn_y$ epilayers with $SnCl_4$ in combination with GeH_4, which is a more conventional and cheaper Ge precursor than Ge_2H_6, was carried out in 2014 [49,120]. However, there have been very limited studies on the $Ge_{1-y}Sn_y$ growth mechanism in the use of GeH_4. One reason could be because it has been believed that Ge_2H_6 has two order of magnitude higher growth rate than GeH_4 when growing Ge under similar growth conditions [101]. Nevertheless, it should also be noted that in order to increase Sn concentration in $Ge_{1-y}Sn_y$, it is necessary to reduce growth temperature [102], which means we cannot simply compare growth rate of $Ge_{1-y}Sn_y$ at very similar growth temperature when using either of GeH_4 or Ge_2H_6. Instead, we need to compare growth rate of similar grown $Ge_{1-y}Sn_y$ when using one of these Ge precursors. The effects of Ge precursors (Ge_2H_6 and GeH_4) on the heteroepitaxy of $Ge_{1-y}Sn_y$ epilayers will be extensively discussed in the next chapter. More recent research successfully achieved grown $Ge_{1-y}Sn_y$ binary alloys using GeH_4 and $SnCl_4$ [49,68,103]. Today not only it is possible to grow high quality $Ge_{1-y}Sn_y$ with relatively high Sn concentration using $SnCl_4$ and GeH_4, but it is also possible to do it at temperature lower than 350 °C [68]. It should also be noted that commercially available GeH_4 is much more cost effective than Ge_2H_6 [60,103] and therefore it is more favourable in commercialisation of $Ge_{1-y}Sn_y$ optoelectronic devices. In this chapter, the heteroepitaxial growth of $Ge_{1-y}Sn_y$ on a Si (001) substrate via a relaxed Ge-VS using commonly available commercial Ge precursors, GeH_4, in combination with $SnCl_4$ precursors, by RP-CVD is comprehensively investigated.

4.2 Heteroepitaxy of $Ge_{1-y}Sn_y$ Epilayers

In this chapter, intrinsic fully strained $Ge_{1-y}Sn_y$ epilayers were grown on Si (001) substrate via a relaxed Ge-VS using RP-CVD. A typical example of grown materials is shown in Figure 4.1, which demonstrates a schematic cross sectional structure of the fully strained $Ge_{1-y}Sn_y$\Ge-VS\Si (001). All crystalline materials were grown on wafers 100 mm diameter Si (001) substrates.

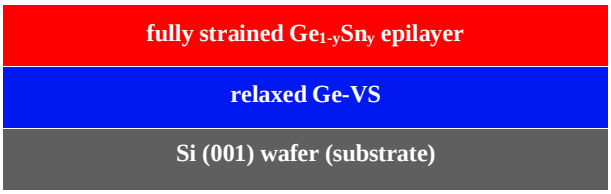

Figure 4.1 Schematic cross sectional structure of a fully strained $Ge_{1-y}Sn_y$ epilayer grown on Si (001) substrate via a relaxed Ge-VS.

For epitaxial growth of fully strained $Ge_{1-y}Sn_y$ binary alloys given in this chapter, $SnCl_4$ was used in combination with GeH_6. Furthermore, purified H_2 was used as a carrier gas and chamber pressure controller.

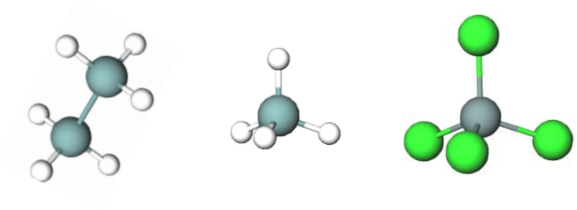

Figure 4.2 Ge_2H_6 (left) or GeH_4 (middle) in combination with $SnCl_4$ (right) were used as Ge and Sn precursors, respectively. These schematics were created using CrystalMaker software.

Using various growth techniques, $Ge_{1-y}Sn_y$ was successfully grown on different substrates, such as InSb, CdTe, ZnSe, InP, GaAs [15-17]. However, soon researchers tend to use Si as substrate as (usually) it is the best substrate in terms of practicability and applicability. As it was discussed in theoretical background, the lattice mismatch between diamond cubic structure of Si (5.431 Å) and α-Sn (6.493 Å) is ~20% [10], as shown in Figure 2.2 on page 8. Such large lattice mismatch between Si and α-Sn (and so $Ge_{1-y}Sn_y$) is not ideal to achieve appropriate growth of $Ge_{1-y}Sn_y$ epilayer with low defect density. On the other hand, the lattice mismatch between diamond cubic structure of Ge (5.658 Å) and α-Sn (6.493 Å) is just below

~15% [10], as shown in Figure 2.2 on page 8. To overcome lattice mismatch challenge between diamond cubic structure Si and α-Sn (and so $Ge_{1-y}Sn_y$), it has been suggested to use relaxed Ge buffer as a VS which has a lattice parameter closer to that of $Ge_{1-y}Sn_y$ epilayer.

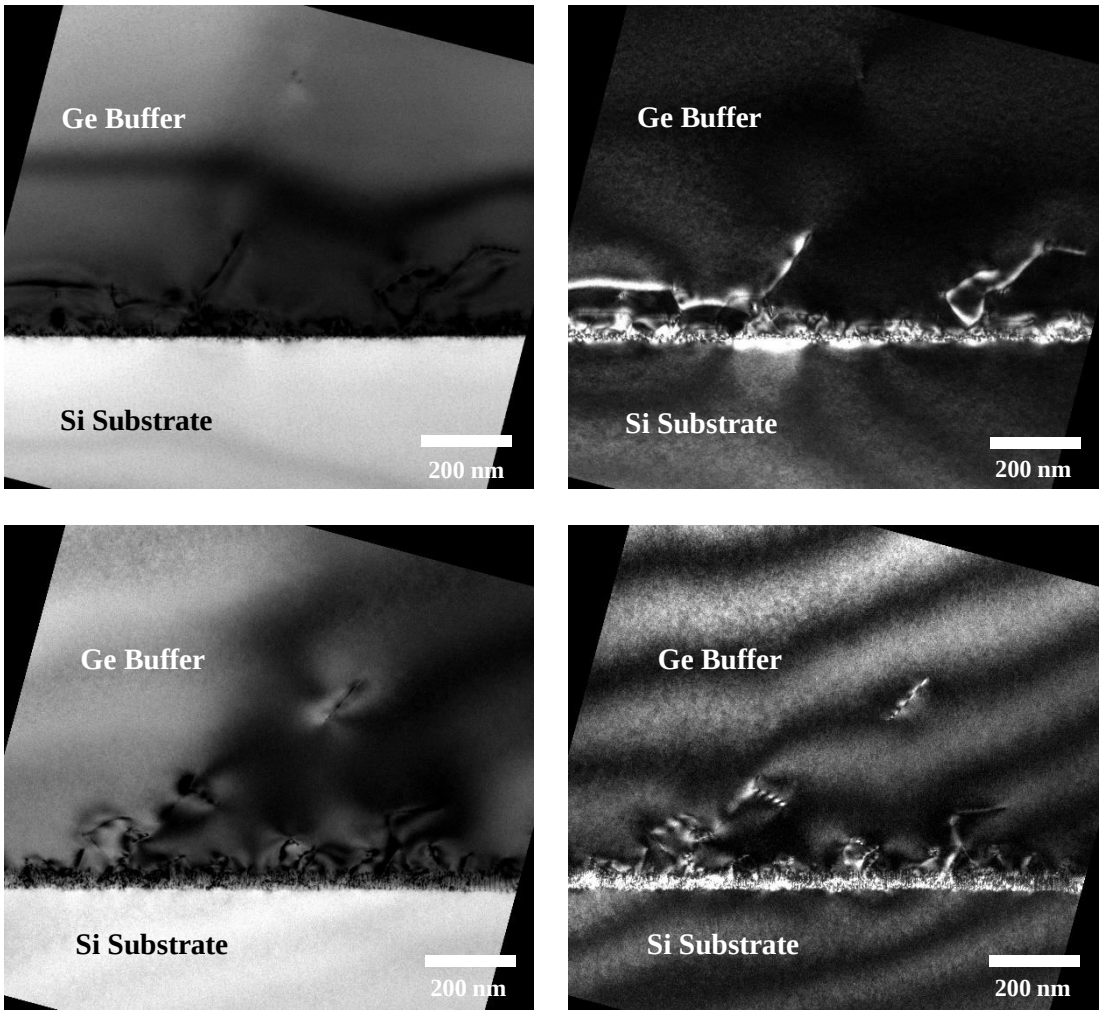

Figure 4.3 X-TEM micrographs of Si-Ge interface in which relaxed Ge buffer layer is grown on top of Si (001) substrate. Top-left: 004 BT diffraction condition. Top-right: 004 DT diffraction condition with. Bottom-left: 220 BT diffraction condition. Bottom-right: 220 DT diffraction condition. The grown Ge buffer layer can be used as a VS for further growth of $Ge_{1-y}Sn_y$ epilayer. Using relaxed Ge buffer layer reduces effective lattice mismatch between diamond cubic structure of Si (001) substrate and $Ge_{1-y}Sn_y$ epilayer.

In this work, relaxed Ge buffer layer with thickness of >0.5 μm was grown on Si (001) as a VS to decrease the effective lattice mismatch between Si (001) and $Ge_{1-y}Sn_y$. As seen in Figure 4.3, Ge buffer layer was grown successfully on Si (001) substrate. By growing thick enough Ge buffer layer on top of Si (001), strain relaxation within the Ge buffer layer is achieved and so effective lattice mismatch between Si substrate and $Ge_{1-y}Sn_y$ epilayer decreases as result of Ge-VS.

4.3 Sn Concentration of $Ge_{1-y}Sn_y$ Epilayers

The Sn concentration of each $Ge_{1-y}Sn_y$ epilayer was estimated using HR-XRD. A HR-XRD ω-2θ coupled scan as well as symmetric and asymmetric RSMs for a typical fully strained $Ge_{1-y}Sn_y$, grown on Si (001) via a relaxed Ge-VS using GeH_4, are shown in Figure 4.4 and Figure 4.5, respectively. The HR-XRD ω-2θ coupled scan in Figure 4.4 shows thickness fringes which provides the thickness of epilayer to be ~22 nm.

In Figure 4.5, the (004) Bragg peaks are aligned in the in-plane reciprocal coordinate (Q_x). Additionally, the asymmetric (224) RSM indicates that the Ge-VS is relaxed to the Si (001) substrate, while the $Ge_{1-y}Sn_y$ epilayer is fully strained to the Ge-VS. The Sn concentration of the $Ge_{1-y}Sn_y$ can be calculated employing the modified Vegard's law as presented previously, Equation 3.9 on page 37. The lattice constant of each epilayer was calculated from the in and out of plane lattice parameters obtained from RSMs. In view of this, the Sn concentration of the $Ge_{1-y}Sn_y$ epilayer, which is given its symmetrical and asymmetric RSMs in Figure 4.5, was calculated to be 6 at.%.

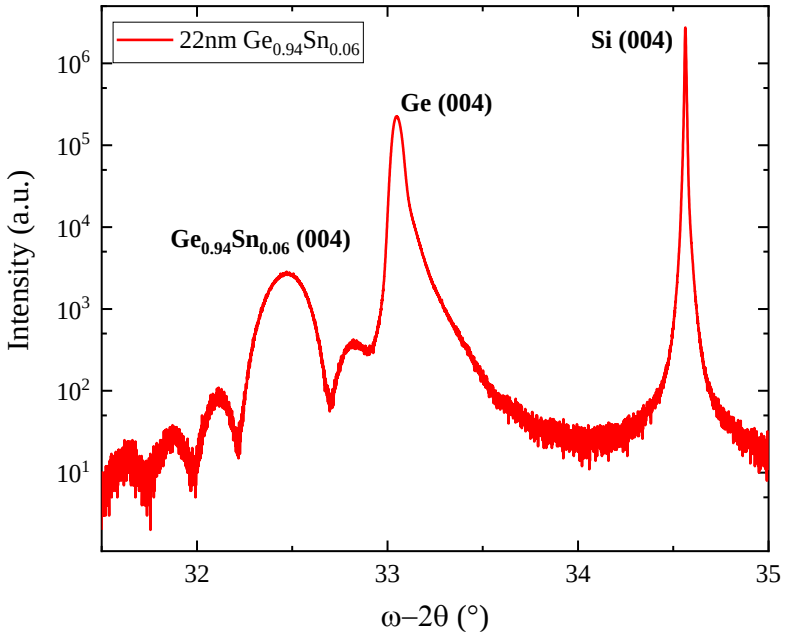

Figure 4.4 HR-XRD ω-2θ coupled scan of a ~22 nm thick fully strained $Ge_{0.94}Sn_{0.06}$ epilayers grown on Si (001) via a relaxed Ge-VS using GeH_4 in combination with $SnCl_4$ at temperature of 280 °C and pressure of 500 Torr.

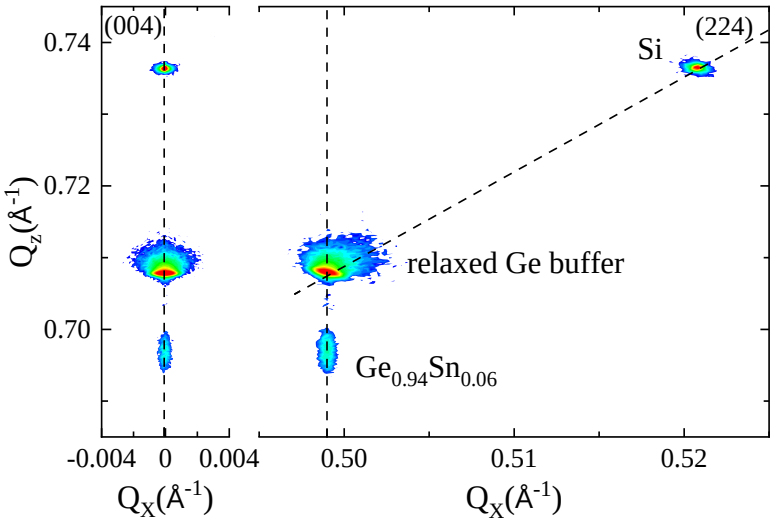

Figure 4.5 Symmetric (left) and asymmetric (right) RSMs for a ~22 nm thick fully strained $Ge_{0.94}Sn_{0.06}$ epilayer grown on Si (001) via a relaxed Ge-VS using GeH_4 in combination with $SnCl_4$ at temperature of 280 °C and pressure of 500 Torr.

4.4 Effects of CVD Conditions on Growth & Quality of $Ge_{1-y}Sn_y$

In this section, we tended to fully understand the effect of CVD growth conditions, such as pressure, temperature and $SnCl_4/GeH_4$ ratio on $Ge_{1-y}Sn_y$ epilayers when using $SnCl_4$ and GeH_4 as Sn and Ge precursors, respectively. We will show how it could be possible to grow high quality $Ge_{1-y}Sn_y$ with high Sn concentration at a very low temperature that was assumed not to be possible before and explore techniques we used to achieve growth rate at a temperature that has been reported not to be possible to grow any $Ge_{1-y}Sn_y$ by other research group. The $SnCl_4/GeH_4$ ratio is considered as the precursor mass flow ratio to understand the effect of precursors on $Ge_{1-y}Sn_y$ growth.

4.4.1 Effect of Pressure on quality & growth of $Ge_{1-y}Sn_y$ Epilayers

Pressure is the first primary CVD growth condition, which has been carefully investigated. In this study, pressure was tuned from 100 Torr to 500 Torr at three different growth temperatures of 270 ℃, 280 ℃, and 290 ℃. All other CVD growth conditions were kept constant for all grown $Ge_{1-y}Sn_y$ binary alloys. For instance, the $SnCl_4/GeH_4$ ratio was maintained at 3.55×10^{-4} for all grown samples. All $Ge_{1-y}Sn_y$ epilayers grown are fully strained and have the same relaxed Ge-VS.

In general, as shown in Figure 4.6, the Sn concentration in the $Ge_{1-y}Sn_y$ epilayers increases with increasing growth pressure at all temperatures. It is also evident that the Sn concentration increases at a higher rate at a lower temperature (270 ℃). It should be noted that we have tried to higher pressure (up to atmospheric pressure ~760 Torr) similar behaviour was detected. It seems the Sn concentration at a given temperature reaches its highest possible level at atmospheric pressure; yet this should be confirmed experimentally. Here, we tend not to draw a conclusion about the effect of pressure at temperatures outside the studied region. In Chapter 6, further studies on lower temperatures are presented.

Similarly, the effect of pressure on growth rate can be investigated using the same grown $Ge_{1-y}Sn_y$ epilayers. As shown in Figure 4.7, the growth rate decreases as pressure increases. Such a behaviour applies to all three growth temperatures, but it should be noted that the reduction rate of growth rate at the lowest examined temperature (270 °C) is lower than that of growth rate at higher temperatures (280 °C and 290 °C).

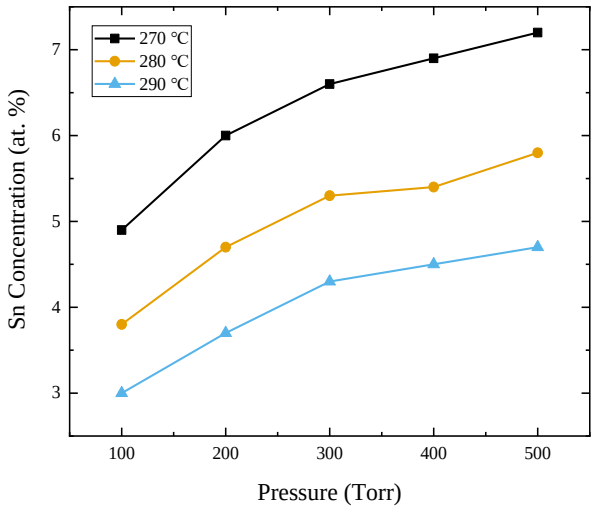

Figure 4.6 Effect of growth pressure on Sn concentration of $Ge_{1-y}Sn_y$ epilayers grown at different temperatures using 3.55×10^{-4} $SnCl_4/GeH_4$.

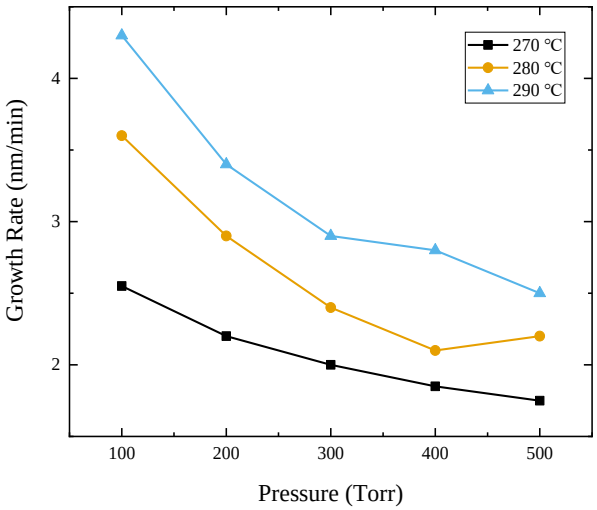

Figure 4.7 Effect of growth pressure on growth rate of $Ge_{1-y}Sn_y$ epilayers grown at different temperatures using 3.55×10^{-4} $SnCl_4/GeH_4$.

In view of both Figure 4.6 and Figure 4.7 simultaneously, we can better understand the behaviour of Sn concentration (at.%) and growth rate (nm/min) for each of the three examined growth temperatures. As seen in Figure 4.8, it is not surprising to find that Sn concentration and growth rate correlate inversely. It is unclear whether there is a causal relationship between these two variables. However, there have been some convincing explanations of how the growth rate can control the Sn concentration at a given temperature.

One explanation is that, assuming that the amount of Sn production remains relatively constant at a given temperature, it is the growth rate that controls the Sn concentration. Thus, if the

growth rate is high, fewer Sn atoms have the chance to incorporate into the $Ge_{1-y}Sn_y$ growing layers, and on the other hand, if the growth rate is low, a greater number of Sn atoms can incorporate into the growing layers. Moreover, what exactly controls the growth rate itself is the amount of Ge atoms available on the growing layer during CVD growth. For example, for $Ge_{1-y}Sn_y$ with a Sn concentration of 7 at.%, the growth rate largely depends on the production of Ge atoms and their incorporation into the growing layers. Given the amount of experimental data we have to date, and taking into account the inference to the best explanation approach, we may be justified to accept this explanation. However, more research is needed to obtain sufficient experimental data and evidence to draw a certain conclusion.

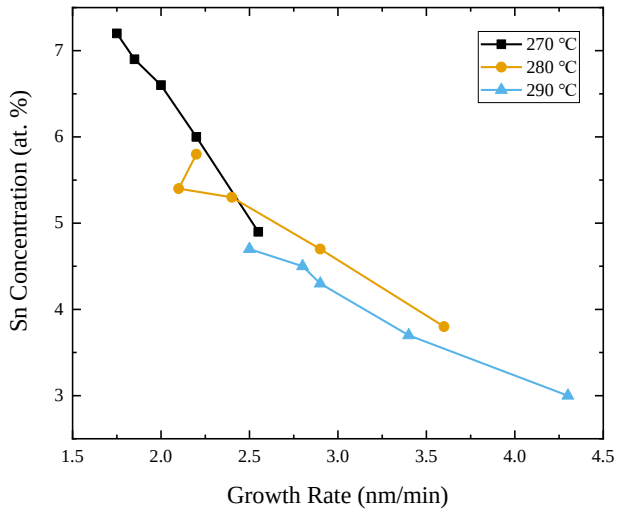

Figure 4.8 Behaviour of Sn concentration (at.%) and growth rate (nm/min) of $Ge_{1-y}Sn_y$ grown at three different growth temperatures. These are the same $Ge_{1-y}Sn_y$ epilayers as shown in Figure 4.6 and Figure 4.7 which were grown by tuning pressure from 100 Torr to 500 Torr.

As shown in Figure 4.8, there is an outlier data point corresponding to the sample grown at a temperature of 280 ℃ and a pressure of 400 Torr. The relation between the growth rate and Sn concentration for $Ge_{1-y}Sn_y$ epilayers grown at temperatures of 280 ℃ and 290 ℃ is similar. However, at a lower growth temperature of 270 ℃, a different behaviour is evident. At this temperature, the Sn concentration increases with a decrease in growth rate with a faster rate. In summary, in order to maximise Sn concentration, it is necessary to take into account the high pressure region (≥ 500 Torr), but how much growth rate is sacrificed depends on the growth temperature used.

Finally, the surface morphology of grown samples was studied using AFM in tapping mode. Examples of AFM scans of $Ge_{1-y}Sn_y$ epilayers at three different temperatures are given in

Figure 4.9. In Figure 4.10, the surface roughness (nm) of each grown $Ge_{1-y}Sn_y$ epilayer at the given growth temperature is shown. Since all $Ge_{1-y}Sn_y$ epilayers grown are fully strained, it is expected to observe low surface roughness of ≤ 1.6 nm for all samples. In addition, the average surface roughness increases slightly as the temperature decreases. This could be due to an increase in Sn concentration in $Ge_{1-y}Sn_y$ epilayers, as other studies have reported. However, we can conclude that the growth pressure may not influence the quality of $Ge_{1-y}Sn_y$ epilayers in terms of surface morphology.

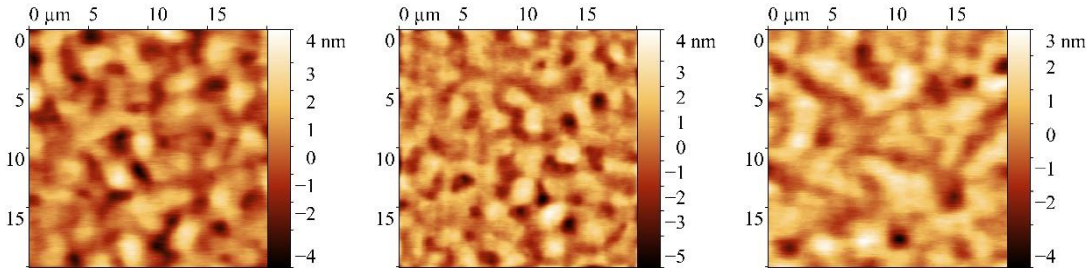

Figure 4.9 AFM scans of $Ge_{1-y}Sn_y$ grown under the same growth conditions (at pressure of 500 Torr and 3.55×10^{-4} $SnCl_4/GeH_4$ ratio) but at different growth temperatures. Left: $Ge_{1-y}Sn_y$ grown at 270 °C. Middle: $Ge_{1-y}Sn_y$ grown at 280 °C. Right: $Ge_{1-y}Sn_y$ grown at 290 °C.

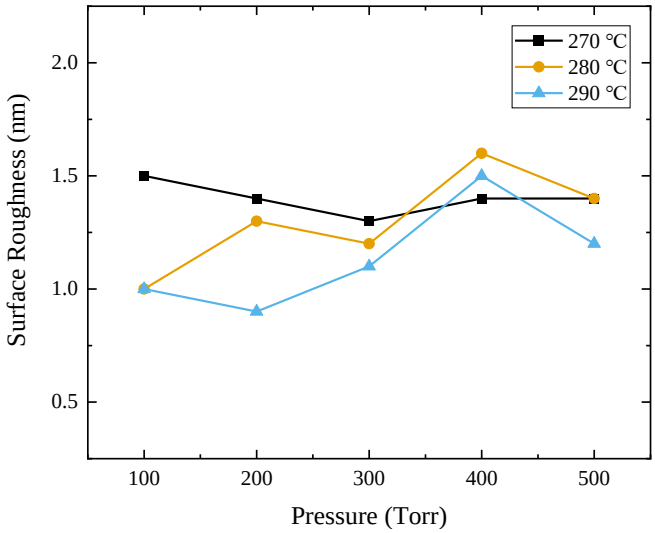

Figure 4.10 Effect of growth pressure on surface roughness of $Ge_{1-y}Sn_y$ epilayers grown at different temperatures using 3.55×10^{-4} $SnCl_4/GeH_4$. The average surface roughness (RMS) for $Ge_{1-y}Sn_y$ epilayers grown at temperatures of 270 °C, 280 °C and 290 °C is 1.4 nm, 1.3 nm and 1.1 nm, respectively.

4.4.2 Effect of $SnCl_4/GeH_4$ ratio on growth of $Ge_{1-y}Sn_y$ Epilayers

To understand the effect of the $SnCl_4/GeH_4$ ratio, both pressure and temperature were set to be constant. This effect of $SnCl_4/GeH_4$ ratio at two pressures, low (100 Torr) and high

(500 Torr), was investigated, as shown in Figure 4.11. It is important to note that the increase in the $SnCl_4/GeH_4$ ratio increases the Sn concentration in $Ge_{1-y}Sn_y$ until a certain level (~1.4×10^{-3} for those grown at 100 Torr). After this level, the increase in the $SnCl_4/GeH_4$ ratio may not only reduce the Sn concentration, but also stops the growth completely. At this point, it seems essential to take high pressure (500 Torr) into account to increase Sn concentration further. Furthermore, the decrease in $SnCl_4/GeH_4$ ratio at low pressure of 100 Torr does not seem to significantly influence the incorporation of Sn into $Ge_{1-y}Sn_y$ epilayer. The lowest $SnCl_4/GeH_4$ ratio which we could successfully grow $Ge_{1-y}Sn_y$ was 3.5×10^{-4}. No growth was achieved when $SnCl_4/GeH_4$ ratio lower than 3.5×10^{-4} was applied.

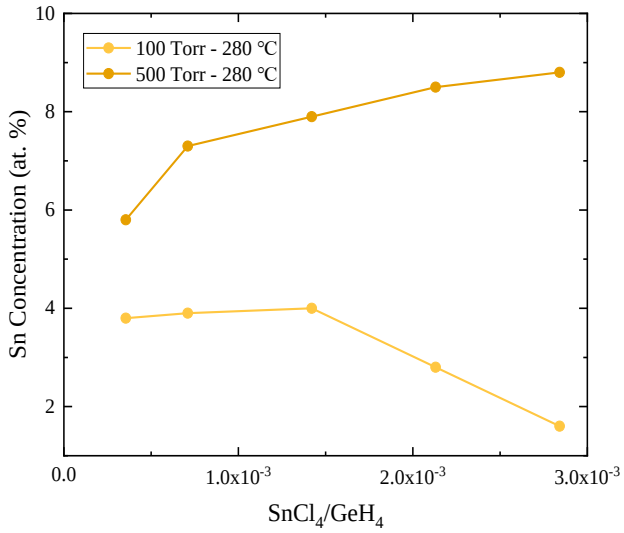

Figure 4.11 Effect of $SnCl_4/GeH_4$ ratio on Sn concentration (at.%) of fully strained $Ge_{1-y}Sn_y$ epilayers at low (100 Torr) and high (500 Torr) growth pressures.

4.4.3 Effect of Temperature on growth of $Ge_{1-y}Sn_y$ Epilayers

Finally, the effect of growth temperature is investigated when using GeH_4 in combination with $SnCl_4$ to grow $Ge_{1-y}Sn_y$ epilayers. It should be noted that careful consideration should be taken to adjust growth temperature appropriately as the most important growth condition and understand its impact on growth rate and Sn concentration of $Ge_{1-y}Sn_y$ epilayers [10]. In general, it has been suggested that it is necessary to take into account low growth temperature due to the metastable properties of $Ge_{1-y}Sn_y$ binary alloys. Nevertheless, it has been unclear how to achieve reactivity for corresponding chemical precursors during epitaxial growth [102]. As shown in Figure 4.12 (top), the Sn concentration increases with the reduction in temperature. This is a similar behaviour when using Ge_2H_6 as a Ge precursor. In the same figure, the effect of temperature on growth rate is shown, which has a positive correlation.

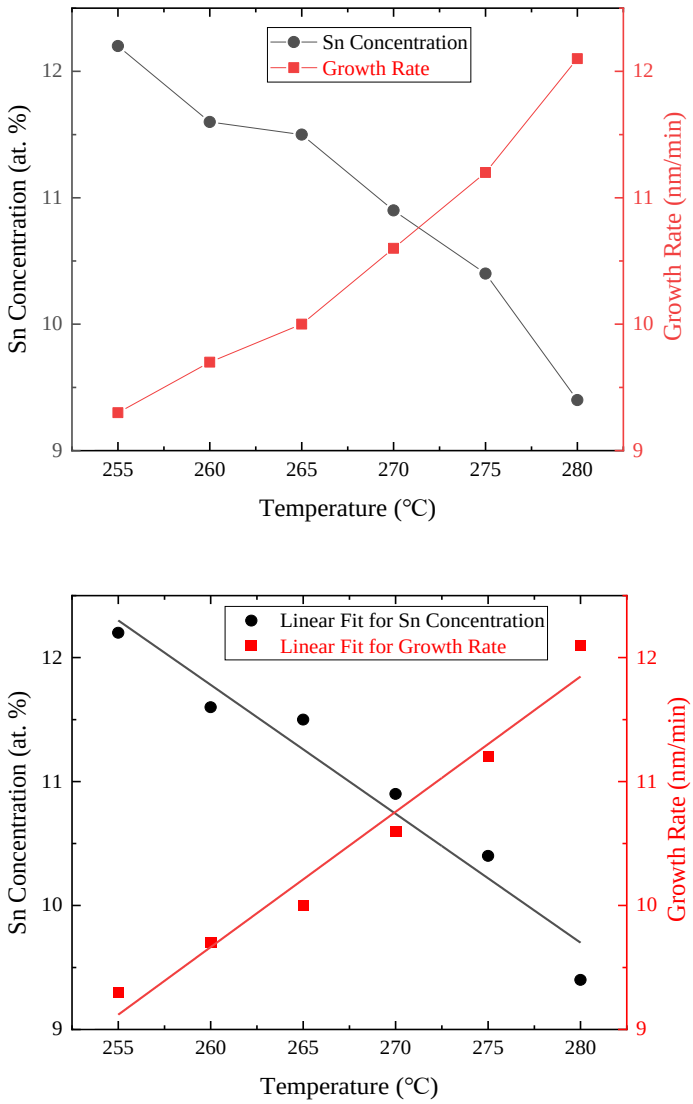

Figure 4.12 Top: Effect of growth temperature (°C) on Sn concentration of $Ge_{1-y}Sn_y$ epilayers grown at 500 Torr using 3.45×10^{-4} $SnCl_4/GeH_4$. Bottom: Linear lines that are fitted to data points with residual sum of squares of ~0.2 (for both linear lines). Equations of these lines are: $y_{\,Sn\ Concentration} = -0.1\,x_{\,Temperature} + 38.8$ and $y_{\,Growth\ Rate} = 0.1\,x_{\,Temperature} - 18.7$.

By fitting linear lines into data points, as shown in Figure 4.12 (bottom), it is possible to find hypothetical minimum and maximum temperature in which growth of $Ge_{1-y}Sn_y$. An important assumption is that Sn concentration and growth rate correlate linearly with temperature at all temperatures. There are two inevitable facts to consider: one is that the growth rate cannot be ≤ 0 nm/min, and the other is that the Sn concentration cannot be ≤ 0 at.%. By taking these two inevitable facts as well as the above assumption into account, together with the following equations, the minimum growth temperature is estimated at 187 °C (Equation 4.1) and the

maximum growth temperature at 388 °C (Equation 4.2). Thus, the growth of the $Ge_{1-y}Sn_y$ epilayer is only allowed when the growth temperature is between 187 °C and 388 °C.

$$y_{\,Growth\ Rate} = 0.1\ x_{\,Temperature} - 18.7 \quad (4.1)$$

$$y_{\,Sn\ Concentration} = -0.1\ x_{\,Temperature} + 38.8 \quad (4.2)$$

It is also possible to determine the maximum Sn concentration and its corresponding growth rate by taking into account the following assumption that growth cannot be achieved at a temperature less than Sn melting point of ~231 °C. It is important to note that the Sn concentration here is the one for fully strained $Ge_{1-y}Sn_y$, and not for partially/fully relaxed $Ge_{1-y}Sn_y$ in which much more Sn can incorporate into it because of its larger in-plane lattice parameter. Based on these assumptions, along with Equations 4.1 and 4.2, the maximum Sn concentration is estimated at 15.7 at.% with growth rate of 4.4 nm/min.

4.5 Conclusion

In this chapter, the heteroepitaxial growth of $Ge_{1-y}Sn_y$ on a Si (001) substrate via a relaxed Ge-VS was investigated using commonly available commercial Ge precursor, GeH_4, in combination with $SnCl_4$ precursors, by RP-CVD. Chemical reactions (initiations) during growth were briefly explained. The effects of CVD growth conditions, such as pressure, temperature and $SnCl_4/GeH_4$ ratio, were carefully studied experimentally. In addition, some explanations were given about Sn segregation and its role in the formation of Sn-rich micro-islands on the surface of the $Ge_{1-y}Sn_y$ epilayer. Surface morphology is important not only for device fabrication, but also for further growth on $Ge_{1-y}Sn_y$ epilayer.

In summary, the higher pressure ($\geq$ 500 Torr) is not only more advantageous to increase Sn concentration, but also to expand the allowed region for other CVD growth conditions, such as $SnCl_4/GeH_4$ ratio and temperature. In terms of growth temperature, lowering the temperature generally increases Sn concentration and reduces growth rate. The temperature can be used as a primary condition to adjust the Sn concentration in $Ge_{1-y}Sn_y$ during CVD growth. After all, the $SnCl_4/GeH_4$ ratio is a challenging growth condition to optimise. It seems the best approach is to choose an appropriate temperature at a high pressure, and then adjust the $SnCl_4/GeH_4$ ratio to make the growth possible and efficient. Here possible means to select a $SnCl_4/GeH_4$ ratio that allows growth, and efficient means not to waste unnecessary amounts of precursors.

Chapter 5

The Effects of Ge Precursor on the Epitaxy & Quality of $Ge_{1-y}Sn_y$

5.1 Introduction

It has already been explained why CVD is the most important growth technique for epitaxial growth of $Ge_{1-y}Sn_y$ in terms of applicability and practicality. It is also important to understand that it is necessary to use inexpensive and commercially available precursors. The most used conventional Ge precursor for the growth of $Ge_{1-y}Sn_y$, which is also used for the growth of crystalline Ge, is Ge_2H_6. After successful growth of $Ge_{1-y}Sn_y$ with $SnCl_4$ and Ge_2H_6 in 2011 [39], GeH_4 was used for the first time in 2014 for CVD growth of $Ge_{1-y}Sn_y$ [49], and we here at the University of Warwick tended not only to grow $Ge_{1-y}Sn_y$ with GeH_4, but also to understand its mechanism and techniques to improve its quality [68]. Since GeH_4 precursor is more cost effective, it is more favourable than Ge_2H_6 precursor. In this chapter, the heteroepitaxial growth of $Ge_{1-y}Sn_y$ on a Si (001) substrate via a relaxed Ge-VS was investigated using two commonly available commercial Ge precursors, GeH_4 and Ge_2H_6 in combination with $SnCl_4$ precursors, by RP-CVD. Both precursors demonstrated growth of strained and relaxed $Ge_{1-y}Sn_y$ epilayers, but incorporation of Sn into $Ge_{1-y}Sn_y$ was relatively higher when using the more reactive Ge precursor, Ge_2H_6. Since Ge_2H_6 is much more expensive, difficult to handle and store than GeH_4, it is of great interest to develop high quality $Ge_{1-y}Sn_y$ epilayers with high Sn concentration using the latter precursor. In this chapter, it has been shown that the main differences between the two precursors are based on process optimisation, which enables the growth of $Ge_{1-y}Sn_y$ binary alloys with sufficient Sn concentration at relatively low cost.

5.2 The Effects of Ge Precursor on the Heteroepitaxy of $Ge_{1-y}Sn_y$ Epilayers

5.2.1 Sn Concentration of $Ge_{1-y}Sn_y$ Epilayers

Similar to the last chapter, the Sn concentration of each $Ge_{1-y}Sn_y$ epilayer was estimated using HR-XRD. A typical symmetric and asymmetric RSMs for a ~131 nm thick fully strained $Ge_{0.919}Sn_{0.081}$ grown on Si (001) via Ge-VS using Ge_2H_6 is shown in Figure 5.1. The (004) Bragg peaks are aligned in the in-plane reciprocal coordinate (Q_x). Additionally, in Figure 5.2, the asymmetric (224) RSM indicates that the Ge-VS is almost fully relaxed to the Si (001) substrate, while the $Ge_{1-y}Sn_y$ epilayer is fully strained to the Ge-VS. The Sn concentration of the $Ge_{1-y}Sn_y$ can be calculated employing the following modified Vegard's law (Equation 3.9 on page 37) as presented in the last chapter, with the same bowing parameter of 0.041 Å [10,41,173].

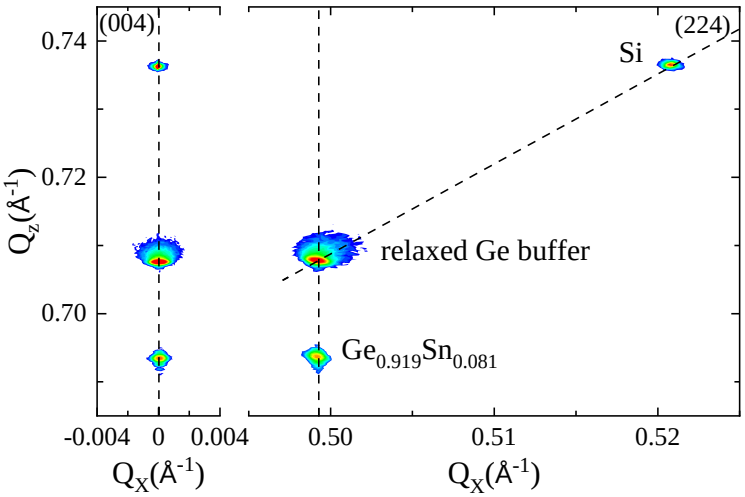

Figure 5.1 Symmetric (left) and asymmetric (right) RSMs for a fully strained $Ge_{0.919}Sn_{0.081}$ epilayer grown on Si (001) via a relaxed Ge-VS.

In this chapter, intrinsic fully strained $Ge_{1-y}Sn_y$ epilayers were grown on Si (001) substrate via a relaxed Ge-VS using RP-CVD. A typical example of grown materials is shown in Figure 4.1 on page 47, which demonstrates a schematic cross sectional structure of the fully strained $Ge_{1-y}Sn_y$\Ge-VS\Si (001). All crystalline materials were grown on wafers 100 mm diameter Si (001) substrates. For epitaxial growth of fully strained $Ge_{1-y}Sn_y$ binary alloys given in this chapter, $SnCl_4$ was used in combination with either Ge_2H_6 or GeH_4 as shown Figure 4.2 on page 47. Furthermore, purified H_2 was used as a carrier gas and chamber pressure controller.

5.2.2 Heteroepitaxy of $Ge_{1-y}Sn_y$ Epilayers Using Ge_2H_6 or GeH_4

The HR-XRD ω-2θ coupled scans for epi-wafers grown by $SnCl_4$ in combination with Ge_2H_6 and GeH_4 are shown in the next page in Figure 5.2 and Figure 5.3, respectively. As can be seen in these figures, the peaks at ~34.6° and ~33.0° are originated from Si (001) substrate and Ge-VS, respectively. There are also strong peaks between 32° and 33°, which indicate the successful growth of $Ge_{1-y}Sn_y$ epilayers using both Ge_2H_6 and GeH_4 precursors. The shift in the Bragg peaks to lower angles in these two figures demonstrates higher Sn incorporation into $Ge_{1-y}Sn_y$ binary alloy. The Sn concentration of each sample was measured from RSMs, and the modified Vegard's law as previously presented in Equation 3.9 on page 37. Thickness fringes that can be observed in the spectra, which are around the $Ge_{1-y}Sn_y$ peak, are due to X-ray interferences from fully strained $Ge_{1-y}Sn_y$ epilayers. The thickness of each $Ge_{1-y}Sn_y$ epilayer was estimated from the thickness fringes of HR-XRD ω-2θ coupled scans and then confirmed using X-TEM micrographs.

To compare the effect of Ge precursors on the growth of $Ge_{1-y}Sn_y$ epilayers, the growth time of all epilayers was kept the same. Thus, $Ge_{1-y}Sn_y$ epilayers with different thicknesses were grown. The pressure was maintained the same at 500 Torr during the epitaxial growth of all these samples. In addition, the same partial pressure of 10 mTorr was used for both Ge_2H_6 and GeH_4, but the partial pressure of $SnCl_4$ was adjusted differently, as shown in Figure 5.2 and Figure 5.3. Finally, the growth temperature was maintained in such a way that enabled the growth of $Ge_{1-y}Sn_y$ epilayers with the same Sn concentration range when using one of the Ge precursors Ge_2H_6 (270 °C) or GeH_4 (280 °C).

As shown in Figure 5.4 and Figure 5.5, an increase in $SnCl_4$ partial pressure leads to an increase in the growth rate of $Ge_{1-y}Sn_y$ epilayer. As explained in the previous chapter, $SnCl_4$ can increase the production of Ge atoms, which is the main driving force for growth rate of $Ge_{1-y}Sn_y$ epilayer. On the other hand, increasing $SnCl_4$ does not necessarily lead to an increase in Sn concentration. This has already been discussed in the previous chapter, how the presence of too much Sn atoms on the surface leads to Sn segregation, if the growth rate is not sufficient to suppress Sn segregation. This can be seen in the case of grown samples using Ge_2H_6 as a Ge precursor (Figure 5.4), where the increase in $SnCl_4$ from 10 mTorr to 15 mTorr led to a reduction in the Sn concentration of the grown $Ge_{1-y}Sn_y$ epilayer. But in the case of grown samples using GeH_4 (Figure 5.5), we have not yet reached such a level, even when $SnCl_4$ reached 40 mTorr.

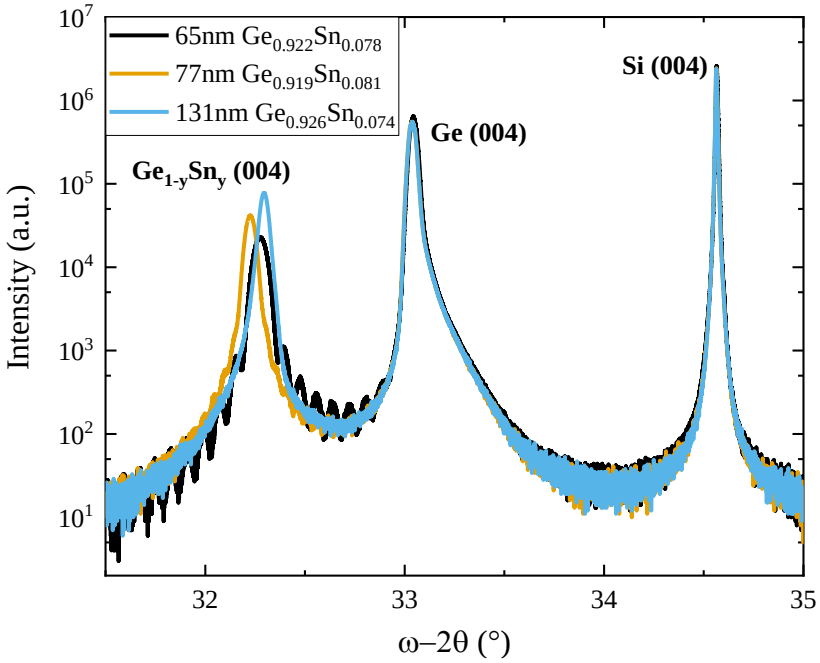

Figure 5.2 HR-XRD ω-2θ coupled scans of $Ge_{1-y}Sn_y$ epilayers grown on Si (001) via Ge-VS at temperature of 270 °C for 18:00 min by 10 mTorr Ge_2H_6 in combination with $SnCl_4$ partial pressure of 5 mTorr, 10 mTorr and 15 mTorr for samples with Sn concentration of 7.8 at.%, 8.1 at.% and 7.4 at.% in $Ge_{1-y}Sn_y$ with thickness of 65 nm, 77 nm and 131 nm, respectively.

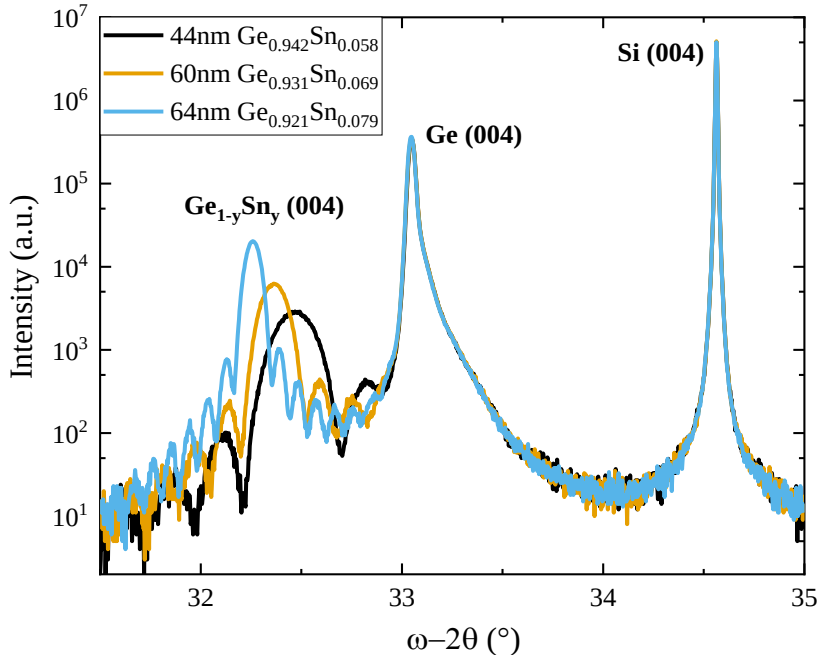

Figure 5.3 HR-XRD ω-2θ coupled scans of $Ge_{1-y}Sn_y$ epilayers grown on Si (001) via Ge-VS at temperature of 280 °C for 18:00 min by 10 mTorr GeH_4 in combination with $SnCl_4$ partial pressure of 10 mTorr, 20 mTorr and 40 mTorr for samples with Sn concentration of 5.8 at.%, 6.9 at.% and 7.9 at.% in $Ge_{1-y}Sn_y$ with thickness of 44 nm, 60 nm and 64 nm, respectively.

Finally, a higher growth rate is expected when Ge_2H_6 is used over GeH_4, even if a lower growth temperature by 10 °C is used. This is because the production of Ge atoms is generally greater when Ge_2H_6 is used compared to GeH_4. For instance, by comparing $Ge_{0.919}Sn_{0.081}$, which was grown with 10 mTorr of Ge_2H_6 with $Ge_{0.942}Sn_{0.058}$, which was grown with 10 mTorr of GeH_4 (despite the higher temperature used), a greater $Ge_{1-y}Sn_y$ growth rate (by 75 %) was achieved in the case of Ge_2H_6 compared to GeH_4.

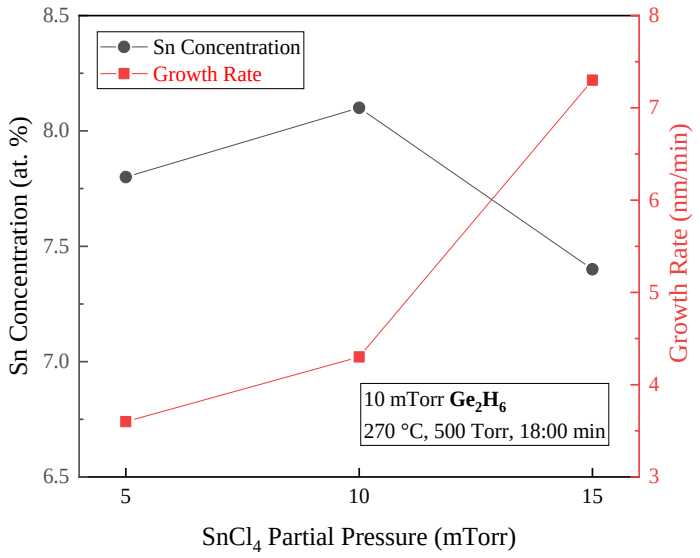

Figure 5.4 The effect of $SnCl_4$ partial pressure on Sn concentration and growth rate of $Ge_{1-y}Sn_y$ epilayers when using 10 mTorr Ge_2H_6 as a Ge precursor.

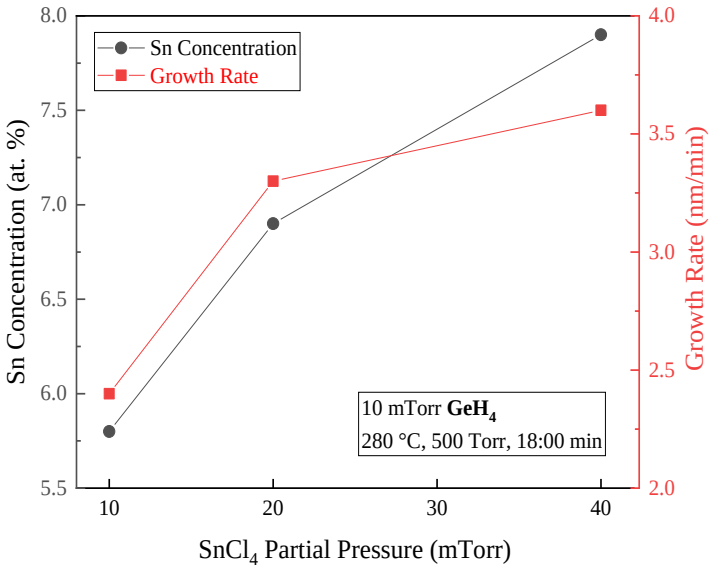

Figure 5.5 The effect of $SnCl_4$ partial pressure on Sn concentration and growth rate of $Ge_{1-y}Sn_y$ epilayers when using 10 mTorr GeH_4 as a Ge precursor.

5.3 The Effects of Ge Precursor on the Quality of $Ge_{1-y}Sn_y$

5.3.1 Thickness Measurements of $Ge_{1-y}Sn_y$ Epilayers

The thicknesses of these layers were measured more accurately using X-TEM. The micrograph on the right in Figure 5.6 shows a typical X-TEM (004) image of the Ge-VS and $Ge_{0.919}Sn_{0.081}$ epilayer grown on the Si (001) substrate. The thickness of the Ge-VS is ~1.4 µm and the thickness of $Ge_{0.919}Sn_{0.081}$ is ~131 nm. For all $Ge_{1-y}Sn_y$ discussed in the previous section, their thicknesses were measured using X-TEM, although these measurements are in line with thicknesses estimated using thickness fringes from their HR-XRD ω-2θ coupled scans shown in Figure 5.2 and Figure 5.3.

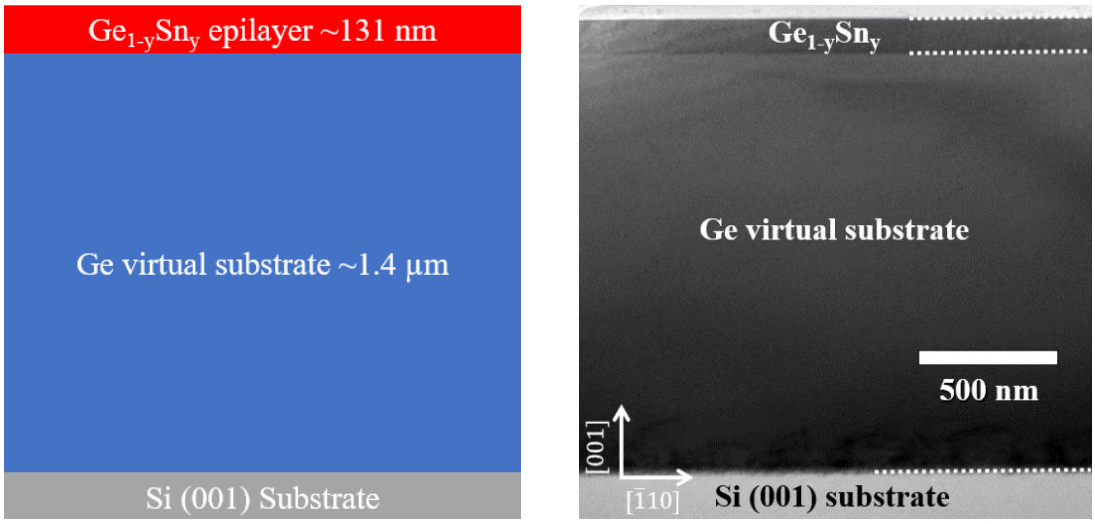

Figure 5.6 Left: The schematic structure of layers. Right: diffraction condition X-TEM micrograph of $Ge_{0.919}Sn_{0.081}$\Ge-VS\Si (001) interfaces with ~1.4 µm thick Ge-VS, and ~131 nm thick $Ge_{0.919}Sn_{0.081}$. The $Ge_{0.919}Sn_{0.081}$ epilayer was grown using 10 mTorr Ge_2H_6 in combination with 15 mTorr $SnCl_4$ at 270 °C.

5.3.2 Quality of $Ge_{1-y}Sn_y$ Epilayers, from Surface to Interfaces

Figure 5.7 shows the lattice resolution of the interface between $Ge_{0.919}Sn_{0.081}$ and Ge-VS. As shown in the X-TEM image obtained in (220) condition in Figure 5.7, the $Ge_{0.919}Sn_{0.081}$\Ge-VS interface is sharp and defect-free. It is clear that $Ge_{0.919}Sn_{0.081}$ is fully strained and no dislocations can be observed. Furthermore, the precipitation on the surface above the $Ge_{0.919}Sn_{0.081}$ layer can be studied by X-TEM, as shown in Figure 5.8, but either the increase in Sn concentration in the $Ge_{1-y}Sn_y$ epilayer or its thickness leads to a degradation of the

epilayer quality and surface morphology. Both effects appear to be a consequence of Sn segregation in the $Ge_{1-y}Sn_y$ epilayer.

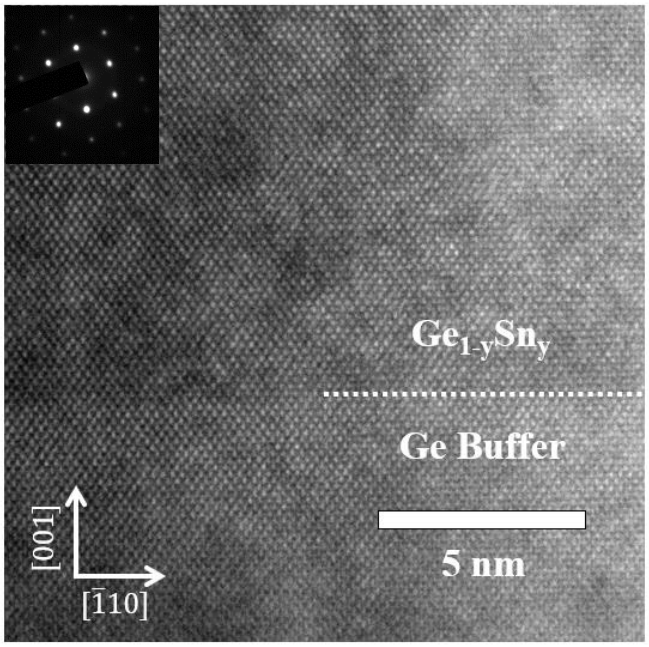

Figure 5.7 Lattice resolved micrograph of the $Ge_{0.919}Sn_{0.081}$\Ge-VS (buffer) interface with corresponding diffraction pattern. The $Ge_{0.919}Sn_{0.081}$ epilayer was grown using 10 mTorr Ge_2H_6 in combination with 15 mTorr $SnCl_4$ at temperature of 270 °C.

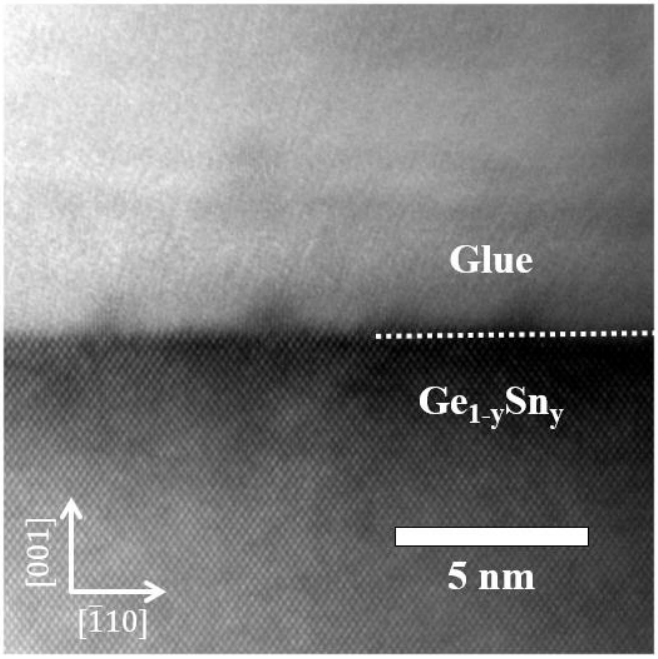

Figure 5.8 Lattice resolved X-TEM micrograph of $Ge_{0.919}Sn_{0.081}$ surface, in which Sn precipitation can be observed. The $Ge_{0.919}Sn_{0.081}$ epilayer was grown using 10 mTorr Ge_2H_6 in combination with 15 mTorr $SnCl_4$ at temperature of 270 °C.

5.3.3 Thickness Uniformity of $Ge_{1-y}Sn_y$ Epilayers Grown by Ge_2H_6 & GeH_4

The thickness uniformity of the epilayers across 100 mm wafer was examined by FTIRS. An example of $Ge_{1-y}Sn_y$ epilayers, grown by GeH_4 and Ge_2H_6, thickness uniformity is shown in Figure 5.9. Thickness uniformity of $Ge_{1-y}Sn_y$ was approximately ~3.5 % for epilayer grown by GeH_4 and is even lower for the epilayer grown by Ge_2H_6, ~1.5 %. For thin $Ge_{1-y}Sn_y$ epilayers (that is below 100 nm) the accuracy of the epilayer thickness measured by FTIRS is limited. Thus, the thicknesses of $Ge_{1-y}Sn_y$ epilayers were obtained more accurately with the support of thickness fringes in HR-XRD ω-2θ coupled scans and X-TEM measurements.

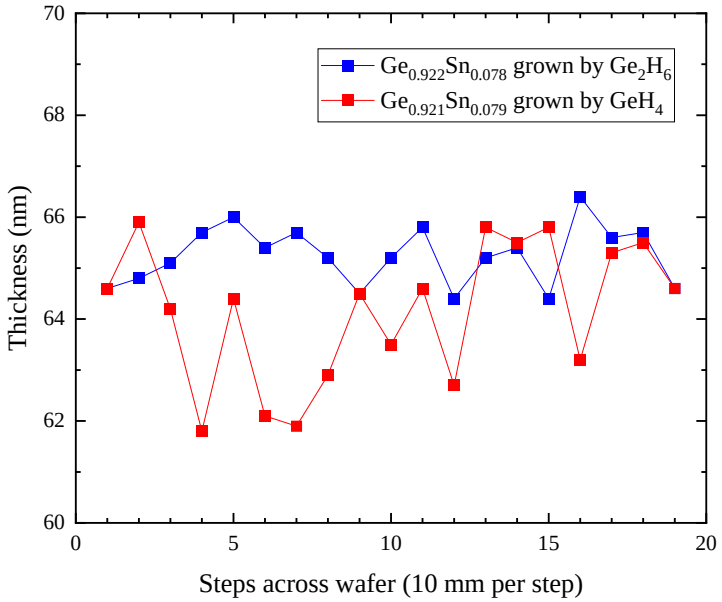

Figure 5.9 The thickness uniformity of two $Ge_{1-y}Sn_y$ epilayers with very similar Sn concentration and thickness grown on Si (001) via Ge-VS using either of Ge_2H_6 or GeH_4 in combination with $SnCl_4$ obtained by FTIRS.

5.3.4 Effect of Ge precursor on Surface Morphology of $Ge_{1-y}Sn_y$ Epilayers

The surface roughness of three $Ge_{1-y}Sn_y$ epilayers grown with the same CVD growth conditions, but with different partial $SnCl_4/H_2$ pressure is shown in Figure 5.10. They are all grown by Ge_2H_6 precursor and as can be seen in the AFM scans; the surface roughness increases with increasing $SnCl_4/H_2$ partial pressure. It should be noted that the surface roughness of $Ge_{1-y}Sn_y$ epilayers generally increases as a consequence of Sn segregation and precipitation, which can be the result of various factors explained below. One factor is an inadequate growth rate in relation to available Sn atoms on the surface. If the growth rate is too slow, available Sn atoms on the surface could segregate, and/or Sn atoms within top

formed layers could precipitate during or shortly after the epitaxial growth. This can be seen in Figure 5.10 when comparing the top two AFM images, in which both epilayers are fully strained with a similar growth rate but slightly different Sn concentration.

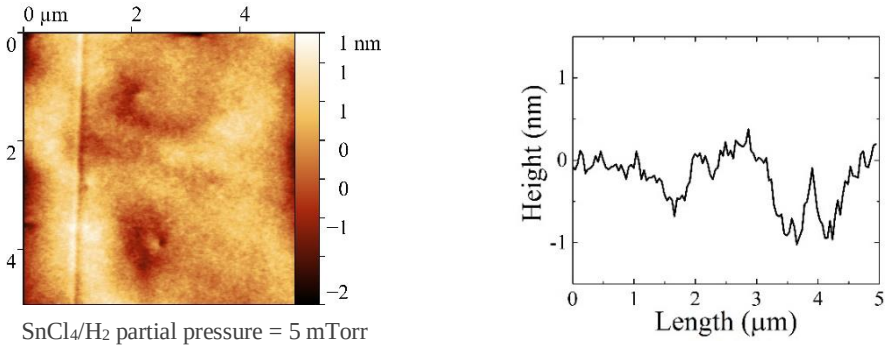

$SnCl_4/H_2$ partial pressure = 5 mTorr
Sn Concentration = 7.8 at.%
Thickness of epilayer = 66 nm
RMS = 1.0 nm

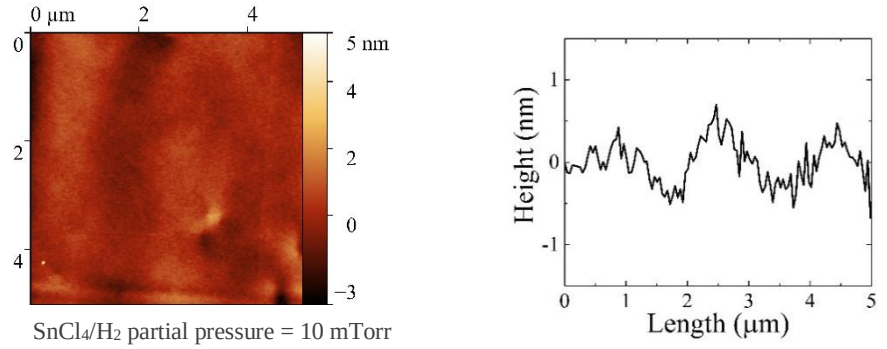

$SnCl_4/H_2$ partial pressure = 10 mTorr
Sn Concentration = 8.1 at.%
Thickness of epilayer = 77 nm
RMS = 1.2 nm

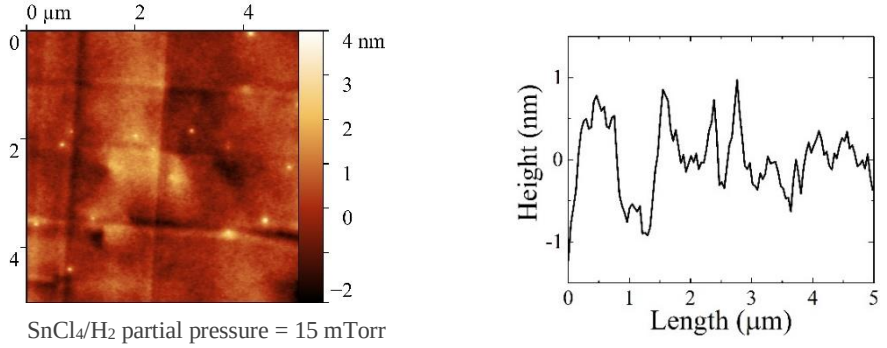

$SnCl_4/H_2$ partial pressure = 15 mTorr
Sn Concentration = 7.4 at.%
Thickness of epilayer = 131 nm
RMS = 3.0 nm

Figure 5.10 Left: AFM scans using tapping mode for the $Ge_{1-y}Sn_y$ grown on Ge-VS/Si (001) by Ge_2H_6 precursor at the temperature of 270 °C with different $SnCl_4/H_2$ partial pressure. Right: Align profile through the centre of each AFM scan. As the partial pressure $SnCl_4/H_2$ increases, Sn segregation occurs, resulting in increasing the surface roughness which were measured in term of root mean square (RMS).

The other factor could be the strain relaxation of the $Ge_{1-y}Sn_y$ epilayer, which can lead not only to defect creation, but also to Sn segregation or precipitation. This is because when strain relaxation begins, growth rate and Sn incorporation vary consequently, which could lead to Sn segregation or precipitation, as already explained. This can be seen in Figure 5.10 when comparing the bottom two AFM images, in which the thicker $Ge_{1-y}Sn_y$ epilayer with a lower Sn concentration, in which its growing layers have begun to relax, has a greater surface roughness. Therefore, it is crucial to precisely tune CVD growth conditions to appropriately suppress Sn segregation and precipitation during the heteroepitaxy of $Ge_{1-y}Sn_y$ epilayers.

The Sn structures appeared on the $Ge_{1-y}Sn_y$ surfaces were investigated by SEM, which was equipped with an EDAX EDS to analyse elemental composition on the surfaces of the samples. The EDS scan of $Ge_{0.919}Sn_{0.081}$, which has a surface roughness of 1.2 nm and has no Sn structures on its surface (the middle AFM scan in Figure 5.10), is presented in Figure 5.11.

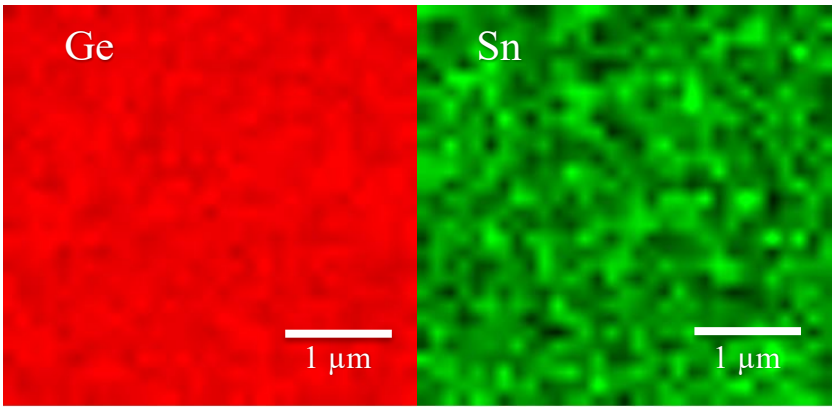

Figure 5.11 EDS scan of $Ge_{0.919}Sn_{0.081}$ epilayer grown by 10 mTorr Ge_2H_6 precursor in combination with 5 mTorr $SnCl_4$ partial pressure. Left: Ge (GeL emission line) Right: Sn (SnL emission line).

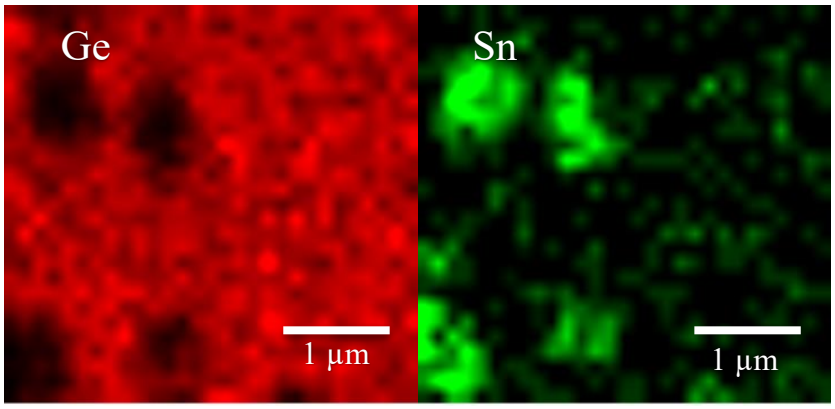

Figure 5.12 EDS scan of $Ge_{0.926}Sn_{0.074}$ epilayer grown by 10 mTorr Ge_2H_6 precursor in combination with 15 mTorr $SnCl_4$ partial pressure. Left: Ge (GeL emission line) Right: Sn (SnL emission line).

For the sample with the highest surface roughness of 3.0 nm, however, $Ge_{0.926}Sn_{0.074}$ (the bottom AFM scan in Figure 5.10), the EDS surface scans are presented in Figure 5.12. As can be seen, the Sn structures appear on the surface of the $Ge_{1-y}Sn_y$ epilayer due to the Sn segregation. In the previous chapter, Figure 2.13 on page 19, we discussed Sn-rich micro-islands, which were approximately ten times larger than these in diameters. As already explained, these structures gradually become larger during the heteroepitaxy of $Ge_{1-y}Sn_y$ epilayers (or simply as the growth time increases).

As already explained, in order to avoid Sn segregation on the surface of the $Ge_{1-y}Sn_y$ epilayer, the growth temperature should be kept at its lowest possible level. It should be noted that the exchange rate between adatoms (Ge) and surface dopant atoms (Sn) is reduced at low growth temperatures. Moreover, increasing growth rates, which can reduce the required time for exchange, can lead to the suppression of Sn segregation. However, Sn precipitation is usually due to post-growth processes, such as annealing processes [10,65].

For either GeH_4 or Ge_2H_6 precursors, the higher Sn concentration in $Ge_{1-y}Sn_y$ epilayer can be achieved by reducing the growth temperature [10,174] as long as the precursors are still reactive, in combination with $SnCl_4$ of course, at such low temperatures. For instance, as the growth temperature decreases from 280 °C to 275 °C for those samples grown by GeH_4, the Sn concentration in $Ge_{1-y}Sn_y$ was increased by 1 at.%, approximately. The further reduction in growth temperature will ultimately lead to a decline in Sn incorporation, as Ge precursors may become unreactive, but this limit has not been reached at the lowest temperatures in this study (270 °C). In the next chapter, we have explored lower temperatures when using GeH_4 as Ge precursor. It should also be noted that to increase Sn concentration in $Ge_{1-y}Sn_y$, it is necessary to reduce growth temperature [102], which means that we cannot simply compare the growth rate of $Ge_{1-y}Sn_y$ at very similar growth temperature when using either GeH_4 or Ge_2H_6. Instead, we need to compare the growth rate of similar grown $Ge_{1-y}Sn_y$ when using one of these Ge precursors.

All fully compressive strained $Ge_{1-y}Sn_y$ epilayers grown by GeH_4 have low surface roughness of less than 1.0 nm. They replicate the surface morphology of the underlying relaxed Ge-VS, which exhibits a smooth surface with RMS surface roughness of just less than 1.0 nm. It can be seen in Figure 5.13 that as the partial pressure of $SnCl_4/H_2$ increases in combination with the GeH_4 precursor, the surface roughness remains low and unaffected. In other words, it seems the Sn segregation and precipitation are being controlled when using GeH_4 instead of

Ge_2H_6 as Ge precursor. This could be a useful practical approach when a thicker $Ge_{1-y}Sn_y$ epilayer is required to grow. However, as mentioned previously, we have not reached the level for $SnCl_4$, where the Sn concentration decreases with an increase with partial pressure of $SnCl_4$. Further research is therefore suggested to confirm our explanation.

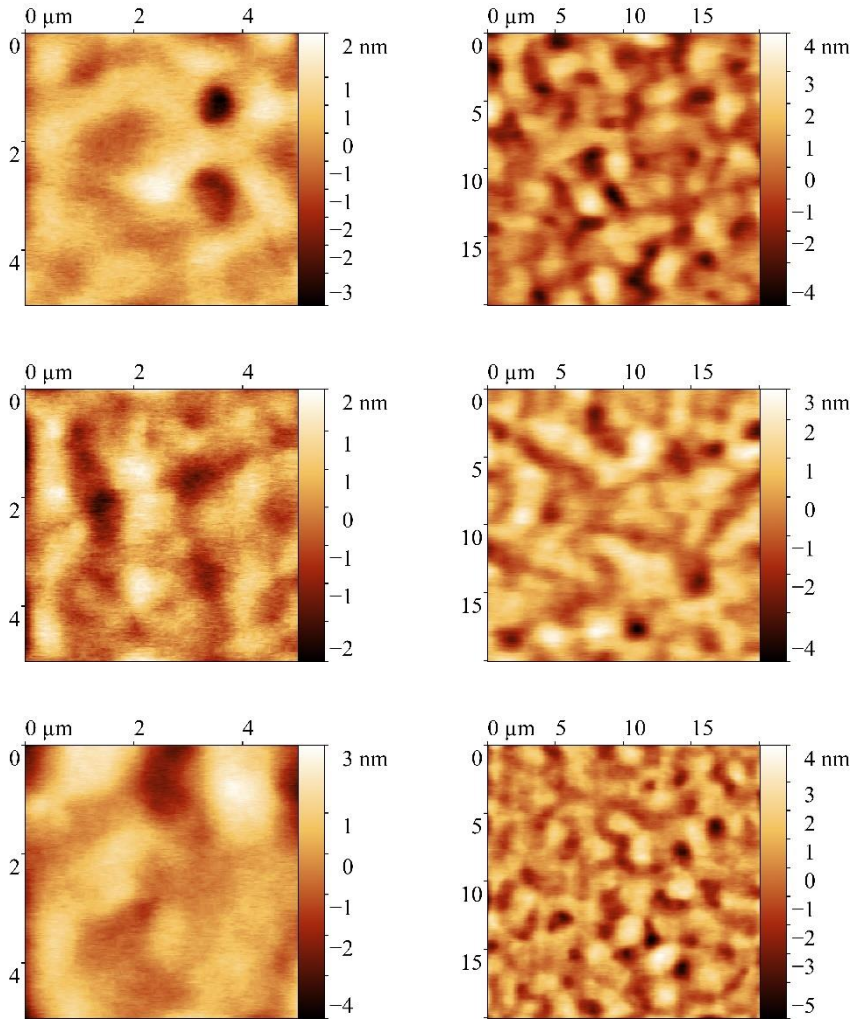

Figure 5.13 AFM scans of $Ge_{1-y}Sn_y$ grown by 10 m Torr GeH_4 in RP-CVD at the temperature of 280 ℃. Top: AFM scans of 44 nm thick $Ge_{0.942}Sn_{0.058}$ grown using 10 mTorr $SnCl_4$ partial pressure with surface roughness of 0.8 nm. Middle: AFM scans of 60 nm thick $Ge_{0.931}Sn_{0.069}$ grown using 20 mTorr $SnCl_4$ partial pressure with surface roughness of 0.8 nm. Bottom: AFM scans of 64 nm thick $Ge_{0.921}Sn_{0.079}$ grown using 40 mTorr $SnCl_4$ partial pressure with surface roughness of 0.9 nm. As the $SnCl_4/H_2$ partial pressure increases, the Sn concentration in $Ge_{1-y}Sn_y$ epilayer increases, while the surface roughness remains low.

It is important to understand that one of the consequences of a reduction in growth temperature is a reduction in growth rate, which has also been observed in our research. The results show that the Sn concentration in $Ge_{1-y}Sn_y$ increases as the $SnCl_4/H_2$ partial pressure increases up until a certain level, where the increase in $SnCl_4/H_2$ partial pressure leads to a reduction in the

Sn concentration which is evident in Figure 5.4. One of the reasons may be that higher $SnCl_4/H_2$ partial pressure leads to Sn segregation, resulting in contamination of the surface as shown in Figure 5.10. Beyond this point, the Sn concentration in the $Ge_{1-y}Sn_y$ epilayer decreases. It is important to identify such critical points for certain growth conditions to maintain a high growth rate and a high Sn concentration with low surface roughness. Understanding such limitations can open up a new path to growth of high quality $Ge_{1-y}Sn_y$ binary alloys with sufficient Sn concentration with a practical growth rate.

Another objective of $Ge_{1-y}Sn_y$ epitaxy is to find the best RP-CVD growth conditions to achieve high quality $Ge_{1-y}Sn_y$ epilayers with the highest possible growth rate without flowing unreacted precursors to increase commercial viability. It should be noted that the temperature required for the growth of $Ge_{1-y}Sn_y$ epilayer with GeH_4 is generally higher than Ge_2H_6. The achieved growth rate for $Ge_{1-y}Sn_y$ epilayers grown by GeH_4 was observed to be approximately twice as slow as for those grown epilayers grown by Ge_2H_6. The advantage of using GeH_4, however, is that the $Ge_{1-y}Sn_y$ epilayers grown by this precursor have relatively better quality, minimising Sn segregation and precipitation.

Our research shows that the fully strained $Ge_{1-y}Sn_y$ epilayers grown by GeH_4 maintain a smooth surface with low surface roughness (RMS of <1 nm), as shown in Figure 5.13. However, the AFM scans and surface roughness of three $Ge_{1-y}Sn_y$ epilayers which were grown using Ge_2H_6 precursor with the same growth conditions but different $SnCl_4/H_2$ partial pressures, confirm the presence of Sn segregation due to the high $SnCl_4/H_2$ partial pressure, as shown in Figure 5.10. The structures on the surface of these $Ge_{1-y}Sn_y$ epilayers were confirmed to be made of Sn, as shown in Figure 5.12.

By using Ge_2H_6 in combination with $SnCl_4$, very high Sn concentration (up to ~14 at.%) can be achieved for relaxed $Ge_{1-y}Sn_y$ epilayers [44,45,66,122,164,175]. Higher Sn incorporation is achieved by reducing growth temperature and suppressing Sn segregation. Furthermore, higher temperatures are required to grow $Ge_{1-y}Sn_y$ epilayers when using GeH_4 as opposed to Ge_2H_6 precursor. This is simply because the GeH_4 is less reactive and therefore requires higher temperatures to break its bonding energy, in addition to chemical reactions that occur in contact with $SnCl_4$.

In order to achieve indirect-to-direct bandgap transition in a $Ge_{1-y}Sn_y$ epilayer, a Sn concentration of over 9 at.% (in partially/fully relaxed $Ge_{1-y}Sn_y$) is required

[10,35,39,106,176]. Further process optimisation is needed to achieve such a high level of Sn incorporation into the $Ge_{1-y}Sn_y$ epilayer, which could be achieved by precisely tuning the $SnCl_4$ partial pressure and reducing the growth temperature, which is discussed in more detail in the next chapter.

Given the cost efficiency and availability of GeH_4 precursor, this source is more favourable than Ge_2H_6. By using GeH_4 as a Ge precursor, high quality $Ge_{1-y}Sn_y$ epilayers can be grown with fewer defects and lower surface roughness than those grown by Ge_2H_6 precursor at similar Sn concentration levels. One possible explanation is the increased purity of GeH_4 or the degradation of the Ge_2H_6 source over longer-term storage. Since the probability of Sn segregation on the surface is lower in the case of GeH_4, high quality thicker $Ge_{1-y}Sn_y$ epilayer can be grown by this precursor, but this must be confirmed in further experiments.

5.4 Conclusion

The heteroepitaxial growth of $Ge_{1-y}Sn_y$ on a Si (001) substrate via a relaxed Ge-VS was investigated using two commonly available commercial Ge precursors, GeH_4 and Ge_2H_6 in combination with $SnCl_4$ precursors, by RP-CVD. Both precursors demonstrated growth of strained and relaxed $Ge_{1-y}Sn_y$ epilayers, but incorporation of Sn into $Ge_{1-y}Sn_y$ was significantly higher when using the more reactive Ge precursor, Ge_2H_6. Since Ge_2H_6 is much more expensive, difficult to handle and store than GeH_4, it is of great interest to develop high quality $Ge_{1-y}Sn_y$ epilayers with high Sn concentration using the latter precursor.

In this chapter, it was shown that the main differences between the two precursors are based on process optimisation, which enables the growth of $Ge_{1-y}Sn_y$ binary alloys with sufficient Sn concentration at relatively lower cost. The results demonstrated that when using GeH_4, a lower $Ge_{1-y}Sn_y$ growth rate was achieved than when using Ge_2H_6 under the very similar growth conditions. $Ge_{1-y}Sn_y$ epilayers grown with GeH_4 had lower surface roughness than epilayers grown with Ge_2H_6. This is because Sn segregation and precipitation could be controlled when GeH_4 was used over Ge_2H_6 as a Ge precursor. This could be crucial for achieving high quality metal contacts on the $Ge_{1-y}Sn_y$ epilayer, the growth of thick $Ge_{1-y}Sn_y$ epilayers for strain relaxation, and further heteroepitaxial growth of multilayers or quantum wells. The results of this investigation show that GeH_4 could be a viable precursor preference for low cost heteroepitaxy of $Ge_{1-y}Sn_y$ epilayers.

Chapter 6

Very Low Temperature Heteroepitaxy of $Ge_{1-y}Sn_y$ Epilayers

6.1 Introduction

GeH_4 was used for the first time in 2014 for CVD growth of $Ge_{1-y}Sn_y$ [49], and we here at the University of Warwick tended not only to grow $Ge_{1-y}Sn_y$ with GeH_4, but also to understand its mechanism and techniques to improve its quality [68] as shown in the previous chapter. In this chapter, the chemical mechanisms accountable for the CVD growth of $Ge_{1-y}Sn_y$ binary alloys using $SnCl_4$ and GeH_4 precursors at very low temperature are discussed. Firstly, the effects of growth temperature and $SnCl_4/GeH_4$ ratio on growth rate and layer composition are examined. After that, thermochemical analyses, which show possible reaction pathways, are presented. In this work, heteroepitaxy of $Ge_{1-y}Sn_y$ is achieved at a very low temperature which has previously been assumed to be an impossible task.

6.2 Heteroepitaxy of $Ge_{1-y}Sn_y$ Epilayers Using GeH_4

It is necessary to consider low growth temperature due to the metastable characteristics of $Ge_{1-y}Sn_y$ binary alloys. Nevertheless, it has been unclear how adequate reactivity can be achieved for corresponding chemical precursors during epitaxial growth [102]. Similar to Ge_2H_6, when using GeH_4 precursor in combination with $SnCl_4$, the reduction of growth temperature increases Sn incorporation in the $Ge_{1-y}Sn_y$ epilayers but can also significantly reduce growth rates [10,174]. Reactive intermediates that enable the reaction to occur in an unexpectedly low temperature region are probably produced by exothermic gas phase reactions [102]. All $Ge_{1-y}Sn_y$ epilayers presented in this chapter were grown using variable $SnCl_4/GeH_4$ ratio at pressure of 500 Torr. In this section, we tend to take an experimental approach to understand how it could be possible to epitaxially grow $Ge_{1-y}Sn_y$ at very low growth temperature.

To enable $Ge_{1-y}Sn_y$ epitaxy at very low growth temperatures, it is necessary to optimise CVD growth conditions precisely. As shown in Chapter 4, growth under high pressure leads to an increase in the Sn concentration of $Ge_{1-y}Sn_y$ epilayers and also offers flexibility in selecting other CVD growth conditions. The growth pressure was therefore set at 500 Torr. The growth time at each temperature was chosen to grow fully strained $Ge_{1-y}Sn_y$ epilayers for better comparison. This is evident in Figure 6.1, in which thickness fringes around $Ge_{1-y}Sn_y$ peaks are observed for each of the grown $Ge_{1-y}Sn_y$ epilayers. The growth temperature was tuned from 280 ℃ down to 240 ℃ with 10 ℃ steps. Then, at each temperature, the $SnCl_4/GeH_4$ ratio was optimised accordingly to heteroepitaxy $Ge_{1-y}Sn_y$ with the highest possible Sn concentration at the given growth temperature, which is discussed in detail in the next section.

Sn concentration of each $Ge_{1-y}Sn_y$ epilayer was measured from RSMs and using the modified Vegard's law set out in Equation 3.9 on page 37. The thicknesses of these $Ge_{1-y}Sn_y$ epilayers were measured from thickness fringes that appeared around the $Ge_{1-y}Sn_y$ peak in HR-XRD ω-2θ coupled scans in Figure 6.1, as they are fully strained, and then confirmed more accurately using X-TEM. As seen in Figure 6.2, it is necessary to reduce temperature to maximise Sn concentration in $Ge_{1-y}Sn_y$ epilayers. For every 10 ℃ reduction in temperature, Sn concentration increases by ~1 at.% at low temperature range. Later we explain how to optimise these growth conditions to achieve high quality growth of $Ge_{1-y}Sn_y$ with very high Sn concentration at very low temperature as shown in Figure 6.2.

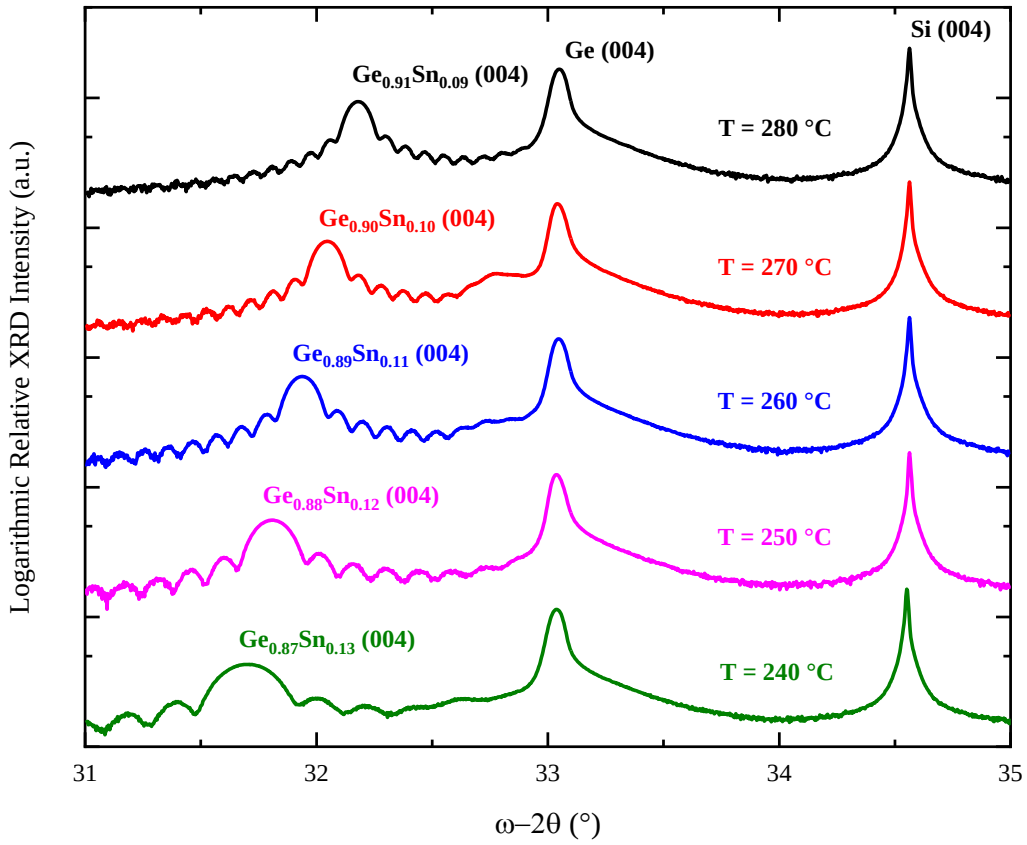

Figure 6.1 HR-XRD ω-2θ coupled scans for fully strained $Ge_{1-y}Sn_y$ grown on Si (001) via a relaxed Ge-VS at 500 Torr using tuned $SnCl_4/GeH_4$ ratio (different $SnCl_4/GeH_4$ ratio was used for different temperatures).

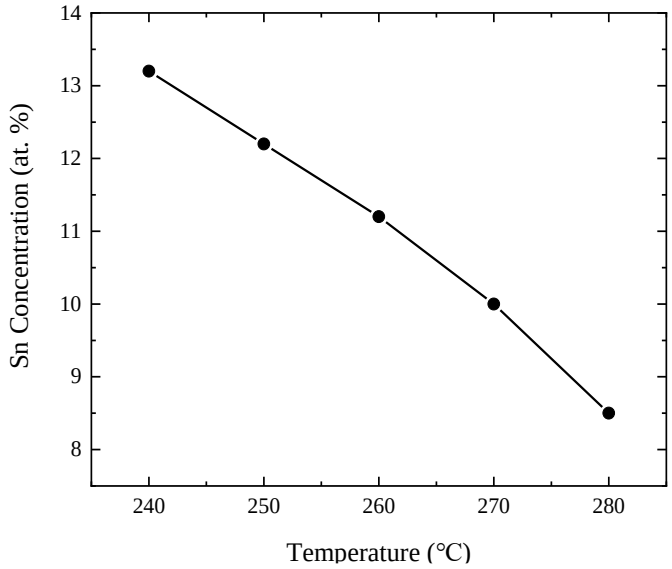

Figure 6.2 Effect of growth temperature on Sn concentration (at.%) of fully strained $Ge_{1-y}Sn_y$ epilayers grown at 500 Torr using tuned $SnCl_4/GeH_4$ ratio (different $SnCl_4/GeH_4$ ratio was used for different temperature) in which $Ge_{1-y}Sn_y$ with highest Sn concentration (at.%) at each temperature has been achieved.

All grown $Ge_{1-y}Sn_y$ epilayers are fully strained and high quality as can be confirmed from HR-XRD ω-2θ coupled scan and the lattice resolved X-TEM in Figure 6.1 and Figure 6.3. There is no shoulder on the left side of the Ge peak in HR-XRD ω-2θ coupled scan of each $Ge_{1-y}Sn_y$ epilayer, which show there are no Sn segregations and noticeable defected layers within the $Ge_{1-y}Sn_y$ epilayers.

In addition, X-TEM micrographs of these fully strained $Ge_{1-y}Sn_y$ were taken not only for thickness measurements, but also to investigate the quality of grown epilayers. An example of X-TEM image of $Ge_{0.89}Sn_{0.11}$\Ge-VS interface as well as lattice resolved X-TEM micrograph of $Ge_{0.89}Sn_{0.11}$ epilayer, are shown in Figure 6.3. This epilayer was grown at 260 ℃ and 500 Torr. As shown in Figure 6.3 (right), there is no defect or Sn segregation on the surface of the epilayer $Ge_{0.89}Sn_{0.11}$ that confirms the high quality of the epilayer.

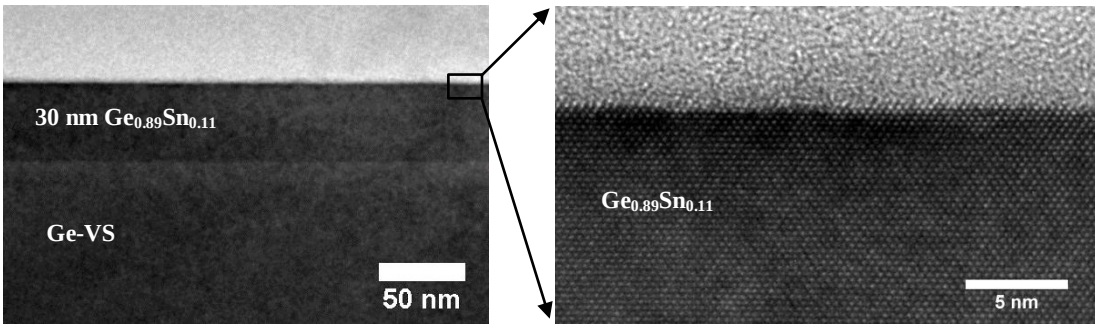

Figure 6.3 Left: X-TEM image of $Ge_{0.89}Sn_{0.11}$\Ge-VS interface. Right: Lattice resolved X-TEM micrograph of $Ge_{0.89}Sn_{0.11}$ showing its smooth surface. This epilayer was grown at 260 ℃ and 500 Torr. Its corresponding HR-XRD ω-2θ coupled scan shown in Figure 6.2.

6.3 Allowed $SnCl_4/GeH_4$ Ratio at Each Growth Temperature

To successfully achieve $Ge_{1-y}Sn_y$ epitaxy at very low temperatures, it is necessary to understand the impact of the $SnCl_4/GeH_4$ ratio on growth by growing enough number of epilayers. Since the epilayers have been grown in different times, it is essential to take into account any feature offset for CVD growth conditions. The most crucial CVD condition in this research is the growth temperature. The temperature measurements in the CVD system used, as with most industrial CVDs, can be changed after every system maintenance. This is because after each maintenance, the temperature sensor cannot be perfectly positioned as it was before, and this can significantly affect its temperature readings. In order to overcome this problem, some materials that are easy to use as reference are usually grown after each maintenance to calibrate the temperature offset.

As shown in Figure 6.4, the growth rate of $Ge_{1-y}Sny$ increases linearly due to the increase in the $SnCl_4/GeH_4$ ratio. The thicknesses of these $Ge_{1-y}Sn_y$ epilayers which are required to estimate their growth rates, were measured from thickness fringes that appeared around the $Ge_{1-y}Sn_y$ peak in HR-XRD ω-2θ coupled scans in Figure 6.1, as they are fully strained, and then confirmed more accurately using X-TEM. As already mentioned in chapter 4, the growth rate is largely driven by the production of Ge atoms and their availability on the surface of growing layers. Since the $SnCl_4/GeH_4$ ratio and growth rate have a positive linear correlation (Figure 6.4), we can expect that the production of Ge atoms increases with the increase in the $SnCl_4/GeH_4$ ratio. The explanation of chemistry is presented in later sections.

Furthermore, the growth stagnation times for all $Ge_{1-y}Sn_y$ epilayers grown at different temperatures were estimated to be less than 3 s. This estimate was achieved by aligning linear lines with data points (shown in Figure 6.4) at each growth temperature and determining their equations' intercepts.

Finally, it should be noted that the allowed region for the $SnCl_4/GeH_4$ ratio, in which epitaxial growth of $Ge_{1-y}Sn_y$ is possible, shrinks as the growth temperature decreases. For instance, at a temperature of 250 °C, no growth was possible when the $SnCl_4/GeH_4$ ratio was out of [~0.003, ~0.004], which means that $\sim 0.003 \leq SnCl_4/GeH_4 \leq \sim 0.004$ must be satisfied to achieve $Ge_{1-y}Sn_y$ growth at this temperature.

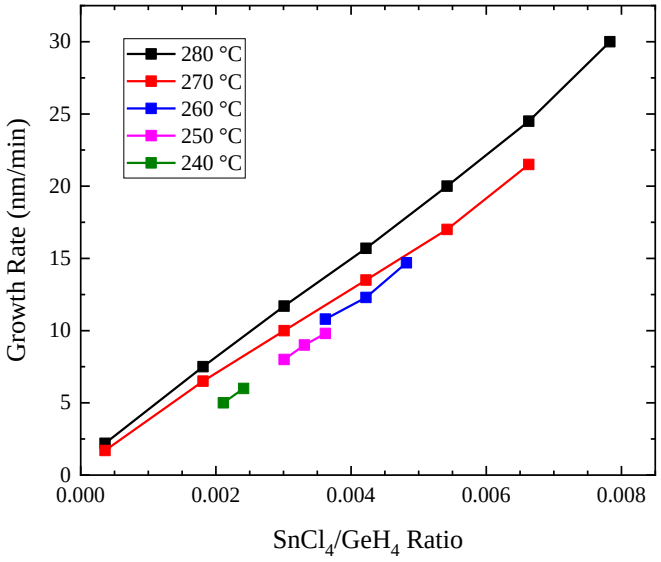

Figure 6.4 Effect of $SnCl_4/GeH_4$ ratio on growth rate (nm/min) of fully strained $Ge_{1-y}Sn_y$ epilayers grown at low growth temperatures. The allowed region for the $SnCl_4/GeH_4$ ratio, in which epitaxial growth of $Ge_{1-y}Sn_y$ is possible, shrinks as the growth temperature decreases.

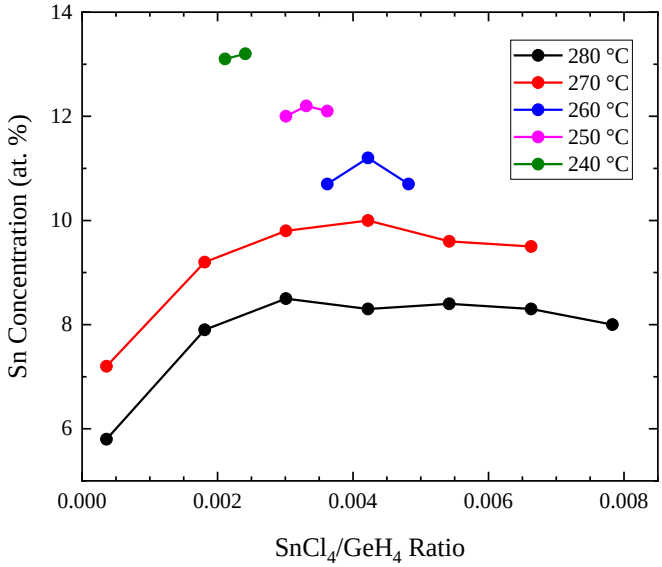

Figure 6.5 Effect of $SnCl_4/GeH_4$ ratio on Sn concentration (at.%) of fully strained $Ge_{1-y}Sn_y$ epilayers grown at low growth temperatures. The allowed region for the $SnCl_4/GeH_4$ ratio, in which epitaxial growth of $Ge_{1-y}Sn_y$ is possible, shrinks as the growth temperature decreases.

In low temperature range (≤ 260 °C), the Sn concentration is almost independent of $SnCl_4/GeH_4$. As seen in Figure 6.5, it is evident that the Sn concentration mainly depends on the growth temperature and not on $SnCl_4/GeH_4$ ratio. In view of this, it is important to modify the growth temperature in the low temperature range in order to control Sn concentration, while precise tuning of the $SnCl_4/GeH_4$ ratio is essential to achieve growth. It can be seen in Figure 6.4 and Figure 6.5 that as the growth temperature decreases, the growth rate slightly

decreases, but Sn concentration increases by a considerable amount of ~1 at.%. As seen in both Figure 6.4 and Figure 6.5, at a very low temperature (for example 240 °C), growth is only possible at a very narrow range of $SnCl_4/GeH_4$ ratio, which is probably the main reason why other research groups could not achieve any growth at this very low temperature.

Allowed $SnCl_4/GeH_4$ ratios at different growth temperature are shown in Figure 6.6. This is the summary of the allowed range for the $SnCl_4/GeH_4$ ratio at each growth temperature, in which epitaxial growth of $Ge_{1-y}Sn_y$ epilayers becomes possible. Considering experimentally collected data, we are able to estimate the allowed $SnCl_4/GeH_4$ ratio for temperatures between the growth temperatures used, as shown in Figure 6.6. It should be noted that more experiments should be considered to collect more data to find the allowed $SnCl_4/GeH_4$ ratio regions more accurately. Additional investigation is needed to investigate the growth of $Ge_{1-y}Sn_y$ at $SnCl_4/GeH_4$ ratio below 0.002, especially at growth temperatures of 270 °C and 280 °C. Finally, the lowest growth temperature in which epitaxial growth of $Ge_{1-y}Sn_y$ epilayer could be achieved was 240 °C. Following the exact pattern of shrinkage of the $SnCl_4/GeH_4$ ratio from 250 °C to 240 °C, and assuming that the same pattern applies from 240 °C to the minimum possible growth temperature, we estimated the lowest possible growth temperature as ~231 °C, which is very close to the Sn melting point of 231.1 °C (at atmospheric pressure). However, it should be noted that the melting point varies due to the pressure. Since the growth pressure used to grow these epilayers was 500 Torr, that is relatively close to atmospheric pressure, the melting point changes only slightly.

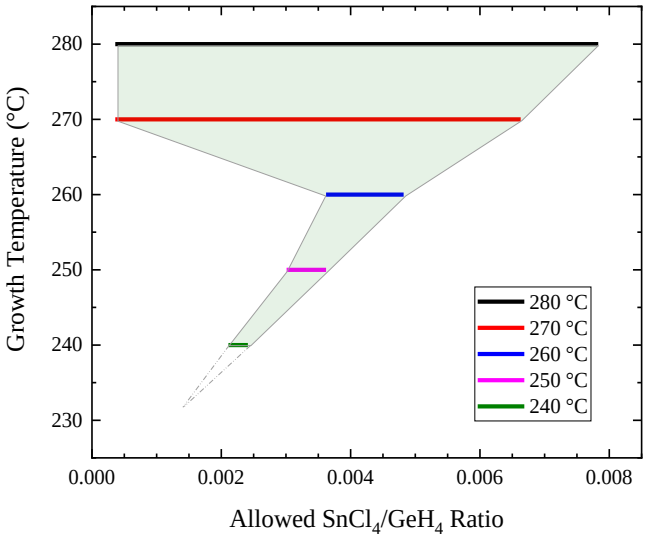

Figure 6.6 Summary of the allowed range for the $SnCl_4/GeH_4$ ratio at each growth temperature in which epitaxial growth of $Ge_{1-y}Sn_y$ epilayers becomes possible. The allowed region for the $SnCl_4/GeH_4$ ratio, in which epitaxial growth of $Ge_{1-y}Sn_y$ is possible, shrinks as the growth temperature decreases.

6.4 Effect of HCl on $Ge_{1-y}Sn_y$

To investigate the effect of HCl on $Ge_{1-y}Sn_y$, HCl was flowed at the same temperature as the growth temperature of $Ge_{1-y}Sn_y$ shortly after the end of $Ge_{1-y}Sn_y$ growth. As it can be seen in Figure 6.7, the shoulder, which appeared during the epitaxial growth of $Ge_{1-y}Sn_y$ on the left side of the Ge peak in HR-XRD ω-2θ coupled scan, was successfully etched by HCl. Such a shoulder is either polycrystalline structures or low quality $Ge_{1-y}Sn_y$ layers with very low Sn concentration, $y < 0.02$, which is similar to Sn solubility of Sn into Ge. As the thickness of $Ge_{1-y}Sn_y$ increases, this appeared shoulder can ultimately terminate epitaxial growth completely and cover the entire surface of the epilayer with low quality $Ge_{1-y}Sn_y$ layers and polycrystalline structures, resulting in a rough surface that is not suitable for further growth. This experiment shows how HCl plays an important role in the CVD growth of $Ge_{1-y}Sn_y$ epilayers by maintaining the condition of the surface of the epilayer suitable.

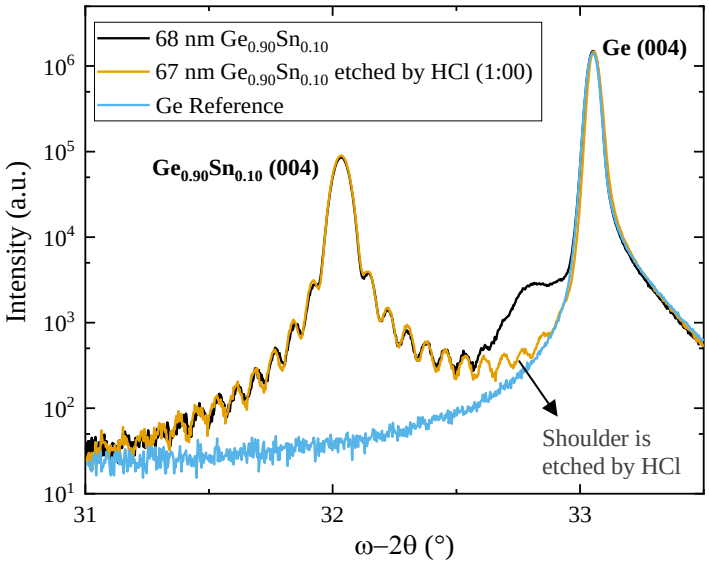

Figure 6.7 Effect of HCl on fully strained $Ge_{1-y}Sn_y$ epilayers after CVD growth. There are two HR-XRD ω-2θ coupled scans of two $Ge_{0.90}Sn_{0.10}$ epilayers that were grown under the same growth conditions, and then only one of them is exposed to HCl at the same temperature as the growth temperature for 1:00 min. HCl successfully etched and removed either very low Sn concentration ($y < 0.02$) $Ge_{1-y}Sn_y$ layers or polycrystalline structures, smoothing the surface of the epilayer. The Si peak is excluded from HR-XRD ω-2θ coupled scans for a better presentation. The HR-XRD ω-2θ coupled scan of a high quality relaxed Ge grown on Si (001) is shown as a reference.

As shown in Figure 6.8, HCl does not etch high quality fully strained $Ge_{1-y}Sn_y$ with high Sn concentration. In this experiment, the same $Ge_{0.90}Sn_{0.10}$ epilayers were etched by HCl, once for 1:00 min and once for 5:00 min. It is evident in Figure 6.8 that there is no sign of etching

due to HCl. It could be assumed that HCl can only etch $Ge_{1-y}Sn_y$ with Sn concentration up to a limit (for example, $y < 0.02$) or polycrystalline structures at a certain temperature. Further research is required to prove this experimentally. As the HCl is just one of the products from very complex possible reaction pathways, it is difficult to fully understand the mechanism of HCl. An important conclusion, however, is that HCl supports to keep the surface free from low quality $Ge_{1-y}Sn_y$ or polycrystalline structures during CVD growth. In other words, if not enough HCl is produced during epitaxial growth of the $Ge_{1-y}Sn_y$ epilayer, we can ultimately end up with a rough surface (which appears as a shoulder on the left side of the Ge peak, similar to the one shown in HR-XRD ω-2θ coupled scan in Figure 6.7), which can potentially entirely terminate growth.

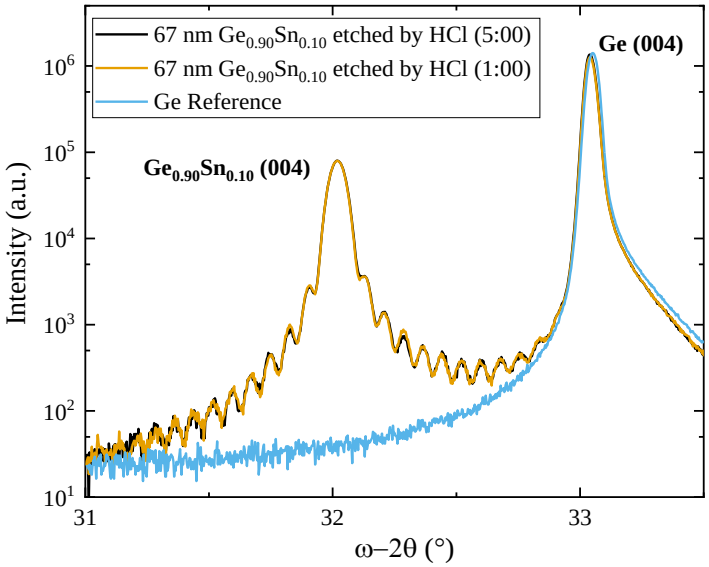

Figure 6.8 Effect of HCl on high quality fully strained $Ge_{0.90}Sn_{0.10}$. There are two HR-XRD ω-2θ coupled scans of two $Ge_{0.90}Sn_{0.10}$ epilayers with the same thickness and Sn concentration grown under the same growth conditions, both of which were exposed to HCl at the same temperature as the growth temperature but for different durations: 1:00 min and 5:00 min. As it can be seen, $Ge_{0.90}Sn_{0.10}$ was not etched by HCl at all. The Si peak is excluded from HR-XRD ω-2θ coupled scans for a better presentation. The HR-XRD ω-2θ coupled scan of a high quality relaxed Ge grown on Si (001) is shown as a reference.

6.5 Chemistry of the Heteroepitaxy of $Ge_{1-y}Sn_y$ Using GeH_4

Based on some reference thermochemical data, reactions occurring in the gas phase, which enable epitaxial growth of $Ge_{1-y}Sn_y$ epilayers, were predicted [102]. In view of this, possible pathways to produce Ge or Sn at low temperatures are as follows:

1) $SnCl_2^* + 2H^* \longrightarrow Sn^* + 2HCl$ $\quad \Delta H_r^{298} = -282$ kJ/mol

2) $GeCl_2^* + 2H^* \longrightarrow Ge^* + 2HCl$ $\quad \Delta H_r^{298} = -73.4$ kJ/mol

3) $GeH_2^* \longrightarrow Ge^* + H_2$ $\quad \Delta H_r^{298} = 126$ kJ/mol

4) $GeH_2^* + SnCl_2^* \longrightarrow GeSn^* + 2HCl$ $\quad \Delta H_r^{298} = -248$ kJ/mol

5) $HSnCl^* \longrightarrow Sn^* + HCl$ $\quad \Delta H_r^{298} = -27.7$ kJ/mol

6) $HGeCl^* \longrightarrow Ge^* + HCl$ $\quad \Delta H_r^{298} = 238$ kJ/mol

It should be noted that H^* is required in order for reactions 1 and 2 to occur. Additionally, the only reactions in which H^* could be produced are the dissociation adsorption of Ge, as shown below:

7) $GeH_4(g) + 2\,{-}^* \longrightarrow GeH_3^* + H^*$

8) $GeH_4(g) + 3\,{-}^* \longrightarrow GeH_2^* + 2H^*$

The radicals produced from these two reactions are highly reactive and require immediate contact from $SnCl2^*$ reactant in reaction 1 and 4, otherwise they react together and the reverse reaction of 7 and 8 would occur. Another pathway that consumes some radicals produced in reaction 8 is reaction 3, which is not favourable compared to 1 and 4 at lower temperatures, given the positive enthalpy of the reaction. Therefore, to have $SnCl_2$ reactants readily available for these radicals, low ratios of $SnCl_4/GeH_4$ are not favourable, as we need a minimum concentration of Sn to successfully achieve epitaxial growth of $Ge_{1-y}Sn_y$. This alone justifies the observation that the reduction of temperature from 270 °C to 260 °C (or lower temperatures), lower $SnCl_4/GeH_4$ ratios do not allow $Ge_{1-y}Sn_y$ growth.

As has already been observed in other studies, all possible pathways that create $SnCl_2$ have a negative enthalpy of reaction, which means a constant ratio that reduces temperature could increase the production of $SnCl_2$ and Sn incorporation into growing $Ge_{1-y}Sn_y$ layers [102]. Thus, at such a low temperature of 240 °C, the critical concentration of $SnCl_2$ for other

reactions (1 and 4) can be fulfilled at very low ratios of $SnCl_4/GeH_4$. Since high exothermic reactions are more favourable at lower temperatures: ($\Delta H < 0 \longrightarrow \Delta S < 0$: $\Delta G = \Delta H - T\Delta S$), this leads to a higher concentration of $SnCl_2$ at lower temperatures. Therefore, the minimum ratio of $SnCl_4/GeH_4$, at which the minimum amount of $SnCl_2$ is satisfied, decreases with the decrease in temperature.

Based on enthalpy data and thermochemical considerations at higher temperatures, reaction 5 can be a more favourable reaction path than 1 or 4 to produce Sn final products. Suppose that reactions 3 and 2 are occurring fast enough at higher temperatures to consume radicals faster than reactions 1 and 4, there is no need for a minimum concentration of $SnCl_2$ as previously discussed. Therefore, assuming that there is a critical temperature below which the reaction pathways switch from 5 and 3 to 1 and 4, the sensitivity of growth to ratios at temperatures below 270 °C (assuming 270 °C is the critical temperature) can be explained.

Overall, a balance for $SnCl_2$ (which is directly related to the ratio of $SnCl_4/GeH_4$) is required at lower temperatures at which reactions 5 and 3 are not dominant, because, given the reaction enthalpies, the most favourable reactions to create Sn^*, Ge^* and $Ge_{1-y}Sn_y$ epilayer are reactions 1, 2 and 4, respectively. If $SnCl_2$ is too high (because of a very high $SnCl_4/GeH_4$ ratio), especially at lower temperatures, reaction 1 prevails over reaction 2 and it therefore produced too much Sn, leading to Sn segregation on the growing layer. On the other hand, if $SnCl_2$ is too low, the radicals of GeH_2^* and H^* can be consumed quickly by reacting together and terminating the growth process. This explains why there is only a small window for the $SnCl_4/GeH_4$ ratio, in which competitive reactions can see a relatively equal speed and $Ge_{1-y}Sn_y$ epilayer can grow as a result.

6.6 Conclusion

We have shown the possibility of heteroepitaxial growth of $Ge_{1-y}Sn_y$ at a very low temperature of 240 °C, which was previously assumed to be not possible. This is because temperature is not the only factor that breaks GeH_4 molecules, but also the amount of $SnCl_4$ to GeH_4 should be taken into account. As growth temperature decreases, the allowed range of the $SnCl_4/GeH_4$ ratio, in which growth is possible, shrinks significantly. If the $SnCl_4/GeH_4$ ratio is too large, growth is stopped due to segregation due to the high amount of Sn atoms. On the other hand, if the $SnCl_4/GeH_4$ ratio is too low, growth is also stopped because there is not enough amount of $SnCl_4$ to break an effective number of GeH_4 molecules to keep up the essential growth rate. Considering these, it is necessary to have the right $SnCl_4/GeH_4$ ratio as well as a high amount of GeH_4. While sacrificing growth rate at this temperature, it is easier to suppress precipitation and segregation in $Ge_{1-y}Sn_y$ epilayers.

The lowest possible growth temperature at which epitaxial growth of $Ge_{1-y}Sn_y$ is allowed was estimated at ~231 °C, which is very close to the melting point of Sn. However, more experiments are required to experimentally determine such a minimum growth temperature. In addition, further research is needed to investigate the growth of $Ge_{1-y}Sn_y$ at $SnCl_4/GeH_4$ ratio below 0.002, especially at growth temperatures of 270 °C and 280 °C. It should also be noted that further investigation is needed to collect more experimental data to find the permitted $SnCl_4/GeH_4$ ratio regions more accurately.

Chapter 7

Strain Relaxation of $Ge_{1-y}Sn_y$ Epilayers

7.1 Introduction

It has been shown that the bandgap energy decreases as a result of the tensile biaxial strain in $Ge_{1-y}Sn_y$, as the effect of the strain is significantly higher in direct gap than in indirect [61,62]. The achievement of $Ge_{1-y}Sn_y$ with a direct bandgap strongly depends on its strain relaxation [10], as shown in Figure 2.8 on page 13. The effect of the biaxial strain on the bandgap structure of $Ge_{1-y}Sn_y$ was theoretically investigated. It has been suggested that tensile and compressive strain reduce and increase the required Sn concentration to achieve indirect-to-direct bandgap transition [50]. Tensile strained $Ge_{1-y}Sn_y$ could be grown on partially or fully relaxed $Ge_{1-y}Sn_y$ [63-66], while compressive strained $Ge_{1-y}Sn_y$ could be grown on Si (001) via Ge-VS [67,68]. Recent predictions show that $Ge_{1-y}Sn_y$ indirect-to-direct bandgap transition may be achieved with Sn concentration of 6–11 at.% [50,69-73]. Therefore, it is essential to fully understand the strain relaxation of $Ge_{1-y}Sn_y$ epilayers, which is studied in this chapter.

7.2 Strain Relaxation of $Ge_{1-y}Sn_y$ Epilayers & its h_c

Fully relaxed $Ge_{1-y}Sn_y$ lattice depends on its Sn concentration. With increasing Sn concentration in fully strained $Ge_{1-y}Sn_y$, its out-of-plane lattice increases. However, a fully relaxed $Ge_{1-y}Sn_y$ epilayer cannot be grown immediately on Ge-VS due to the large lattice mismatch between them. When epitaxial growth of $Ge_{1-y}Sn_y$ on the VS begins, grown layers are fully compressively strained, which means they have the same inner lattice parameter as the Ge-VS, but a larger outer lattice parameter, as shown in Figure 2.6 in page 11. Fully strained $Ge_{1-y}Sn_y$ can be grown up to a certain thickness, h_c, which mainly depends on Sn concentration (y). Above h_c, $Ge_{1-y}Sn_y$ epilayer gradually begins to relax the tensile strain by forming misfit dislocations, as shown in Figure 2.6 in page 11. In this section h_c and effects of strain relaxation in $Ge_{1-y}Sn_y$ layers are investigated.

It was explained that very low growth temperatures are used in modern epitaxy methods, where lattice diffusion is minimised and h_c is increased [75]. In this work, the h_c of $Ge_{1-y}Sn_y$, where strain relaxation begins in the epilayer, is investigated. The $Ge_{1-y}Sn_y$ epilayers were grown on Si (001) via a relaxed Ge-VS at 260 °C and 500 Torr with a fixed $SnCl_4/GeH_4$ ratio of 3.3×10^{-3}. The Sn concentration of 11.6 at.% was estimated for the fully strained $Ge_{1-y}Sn_y$ epilayers. The Sn concentration for each of these samples was measured from RSMs and using the modified Vegard's law given in Equation 3.9 on page 37. Five $Ge_{1-y}Sn_y$ epilayers were grown under the same CVD growth conditions, but with different growth times were grown. As shown in Figure 7.1, the thickness fringes around $Ge_{1-y}Sn_y$ peak in HR-XRD ω-2θ coupled scan for the $Ge_{1-y}Sn_y$ epilayer grown for 10:00 min began to disappear completely. This is an indication of the beginning of strain relaxation in the $Ge_{1-y}Sn_y$ epilayer. The thickness of the $Ge_{1-y}Sn_y$ epilayer grown for 10:00 was measured using X-TEM as 95 nm. This shows the h_c of ~0.10 µm for $Ge_{1-y}Sn_y$ epilayers grown under the given CVD growth conditions.

A thicker $Ge_{1-y}Sn_y$ epilayer was also grown for 15:00 min under the same growth conditions, indicating a relaxation of strain in the epilayer. As seen in Figure 7.1, there is an additional peak next to each of the HR-XRD ω-2θ coupled scans of $Ge_{1-y}Sn_y$ epilayers (with apparent strain relaxation), which were grown for 10:00 min and 15:00 min. It is important to note, as already explained in previous chapters, that such peaks or shoulders on the left side of the Ge peak in HR-XRD ω-2θ coupled scans are usually due to polycrystalline $Ge_{1-y}Sn_y$ or $Ge_{1-y}Sn_y$ with very low Sn concentration (around Sn solubility in Ge). Nevertheless, as can be seen in

Figure 7.1, such peaks or shoulders do not exist in HR-XRD ω-2θ coupled scans of fully strained $Ge_{1-y}Sn_y$ epilayers grown under the same CVD conditions. Because of this, apparent peaks or shoulders are presumably there because of defects in the $Ge_{1-y}Sn_y$ layers due to strain relaxation. Further study can be done to investigate whether the shoulder can be removed with HCl in a similar way that was previously achieved as shown in Figure 6.7 on page 81.

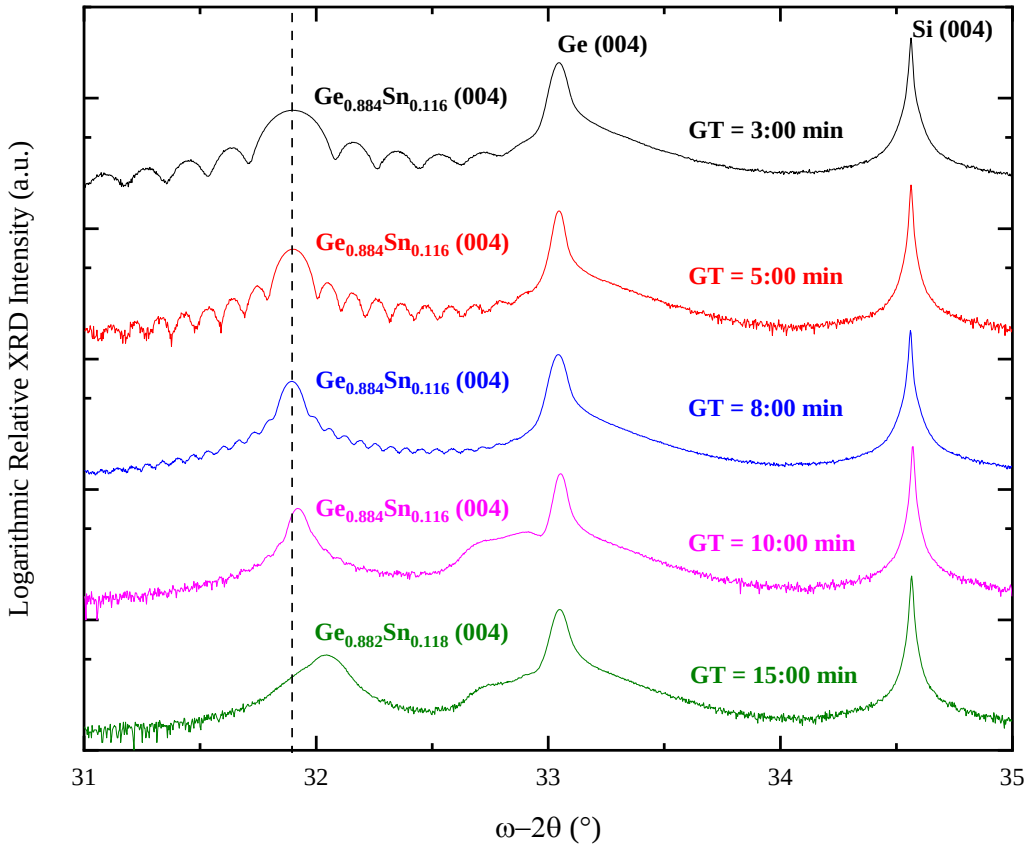

Figure 7.1 HR-XRD ω-2θ coupled scans for $Ge_{1-y}Sn_y$ grown on Si (001) via a relaxed Ge-VS at 260 °C and 500 Torr using a fixed $SnCl_4/GeH_4$ ratio of 3.3×10^{-3}. Sn concentration for each of these samples was measured from RSMs and using the modified Vegard's law given in Equation 3.9 on page 37. The thickness of each $Ge_{1-y}Sn_y$ epilayer was measured using thickness fringes appeared around the $Ge_{1-y}Sn_y$ peak and confirmed using the X-TEM.

7.3 Effects of Strain Relaxation on $Ge_{1-y}Sn_y$ Epilayers

7.3.1 Effect of Strain Relaxation on Sn Concentration

When comparing HR-XRD ω-2θ coupled scans of $Ge_{1-y}Sn_y$ epilayers shown in Figure 7.1, it becomes clear that as more strain relaxation is achieved, the $Ge_{1-y}Sn_y$ peak in the HR-XRD ω-2θ coupled scan begins to shift to the right. This is solely due to strain relaxation within the layers of $Ge_{1-y}Sn_y$ and not to a reduction in Sn concentration. This is demonstrated when measuring the Sn concentration using XRD RSMs.

As shown in Figure 7.2 (top), the $Ge_{1-y}Sn_y$ grown for 8:00 min is fully strained, and its peak appeared exactly under relaxed Ge-VS in the asymmetric RSM. However, for the $Ge_{1-y}Sn_y$ grown for 10:00 min, as shown in Figure 7.2 (middle), the $Ge_{1-y}Sn_y$ peak in the asymmetric RSM is slightly shifted to the left, indicating the appearance of strain relaxation in the $Ge_{1-y}Sn_y$ layers. In addition, for the $Ge_{1-y}Sn_y$ grown for 15:00 min, as shown in Figure 7.2 (bottom), the $Ge_{1-y}Sn_y$ peak in the asymmetric RSM is significantly shifted to the left, indicating a greater degree of strain relaxation in the $Ge_{1-y}Sn_y$ layers compared to the previous epilayer, which was grown for only 10:00 min. As shown in Figure 7.2 (bottom), the Sn concentration of $Ge_{1-y}Sn_y$ epilayer grown under the same CVD growth conditions has indeed increased due to strain relaxation. In the next section, the reason is tended to be explained. The $Ge_{1-y}Sn_y$ epilayer grown for 15:00 min has 0.2 at.% more Sn concentration than the fully strained $Ge_{1-y}Sn_y$ epilayer grown for 8:00 min. For the $Ge_{1-y}Sn_y$ epilayer, which was grown for 10:00 min, no change in Sn concentration was observed. The reason for this is that the epilayer has just begun to relax at the h_c of ~0.10 µm.

To confirm the effect of strain relaxation on Sn concentration, a thicker $Ge_{1-y}Sn_y$ epilayer was grown for 20:00 min under the same growth conditions. Symmetric and asymmetric RSMs of the heterostructure are shown in Figure 7.3. At first glance, two $Ge_{1-y}Sn_y$ peaks in the asymmetric RSM can be noticed. Before discussing double $Ge_{1-y}Sn_y$ peaks, it is important to note that both of $Ge_{1-y}Sn_y$ peaks are more relaxed (shifted more to the left in asymmetric RSM) than the $Ge_{1-y}Sn_y$ peak in asymmetric RSM of thinner $Ge_{1-y}Sn_y$ epilayers. In addition, both $Ge_{1-y}Sn_y$ peaks indicate higher Sn concentrations than thinner $Ge_{1-y}Sn_y$, as shown in Figure 7.2, which confirms an increase in Sn concentration due to strain relaxation.

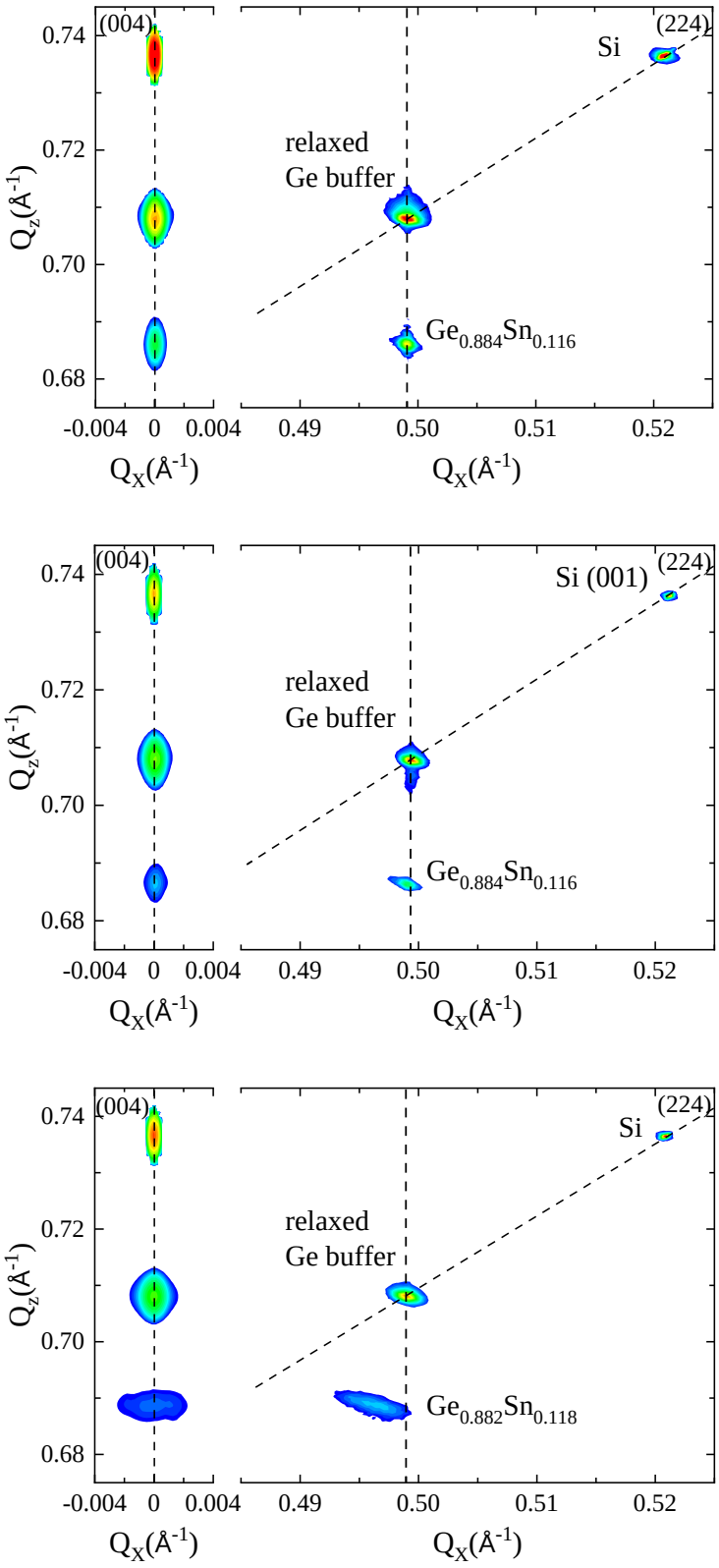

Figure 7.2 Symmetric and asymmetric RSMs for $Ge_{1-y}Sn_y$ grown with different growth times on Si (001) via Ge-VS at 260 °C and 500 Torr using a fixed $SnCl_4/GeH_4$ ratio of 3.3×10^{-3}. Their HR-XRD ω-2θ coupled scans are shown in Figure 7.1. Top: 79 nm thick $Ge_{0.884}Sn_{0.116}$ grown for 8:00 min. Middle: 95 nm thick $Ge_{0.884}Sn_{0.116}$ grown for 10:00 min. Bottom: 128 nm thick $Ge_{0.882}Sn_{0.118}$ grown for 15:00 min.

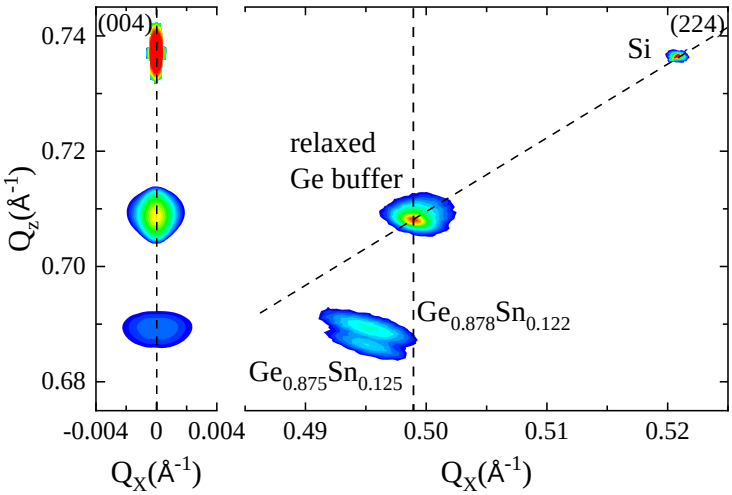

Figure 7.3 Symmetric and asymmetric RSMs for 150 nm thick $Ge_{0.878}Sn_{0.122}$ grown with growth time of 20:00 min on Si (001) via relaxed Ge-VS at 260 °C and 500 Torr using a fixed $SnCl_4/GeH_4$ ratio of 3.3×10^{-3}.

It is important to discuss the reasons for the appearance of two $Ge_{1-y}Sn_y$ peaks (as can be seen in Figure 7.3) in asymmetric RSM of $Ge_{1-y}Sn_y$ epilayer grown for 20:00 min. This behaviour is observed in later chapters, in which very thick $Ge_{1-y}Sn_y$ epilayers are grown. The justification for this behaviour is as follows: the second peak, which indicates that $Ge_{1-y}Sn_y$ layers with a slightly higher Sn concentration can be grown when a certain strain relaxation is achieved. The Sn concentration increases gradually and steadily as the layers relax (as the thickness of the epilayer increases) until a certain point, which is discussed in the next section. After this certain point, there is a sudden transition to Sn concentration, because the top layers (which now act as an intermediate substrate) allow $Ge_{1-y}Sn_y$ to grow with such a higher Sn concentration. This effect itself can be due to two reasons, which will be also discussed in the next section.

A summary of the effect of strain relaxation on the incorporation of Sn into $Ge_{1-y}Sn_y$ epilayers is shown in Figure 7.4. For the $Ge_{1-y}Sn_y$ epilayer with growth time of 20:00, only one peak is included (the one with lower Sn concentration). It should be noted that this summary is only valid for $Ge_{1-y}Sn_y$ epilayers grown under the same CVD conditions using the same precursors and respective partial pressures. This is because each of these CVD conditions can influence lattice diffusion and thus h_c. For example, as the growth temperature decreases, lattice diffusion is minimised which increases the h_c [166]. Another example is the Sn concentration itself: as the Sn concentration in the $Ge_{1-y}Sn_y$ epilayer increases, the h_c decreases, so the epilayer strain relaxation is achieved more quickly.

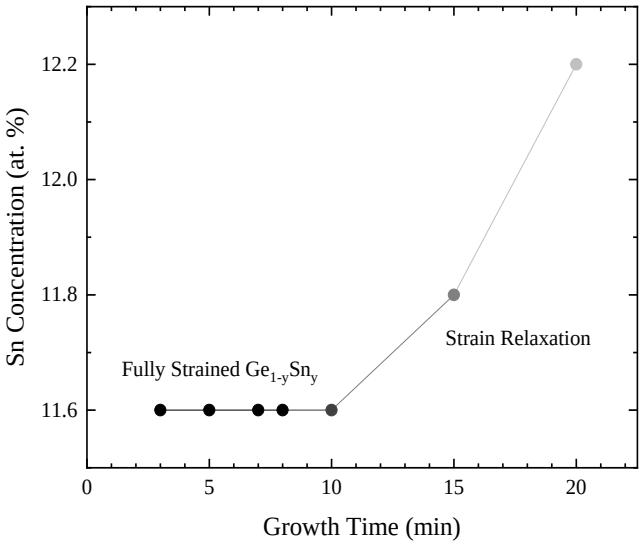

Figure 7.4 Effect of growth time and strain relaxation on the Sn concentration in $Ge_{1-y}Sn_y$ epilayers grown at 500 Torr and 260 ℃ using 3.3×10^{-3} $SnCl_4/GeH_4$ ratio.

7.3.2 Effect of Strain Relaxation on Growth Rate

In this section, the effect of strain relaxation on the growth rate of $Ge_{1-y}Sn_y$ epilayers, which were grown at 260 ℃ and 500 Torr with 3.3×10^{-3} $SnCl_4/GeH_4$, is investigated. As shown in Figure 7.5, the growth rate of $Ge_{1-y}Sn_y$ epilayers decreases with increasing growth time. The growth rate shown in Figure 7.5 is the growth rate for the entire $Ge_{1-y}Sn_y$ epilayers and it is important to note that these are the growth rates for the entire growth time. To understand the effect of strain relaxation on growth rate, it is therefore necessary to investigate the relationship between growth rate and thickness of $Ge_{1-y}Sn_y$ epilayers.

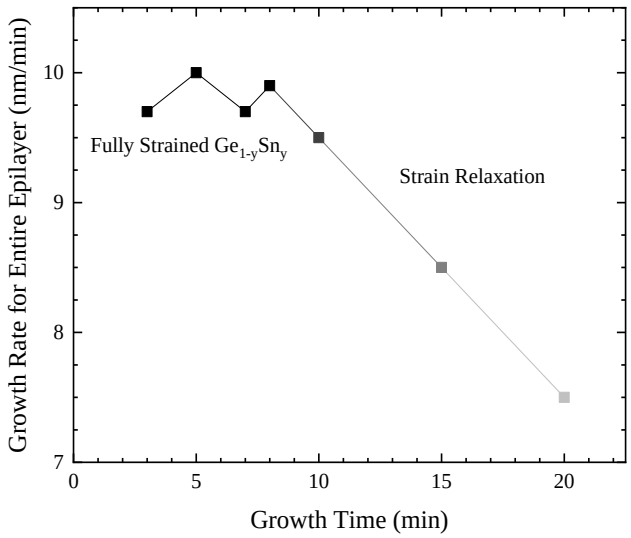

Figure 7.5 Effect of growth time and strain relaxation on the growth rate of $Ge_{1-y}Sn_y$ epilayers grown at 500 Torr and 260 ℃ using 3.3×10^{-3} $SnCl_4/GeH_4$ ratio.

As shown in Figure 7.6 (top), the average growth rate for fully strain $Ge_{1-y}Sn_y$ grown up to 10:00 min under the given CVD conditions was 9.8 nm/min. In addition, for partially relaxed $Ge_{1-y}Sn_y$ epilayers, which were grown for 15:00 min and 20:00 min, we assumed that the growth rate for the initial 10:00 min was exactly the same as the growth rate for those fully strained $Ge_{1-y}Sn_y$ epilayers. In view of this assumption, the average growth rate from 10:00 min to 15:00 min was measured at 6.1 nm/min and the average growth rate from 15:00 min to 20:00 min was measured at 4.4 nm/min. These growth rates are simply calculated by growing $Ge_{1-y}Sn_y$ with different growth times.

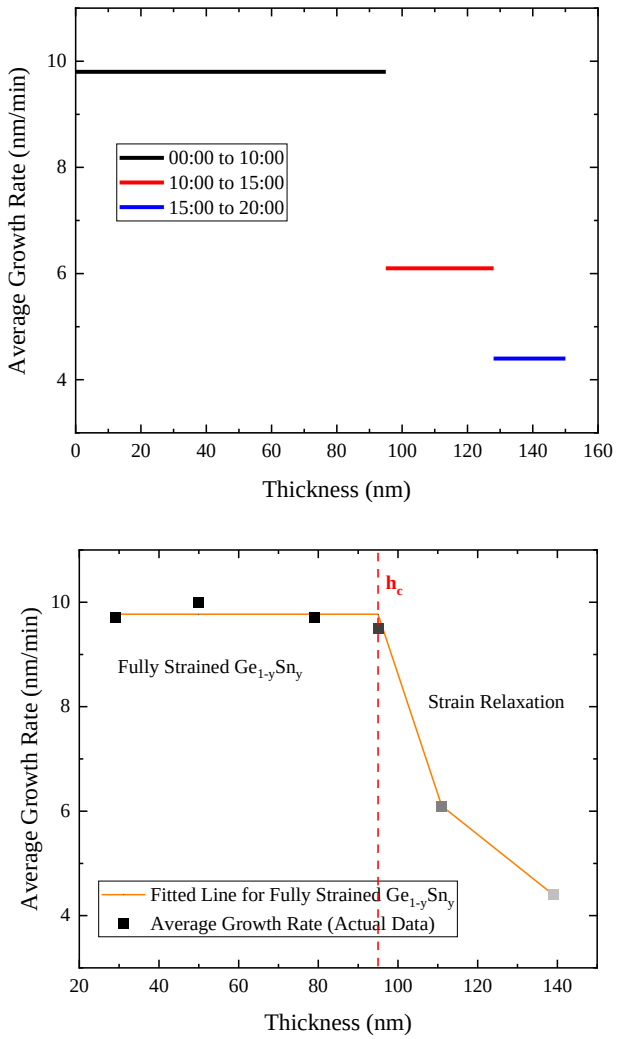

Figure 7.6 Top: Average growth rate (nm/min) at the given thickness (nm) of the $Ge_{1-y}Sn_y$ epilayer and its relevant growth time (min). As the thickness of the $Ge_{1-y}Sn_y$ epilayer increases, the growth rate decreases. Bottom: Average growth rate (nm/min) actual data points collected experimentally.

Considering the average growth rates of epilayers depending on their thickness, which are shown in Figure 7.6 (top), it could be possible to understand the effect of strain relaxation on

growth rates. As shown in Figure 7.6 (bottom), a straight line (orange colour) is fitted to the data, which represents the average growth rate at the given thickness of the $Ge_{1-y}Sn_y$ epilayer. It can be assumed that the growth rate remains constant for thicknesses below the h_c, in which all $Ge_{1-y}Sn_y$ epilayers are fully strained. Therefore, a straight horizontal line was fitted to those epilayers with thickness of up to h_c. The epilayers, grown with thickness of above h_c, are partially relaxed, and their degree of relaxation is discussed in the next section. It is also evident that the rate of suppression in the average growth rate is at its highest level just after the $Ge_{1-y}Sn_y$ epilayer passes the h_c, and gradually the rate of reduction in the average growth rate decreases as the thickness of the epilayer increases.

7.3.3 Effect of Strain Relaxation on Quality of $Ge_{1-y}Sn_y$ Epilayers

If $Ge_{1-y}Sn_y$ epilayer thickness is greater than the h_c, at the two ends of the misfit dislocations can form [55], as shown in Figure 2.6 on page 11. These dislocations could create a loop so that the two ends can join or thread onto the surface, which could potentially restrict relaxed of $Ge_{1-y}Sn_y$ applications [56,57]. However, in this section only the effect of strain relaxation on surface morphology is investigated. Surface roughness in terms of RMS for all $Ge_{1-y}Sn_y$ epilayers grown in this chapter is shown in Figure 7.7. It is obvious that the surface roughness remained low for all fully strained $Ge_{1-y}Sn_y$ epilayers, and as soon as a h_c of ~0.1 µm was achieved (at growth time of ~10:00 min), the surface roughness began to increase. This is probably due to Sn precipitation, which is a consequence of strain relaxation [6], and also to Sn segregation on the surface of $Ge_{1-y}Sn_y$ epilayers.

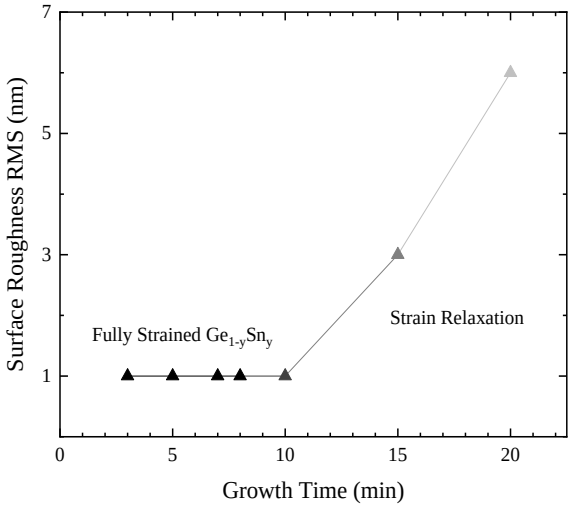

Figure 7.7 Surface roughness RMS of $Ge_{1-y}Sn_y$ epilayers grown on Si (001) via a relaxed Ge-VS at 260 °C and 500 Torr using 3.3×10^{-3} $SnCl_4/GeH_4$ ratio. Surface roughness increased with the increase in growth time, especially after the h_c of ~0.1 um, which was achieved at the growth time of 10:00 min.

7.4 Explanation of Effect of Thickness & Strain Relaxation on $Ge_{1-y}Sn_y$ Epilayers

In this section, the effects of strain relaxation on Sn concentration and growth rate of $Ge_{1-y}Sn_y$ epilayers are explored. The in-plane and out-of-plane strain of $Ge_{1-y}Sn_y$ epilayers grown were estimated using the following equations:

$$Strain_{in-plane} = \frac{a_{\parallel}^{GeSn} - a_0^{GeSn}}{a_0^{GeSn}} \quad (7.1)$$

$$Strain_{out-of-plane} = \frac{a_{\perp}^{GeSn} - a_0^{GeSn}}{a_0^{GeSn}} \quad (7.2)$$

Where $a_{\parallel}$ and $a_{\perp}$ are in-plane and out-of-plane of the lattice respectively as shown in Figure 7.8. Also a_0^{GeSn} refers to the relaxed lattice constant for $Ge_{1-y}Sn_y$ at a given Sn concentration, and $GeSn$ refers to the actual $Ge_{1-y}Sn_y$ epilayer grown and its HR-XRD ω-2θ coupled scan and RSMs were collected.

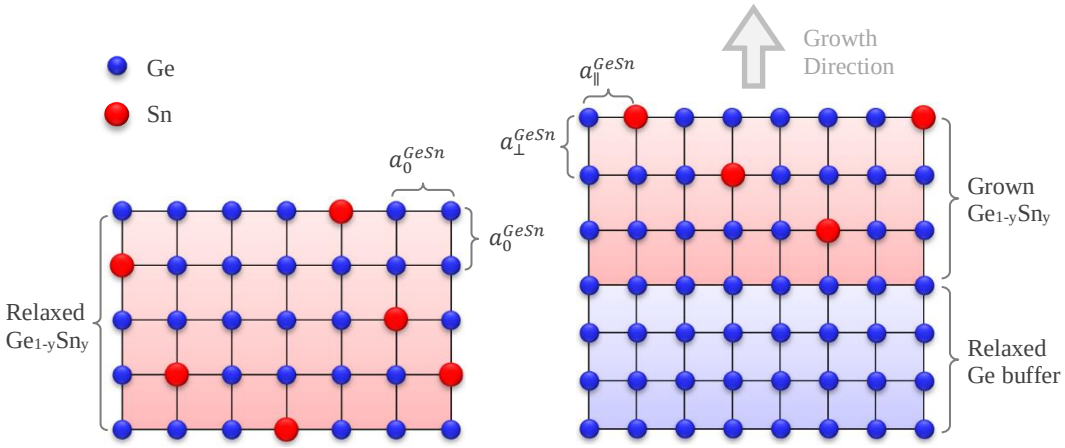

Figure 7.8 Left: two dimensional schematic of diamond cubic structure of fully relaxed $Ge_{1-y}Sn_y$ lattice. Right: two-dimensional schematic of diamond cubic structure of $Ge_{1-y}Sn_y$ lattice, which can be fully strained or partially/fully relaxed, grown on a relaxed Ge buffer. Exaggerated differences for both lattice constants and size of atoms are considered for a better representation.

By using Equations 7.1 and 7.2, in-plane and out-of-plane strain of grown $Ge_{1-y}Sn_y$ epilayers in this chapter were calculated and given in Table 3. It is evident that the thickness of the $Ge_{1-y}Sn_y$ epilayer does not affect in-plane or out-of-plane strain if the thickness is less than the h_c (~0.10 µm). However, when the thickness of the $Ge_{1-y}Sn_y$ epilayer exceeds the h_c, the strain relaxation begins and both in-plane and out-of-plane of the epilayer converge towards relaxed

lattice constant, a_0^{GeSn}. It should also be noted that grown $Ge_{1-y}Sn_y$ epilayers are compressively strained, as shown in Figure 2.8 on page 13.

Growth Time (min)	Thickness (nm)	In-plane Strain	Out-of-plane Strain	Average Sn Concentration (at. %)	Average Growth Rate (nm/min)
3:00	29	-15.4×10^{-3}	12.1×10^{-3}	11.6	9.7
5:00	50	-15.6×10^{-3}	12.2×10^{-3}	11.6	10.0
8:00	79	-15.8×10^{-3}	12.4×10^{-3}	11.6	9.9
10:00	95	-15.6×10^{-3}	12.3×10^{-3}	11.6	9.5
15:00	128	-11.1×10^{-3}	8.7×10^{-3}	11.8	8.5
20:00	150	-9.8×10^{-3}	7.7×10^{-3}	Two peaks: 12.2 and 12.5	7.5
		-9.3×10^{-3}	7.3×10^{-3}		

Table 3 Summary of effects of strain relaxation on Sn concentration and growth rate of $Ge_{1-y}Sn_y$ epilayers grown at 260 °C and 500 Torr on Si (001) via a relaxed Ge-VS.

Considering the measured in-plane and out-of-plan strain, it is possible to investigate the effect of strain relaxation on both growth rate and Sn concentration of $Ge_{1-y}Sn_y$ epilayers. As shown in Table 3, the average growth rate decreases as more strain relaxation is achieved. These average growth rates are the growth rate for the entire $Ge_{1-y}Sn_y$ epilayers, not at a given in-plane/out-of-plane strain (or simply at a given thickness). In order to have a true growth rate at the given thickness, the fitted line to the actual data shown in Figure 7.6 (bottom) can be used. In this way, the growth rate at a thickness of 128 nm was estimated at ~5 nm/min and at a thickness of 150 nm was estimated at ~4 nm/min. Based on these estimates, the effect of strain relaxation on growth rate at given thicknesses can be explored. As shown in Figure 7.9, the growth rate at the given thickness of the $Ge_{1-y}Sn_y$ epilayer is (almost) linearly dependent on the in-plane and out-of-plane strain. Since only two data points are available for partially relaxed $Ge_{1-y}Sn_y$, more studies are proposed to investigate the effect of strain relaxation on the growth rate of the $Ge_{1-y}Sn_y$ epilayer at a given thickness.

As explained previously, the growth rate of $Ge_{1-y}Sn_y$ mainly depends on the Ge incorporation in the growing layers. Since all growth conditions remained the same over the growth of all $Ge_{1-y}Sn_y$ epilayers in this chapter, the production of Ge atoms remained constant. Therefore,

the suppression of the Ge incorporation in growing layers cannot be due to the lack of Ge adatoms produced in the chamber. It seems that the strain relaxation directly influences the incorporation of Ge. As $Ge_{1-y}Sn_y$ relaxes more, a lower percentage of available Ge atoms on layers can be incorporated into the growing layers, resulting in a reduction in the growth rate.

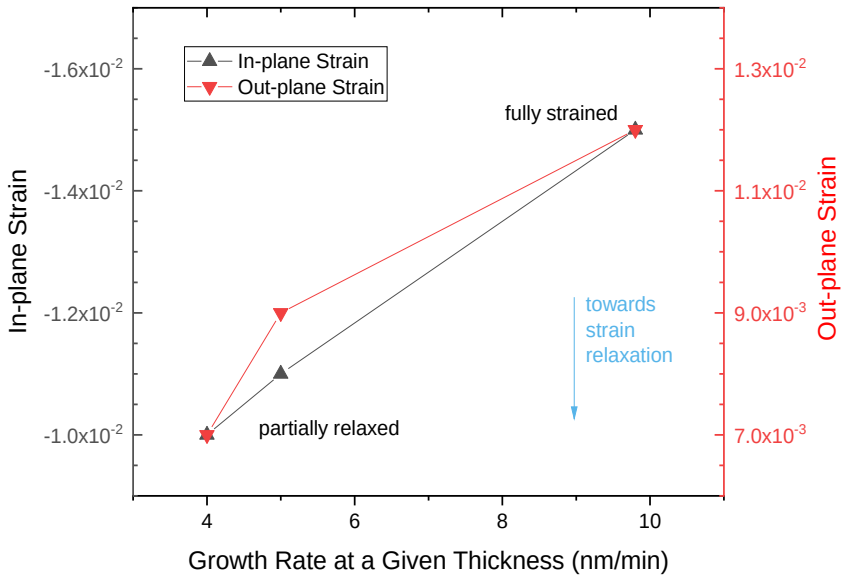

Figure 7.9 The effect of strain relaxation, which is due to the thickness of $Ge_{1-y}Sn_y$ epilayer, on the growth rate of the epilayer. The growth rate at given strain relaxation state were estimated using the fitted line to actual data points given in Figure 7.6. In-plane and out-of-plane strain were calculated by Equations 7.1 and 7.2.

Finally, the effect of strain relaxation on average Sn concentration can be examined. It should be noted that here we only discuss the average Sn concentration across the entire $Ge_{1-y}Sn_y$ epilayer, and not the Sn concentration at a given thickness of $Ge_{1-y}Sn_y$ epilayer. As shown in Table 3, the average Sn concentration increases as a result of strain relaxation. This can be explained simply by taking into account the effect of the growth rate on the average Sn concentration of $Ge_{1-y}Sn_y$ epilayers. As shown in Figure 4.12 on page 56, the average Sn concentration increases as the growth rate decreases. Similar behaviour was also observed for $Ge_{1-y}Sn_y$ epilayers grown at lower growth temperatures, as shown in Figure 6.4 and Figure 6.5 on page 79. Like Ge production, as CVD growth conditions remained the same, the Sn production remained the same during the growth of $Ge_{1-y}Sn_y$ epilayer. Therefore, as the growth rate decreases, more of produced Sn atoms have the chance to incorporate into $Ge_{1-y}Sn_y$ growing layers, leading to an increase in Sn concentration.

7.5 Conclusion

The effect of strain relaxation in compressive strained $Ge_{1-y}Sn_y$ on growth rate and Sn concentration of $Ge_{1-y}Sn_y$ epilayers, which were grown at 260 °C and 500 Torr with $SnCl_4/GeH_4$ ratio of 3.3×10^{-3}, was investigated. It is important to note that strain relaxation could be different in $Ge_{1-y}Sn_y$ epilayers with the same Sn concentration but grown under different CVD growth conditions. More experiments should therefore be carried out to investigate strain relaxation for $Ge_{1-y}Sn_y$ epilayers grown under different CVD growth conditions. Moreover, since the strain relaxation in $Ge_{1-y}Sn_y$ epilayers affects the electrical, for example indirect-to-direct bandgap transition [50,69-73], and the physical properties of epilayers, it is therefore essential to consider further investigations in order to fully understand the mechanism of strain relaxation of $Ge_{1-y}Sn_y$ epilayers.

Chapter 8

$Ge_{1-y}Sn_y$ Epitaxy Using $SnCl_4/GeH_4$ Grading Technique

8.1 Introduction

In this chapter, we examined the impact of grading the $SnCl_4/GeH_4$ ratio during epitaxial growth of $Ge_{1-y}Sn_y$ epilayers on their growth and quality. Here, the grading means that the $SnCl_4$ flow rate is tuned at a constant rate from a very low level (for example 5 sccm) to an appropriate level (for example 100 sccm) during growth. $SnCl_4/GeH_4$ grading was tested at two temperatures: 280 ℃ and 260 ℃, and the respective results are given and discussed in this chapter. This technique was not tested for epitaxial growth of $Ge_{1-y}Sn_y$ binary alloys. This method is proposed to achieve a high Sn concentration $Ge_{1-y}Sn_y$ using $Ge_{1-y}Sn_y$ with lower Sn concentration as an intermediate epilayer (similar to a VS) to minimise the effective lattice mismatch. However, to achieve this, it is necessary to grow thick enough $Ge_{1-y}Sn_y$ with low Sn concentration to achieve some relaxation. Otherwise, the use of fully strained $Ge_{1-y}Sn_y$ offers the same in-plane lattice constant as that of the relaxed Ge-VS.

8.2 $Ge_{1-y}Sn_y$ Epitaxy with Grading Technique at 280 °C

8.2.1 Heterostructures of $Ge_{1-y}Sn_y$ Epilayers Grown at 280 °C Using Grading

For this study, $Ge_{1-y}Sn_y$ epilayers were grown on Si (001) substrate via a ~0.7 µm thick relaxed Ge-VS at 280 °C and 500 Torr using 70 sccm $SnCl_4$ with $SnCl_4/H_2$ ratio of 0.25 % (70 sccm gas flow of $SnCl_4$ diluted at 0.25% in H_2 carrier gas). Fully strained $Ge_{0.914}Sn_{0.086}$, Figure 8.1 (a), as well as partially relaxed $Ge_{1-y}Sn_y$, Figure 8.1 (b), both of which were grown under the same growth conditions, are presented to understand the effect of intermediate grown graded $Ge_{1-y}Sn_y$. As shown in Figure 8.1 (c), the graded $Ge_{1-y}Sn_y$ was grown with variable $SnCl_4$-H_2 gas flow, tuned from 5 sccm to 70 sccm, over its growth time of 40:00 min. The total growth time for Figure 8.1 (c), graded $Ge_{1-y}Sn_y$ (variable $SnCl_4$-H_2) plus $Ge_{1-y}Sn_y$ (fixed $SnCl_4$-H_2), was kept at 50:00 min for a better comparison with Figure 8.1 (b) which has a total growth time of 50:00 min for its $Ge_{1-y}Sn_y$ growth.

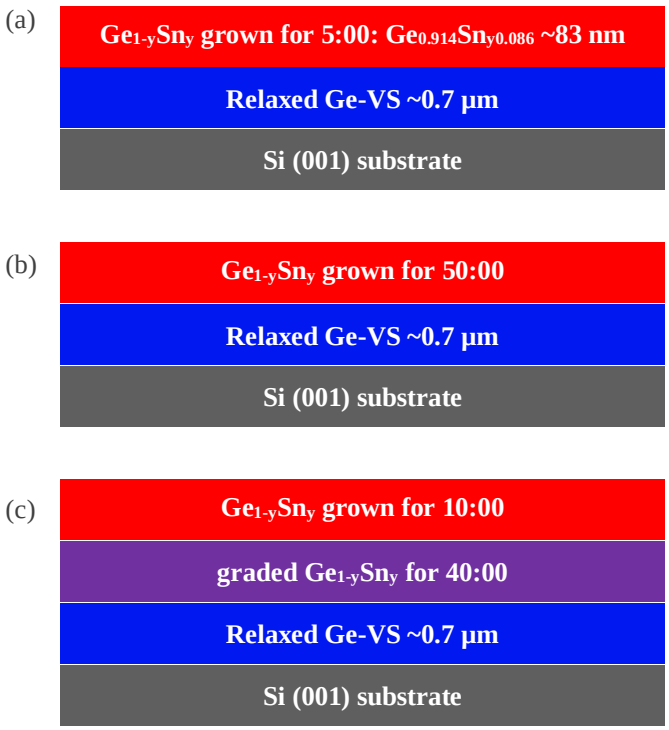

Figure 8.1 Cross sectional schematic of $Ge_{1-y}Sn_y$ as well as graded $Ge_{1-y}Sn_y$ grown on Si (001) substrate via relaxed Ge-VS. All $Ge_{1-y}Sn_y$ layers were grown with the RP-CVD system at 280 °C and 500 Torr using fixed $SnCl_4$-H_2 flow rate of 70 sccm. However, for graded $Ge_{1-y}Sn_y$ epilayer, $SnCl_4$-H_2 flow rate was tuned from 5 sccm to 70 sccm over its growth time.

8.2.2 ω-2θ Coupled Scan of $Ge_{1-y}Sn_y$ Epilayers Grown at 280 °C Using Grading

HR-XRD ω-2θ coupled scans of the given heterostructures (given in Figure 8.1), are shown in Figure 8.2. As expected, thickness fringes are visible in the ω-2θ coupled scan of fully strained $Ge_{0.914}Sn_{0.086}$\Ge-VS\Si (001), Figure 8.2 (a), which confirms that the epilayer is fully strained. However, for other two ω-2θ coupled scans, Figure 8.2 (b) and (c), no thickness fringes are visible and there are also two peaks that correspond to $Ge_{1-y}Sn_y$ (between ~32° and ~32.5°). As explained and shown in Figure 7.3 on page 91 in chapter 7, strain relaxation in the $Ge_{1-y}Sn_y$ epilayers can cause the appearance of double $Ge_{1-y}Sn_y$ peaks.

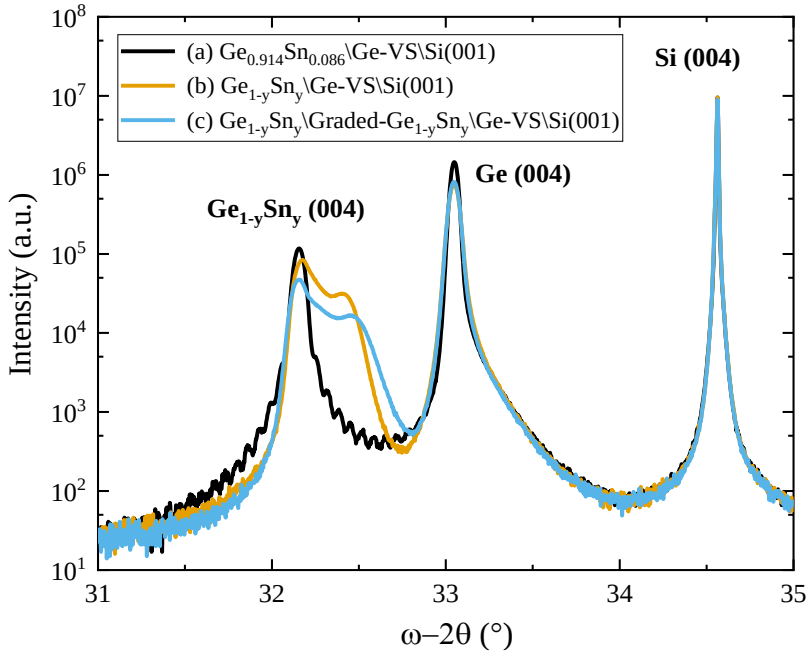

Figure 8.2 HR-XRD ω-2θ coupled scan of (a) 83 nm thick fully strained $Ge_{0.914}Sn_{0.086}$\Ge-VS\Si (001), (b) Partially relaxed $Ge_{1-y}Sn_y$\Ge-VS\Si (001), and (c) $Ge_{1-y}Sn_y$\Graded-$Ge_{1-y}Sn_y$\Ge-VS\Si (001), which their heterostructures are all shown in Figure 8.1. For (b) and (c), the total growth time of all grown $Ge_{1-y}Sn_y$ (including any graded) was kept the same at 50:00 min for a better comparison.

In addition, HR-XRD ω-2θ coupled scan of $Ge_{1-y}Sn_y$\Graded-$Ge_{1-y}Sn_y$\Ge-VS\Si (001), Figure 8.2 (c), compared to that of partially relaxed $Ge_{1-y}Sn_y$\Ge-VS\Si (001), Figure 8.2 (b), shows a slightly broader $Ge_{1-y}Sn_y$ peak with a larger range of Sn concentration. However, the use of the grading technique (varying $SnCl_4$-H_2 gas flow) did not provide $Ge_{1-y}Sn_y$ with tuned y from 0 to its possible maximum at this growth temperature. As discussed in chapter 6, it is not possible to achieve any Sn concentration at a specific CVD growth conditions (shown in Figure 6.5 on page 79), and also growth is not allowed with any range of $SnCl_4/GeH_4$ ratio at

a given growth temperature (shown in Figure 6.6 on page 80). This means that during the growth of the graded $Ge_{1-y}Sn_y$, no $Ge_{1-y}Sn_y$ was successfully grown until a certain $SnCl_4/GeH_4$ ratio was reached. This confirms why the $Ge_{1-y}Sn_y$ peak of graded-$Ge_{1-y}Sn_y$, Figure 8.2 (c), is lower than that of partially relaxed $Ge_{1-y}Sn_y$, Figure 8.2 (b), although the growth times of $Ge_{1-y}Sn_y$ epilayers were the same at 50:00 min for both samples.

8.2.3 RSMs of $Ge_{1-y}Sn_y$ Epilayers Grown at 280 °C Using Grading

Symmetric and asymmetric RSMs were scanned on both partially relaxed $Ge_{1-y}Sn_y$\Ge-VS\Si (001) and $Ge_{1-y}Sn_y$\Graded-$Ge_{1-y}Sn_y$\Ge-VS\Si (001) to estimate the tilt and strain state of the epilayers as well as the Sn concentration at each of the two peaks shown in respective ω-2θ coupled scans. For a better comparison, symmetric and asymmetric RSMs of fully strained $Ge_{0.914}Sn_{0.086}$\Ge-VS\Si (001) are also shown in Figure 8.3 (b). A higher Sn concentration (~0.5 at.% more) was achieved for partially relaxed $Ge_{1-y}Sn_y$ epilayer Figure 8.3 (b) compared to the heterostructure that graded-$Ge_{1-y}Sn_y$ was grown as an intermediate layer, Figure 8.3 (c). As already mentioned, this is because no $Ge_{1-y}Sn_y$ could be grown during the growth of graded-$Ge_{1-y}Sn_y$ until $SnCl_4$-H_2 reached a certain level. So, a thinner $Ge_{1-y}Sn_y$ could be grown and less strain relaxation was achieved, resulting in less Sn incorporation into the $Ge_{1-y}Sn_y$ epilayer. The details of in-plane and out-of-plane strain values as well as the Sn concentrations of $Ge_{1-y}Sn_y$ epilayers are shown in Table 4.

Growth Time (min)	**In-plane Strain**	**Out-of-plane Strain**	**Sn Concentration (at. %)**
5:00	-11.8×10^{-3}	9.2×10^{-3}	8.6
50:00	-3.3×10^{-3}	2.6×10^{-3}	12.5
40:00 graded + 10:00	-5.4×10^{-3}	4.2×10^{-3}	12.0

Table 4 Summary of in-plane and out-of-plane strain values, as well as the Sn concentrations of $Ge_{1-y}Sn_y$ epilayers discussed in this section.

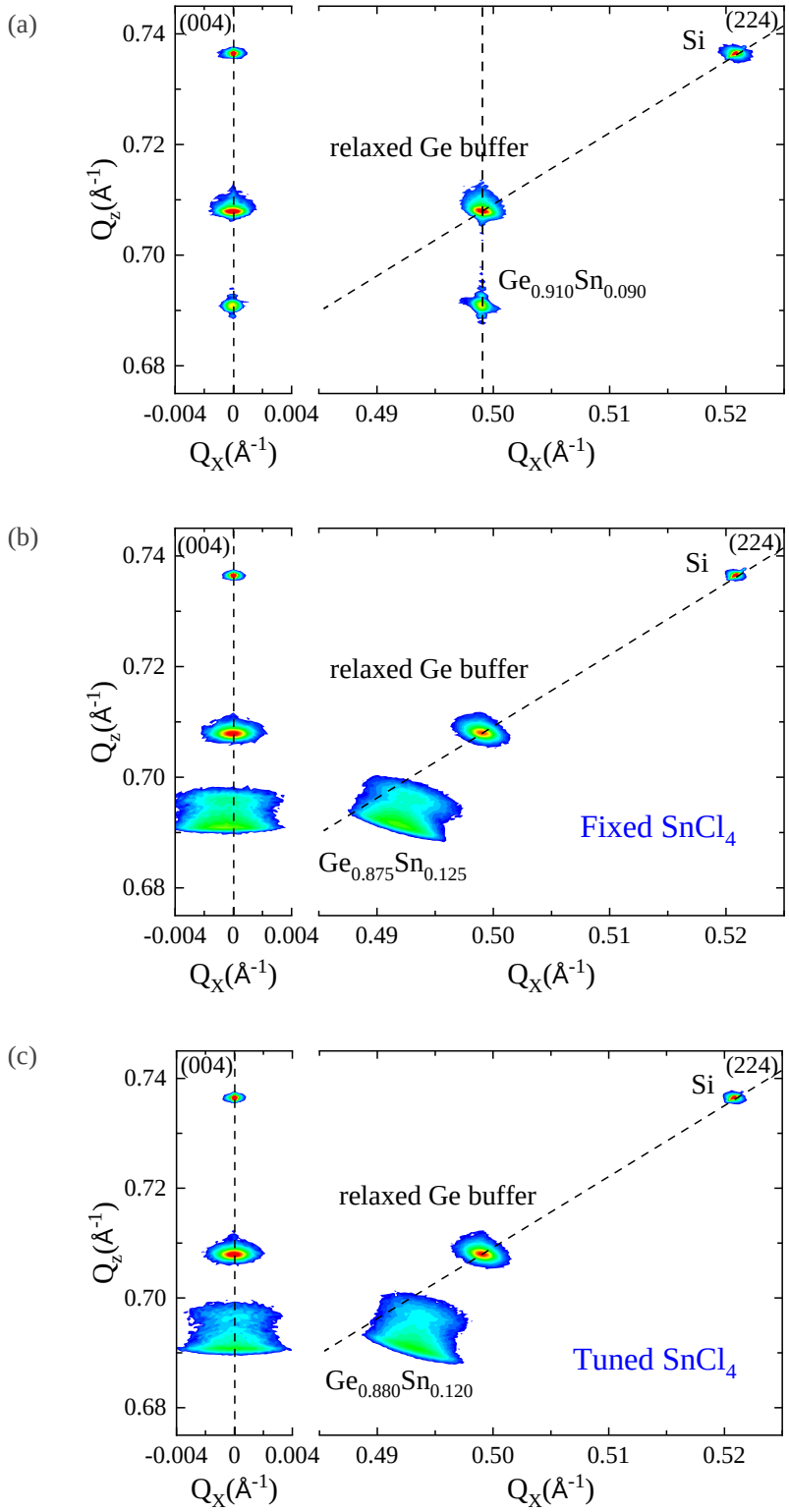

Figure 8.3 Symmetric and asymmetric RSMs for $Ge_{1-y}Sn_y$ heterostructures which are shown in Figure 8.1 with respective ω-2θ coupled scans given in Figure 8.2. As it can be seen here, the use of graded $Ge_{1-y}Sn_y$ does not support to achieve a higher Sn concentration in $Ge_{1-y}Sn_y$ as growth is not allowed at all $SnCl_4/GeH_4$ ratios. Therefore, thinner $Ge_{1-y}Sn_y$ and less strain relaxation were achieved while graded $Ge_{1-y}Sn_y$ was grown which results in lower Sn concentration.

8.3 $Ge_{1-y}Sn_y$ Epitaxy with Grading Technique at 260 °C

8.3.1 Heterostructures of $Ge_{1-y}Sn_y$ Epilayers Grown at 260 °C Using Grading

For further investigation of the effect of $Ge_{1-y}Sn_y$ grading at different growth temperatures, $Ge_{1-y}Sn_y$ epilayers are grown on Si (001) substrate via ~0.66 µm thick relaxed Ge-VS at a 260 °C and 500 Torr using 100 sccm $SnCl_4$ with $SnCl_4/H_2$ ratio of 0.25 % (100 sccm gas flow of $SnCl_4$ diluted at 0.25% in H_2 carrier gas). Fully strained $Ge_{0.884}Sn_{0.116}$, Figure 8.4 (a), as well as partially relaxed $Ge_{1-y}Sn_y$, Figure 8.4 (b), both of which were grown under the same growth conditions, are presented to examine the effect of intermediate graded $Ge_{1-y}Sn_y$. As shown in Figure 8.4 (c), the graded $Ge_{1-y}Sn_y$ was grown with variable $SnCl_4$-H_2 gas flow, tuned from 5 sccm to 100 sccm, over its growth time of 50:00 min. The total growth time for Figure 8.4 (c), graded $Ge_{1-y}Sn_y$ (variable $SnCl_4$-H_2) plus $Ge_{1-y}Sn_y$ (fixed $SnCl_4$-H_2), was maintained at 70:00 min for a better comparison with Figure 8.4 (b) which also had a total growth time of 70:00 min for its $Ge_{1-y}Sn_y$ growth.

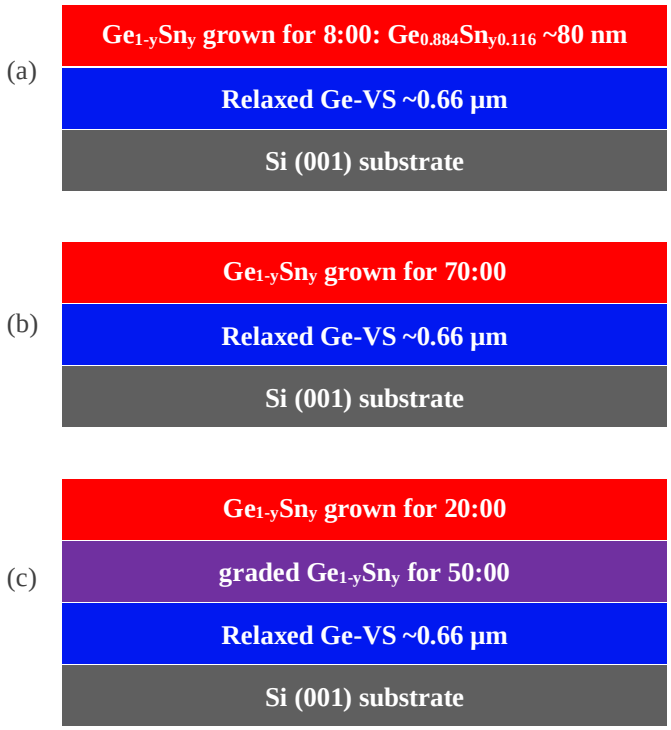

Figure 8.4 Cross sectional schematic of $Ge_{1-y}Sn_y$ as well as graded $Ge_{1-y}Sn_y$ grown on Si (001) substrate via relaxed Ge-VS. All $Ge_{1-y}Sn_y$ layers were grown at 260 °C and 500 Torr with a fixed $SnCl_4$-H_2 flow rate of 100 sccm. But, for graded $Ge_{1-y}Sn_y$ epilayer, $SnCl_4$-H_2 flow rate was tuned from 5 sccm to 100 sccm over its growth time.

8.3.2 ω-2θ Coupled Scan of $Ge_{1-y}Sn_y$ Epilayers Grown at 260 °C Using Grading

HR-XRD ω-2θ coupled scans of the heterostructures (given in Figure 8.4), are shown in Figure 8.5. As expected, thickness fringes are visible in the ω-2θ coupled scan of fully strained $Ge_{0.884}Sn_{0.116}$\Ge-VS\Si (001), Figure 8.5 (a), which confirms that the epilayer is fully strained. For the heterostructure in which its $Ge_{1-y}Sn_y$ epilayer was grown for 70:00 min, as shown in Figure 8.5 (b), there is a peak of just below 32°, which corresponds to the $Ge_{1-y}Sn_y$ with a Sn concentration similar to that obtained for the fully strained $Ge_{1-y}Sn_y$ grown under the same growth conditions. However, for this heterostructure, as shown in Figure 8.5 (b), the growth of $Ge_{1-y}Sn_y$ with high Sn concentration was terminated shortly, and only the growth of $Ge_{1-y}Sn_y$ with Sn concentration up to Sn solubility (~1.1 at.%) was achieved.

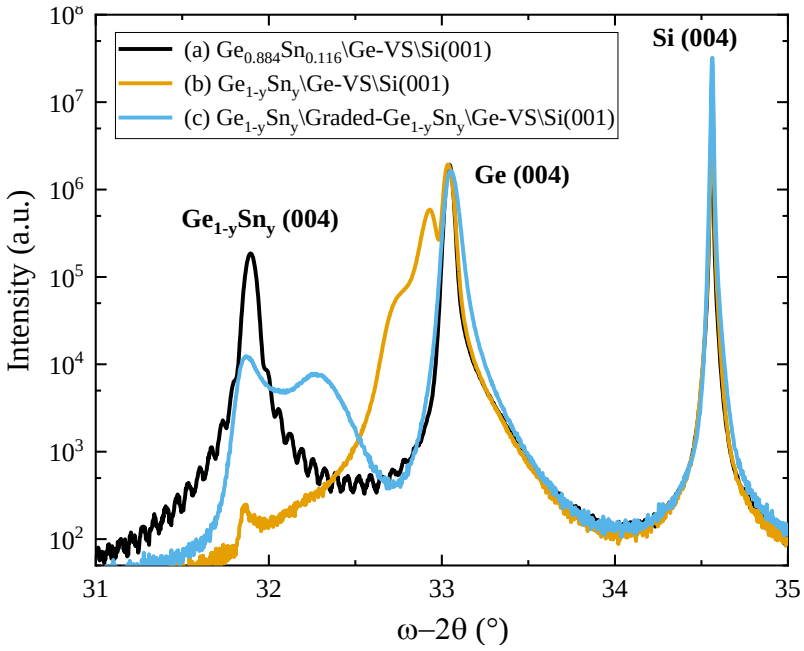

Figure 8.5 HR-XRD ω-2θ coupled scan of (a) 80 nm fully strained $Ge_{0.884}Sn_{0.116}$\Ge-VS\Si (001), (b) Partially relaxed $Ge_{1-y}Sn_y$\Ge-VS\Si (001), and (c) $Ge_{1-y}Sn_y$\Graded-$Ge_{1-y}Sn_y$\Ge-VS\Si (001), which their heterostructures are all shown in Figure 8.4. For (b) and (c), the total growth time of all grown $Ge_{1-y}Sn_y$ (including any graded) was kept the same at 70:00 min for a better comparison.

For the $Ge_{1-y}Sn_y$\Graded-$Ge_{1-y}Sn_y$\Ge-VS\Si (001) heterostructure, in which $SnCl_4$-H_2 was tuned from 5 sccm to 100 sccm to grow graded $Ge_{1-y}Sn_y$, the growth of $Ge_{1-y}Sn_y$ was not stopped. It seems the grading technique is useful to enable growth at this growth temperature. As shown in Figure 8.5 (c), partially relaxed $Ge_{1-y}Sn_y$ with high Sn concentration with two peaks, which correspond to $Ge_{1-y}Sn_y$ (between ~31.5° and ~32.5°), was achieved. As explained

and shown in Figure 7.3 on page 91 in chapter 7, strain relaxation in the $Ge_{1-y}Sn_y$ epilayers can cause the appearance of double $Ge_{1-y}Sn_y$ peaks. Similar to the ω-2θ coupled scan of graded $Ge_{1-y}Sn_y$ grown at 280 ℃ (Figure 8.2 (c) on page 101), the ω-2θ coupled scan of graded $Ge_{1-y}Sn_y$ grown at 260 ℃ (Figure 8.5 (c)) clearly shows that the grading technique did not provide $Ge_{1-y}Sn_y$ with tuned y from 0 to its possible maximum at the growth temperature. As discussed in the previous section, it is impossible to achieve any Sn concentration at specific CVD growth conditions (shown in Figure 6.5 on page 79), and also growth cannot be achieved using any range of $SnCl_4/GeH_4$ ratio at a given growth temperature (shown in Figure 6.6 on page 80). The allowed range for $SnCl_4/GeH_4$ ratio also shrinks as the growth temperature decreases (shown in Figure 6.6 on page 80). This means that during the growth of the graded $Ge_{1-y}Sn_y$, no $Ge_{1-y}Sn_y$ was successfully grown until a certain $SnCl_4/GeH_4$ ratio was reached.

8.3.3 RSMs of $Ge_{1-y}Sn_y$ Epilayers Grown at 260 ℃ Using Grading

Symmetric and asymmetric RSMs were scanned for all heterostructures shown in Figure 8.4 to estimate the tilt and strain state of the $Ge_{1-y}Sn_y$ epilayers and their Sn concentrations. As shown in Figure 8.6 (a) and (b), the comparison of symmetric and asymmetric RSMs of fully strained $Ge_{0.884}Sn_{0.116}$\Ge-VS\Si(001) with those of $Ge_{1-y}Sn_y$\Graded-$Ge_{1-y}Sn_y$\Ge-VS\Si(001) shows how the growth of $Ge_{1-y}Sn_y$ with high Sn concentration was stopped due to increased growth time. For the observed peak of just below 32° of ω-2θ coupled scan of $Ge_{1-y}Sn_y$\Ge-VS\Si (001), shown in Figure 8.5 (b), there is no corresponding peak in its asymmetric RSM, which is shown in Figure 8.6 (b). The Sn concentration of $Ge_{1-y}Sn_y$ which was grown for 70:00 min was measured at 1.0 at.%, just about the Sn solubility in Ge.

For the $Ge_{1-y}Sn_y$\Graded-$Ge_{1-y}Sn_y$\Ge-VS\Si (001) heterostructure, however, the partially relaxed $Ge_{1-y}Sn_y$ with two peaks is evident in Figure 8.6 (c). The Sn concentration of $Ge_{1-y}Sn_y$, which corresponds to the peak with the highest Sn concentration, was measured at 14.9 at.%. The Sn concentration has increased as a result of strain relaxation. The details of the in-plane and out-of-plane strain values as well as the Sn concentrations of $Ge_{1-y}Sn_y$ epilayers are shown in Table 5. Comparing Figure 8.6 (a) and (c) with the consideration of the in-plane and out-of-plane strain, it is clear that due to strain relaxation, the $Ge_{1-y}Sn_y$ in the $Ge_{1-y}Sn_y$\Graded-$Ge_{1-y}Sn_y$\Ge-VS\Si (001) heterostructure has 3.3 at.% more Sn concentration than that of the fully strain $Ge_{1-y}Sn_y$ grown under the same growth conditions.

Finally, it should also be noted that the $Ge_{1-y}Sn_y$ epilayer in $Ge_{1-y}Sn_y$\Ge-VS\Si (001) heterostructure with a growth time of 70:00 min, has almost the same in-plane and out-of-plane lattice as that of a relaxed Ge-VS, as shown in Table 5. This is because of the very low Sn concentration of the $Ge_{1-y}Sn_y$ that is almost about Sn solubility of Sn in bulk Ge.

Growth Time (min)	**In-plane Strain**	**Out-of-plane Strain**	**Sn Concentration (at. %)**
8:00	-15.8×10^{-3}	12.4×10^{-3}	11.6
70:00	-0.1×10^{-3}	0.1×10^{-3}	1.0
50:00 graded + 20:00	-15.1×10^{-3}	11.9×10^{-3}	14.9

Table 5 Summary of in-plane and out-of-plane strain and Sn concentrations of $Ge_{1-y}Sn_y$ epilayers in this section.

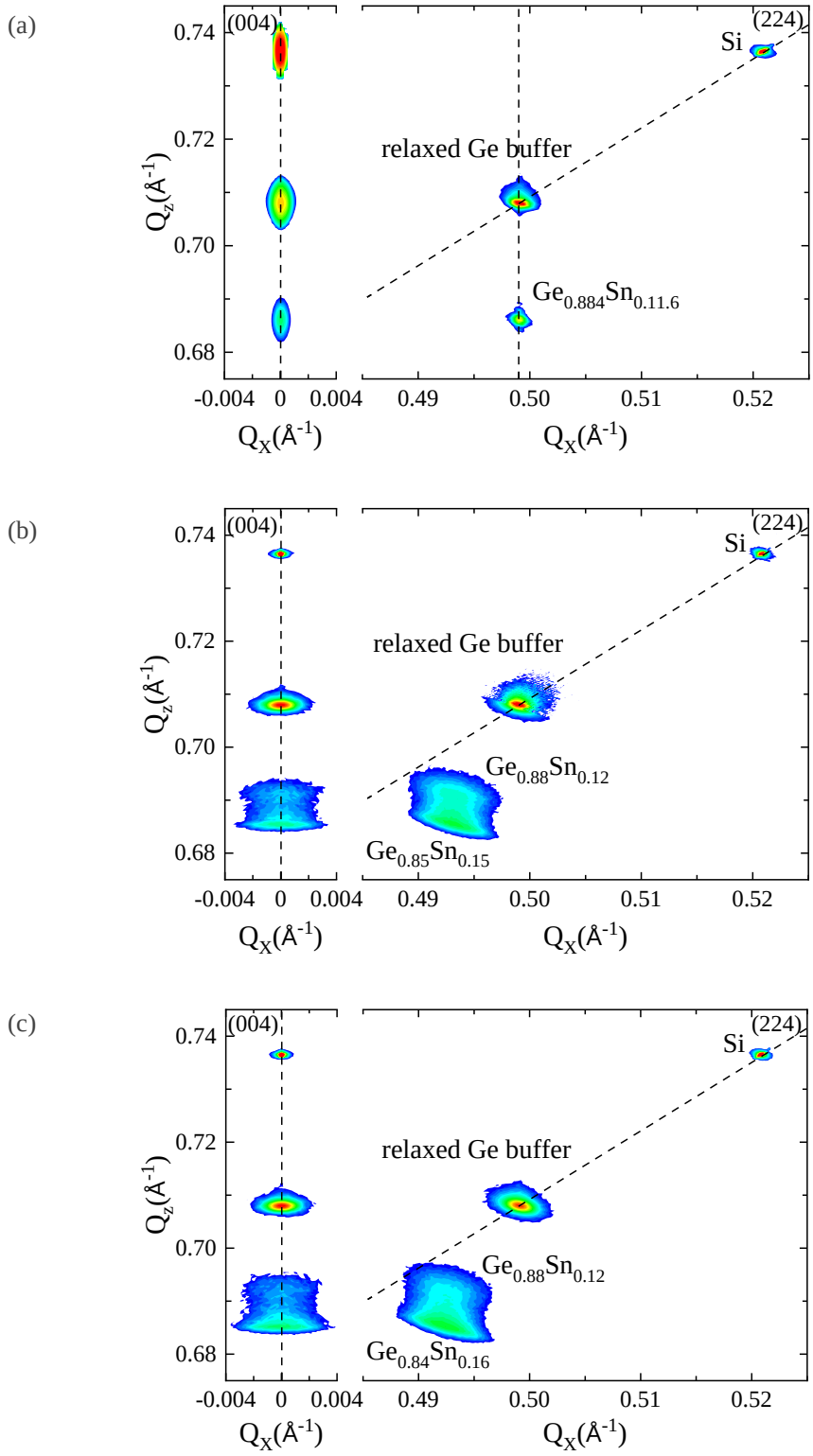

Figure 8.6 Symmetric and asymmetric RSMs for $Ge_{1-y}Sn_y$ heterostructures which are shown in Figure 8.4 with respective ω-2θ coupled scans given in Figure 8.5. As can be seen here, the use of graded $Ge_{1-y}Sn_y$ enabled the growth of $Ge_{1-y}Sn_y$. When the grading technique was not used, the growth of $Ge_{1-y}Sn_y$ with high Sn concentration terminated shortly, and only the growth of $Ge_{1-y}Sn_y$ with Sn concentration up to Sn solubility in Ge bulk (~1.1 at.%) was achieved.

8.3.4 Surface Morphology of $Ge_{1-y}Sn_y$ Epilayers Grown on Graded $Ge_{1-y}Sn_y$

As shown in Figure 8.7 (middle scans), Sn segregation is evident when $SnCl_4$-H_2 was fixed at 100 sccm during the growth of the $Ge_{1-y}Sn_y$ epilayer for 70:00 min. However, as it can be seen in Figure 8.7 (bottom scans), the Sn segregation, which can potentially terminate growth of $Ge_{1-y}Sn_y$, was controlled when a grading technique was used. Another reason for suppressing Sn segregation is not only the grading technique itself, but also the thinner $Ge_{1-y}Sn_y$ was grown when $SnCl_4$-H_2 was tuned from 5 sccm to 100 sccm.

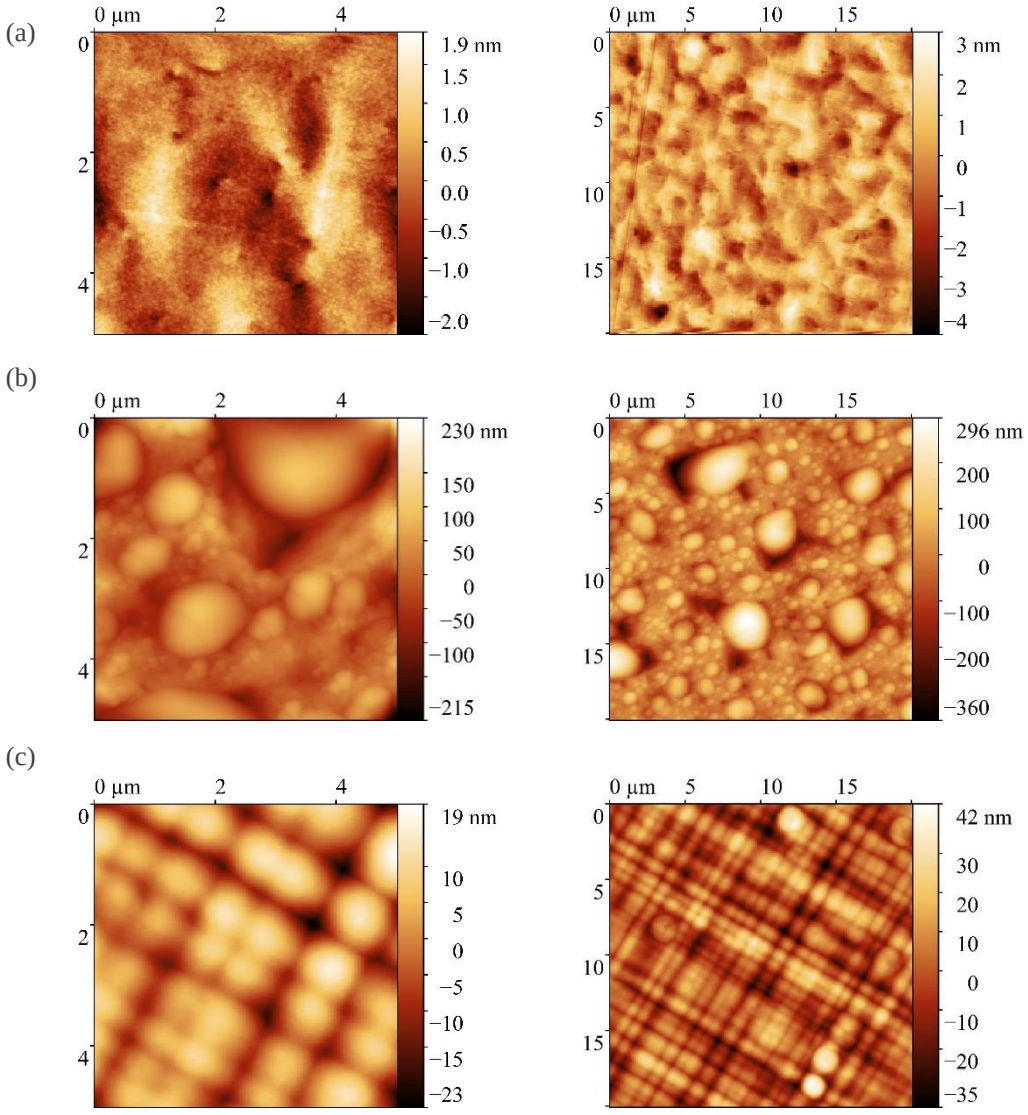

Figure 8.7 AFM scans of (a) Fully strained $Ge_{0.884}Sn_{0.116}$\Ge-VS\Si (001) with RMS of ~1 nm, (b) Partially relaxed $Ge_{1-y}Sn_y$\Ge-VS\Si (001) with RMS of ~79 nm, and (c) $Ge_{1-y}Sn_y$\Graded-$Ge_{1-y}Sn_y$\Ge-VS\Si (001) with RMS of ~12 nm. Their heterostructures are all given in Figure 8.4.

8.4 Mechanism of Growth & Quality of Graded $Ge_{1-y}Sn_y$

8.4.1 Heterostructures of Graded $Ge_{1-y}Sn_y$

To measure the growth rate of the graded $Ge_{1-y}Sn_y$, in which $SnCl_4$-H_2 was tuned during its growth, the following heterostructures, as shown in Figure 8.8, were grown and investigated. All graded $Ge_{1-y}Sn_y$ epilayers were grown on Si (001) substrate via ~0.66 µm thick relaxed Ge-VS at a temperature of 260 °C and pressure of 500 Torr using $SnCl_4$, which varied from 5 sccm to 100 sccm during growth, with $SnCl_4/H_2$ ratio of 0.25 % (100 sccm gas flow of $SnCl_4$ diluted at 0.25% in H_2 carrier gas).

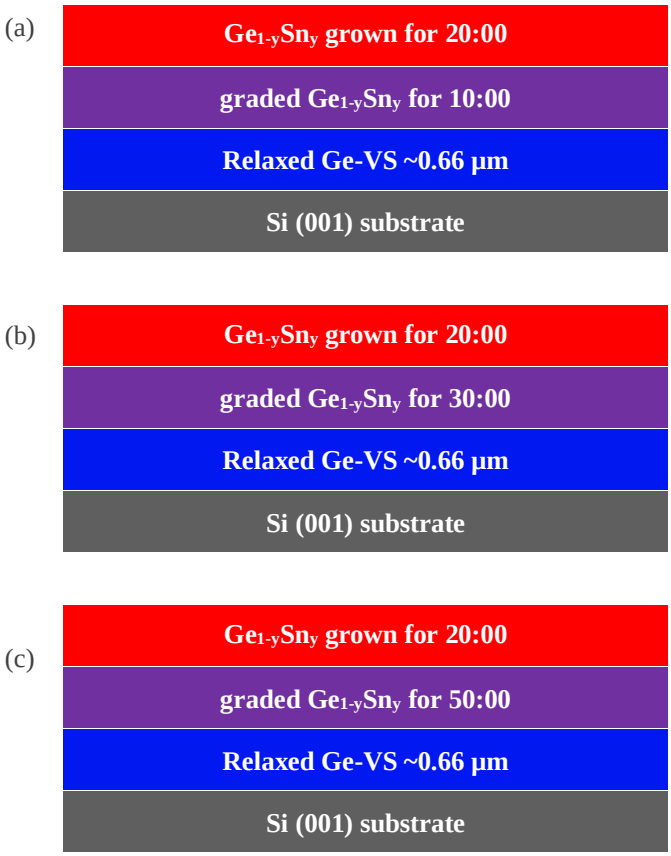

Figure 8.8 Cross sectional schematic of $Ge_{1-y}Sn_y$\Graded-$Ge_{1-y}Sn_y$\Ge-VS\Si (001) heterostructures in which $Ge_{1-y}Sn_y$ epilayers were all grown at 260 °C and 500 Torr. For the graded $Ge_{1-y}Sn_y$ epilayers $SnCl_4$-H_2 flow rate was tuned from 5 sccm to 100 sccm over its growth time of either 10:00 min, 30:00 min or 50:00 min. However, for $Ge_{1-y}Sn_y$ epilayers grown on top of the graded ones, a fixed $SnCl_4$-H_2 flow rate of 100 sccm was used over the growth time of 20:00 min.

While using the same growth conditions for each of these heterostructures, different growth times were used for each of the graded $Ge_{1-y}Sn_y$ epilayers to investigate their growth rates at this temperature. As shown in Figure 8.8, the growth times for graded $Ge_{1-y}Sn_y$ were chosen to be at 10:00 min, 30:00 min and 50:00 min. In addition to graded $Ge_{1-y}Sn_y$ epilayers, a $Ge_{1-y}Sn_y$ epilayer was grown under the same growth conditions, but with a fixed $SnCl_4$ of 100 sccm, for 20:00 min for each heterostructure. This could support us to investigate the effects of graded $Ge_{1-y}Sn_y$ (as intermediate layer) on the quality of the $Ge_{1-y}Sn_y$ epilayer grown above.

8.4.2 ω-2θ Coupled Scans & RSMs

HR-XRD ω-2θ coupled scans of the heterostructures (given in Figure 8.8), are shown in Figure 8.9. For all $Ge_{1-y}Sn_y$\Graded-$Ge_{1-y}Sn_y$\Ge-VS\Si (001) heterostructures, two peaks, which correspond to $Ge_{1-y}Sn_y$ (between ~31.5° and ~32.5°) can be observed, showing growth of partially relaxed $Ge_{1-y}Sn_y$, as explained in previous sections.

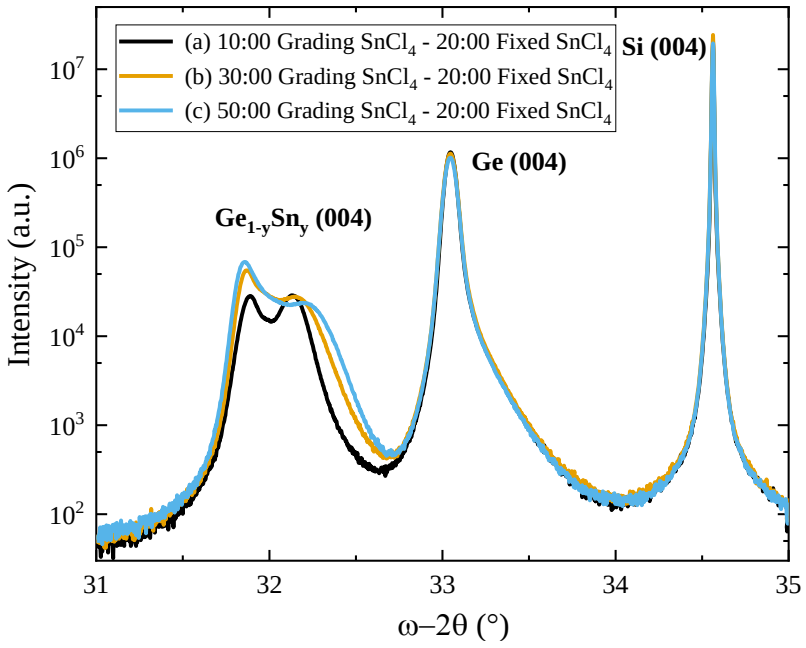

Figure 8.9 HR-XRD ω-2θ coupled scan of $Ge_{1-y}Sn_y$\Graded-$Ge_{1-y}Sn_y$\Ge-VS\Si (001) heterostructures shown in Figure 8.8. The only difference between these heterostructures is the growth rate of their graded $Ge_{1-y}Sn_y$ epilayers.

Similar to the ω-2θ coupled scans of graded $Ge_{1-y}Sn_y$ presented in the previous sections, the ω-2θ coupled scans of heterostructures in this section, shown in Figure 8.9, clearly show that the grading technique did not provide $Ge_{1-y}Sn_y$ with tuned y from 0 to its possible maximum

at the growth temperature. As discussed in the previous sections, it is impossible to achieve any Sn concentration at specific CVD growth conditions (shown in Figure 6.5 on page 79), and also not all values for $SnCl_4/GeH_4$ ratio at a given growth temperature could provide successful growth (shown in Figure 6.6 on page 80). The allowed range for $SnCl_4/GeH_4$ ratio also shrinks as the growth temperature decreases (shown in Figure 6.6 on page 80). This means that during the growth of the graded $Ge_{1-y}Sn_y$, no $Ge_{1-y}Sn_y$ was successfully grown until a certain $SnCl_4/GeH_4$ ratio was reached.

Symmetric and asymmetric RSMs were scanned for all heterostructures shown in Figure 8.8 to estimate the tilt and strain state of the $Ge_{1-y}Sn_y$ epilayers and their Sn concentrations. As shown in Figure 8.10, the partially relaxed $Ge_{1-y}Sn_y$ with two peaks is evident for all heterostructures. More strain relaxation is achieved as the growth time of the graded $Ge_{1-y}Sn_y$ is increased. In addition, the Sn concentration is slightly increased due to the increased growth time of the graded $Ge_{1-y}Sn_y$. It was difficult to find the exact position of the $Ge_{1-y}Sn_y$ peak in RSMs to estimate the Sn concentration with higher precision, so more RSM scans with better resolution should be taken.

Although it is obvious that a higher Sn concentration was achieved as a result of strain relaxation, and strain relaxation was probably achieved due to an increase in the thickness of $Ge_{1-y}Sn_y$, it is necessary to accurately measure the thickness of $Ge_{1-y}Sn_y$ epilayers. In the next section, X-TEM micrographs were taken to measure thickness and investigate the quality of epilayers.

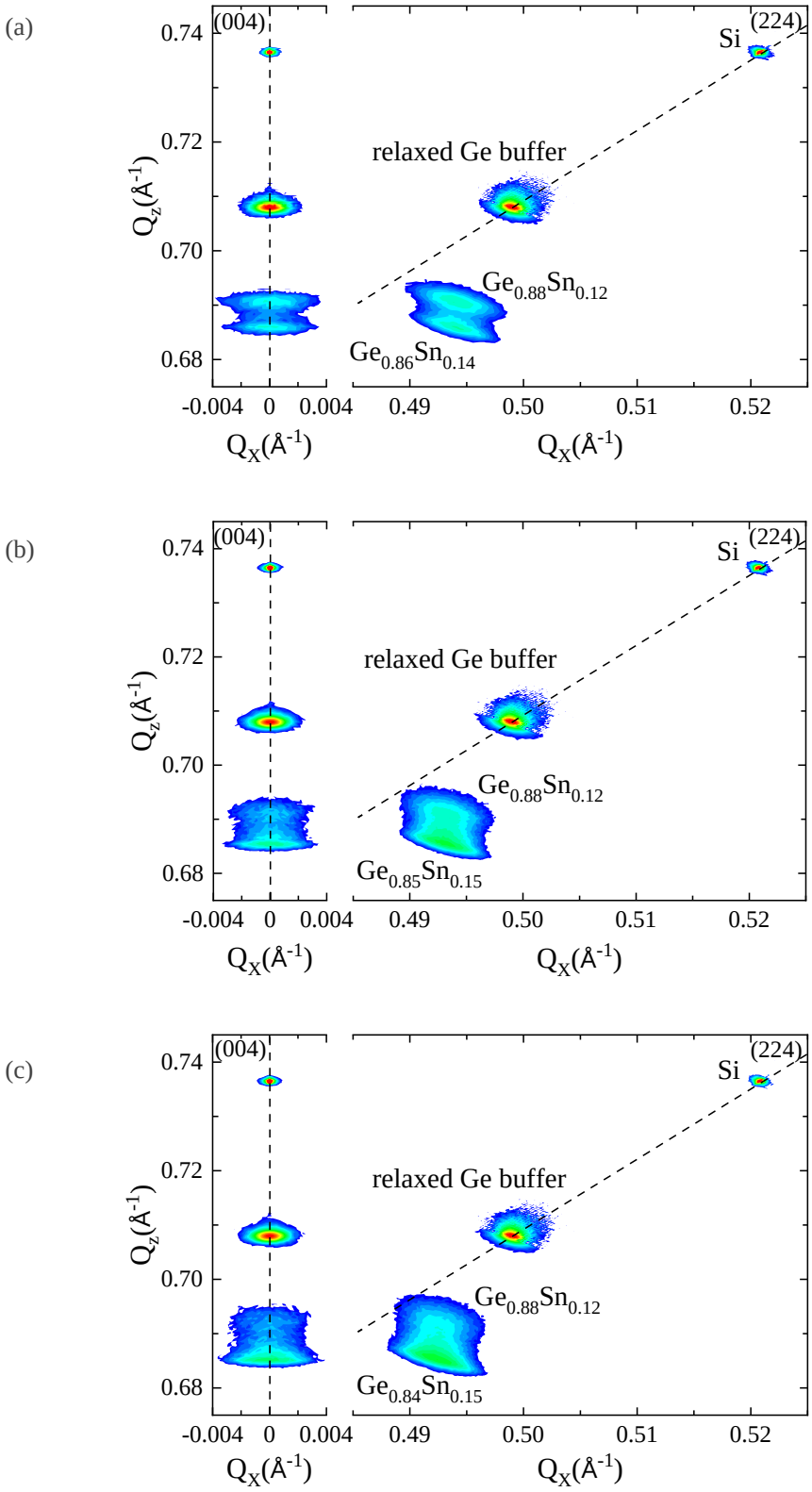

Figure 8.10 Symmetric and asymmetric RSMs for heterostructures which are shown in Figure 8.8 with respective ω-2θ coupled scans given in Figure 8.9. The only difference between these heterostructures is the growth rate of their graded $Ge_{1-y}Sn_y$ epilayers.

8.5 Quality of $Ge_{1-y}Sn_y$\Graded-$Ge_{1-y}Sn_y$\Ge-VS\Si (001)

8.5.1 Epilayer Thickness & Defect Studies

All thicknesses for partially relaxed $Ge_{1-y}Sn_y$ as well as thicknesses of heterostructures given in Figure 8.8 (a), (b) and (c) were all measured using X-TEM as there would be no thickness fringes in their ω-2θ coupled scans. It should be noted that it is impossible to distinguish $Ge_{1-y}Sn_y$ grown with variable (grading) $SnCl_4$ or fixed $SnCl_4$ gas flow in X-TEM. The growth rate of $Ge_{1-y}Sn_y$ at fixed $SnCl_4$ gas flow was measured separately from other samples in which no grading was performed, but the growth rate varies due to strain relaxation, as shown in chapter 7. The change in growth rate due to strain relaxation cannot be disregarded, as it can vary significantly.

Thicknesses of total grown $Ge_{1-y}Sn_y$ for Figure 8.8 (a), (b) and (c) are ~200 nm, ~280 nm, and ~350 nm, respectively. As a result, the average $Ge_{1-y}Sn_y$ growth rates for the entire $Ge_{1-y}Sn_y$ (including fixed or grading $SnCl_4$) for Figure 8.8 (a), (b) and (c) were estimated at 6.7 nm/min, 5.6 nm/min and 5.0 nm/min, respectively. The growth rate of fully strain $Ge_{1-y}Sn_y$ grown under the same CVD growth conditions was estimated at 9.8 nm/min, as shown in Figure 7.6 on page 93. Considering Figure 7.5 on page 92, which shows the average growth rate for the entire $Ge_{1-y}Sn_y$ epilayer grown under the same growth conditions, we realised that the average growth rates of $Ge_{1-y}Sn_y$ epilayers for Figure 8.8 (a), (b) and (c) are lower than expected. This is because growth is not allowed at all $SnCl_4/GeH_4$ ratios under these CVD growth conditions. As shown in Figure 6.6 on page 80, there is only a narrow range of $SnCl_4/GeH_4$ ratio, ~3.5×10^{-3} to ~5.0×10^{-3}, that growth of $Ge_{1-y}Sn_y$ is allowed at temperature of 260 °C and pressure of 500 Torr. The decrease in the average growth rate is due to strain relaxation, as described in chapter 7, and shown in Figure 7.5 on page 92. Therefore, the following equation was used for each heterostructure shown in Figure 8.8 to estimate the average growth rate for entire $Ge_{1-y}Sn_y$ in each of the heterostructures:

$$Average\ GR_{Ge_{1-y}Sn_y} = \frac{Thickness_{Ge_{1-y}Sn_y}}{GT_{Ge_{1-y}Sn_y}} \qquad (8.1)$$

Using the equation given above, the average growth rate for the entire $Ge_{1-y}Sn_y$ (both $Ge_{1-y}Sn_y$ epilayers in which $SnCl_4$ was either fixed or varied) was estimated at 6.7 nm/min, 5.6 nm/min and 5.0 nm/min for Figure 8.8 (a), (b) and (c), respectively. However, as already explained, the growth rate decreases due to strain relaxation. Therefore, the following equation was

proposed to estimate the average growth rate of partially relaxed $Ge_{1-y}Sn_y$. It should be noted that the growth rate for fully strained $Ge_{1-y}Sn_y$ as well as its growth time are known and given in chapter 7, Figure 7.5 and Figure 7.6 on pages 92 and 93.

$$Total\ Thickness_{Ge_{1-y}Sn_y} = [GR \times GT]_{fully\ strained} + [GR \times GT]_{partially\ relaxed} \quad (8.2)$$

Where GR and GT are growth rate and growth time of $Ge_{1-y}Sn_y$ at a given strain relaxation state. Using the equation above with consideration of h_c of ~100 nm and the required growth time of ~10:00 min which after this point strain relaxation begins under these CVD growth conditions, the average growth rate for partially relaxed $Ge_{1-y}Sn_y$ for each heterostructure was calculated. The average growth rate for partially relaxed $Ge_{1-y}Sn_y$ was estimated at 5.0 nm/min, 4.5 nm/min and 4.2 nm/min for Figure 8.8 (a), (b) and (c), respectively. These values are lower than expected compared to the results given in chapter 7, Figure 7.5 and Figure 7.6 on pages 92 and 93. This is simply because growth of $Ge_{1-y}Sn_y$ was impossible for all $SnCl_4/GeH_4$ ratios, and therefore no $Ge_{1-y}Sn_y$ was grown when $SnCl_4$-H_2 was in an unacceptable range.

Finally, X-TEM micrographs were used to investigate the quality of layers in heterostructures as shown in Figure 8.8. As shown in the X-TEM lattice resolution in Figure 8.11, a smooth surface was achieved when grading was used. However, the grading has a negative impact on the interface between graded $Ge_{1-y}Sn_y$ and Ge-VS. This is because when $SnCl_4$ starts to tune from its lowest level of 5 sccm, very low Ge can be produced, which leads to almost no growth. Similarly, because there is too much Sn on the surface, segregation could occur at some points, as discussed in chapter 4.

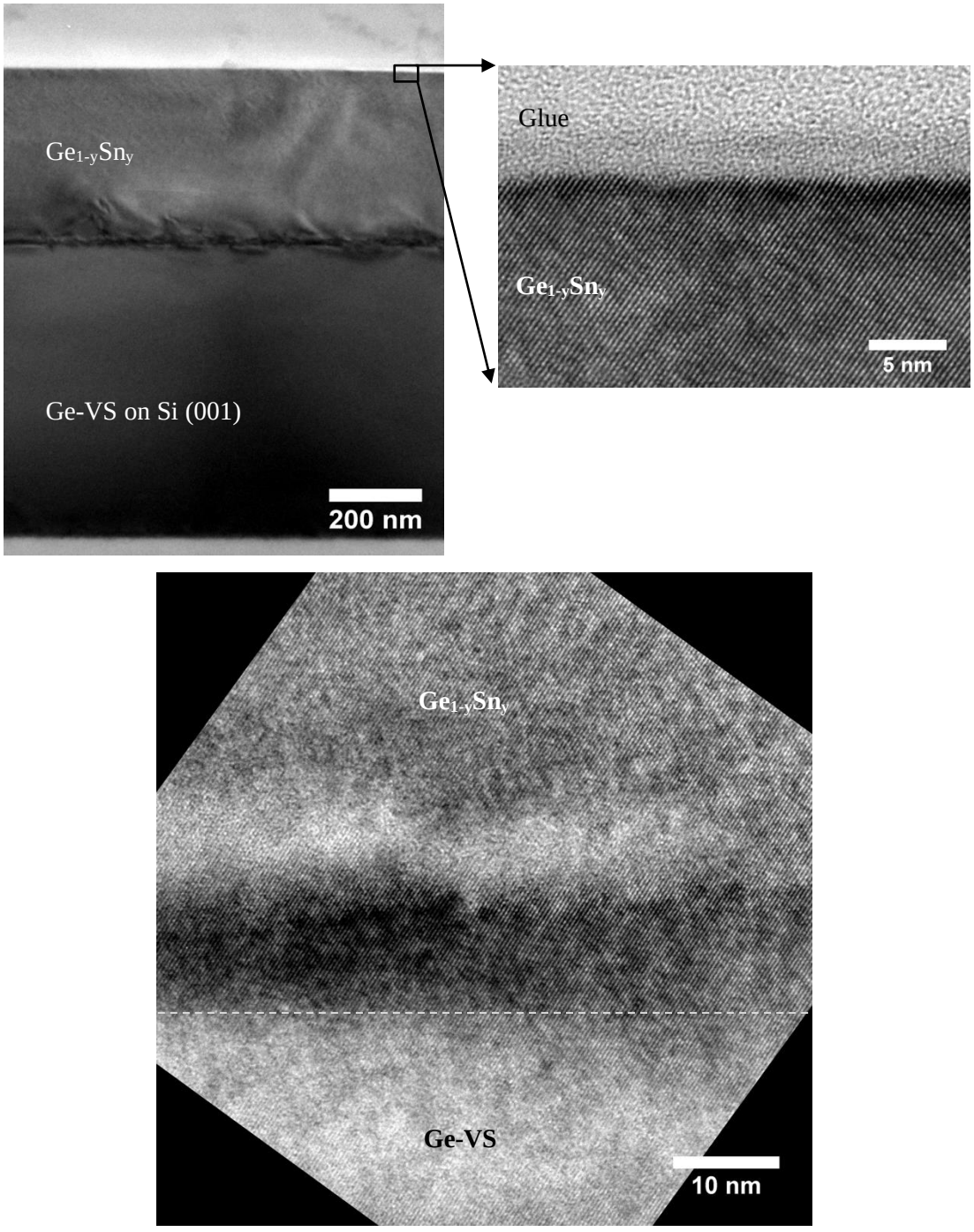

Figure 8.11 X-TEM micrographs of $Ge_{1-y}Sn_y$\Graded-$Ge_{1-y}Sn_y$\Ge-VS\Si (001) heterostructure in which its $Ge_{1-y}Sn_y$ was grown for 70:00 min (50:00 min varied $SnCl_4$-H_2 and 20:00 min fixed $SnCl_4$-H_2) which its schematic cross sectional is given in Figure 8.8 (c). Left: X-TEM using ST diffraction condition. The thickness of total $Ge_{1-y}Sn_y$ grown is measured at ~350 nm with Ge-VS at 0.66 µm. Right: Smooth surface is evident with lattice resolution using high resolution ST diffraction condition. Bottom: Lattice resolution of Graded-$Ge_{1-y}Sn_y$\Ge-VS interface using ST diffraction condition. When tuning $SnCl_4$, it is obvious that some layers with high defects due to too much Sn are formed, but gradually appropriate crystalline $Ge_{1-y}Sn_y$ is grown when the right $SnCl_4$/GeH_4 ratio is reached.

8.5.2 Surface Morphology of $Ge_{1-y}Sn_y$ Epilayers Grown on Graded $Ge_{1-y}Sn_y$

AFM scans of $Ge_{1-y}Sn_y$\Graded-$Ge_{1-y}Sn_y$\Ge-VS\Si (001) heterostructures which are given in Figure 8.8, are presented in Figure 8.12. Considering the studies of surface morphology and the X-TEM lattice resolution micrographs of the surface of $Ge_{1-y}Sn_y$ epilayers, it is clear that a smooth surface could be achieved when the grading technique is used.

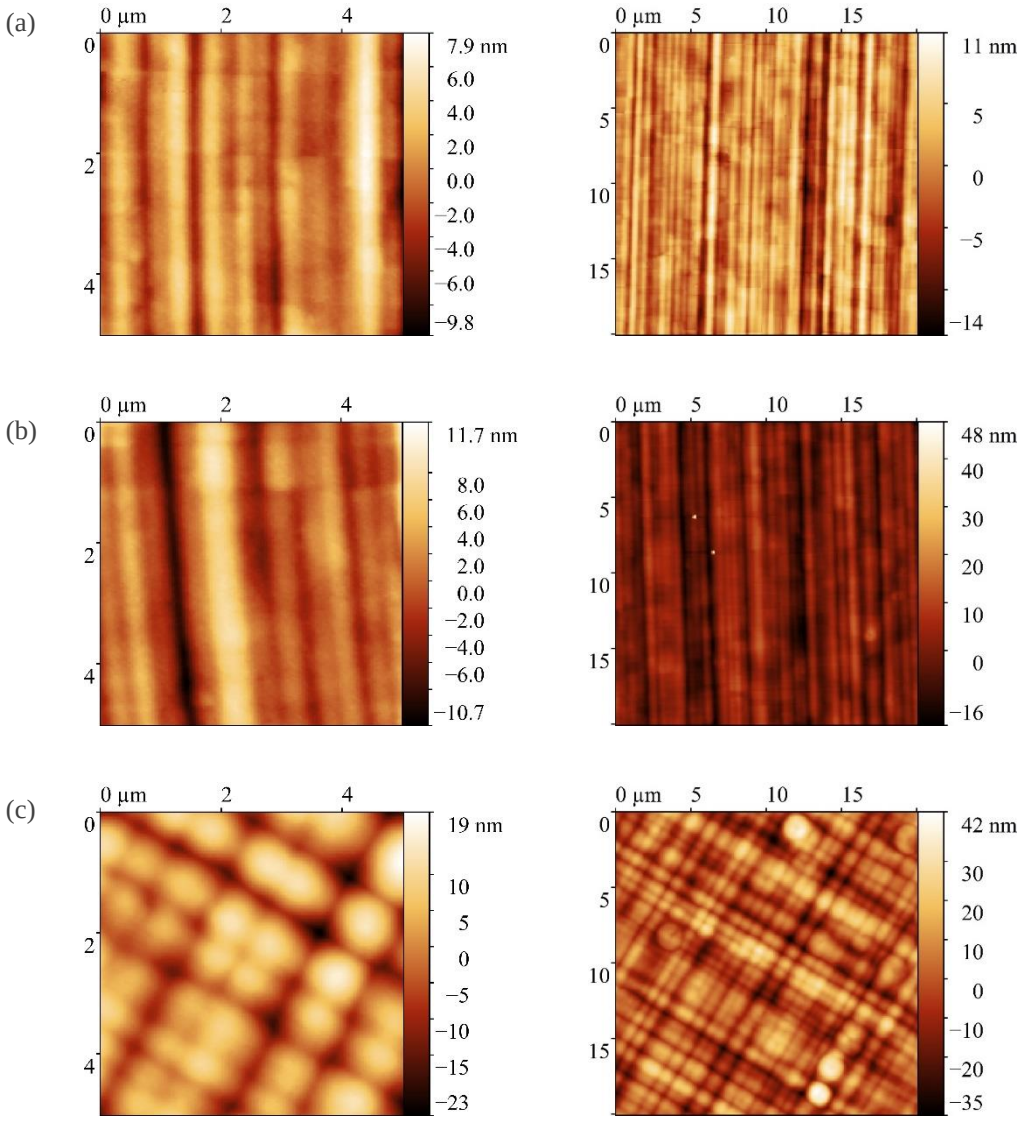

Figure 8.12 AFM scans of $Ge_{1-y}Sn_y$\Graded-$Ge_{1-y}Sn_y$\Ge-VS\Si (001) heterostructures shown in Figure 8.8. Top: RMS of ~4 nm for heterostructure, in which graded $Ge_{1-y}Sn_y$ was grown for 10:00 min. Middle: RMS of ~5 nm for heterostructure, in which graded $Ge_{1-y}Sn_y$ was grown for 30:00 min. Bottom: RMS of ~12 nm for heterostructure, in which graded $Ge_{1-y}Sn_y$ was grown for 50:00 min. To measure each RMS, corresponding 20µm×20µm AFM scan was considered.

By measuring surface roughness (RMS) values for these heterostructures, a summary plot was produced, as shown in Figure 8.13. Considering the results, it is possible to investigate the effect of the growth time of the graded $Ge_{1-y}Sn_y$ epilayers on the surface roughness of the following $Ge_{1-y}Sn_y$ epilayers grown above them. As the growth time of the graded $Ge_{1-y}Sn_y$ epilayer in the heterostructures increases, the surface roughness of the following $Ge_{1-y}Sn_y$ grown above it increases significantly. This is probably solely because of the Sn segregation, which is due to strain relaxation that is occurred as a consequence of an increase in thickness.

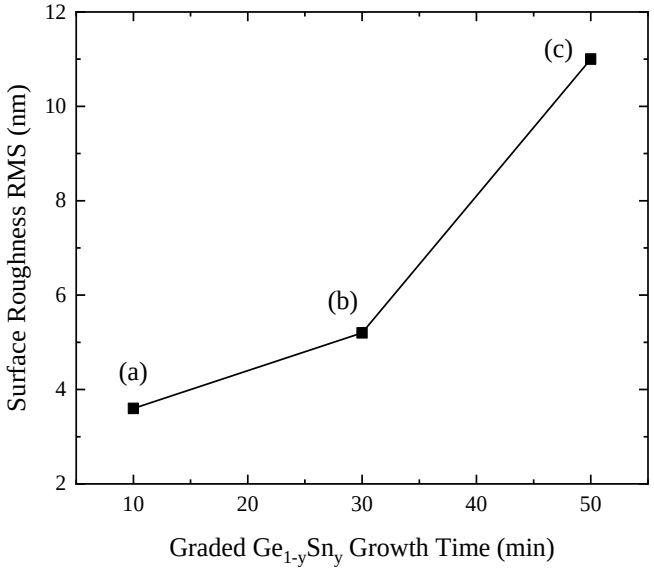

Figure 8.13 Surface roughness of $Ge_{1-y}Sn_y$\Graded-$Ge_{1-y}Sn_y$\Ge-VS\Si (001) heterostructures shown in Figure 8.8. The effect of the growth time of the graded $Ge_{1-y}Sn_y$ epilayers on the surface roughness of the following $Ge_{1-y}Sn_y$ epilayers grown above them. Corresponding HR-XRD ω-2θ coupled scans and symmetric and asymmetric RSMs are shown in Figure 8.9 and Figure 8.10, respectively.

8.6 Conclusion

The grading technique, in which $SnCl_4$-H_2 (or $SnCl_4/GeH_4$ ratio) is tuned during the growth of $Ge_{1-y}Sn_y$, was performed at pressure of 500 Torr and two different temperatures of 280 °C and 260 °C. The effect of the grading technique on the quality of the graded $Ge_{1-y}Sn_y$ was investigated. It was shown how the grading technique enabled the growth of thick $Ge_{1-y}Sn_y$ by suppressing Sn segregation at a lower growth temperature of 260 °C. It should also be noted that the thickness of $Ge_{1-y}Sn_y$ was lower when using the grading technique than when fixed $SnCl_4$-H_2 was used. This is because not all values for the $SnCl_4/GeH_4$ ratio are allowed at a given growth temperature (shown in Figure 6.6 on page 80). This also means that during the growth of $Ge_{1-y}Sn_y$ using the grading technique, no growth was achieved, and all precursors were wasted when the $SnCl_4/GeH_4$ ratio was at unacceptable value during the growth.

The effect of the graded $Ge_{1-y}Sn_y$ (as an intermediate layer) on the quality and growth of the following $Ge_{1-y}Sn_y$ grown above it was also examined. Higher quality $Ge_{1-y}Sn_y$ with a smoother surface (low surface roughness) was achieved with the grading technique than with fixed $SnCl_4$-H_2. Furthermore, the grading technique was not found useful to improve the quality of the interface between Ge-VS and $Ge_{1-y}Sn_y$, as shown in Figure 8.11 (bottom).

Further research is proposed to investigate the mechanism of grading technique when growing $Ge_{1-y}Sn_y$ epilayers in more detail. For example, how it supports suppressing segregation during the growth of $Ge_{1-y}Sn_y$, the effect of the technique at other growth temperatures and pressures, how its growth rate behaves and changes during the growth of $Ge_{1-y}Sn_y$, and how it influences the h_c in which strain relaxation begins.

Chapter 9

Epitaxial Growth of Doped $Ge_{1-y}Sn_y$ Epilayers

9.1 Introduction

In this chapter, attempt of doping $Ge_{1-y}Sn_y$ binary alloys is investigated. Doped $Ge_{1-y}Sn_y$ epilayers offer more flexibility to control physical, electrical, and optical properties over ordinary $Ge_{1-y}Sn_y$ binary alloys. The ability to carefully control the incorporation of dopant into $Ge_{1-y}Sn_y$ binary alloys is essential for the development of efficient and effective nanoelectronic devices, such as TFETs and MOSFETs, as well as optoelectronic devices, such as LASER diodes and LEDs. In this chapter, the incorporation of Si into $Ge_{1-y}Sn_y$ (as known as $Ge_{1-x-y}Si_xSn_y$) is also investigated. Many precursors have previously been used to achieve doped $Ge_{1-y}Sn_y$, such as $P(SiH_3)_3$, $P(GeH_3)_3$, PH_3, $As(SiH_3)_3$, and B_2H_6 [100,120,177-180]. However, in this research, only two precursors were used: B_2H_6 was used to achieve B doped $Ge_{1-y}Sn_y$, and PH_3 was used to achieve n-type $Ge_{1-y}Sn_y$ binary alloys.

Furthermore, attempt of epitaxial growth of $Ge_{1-x-y}Si_xSn_y$ ternary alloys was investigated. Compared to $Ge_{1-y}Sn_y$, a substantially greater incorporation of Sn into $Ge_{1-x-y}Si_xSn_y$ epilayer is therefore required to achieve indirect-to-direct bandgap transition [10]. Incorporation of Si into $Ge_{1-y}Sn_y$ epilayers not only improves the physical properties of the epilayers, but also influences their optical and electrical properties, which can be used for device fabrications. As incorporation of Si into $Ge_{1-y}Sn_y$ epilayers leads to a faster increase in bandgap at the Γ-point compared to that at the L-point, the indirect-to-direct bandgap transition in $Ge_{1-x-y}Si_xSn_y$ mostly depends on the concentration of Si rather than Sn [10].

9.2 Attempt of Heteroepitaxial Growth of P-type or N-type $Ge_{1-y}Sn_y$ Epilayers

9.2.1 B Doped $Ge_{1-y}Sn_y$

Fully strained B doped $Ge_{1-y}Sn_y$\Ge-VS\Si (001) heterostructures were attempt to grown for 3:00 min at temperature of 260 °C and pressure of 500 Torr using B_2H_6 and 3.33×10^{-3} $SnCl_4/GeH_4$ ratio. Three levels of B_2H_6 flow were considered: 0.19 ADC, 25.46 ADC, and 200 ADC. Here, the ADC unit is used to convert the analogue signal from a mass flow controller into a digital signal that can be interpreted by the machine. This data is subsequently used to control the flow of precursors into the CVD chamber. HR-XRD ω-2θ coupled scans of B doped $Ge_{1-y}Sn_y$\Ge-VS\Si (001) epilayers are shown in Figure 9.1. The thickness of each B doped $Ge_{1-y}Sn_y$ was measured using thickness fringes that appeared in ω-2θ coupled scans. The Sn concentration of each of these B doped $Ge_{1-y}Sn_y$ epilayers was determined by symmetrical and asymmetrical RSMs.

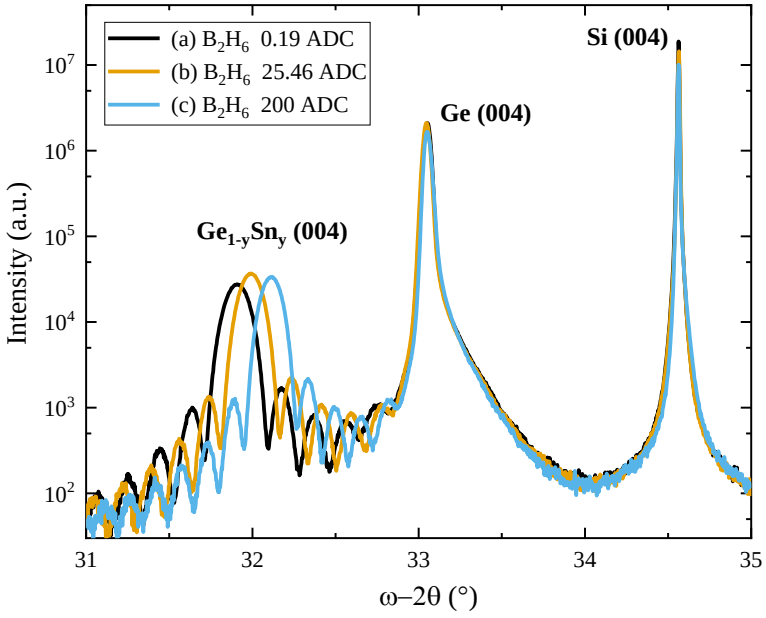

Figure 9.1 HR-XRD ω-2θ coupled scans of B doped $Ge_{1-y}Sn_y$ epilayers, which were grown for 3:00 min at temperature of 260 °C and pressure of 500 Torr using B_2H_6 and 3.33×10^{-3} $SnCl_4/GeH_4$. (a) 27 nm thick B doped $Ge_{0.884}Sn_{0.116}$\Ge-VS\Si (001), (b) 30 nm thick B doped $Ge_{0.894}Sn_{0.106}$\Ge-VS\Si (001), and (c) 33 nm thick B doped $Ge_{0.905}Sn_{0.095}$\Ge-VS\Si (001).

At first glance, the apparent shift in the $Ge_{1-y}Sn_y$ epilayers peaks in HR-XRD ω-2θ coupled scans seems to be due to the incorporation of B dopant into the epilayers. However, by careful consideration of the thicknesses of $Ge_{1-y}Sn_y$ epilayers, all of which were grown for 3:00 min, different growth rates were observed. In previous chapters, it has been shown how the growth rate can influence Sn concentration in $Ge_{1-y}Sn_y$ epilayers. In general, with increases in the growth rate of $Ge_{1-y}Sn_y$ epilayers, the Sn concentration should be reduced accordingly. The effect of B_2H_6 on the growth of $Ge_{1-y}Sn_y$ epilayers is shown in Figure 9.2; the growth rate for B doped $Ge_{1-y}Sn_y$ epilayers increases with the increase in the flow of B_2H_6, and therefore the Sn concentration decreases.

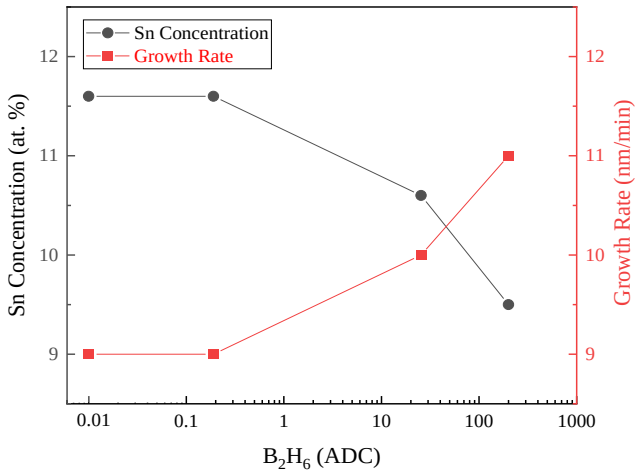

Figure 9.2 Effect of B_2H_6 precursor on the growth of $Ge_{1-y}Sn_y$ epilayers, which were grown at temperatures of 260 °C and pressure of 500 Torr using 3.33×10^{-3} $SnCl_4/GeH_4$. Precise B_2H_6 used during the growth of these epilayers: 0 ADC, 0.19 ADC, 25.46 ADC, and 200 ADC.

It may seem that Sn is replaced by B in $Ge_{1-y}Sn_y$ epilayers; As B_2H_6 increases, the incorporation of B into $Ge_{1-y}Sn_y$ increases, while the Sn incorporation decreases. However, a better explanation can be given by taking into account both Sn concentration and growth rate simultaneously, as shown in previous chapters, how closely these two are linked. As B_2H_6 increases, the growth rate increases, which (probably) led to a reduction in Sn concentration in $Ge_{1-y}Sn_y$ epilayers. As we have already seen, the growth rate depends closely on the Ge adatoms, which means how many Ge atoms are produced in the CVD chamber, while the Sn concentration normally depends on the growth temperature. It seems that the presence of B_2H_6 can support Ge production during the growth, yet it is difficult to simply conclude this solely on the plot given in Figure 9.2. This could only be true if the amount Sn adatoms remains the same as B_2H_6 increases, and its presence does not affect Sn production.

9.2.2 P Doped $Ge_{1-y}Sn_y$ ($Ge_{1-y}Sn_y$ with n-doping)

Similarly, fully strained P doped $Ge_{1-y}Sn_y$\Ge-VS\Si (001) heterostructures were grown for 3:00 min at temperature of 260 °C and pressure of 500 Torr using PH_3 and 3.33×10^{-3} $SnCl_4/GeH_4$. Three levels of PH_3 flow were considered: 0.19 ADC, 25.46 ADC, and 200 ADC. HR-XRD ω-2θ coupled scans of P doped $Ge_{1-y}Sn_y$\Ge-VS\Si (001) epilayers are shown in Figure 9.3. The thickness of each P doped $Ge_{1-y}Sn_y$ was measured using thickness fringes that appeared in ω-2θ coupled scans. The Sn concentration of each of these P doped $Ge_{1-y}Sn_y$ epilayers was determined by symmetrical and asymmetrical RSMs.

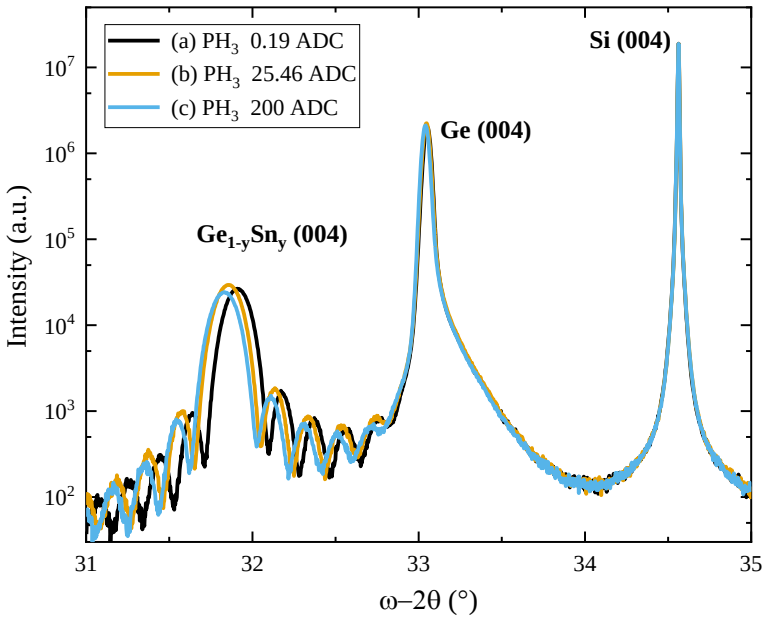

Figure 9.3 HR-XRD ω-2θ coupled scans of P doped $Ge_{1-y}Sn_y$ epilayers, which were grown for 3:00 min at temperature of 260 °C and pressure of 500 Torr using PH_3 and 3.33×10^{-3} $SnCl_4/GeH_4$. (a) 27 nm thick $Ge_{0.884}Sn_{0.116}$\Ge-VS\Si (001), (b) 27 nm thick $Ge_{0.881}Sn_{0.119}$\Ge-VS\Si (001), and (c) 27 nm thick $Ge_{0.878}Sn_{0.122}$\Ge-VS\Si (001).

Unlike the case of B doped $Ge_{1-y}Sn_y$ epilayers, there is a negligible shift in the $Ge_{1-y}Sn_y$ epilayers peaks in HR-XRD ω-2θ coupled scans. The thicknesses of $Ge_{1-y}Sn_y$ epilayers, all of which were grown for 3:00 min, are the same: ~27 nm, representing the same growth rate of approximately 9 nm/min for all P doped $Ge_{1-y}Sn_y$ epilayers. Therefore, the slight apparent shift in the $Ge_{1-y}Sn_y$ epilayers peaks in HR-XRD ω-2θ coupled scans could only be due to the slight change in Sn concentration or perhaps the incorporation of P dopant into the epilayers. As shown in Figure 9.4, the growth rate for P doped $Ge_{1-y}Sn_y$ epilayers remains constant with the

increase in flow of PH_3, but the Sn concentration calculated from HR-XRD ω-2θ coupled scans and symmetrical and asymmetric RSMs increases slightly, in the range of 0.1 at.%.

It has been explained in earlier chapters that the growth rate of $Ge_{1-y}Sn_y$ is mainly determined by the production of Ge adatoms during the CVD growth. As shown in Figure 9.4, since the growth rate of the P doped $Ge_{1-y}Sn_y$ epilayers is constant and does not depend on the flow of PH_3, it can be concluded that the presence of PH_3 does not affect the production of Ge adatoms.

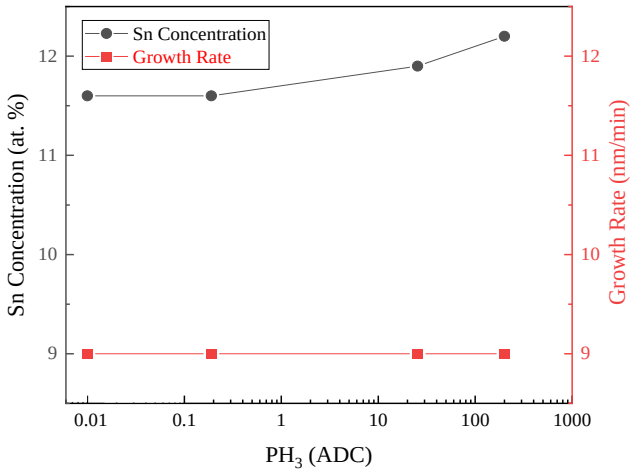

Figure 9.4 Effect of PH_3 precursor on the growth of $Ge_{1-y}Sn_y$ epilayers, which were grown at temperatures of 260 °C and pressure of 500 Torr using 3.33×10^{-3} $SnCl_4/GeH_4$. Precise PH_3 used during the growth of these epilayers: 0 ADC, 0.19 ADC, 25.46 ADC, and 200 ADC.

It should also be noted that the use of 0.19 ADC of PH_3 in a similar way to the use of 0.19 ADC of B_2H_6 has no influence on the growth of $Ge_{1-y}Sn_y$ epilayers. On both Figure 9.2 and Figure 9.4 we can see that when 0.19 ADC of B_2H_6 or PH_3 was used, the same $Ge_{1-y}Sn_y$ in terms of Sn concentration and growth rate as the intrinsic $Ge_{1-y}Sn_y$ epilayer (when no B_2H_6 or PH_3 were used) was achieved.

9.2.3 Surface Morphology of B or P Doped $Ge_{1-y}Sn_y$

AFM scans of intrinsic, B doped and P doped $Ge_{1-y}Sn_y$ which were grown on Si (001) via relaxed Ge-VS in RP-CVD are shown in Figure 9.5. AFM scans of highly doped $Ge_{1-y}Sn_y$ are presented for a better investigation of the effect of dopant incorporation on the surface of epilayers.

All $Ge_{1-y}Sn_y$ epilayers were grown for 3:00 min at temperature of 260 °C and pressure of 500 Torr using 3.33×10^{-3} $SnCl_4/GeH_4$. Their respective HR-XRD ω-2θ coupled scans are

shown in Figure 9.1 and Figure 9.3. As it can be seen in AFM scans shown in Figure 9.5, the surface quality of both B doped and P doped $Ge_{1-y}Sn_y$ epilayers remained high and RMS for each of them remained as low as ~1 nm. On the surface of the grown doped $Ge_{1-y}Sn_y$ epilayers, no Sn segregation or Sn-rich islands or surface defects were observed.

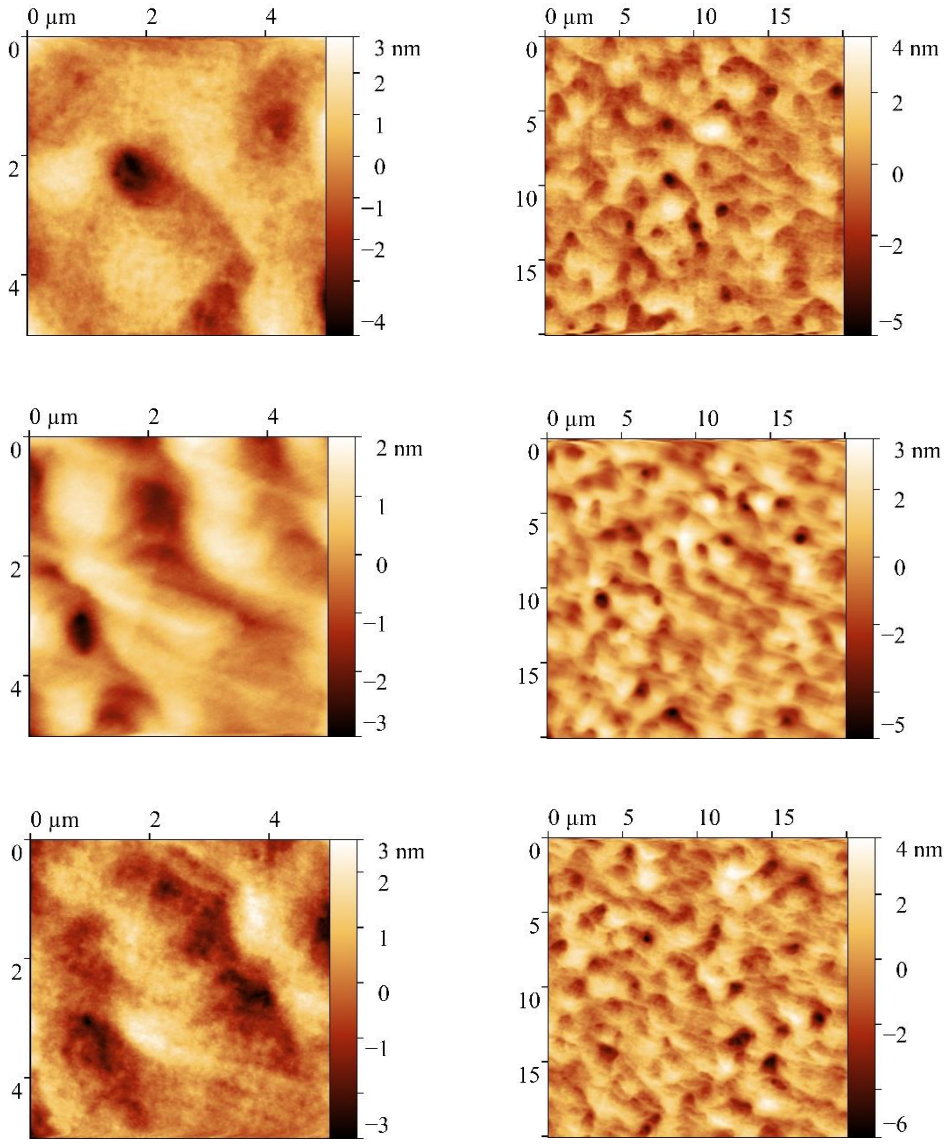

Figure 9.5 AFM scans of intrinsic, B and P doped $Ge_{1-y}Sn_y$ which were grown on Si (001) via relaxed Ge-VS in RP-CVD. Their respective HR-XRD ω-2θ coupled scans are shown in Figure 9.1 and Figure 9.3. All $Ge_{1-y}Sn_y$ epilayers were grown for 3:00 min at temperature of 260 °C and pressure of 500 Torr using 3.33×10^{-3} $SnCl_4/GeH_4$. Top: AFM scans of fully strained intrinsic-$Ge_{0.884}Sn_{0.116}$\Ge-VS\Si (001) with RMS = 1.0 nm. Middle: AFM scans of fully strained B doped $Ge_{0.905}Sn_{0.095}$\Ge-VS\Si (001) with RMS = 1.1 nm. Bottom: AFM scans of fully strained P doped $Ge_{0.878}Sn_{0.122}$\Ge-VS\Si (001) with RMS = 1.1 nm. All these AFM scans were taken in tapping mode. AFM scans of highly doped $Ge_{1-y}Sn_y$ are presented for a better investigation of the effect of dopant incorporation on the surface of epilayers.

The surface roughness of all doped $Ge_{1-y}Sn_y$ epilayers has remained low with RMS of ~1 nm. As seen in Figure 9.6 incorporation of B or P dopants into $Ge_{1-y}Sn_y$ epilayer does not have any adverse effect on its surface roughness.

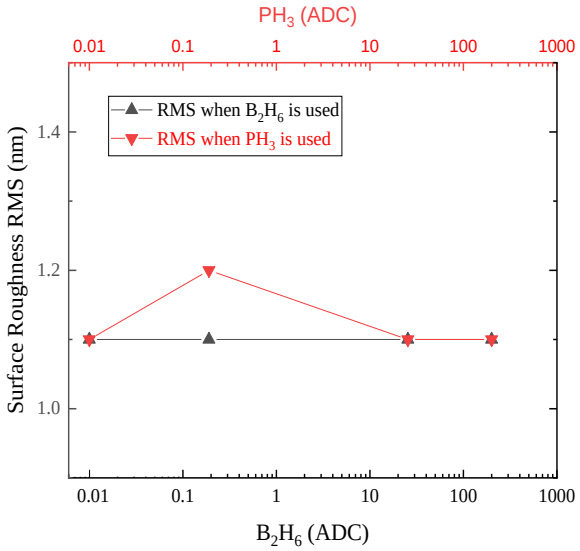

Figure 9.6 Surface roughness of the intrinsic, B doped, and P doped $Ge_{1-y}Sn_y$ grown on Si (001) substrate via Ge-VS. Their respective HR-XRD ω-2θ coupled scans are shown in Figure 9.1 and Figure 9.3. All $Ge_{1-y}Sn_y$ epilayers were grown for 3:00 min at temperature of 260 °C and pressure of 500 Torr using 3.33×10^{-3} $SnCl_4/GeH_4$.

9.3 $Ge_{1-x-y}Si_xSn_y$ Epilayers

In this section, growth of $Ge_{1-x-y}Si_xSn_y$ epilayers was investigated. Incorporation of Si into $Ge_{1-y}Sn_y$ epilayers not only improves the physical properties of the epilayers, but also influences their optical and electrical properties, which can be used for device fabrication. Si_2H_6 was used as Si precursor.

Figure 9.7 shows the cross sectional schematic structure of the layers that are epitaxially grown in CVD. All $Ge_{1-x-y}Si_xSn_y$ epilayers were grown on Si (001) via 0.7 µm relaxed Ge-VS at growth pressure of 500 Torr with growth time of 8:00 min and 70 sccm of $SnCl_4$ in combination with GeH_4. However, two different growth temperatures of 260 °C and 280 °C were used to study the effects of Si precursor and Si incorporation on epitaxial growth of $Ge_{1-x-y}Si_xSn_y$ epilayers.

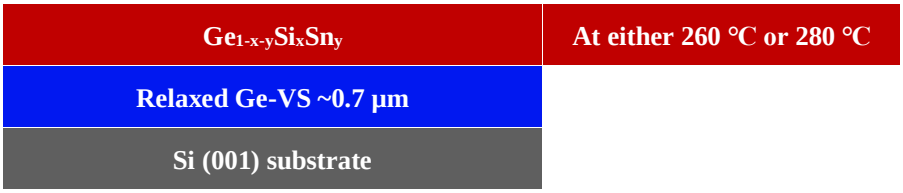

Figure 9.7 Cross sectional schematic diagram of the $Ge_{1-x-y}Si_xSn_y$ epilayer grown at either 260 °C or 280 °C on Si (001) via 0.7 µm relaxed Ge-VS at growth pressure of 500 Torr with 70 sccm of $SnCl_4$ in combination with GeH_4 with growth time of 8:00 min.

Two $Ge_{1-y}Sn_y$ epilayers were grown under the same growth conditions as those $Ge_{1-x-y}Si_xSn_y$ epilayers. In Figure 9.8, the HR-XRD ω-2θ coupled scans of these two $Ge_{1-y}Sn_y$ are shown. As expected, higher Sn incorporation into $Ge_{1-y}Sn_y$ and lower growth rate were achieved at lower temperatures. At growth temperature of 260 °C, $Ge_{0.89}Sn_{0.11}$ was achieved with growth rate of ~12 nm/min. On the other hand, at a growth temperature of 280 °C, $Ge_{0.92}Sn_{0.08}$ was achieved with growth rate of ~16 nm/min. Both $Ge_{1-y}Sn_y$ epilayers are fully strained, and their thicknesses were estimated from thickness fringes that appeared around the $Ge_{1-y}Sn_y$ peak on HR-XRD ω-2θ coupled scans.

Epitaxial growth of $Ge_{1-x-y}Si_xSn_y$ epilayers on Si (001) via ~0.7 µm thick relaxed Ge-VS was investigated at two growth temperatures of 260 °C and 280 °C, under the same CVD growth conditions used to grow $Ge_{1-y}Sn_y$ epilayers shown in Figure 9.8. The only CVD condition that was used differently for epitaxial growth of $Ge_{1-x-y}Si_xSn_y$ epilayers was the growth time.

$Ge_{1-x-y}Si_xSn_y$ epilayers were grown for 8:00 min instead of 4:00 min. At each growth temperature, three different Si_2H_6 partial flows were used to explore the effects of Si_2H_6 flow on Si incorporation and the growth of the epilayers.

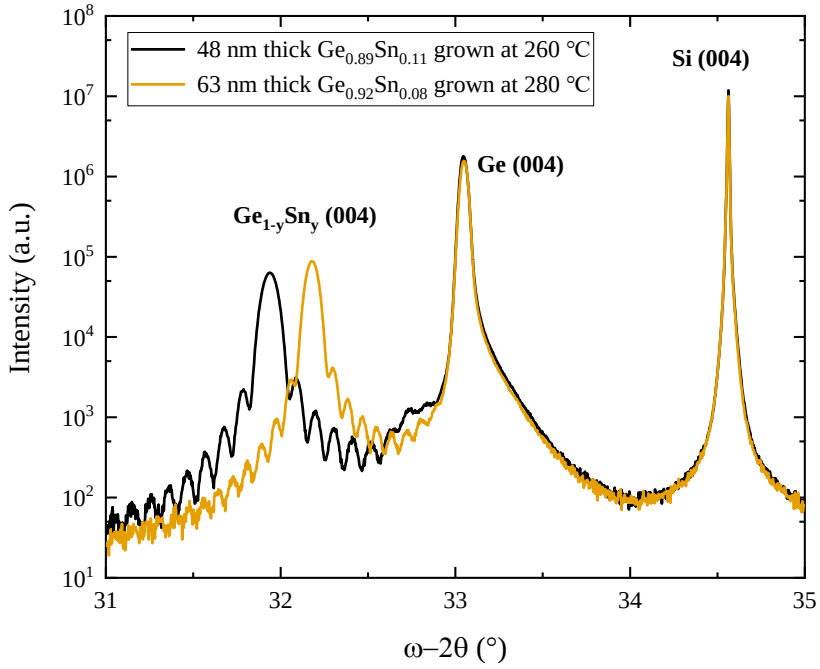

Figure 9.8 HR-XRD ω-2θ coupled scans for $Ge_{1-y}Sn_y$ grown at either 260 °C or 280 °C on Si (001) via a 0.7 µm thick relaxed Ge-VS at pressure of 500 Torr using 70 sccm of $SnCl_4$ in combination with GeH_4 with growth time of 4:00 min. These two $Ge_{1-y}Sn_y$ epilayers were grown under the same growth conditions as those $Ge_{1-x-y}Si_xSn_y$ epilayers.

Figure 9.9 shows three $Ge_{1-x-y}Si_xSn_y$ epilayers grown at 280 °C with 0.7, 1.5, and 2.0 sccm Si_2H_6. As shown in the figure, the $Ge_{1-x-y}Si_xSn_y$ epilayer grown with 0.7 sccm Si_2H_6 has the same peak as the $Ge_{1-y}Sn_y$ grown at this temperature, as shown in Figure 9.8. Thickness fringes disappeared due to longer growth time and strain relaxation of the epilayer. At first glance, it seems as a consequence of Si incorporation, there is no change in the $Ge_{1-y}Sn_y$ peak. The peak responsible for $Ge_{1-x-y}Si_xSn_y$ did not move towards the Si peak, but this cannot simply be concluded by looking at the HR-XRD ω-2θ coupled scan. This is because the incorporation of Sn can shift the peak to the left and cancel the shift made because of Si, thereby effectively keeping the peak at the same point.

Moreover, for $Ge_{1-x-y}Si_xSn_y$ epilayers grown with higher Si_2H_6 at 280 °C, there is a very slight shift in primary $Ge_{1-x-y}Si_xSn_y$ peak at ~32°, as shown in Figure 9.9. The shoulders appeared next to the peak of Ge may be due to the $Ge_{1-x-y}Si_xSn_y$ layers with low Sn concentration close

to solubility of Sn into Ge. These shoulders could also be due to the very high incorporation of Si into $Ge_{1-x-y}Si_xSn_y$, which should be confirmed by measuring the Si and Sn concentration of these epilayers. HR-XRD ω-2θ coupled scan of relaxed Ge grown on Si (001) is provided as a reference.

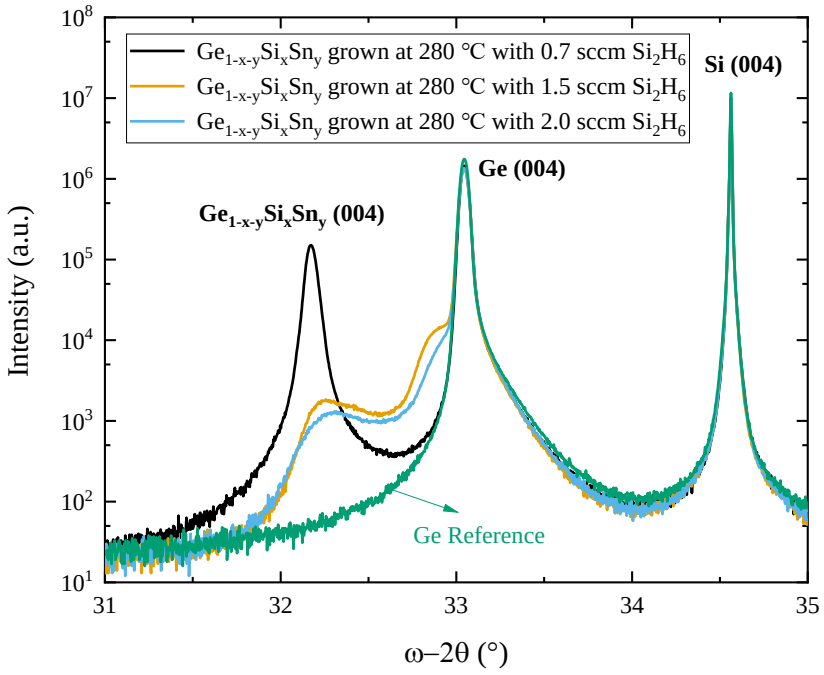

Figure 9.9 HR-XRD ω-2θ coupled scans for $Ge_{1-x-y}Si_xSn_y$ grown on Si (001) via a relaxed Ge-VS at temperature of 280 °C and pressure of 500 Torr using 70 sccm of $SnCl_4$ in combination with GeH_4 with growth time of 8:00 min.

Similarly, Figure 9.10 shows three $Ge_{1-x-y}Si_xSn_y$ epilayers grown at a lower temperature of 260 °C with the same Si_2H_6 partial pressure of 0.7, 1.5, and 2.0 sccm. The $Ge_{1-x-y}Si_xSn_y$ epilayer grown with 0.7 sccm Si_2H_6, unlike the one grown at 280 °C, follows the similar behaviour of those grown with 1.5 and 2.0 sccm Si_2H_6. For each of the $Ge_{1-x-y}Si_xSn_y$ epilayers grown at 260 °C, there is a clear shift in peak around $Ge_{1-y}Sn_y$, as shown in Figure 9.10. In addition, the shoulders appeared next to the peak of Ge may be due to the $Ge_{1-x-y}Si_xSn_y$ layers with low Sn concentration close to the solubility of Sn into Ge.

It should be noted that Sn and Si concentrations of $Ge_{1-x-y}Si_xSn_y$ cannot be measured from HR-XRD ω-2θ coupled scans or symmetric or asymmetric RSMs. This is because incorporation of Si shifts the $Ge_{1-x-y}Si_xSn_y$ peak to the right, while incorporation of Sn shifts the $Ge_{1-x-y}Si_xSn_y$ peak to the left. This means that different combinations of Sn and Si concentrations in the $Ge_{1-x-y}Si_xSn_y$ epilayer can have the same peak at the same ω-2θ (°).

Therefore, XPS was used to measure Si and Sn concentrations in the grown $Ge_{1-x-y}Si_xSn_y$ epilayers.

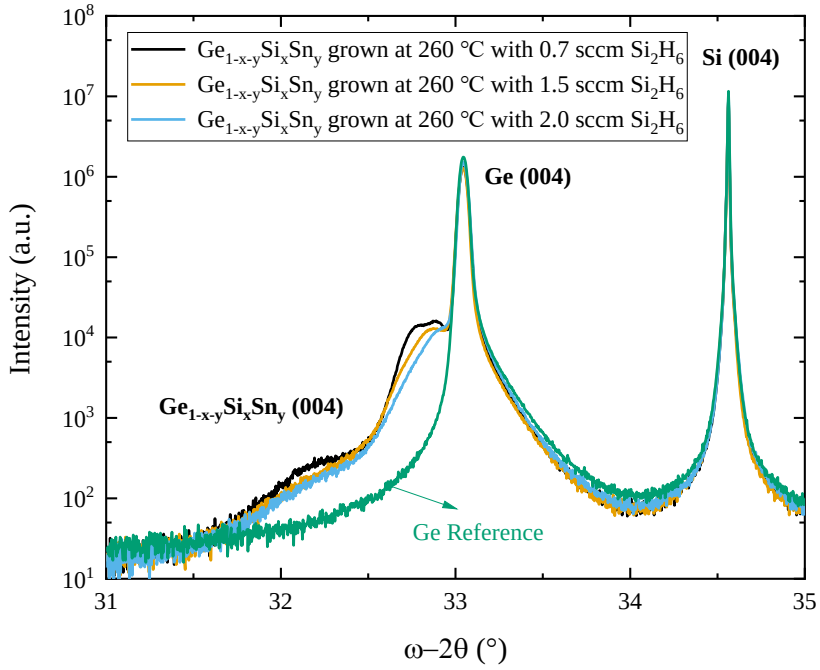

Figure 9.10 HR-XRD ω-2θ coupled scans for $Ge_{1-x-y}Si_xSn_y$ grown on Si (001) via a relaxed Ge-VS at temperature of 260 °C and pressure of 500 Torr using 70 sccm of $SnCl_4$ in combination with GeH_4 with growth time of 8:00 min.

Three $Ge_{1-x-y}Si_xSn_y$ epilayers were selected for the XPS study. One was $Ge_{1-x-y}Si_xSn_y$ which was grown at 260 °C with 0.7 sccm Si_2H_6. Other two $Ge_{1-x-y}Si_xSn_y$ grown at 260 °C with higher Si_2H_6 partial pressure have similar HR-XRD ω-2θ coupled scans which were therefore disregarded from XPS measurements. The other two $Ge_{1-x-y}Si_xSn_y$ considered for XPS measurements were grown at 280 °C with 0.7 and 1.5 sccm Si_2H_6. The other $Ge_{1-x-y}Si_xSn_y$ epilayer grown at 280 °C with 2.0 sccm Si_2H_6, which has similar HR-XRD ω-2θ coupled scan as the one grown with 1.5 sccm Si_2H_6, was excluded.

The XPS measurements of these $Ge_{1-x-y}Si_xSn_y$ epilayers in the range of 499 eV to 483 eV are shown in Figure 9.11. An example of background noise is provided in each figure. For each $Ge_{1-x-y}Si_xSn_y$, the Sn amount on the epilayer after ~10 nm etching was estimated using the XPS spectra of the Sn $3d_{3/2}$ and Sn $3d_{5/2}$. As expected, no SnO_x was detected after the etching. The Sn amount detected on the surface could be misleading, as it could be due to Sn segregation on the surface of the $Ge_{1-x-y}Si_xSn_y$ epilayer. Because of this, the $Ge_{1-x-y}Si_xSn_y$ epilayer was etched for ~10 nm and the XPS measurement was performed shortly after.

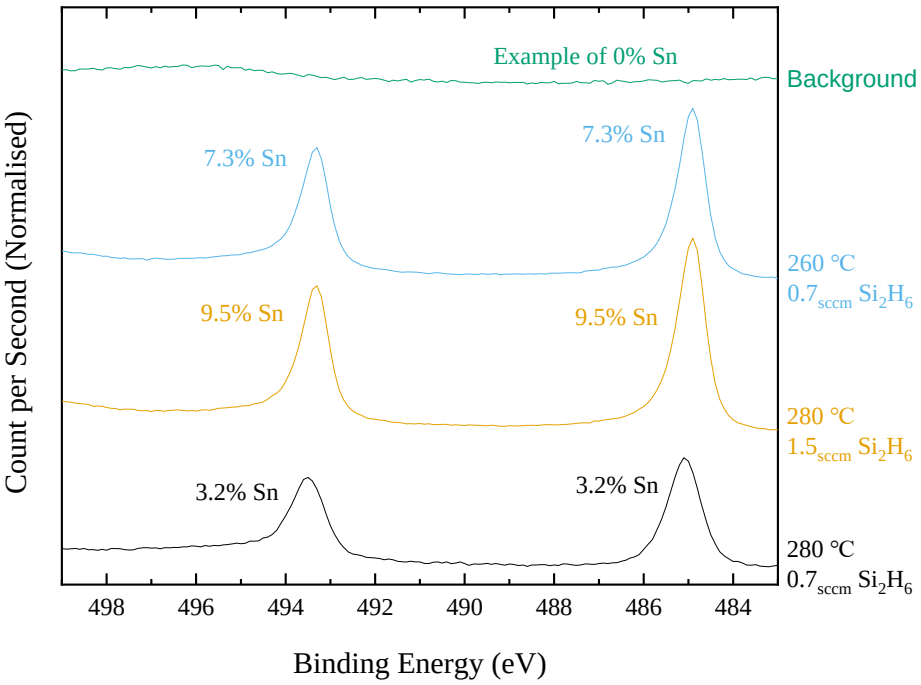

Figure 9.11 XPS spectra of the Sn: $3d_{3/2}$ (left Sn peak) and $3d_{5/2}$ (right Sn peak). The measurements were performed using Monochromated Al Kα XPS after etching the $Ge_{1-x-y}Si_xSn_y$ epilayer for ~10 nm. An example of background is given as a reference.

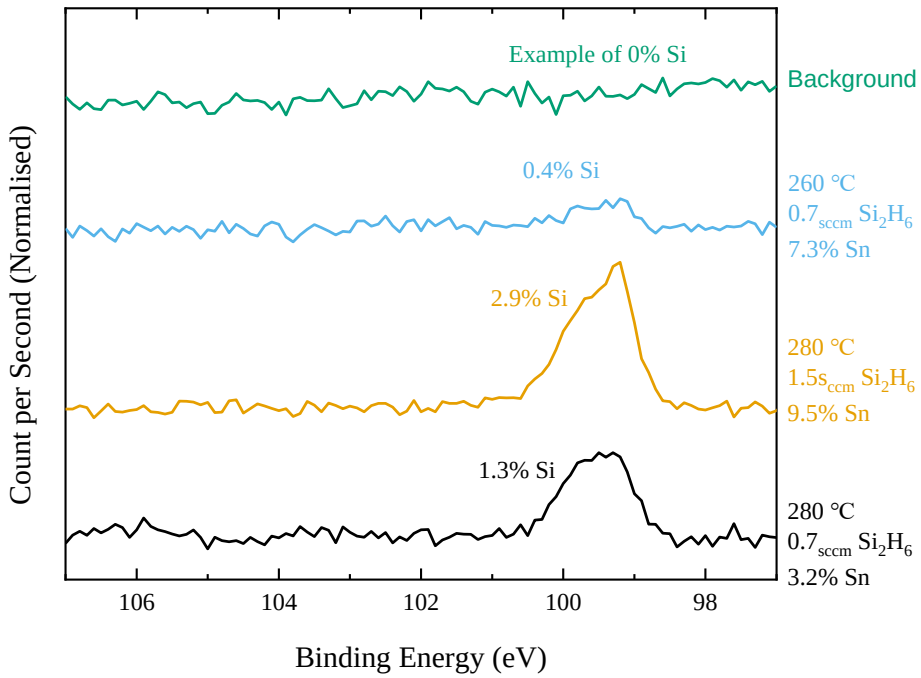

Figure 9.12 XPS spectra of the Si: 2p. The measurements were performed using Monochromated Al Kα XPS after etching the $Ge_{1-x-y}Si_xSn_y$ epilayer for ~10 nm. An example of background is given as a reference.

As shown in Figure 9.11, the Sn concentration of $Ge_{1-x-y}Si_xSn_y$ epilayer grown at 260 ℃ with 0.7 sccm Si_2H_6 was estimated as 7.3 at.%. This is approximately ~4 at.% lower than the $Ge_{1-y}Sn_y$ epilayer, which was grown under the same CVD growth conditions, as shown in Figure 9.8. It seems that the presence of Si_2H_6 as a Si precursor reduced Sn incorporation into $Ge_{1-x-y}Si_xSn_y$ epilayer grown at 260 ℃. However, it should be noted that the amount of Sn could possibly be lower at deeper layers of the epilayer. In addition, the etching process could damage the layers and influence them in such a way that less Sn remains on the surface after the etching. Therefore, XPS measurements should only be used with each other, not with other measurements made by other techniques such as HR-XRD.

For $Ge_{1-x-y}Si_xSn_y$ epilayer grown at 280 ℃ with 0.7 sccm Si_2H_6, the presence of Si precursor significantly suppressed Sn incorporation. The amount of Sn after ~10 nm etching, as shown in Figure 9.11, was estimated at 3.2 at.%, which is ~5 at.% lower than the $Ge_{1-y}Sn_y$ epilayer, which was grown under the same CVD growth conditions, as shown in Figure 9.8. This is similar to the $Ge_{1-x-y}Si_xSn_y$ epilayer grown at 260 ℃ with 0.7 sccm Si_2H_6. It seems that the growth temperature does not change the effect of 0.7 sccm Si_2H_6 on the incorporation of Sn into epilayers. However, a different behaviour was observed for the $Ge_{1-x-y}Si_xSn_y$ epilayer grown at 280 °C with 1.5 sccm Si_2H_6. The increase in Si_2H_6 from 0.7 sccm to 1.5 sccm led to an increased Sn incorporation in the $Ge_{1-x-y}Si_xSn_y$ epilayer. Comparing $Ge_{1-x-y}Si_xSn_y$ grown at 280 °C with 1.5 sccm Si_2H_6 with the $Ge_{1-y}Sn_y$ epilayer grown at 280 °C, it is evident that ~2 at.% higher Sn incorporation was achieved due to the presence of Si precursor.

The XPS measurements of $Ge_{1-x-y}Si_xSn_y$ epilayers, as well as examples of background noise in the range of 107 eV to 97 eV are shown in Figure 9.12. For each $Ge_{1-x-y}Si_xSn_y$, the Si amount on the epilayer after ~10 nm etching was measured using the XPS spectra of the Si 2p. As expected, no SiO_2 was detected after the etching. The Si amount detected on the surface could be misleading, for instance as a result of diffusion or Sn segregation on the surface of $Ge_{1-x-y}Si_xSn_y$ epilayer. Because of this, the $Ge_{1-x-y}Si_xSn_y$ epilayer was etched for ~10 nm and the XPS measurement was performed afterwards, in a similar manner as presented previously.

Comparing $Ge_{1-x-y}Si_xSn_y$ epilayers grown with 0.7 sccm Si_2H_6 at two different temperatures of 260 ℃ and 280 ℃, it is clear that Si incorporation into $Ge_{1-x-y}Si_xSn_y$ epilayer increases with increasing growth temperature. However, there is an important assumption that the incorporation of Sn does not affect the incorporation of Si into the epilayer. These two

$Ge_{1-x-y}Si_xSn_y$ epilayers do not have the same Sn concentration, and to confirm the above conclusion, more experiments are required.

Finally, the comparison of $Ge_{1-x-y}Si_xSn_y$ epilayers, which were grown at 280 °C but with different Si_2H_6 partial pressure, shows that increasing partial pressure of Si precursor increases Si incorporation into $Ge_{1-x-y}Si_xSn_y$ epilayer. Approximately ~114 % increase in Si_2H_6 partial pressure increased the Si incorporation by ~223 %. As already mentioned, there is an important assumption that the incorporation of Sn does not affect the incorporation of Si in the epilayer. The two $Ge_{1-x-y}Si_xSn_y$ epilayers do not have the same Sn concentration, and to confirm the above conclusion, more studies are required.

9.4 Conclusion

In this chapter, doping $Ge_{1-y}Sn_y$ binary alloys were studied and presented. Two precursors were used: B_2H_6 was used to achieve B doped $Ge_{1-y}Sn_y$, and PH_3 was used to achieve P doped $Ge_{1-y}Sn_y$ binary alloys. The incorporation of B and P into $Ge_{1-y}Sn_y$ epilayers did not affect the quality of epilayers. However, they slightly influenced the Sn concentration and growth rate of the epilayers.

Since doped $Ge_{1-y}Sn_y$ epilayers could offer more flexibility to control physical, electrical and optical properties over ordinary $Ge_{1-y}Sn_y$ binary alloys, it is crucial to understand mechanisms that can control the incorporation of dopant into $Ge_{1-y}Sn_y$ epilayers. Further studies are proposed to understand the effects of B and P incorporation into $Ge_{1-y}Sn_y$ epilayers, including Sn concentration, growth rate of epilayers. Finally, explanations of chemical reactions in the CVD chamber could open up a new path to the development of high quality doped $Ge_{1-y}Sn_y$ epilayers.

The incorporation of Si into $Ge_{1-y}Sn_y$ (as known as $Ge_{1-x-y}Si_xSn_y$) was also investigated. The incorporation of Si up to ~3 at.% into $Ge_{1-x-y}Si_xSn_y$ with a Sn concentration of 9.5 at.% was successfully achieved. The effects of growth temperature on epitaxial growth of $Ge_{1-x-y}Si_xSn_y$ epilayers were studied. Since the presence of Si precursors and the incorporation of Si into $Ge_{1-x-y}Si_xSn_y$ influence the incorporation of Sn, it can be difficult to reconcile both the incorporation of Si and Sn simultaneously. Further research is required to understand the mechanism of epitaxial growth of $Ge_{1-x-y}Si_xSn_y$ epilayers.

Chapter 10

Epitaxial Growth of $Ge_{1-y}Sn_y$\Ge & $Ge_{1-y}Sn_y$\$Ge_{1-z}Sn_z$ ($y \neq z$) Multilayers

10.1 Introduction

For device fabrication and commercialisation of $Ge_{1-y}Sn_y$ devices, it is essential to develop appropriate techniques for growth of $Ge_{1-y}Sn_y$\Ge multilayers, Ge\$Ge_{1-y}Sn_y$\Ge quantum wells and $Ge_{1-y}Sn_y$\$Ge_{1-z}Sn_z$ in which $y \neq z$. As already explained, Ge growth at low temperatures (300 °C) is not possible because Ge atoms cannot be produced without the presence of $SnCl_4$ when GeH_4 precursor is used at low growth temperatures. Similarly, since the Sn concentration in $Ge_{1-y}Sn_y$ closely depends on the growth temperature, it is impossible to grow $Ge_{1-y}Sn_y$ with very different Sn concentrations at the same growth temperature. It should be noted that it is still possible to slightly vary the Sn concentration (by not more than approximately 2 at.%) by changing other CVD conditions, such as the modification of the $SnCl_4/GeH_4$ ratio. Nevertheless, such Sn concentration variations are limited and may not be an appropriate technique. Therefore, changing growth temperature during CVD growth seems necessary to optimise the characteristics of each epilayer. In this chapter, such a method is investigated and examined in detail.

10.2 Growth of Ge Cap Layer on $Ge_{1-y}Sn_y$

Ge cap layer with thickness of ~146 nm has been successfully grown on ~8 nm fully strained $Ge_{0.91}Sn_{0.09}$. This was achieved by increasing the growth temperature from 280 °C to 350 °C, just after growth of ~8 nm thick $Ge_{0.91}Sn_{0.09}$ epilayer. This is because the GeH_4 precursor is not reactive at such low temperature without the presence of $SnCl_4$ (as well as its intermediates, as explained in previous chapters). It is therefore essential to increase the growth temperature to an appropriate level in order to grow the Ge Cap Layer (or any Ge epilayer). Other growth conditions, such as pressure, could, however, remain the same. The cross sectional schematic diagram of the Ge-cap-layer\$Ge_{0.91}Sn_{0.09}$\Ge-VS\Si (001) is shown in Figure 10.1.

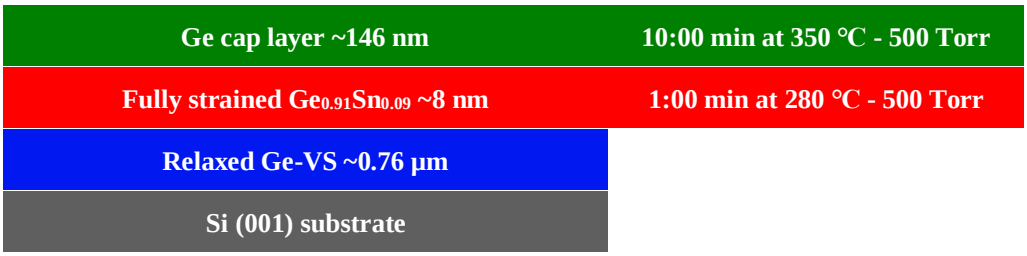

Figure 10.1 Cross sectional schematic diagram of the Ge cap layer grown at 350 °C on fully strained $Ge_{0.91}Sn_{0.09}$ grown at 280 °C on Si (001) substrate via relaxed Ge-VS. Growth pressure was kept fixed at 500 Torr; however, its growth temperature was tuned and flow of $SnCl_4$-H_2 precursor was stopped when growing Ge cap layer on fully strained $Ge_{0.91}Sn_{0.09}$.

It is important to note that Sn concentration in fully strained $Ge_{0.91}Sn_{0.09}$ epilayer was not directly measured from this sample, but instead the same $Ge_{0.91}Sn_{0.09}$ epilayer was grown with exact growth conditions without the Ge cap layer, and then its thickness and Sn concentration was measured using HR-XRD ω-2θ coupled scan and corresponding symmetrical and asymmetric RSMs. In Figure 10.2, HR-XRD ω-2θ coupled scan of $Ge_{0.91}Sn_{0.09}$\Ge-VS\Si(001) heterostructure is shown. Growth of ~31 nm thick fully strained $Ge_{0.91}Sn_{0.09}$ on Si (001) via Ge-VS was done at temperature of 280 °C, pressure of 500 Torr and growth time of 4:00 min. Considering the growth time, the growth rate of $Ge_{0.91}Sn_{0.09}$ epilayer is ~8 nm/min. The same CVD growth conditions were used to grow $Ge_{0.91}Sn_{0.09}$ epilayer in Ge-cap-layer\$Ge_{0.91}Sn_{0.09}$\Ge-VS\Si (001) heterostructure, which its schematic cross sectional diagram is shown in Figure 10.1.

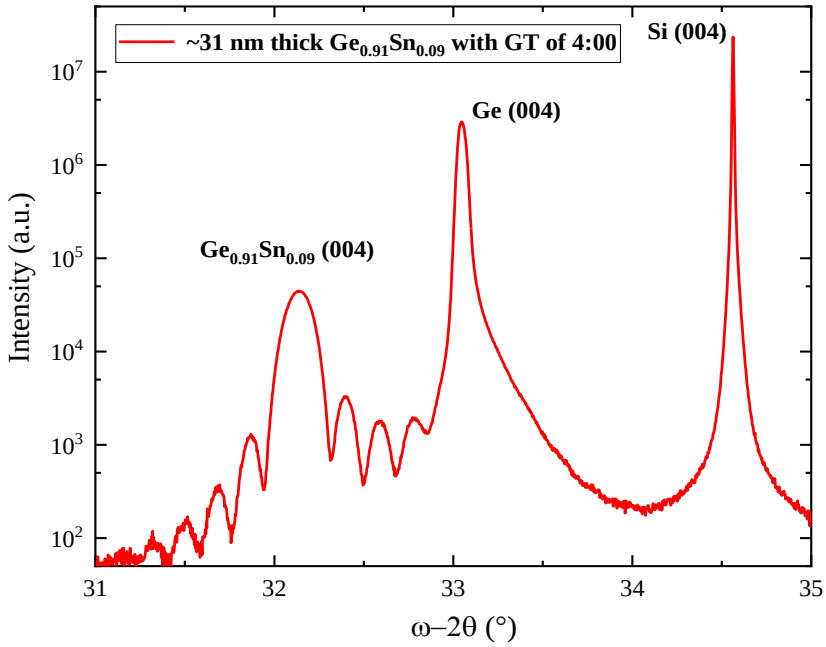

Figure 10.2 HR-XRD ω-2θ coupled scan of $Ge_{0.91}Sn_{0.09}$\Ge-VS\Si (001) heterostructure. Growth of ~31 nm thick fully strained $Ge_{0.91}Sn_{0.09}$ on Si (001) via Ge-VS was done at temperature of 280 °C, pressure of 500 Torr and growth time of 4:00 min. Considering the growth time, the growth rate of $Ge_{0.91}Sn_{0.09}$ epilayer is ~8 nm/min. The same growth conditions were used to grow $Ge_{0.91}Sn_{0.09}$ epilayer in Ge-cap-layer\$Ge_{0.91}Sn_{0.09}$\Ge-VS\Si (001) heterostructure, which its schematic cross sectional diagram is shown in Figure 10.1.

Thickness measurements were done using X-TEM, as shown in Figure 10.3. Thick Ge-VS was grown not only to achieve strain relaxation, but also to avoid Lomer dislocations. The appeared defect in the Ge buffer is made during sample preparation for TEM, not during CVD growth. Growth times for fully strained $Ge_{0.91}Sn_{0.09}$ and Ge cap layer are 1:00 min and 10:00 min, respectively. This suggests the growth rate of ~8 nm/min for $Ge_{0.91}Sn_{0.09}$ epilayer and ~14.6 nm/min Ge cap layer. The growth rate of $Ge_{0.91}Sn_{0.09}$ epilayer measured using X-TEM confirms the growth rate of $Ge_{0.91}Sn_{0.09}$ epilayer, which was grown separately, measured using HR-XRD ω-2θ coupled scan thickness fringes.

Lattice resolution X-TEM micrograph is given in Figure 10.4 which presents high quality of grown epilayers with no defects at interfaces. One important reason for this is because all these three epilayers (Ge-VS, fully strained $Ge_{0.91}Sn_{0.09}$, and Ge cap layer) have the same in-plane lattice parameter. Therefore, growing the cap layer above fully strained $Ge_{0.91}Sn_{0.09}$ may not be a challenging task. However, if thicker $Ge_{1-y}Sn_y$ (with therefore some strain relaxation) is required, we can expect some defects at the Ge-cap layer $Ge_{1-y}Sn_y$ interface, depending on how much strain relaxation is in the $Ge_{1-y}Sn_y$ epilayer. In addition, the short gap time between

the growth of $Ge_{0.91}Sn_{0.09}$ and the Ge cap layer, in which the growth temperature was changed from 280 °C to 350 °C, did not cause Sn precipitation from the $Ge_{0.91}Sn_{0.09}$ epilayer. Instead, the Sn precipitation can be suppressed by the Ge cap layer, even if the heterostructure goes through rapid thermal annealing processes at relatively high temperatures.

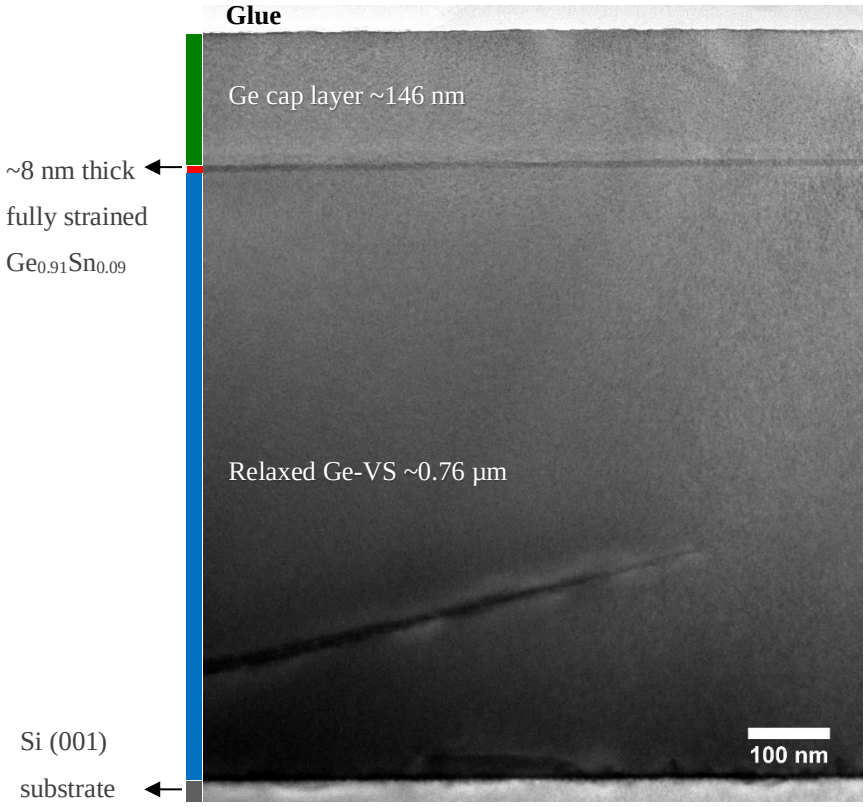

Figure 10.3 X-TEM micrograph of Ge-cap-layer\$Ge_{0.91}Sn_{0.09}$\Ge-VS\Si (001) heterostructure grown which its cross sectional schematic diagram is given in Figure 10.1. Ge cap layer was grown at 350 °C on fully strained $Ge_{0.91}Sn_{0.09}$ which was grown at 280 °C on Si (001) via relaxed Ge-VS. Both Ge cap and $Ge_{0.91}Sn_{0.09}$ epilayer were grown at fixed pressure of 500 Torr. The X-TEM micrograph was taken using TEM 2100 in ST diffraction condition. The appeared defect in Ge-VS was created during TEM sample preparation.

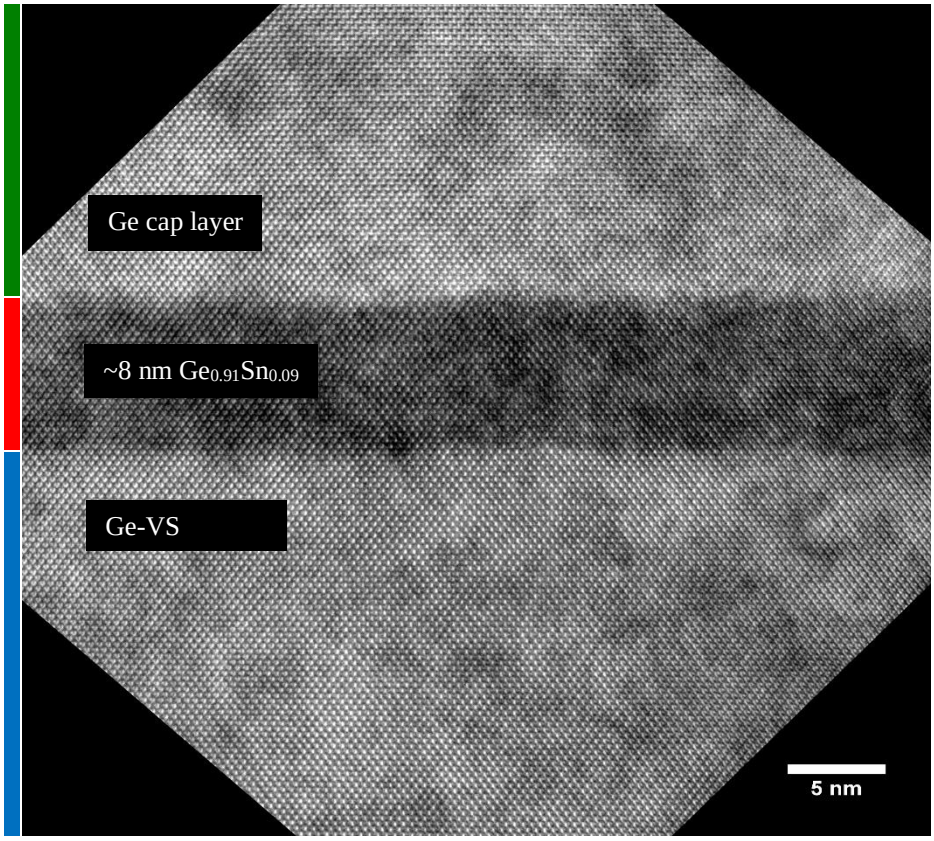

Figure 10.4 X-TEM micrograph of grown heterostructure Ge-cap-layer\$Ge_{0.91}Sn_{0.09}$\Ge-VS\Si (001) which its cross sectional schematic diagram is given in Figure 10.1. Ge cap layer was grown at 350 °C on a fully strained $Ge_{0.91}Sn_{0.09}$ epilayer which was grown at 280 °C on Si (001) substrate via relaxed Ge-VS. Both Ge cap and $Ge_{0.91}Sn_{0.09}$ are grown at fixed pressure of 500 Torr. High quality interfaces between epilayers can be seen in this lattice resolution micrograph, which was taken using ST diffraction condition.

10.3 Growth of Ge\$Ge_{1-y}Sn_y$ Multilayers

The growth of Ge\$Ge_{1-y}Sn_y$ multilayers was investigated using RP-CVD with varied growth temperature. Several Ge epilayers with different growth times were grown on $Ge_{0.91}Sn_{0.09}$ epilayers. Growth temperatures for Ge and $Ge_{0.91}Sn_{0.09}$ were kept at 350 °C and 280 °C respectively. While growth pressure was fixed at 500 Torr during growth, $SnCl_4$ was stopped when the Ge epilayer was growing and GeH_4 precursor was tuned accordingly. The entire cross sectional schematic diagram (with respective growth conditions of each epilayer) of Ge\$Ge_{0.91}Sn_{0.09}$\Ge\$Ge_{0.91}Sn_{0.09}$\Ge\$Ge_{0.91}Sn_{0.09}$\Ge-VS\Si (001) is shown in Figure 10.5. It should be noted that the Sn concentration of $Ge_{1-y}Sn_y$ in this heterostructure was estimated separately from another sample by growing the same $Ge_{1-y}Sn_y$ using the same CVD growth conditions. This estimate is valid as we have considered fully strained epilayers with the same in-plane lattice parameter.

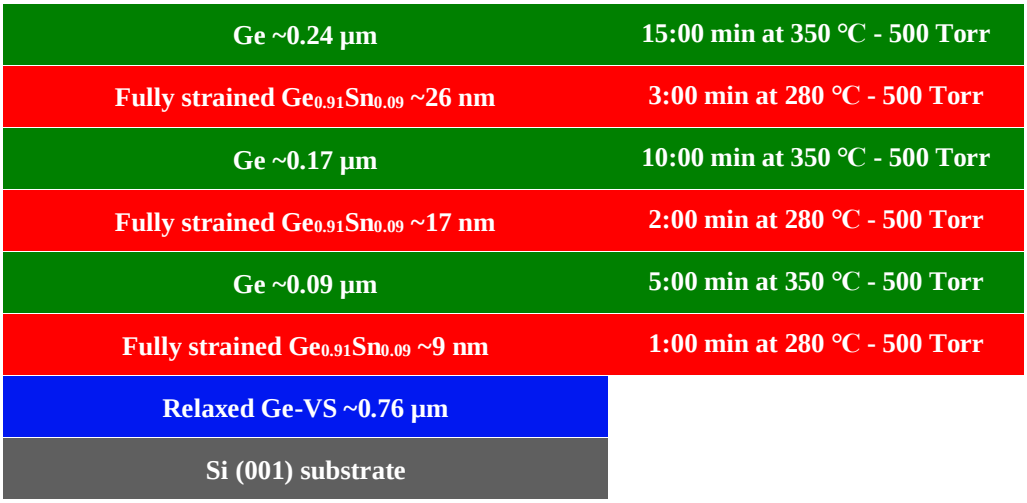

Figure 10.5 The entire cross sectional diagram of Ge\$Ge_{0.91}Sn_{0.09}$\Ge\$Ge_{0.91}Sn_{0.09}$\Ge\$Ge_{0.91}Sn_{0.09}$\Ge-VS\Si (001) heterostructure. Corresponding used growth conditions for each epilayer are also given. Ge epilayers were all grown at 350 °C above a fully strained $Ge_{0.91}Sn_{0.09}$ which were all grown at 280 °C. Growth pressure was maintained at 500 Torr. However, the growth temperature was modified and the flow of $SnCl_4$-H_2 was stopped during the growth of the Ge Cap layer. These epilayers were grown with different growth time to carefully investigate their growth rate.

The thickness measurements of all epilayers shown in Figure 10.5 are achieved using X-TEM, as shown in Figure 10.6. Thick enough Ge-VS was grown not only to achieve full strain relaxation, but also to avoid Lomer dislocations. Since different growth times for each epilayer were used, different thicknesses were achieved. The growth rate for fully strained $Ge_{0.91}Sn_{0.09}$

is 9 nm/min, which is the same for all three epilayers. This is expected as they are all fully strained $Ge_{0.91}Sn_{0.09}$ with the same Sn concentration of 9 at.% (y = 0.09) and no strain relaxation was observed for these thicknesses. However, the growth rate for Ge epilayers slightly decreases as growth time increases. This could be due to several engineering factors, such as the flow rate of GeH_4, which could reduce slightly over time. It should be noted that there is no occurrence of strain relaxation in Ge epilayers, all of which are already relaxed. The growth rate for Ge epilayers was observed to be ~17 ± 1 nm/min.

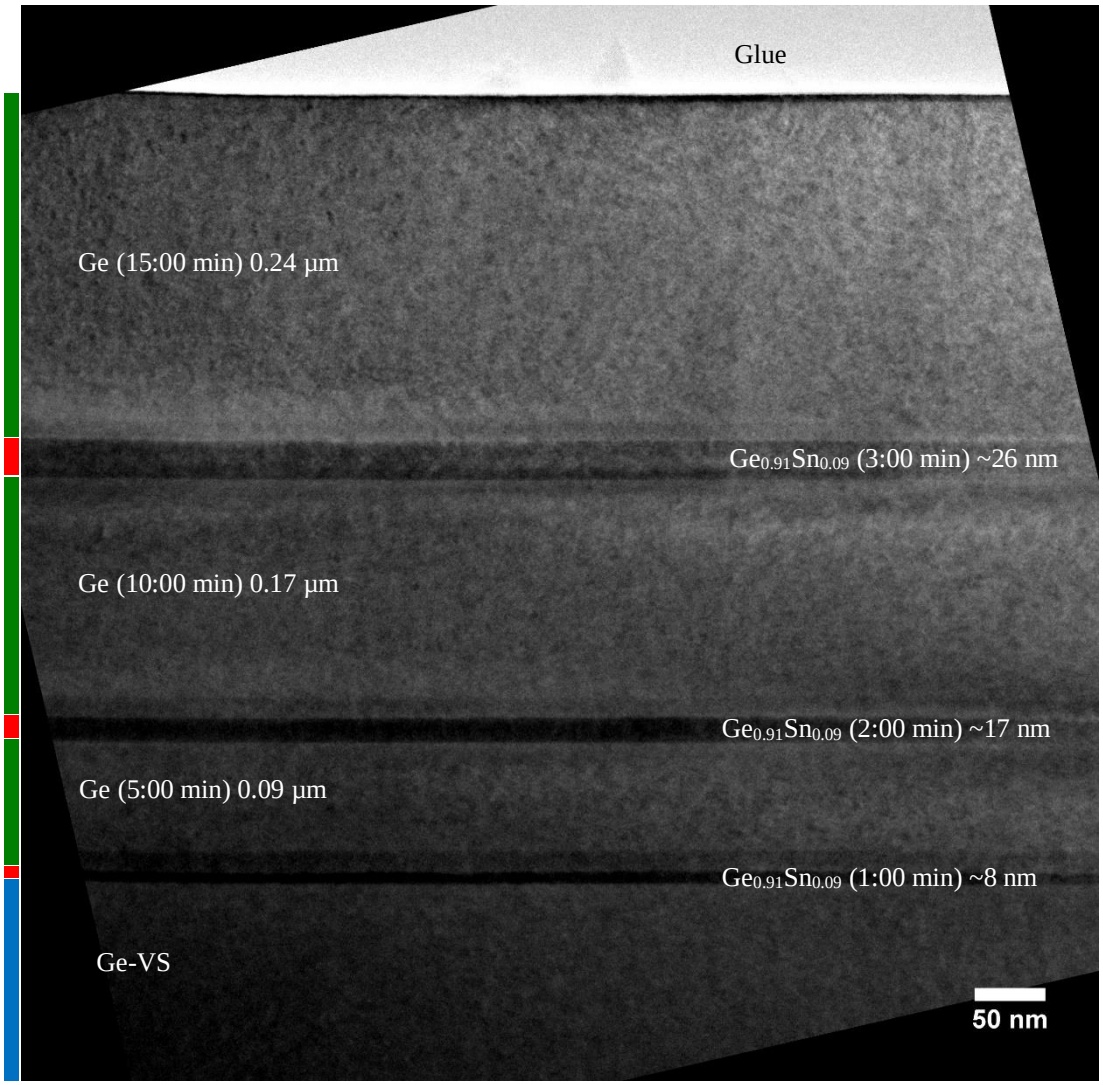

Figure 10.6 X-TEM micrograph of Ge\$Ge_{0.91}Sn_{0.09}$\Ge\$Ge_{0.91}Sn_{0.09}$\Ge\$Ge_{0.91}Sn_{0.09}$\Ge-VS\Si (001) heterostructure which its cross sectional schematic diagram is given in Figure 10.5. All Ge epilayers were grown at 350 °C on fully strained $Ge_{0.91}Sn_{0.09}$ that was grown at 280 °C. The whole heterostructure is grown on Si (001) substrate via a Ge-VS at a fixed pressure of 500 Torr. The X-TEM micrograph is taken using TEM 2100 in ST diffraction condition.

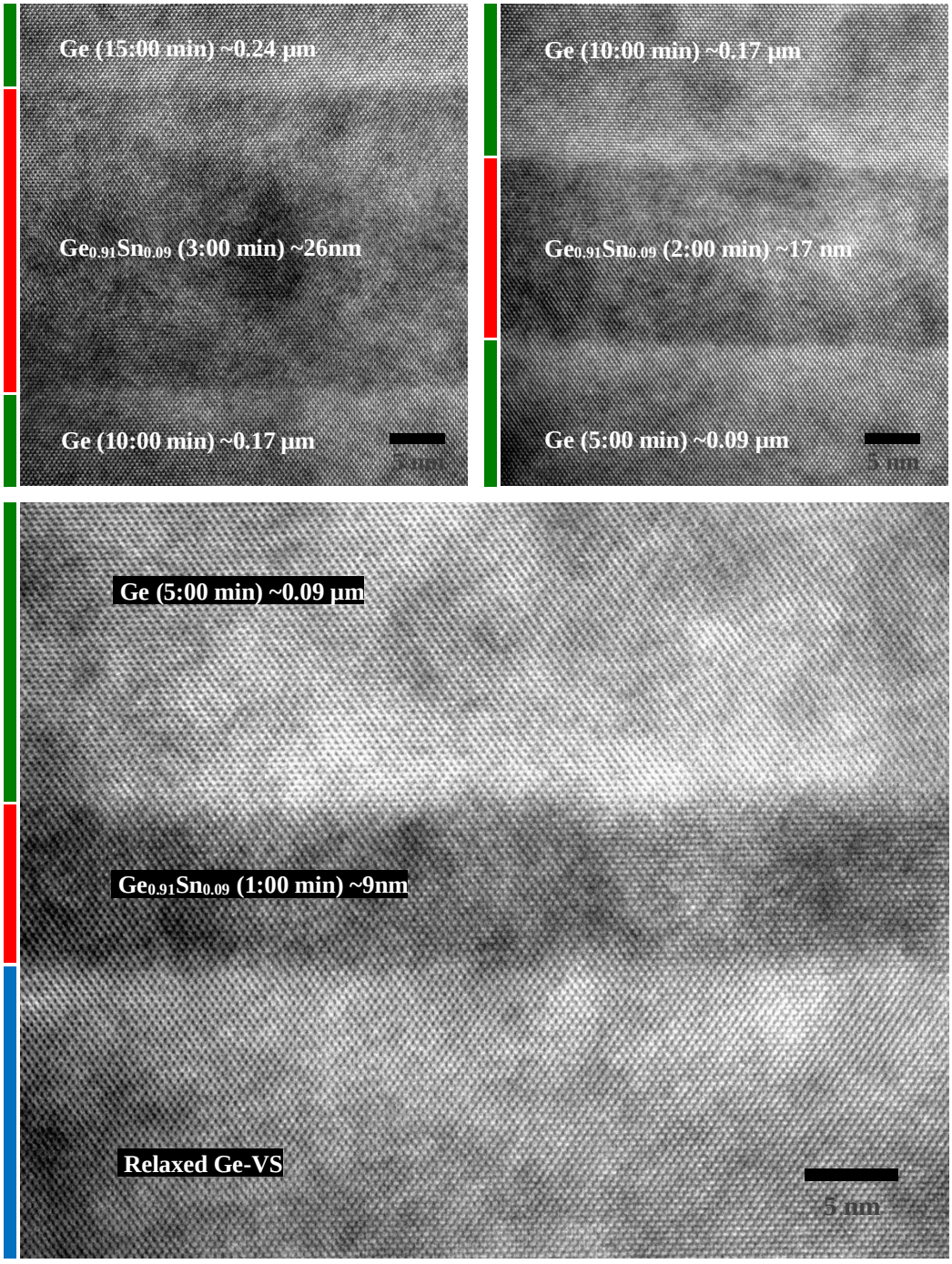

Figure 10.7 Lattice resolution X-TEM micrographs of Ge\$Ge_{0.91}Sn_{0.09}$\Ge\$Ge_{0.91}Sn_{0.09}$\Ge\$Ge_{0.91}Sn_{0.09}$\Ge-VS\Si heterostructure which its cross sectional schematic diagram is given in Figure 10.5. Each Ge epilayer was grown at 350 °C on a fully strained $Ge_{0.91}Sn_{0.09}$ that was grown at 280 °C. All these multilayers are grown on Si (001) via a Ge-VS with a fixed pressure of 500 Torr. High quality interfaces between epilayers can be seen in these lattice resolution micrographs, which were taken with direct diffraction condition. The thickness of each epilayer was carefully measured via corresponding X-TEM micrograph. Bottom: the first grown $Ge_{0.91}Sn_{0.09}$ epilayer with growth time of 1:00 min. Top-right: the second grown $Ge_{0.91}Sn_{0.09}$ epilayer with growth rate of 2:00 min. Top-left: the third (and final) grown $Ge_{0.91}Sn_{0.09}$ epilayer with growth rate of 3:00 min.

There are some contrast issues with the X-TEM micrograph shown in Figure 10.6 due to lack of proper focus. This is because the whole heterostructure is thick, making it difficult to consider appropriate focus for all epilayers. Instead, higher magnifications were used for each epilayer to confirm their thickness.

Lattice resolution X-TEM micrographs are presented in Figure 10.7 which presents a high quality of grown epilayers without defects at interfaces. This is because all grown epilayers have the same in-plane lattice parameter. Growing these epilayers may therefore not be a challenging task. However, if, for instance, thicker $Ge_{1-y}Sn_y$ (with partial strain relaxation) has been grown, some defects may appear at interfaces that depend on how much strain relaxation is in the corresponding $Ge_{1-y}Sn_y$ epilayer.

10.4 Growth of $Ge_{1-y}Sn_y\backslash Ge_{1-z}Sn_z$ ($y \neq z$) Multilayers

In this section, we tended to grow $Ge_{1-y}Sn_y\backslash Ge_{1-z}Sn_z$ heterostructure, in which $y \neq z$, on Si (001) via Ge-VS. This could open up new possibilities to improve the quality of grown epilayers by controlling and suppressing defects at interfaces and Sn segregation. In addition, more complex Sn-based group IV semiconductor multilayers could be grown, by using a similar approach, for appropriate device applications. In Figure 10.8, cross sectional schematic diagram of three heterostructures (with different growth time) in which $Ge_{1-y}Sn_y$ and $Ge_{1-z}Sn_z$ epilayers with different Sn concentration ($y \neq z$) were grown on Si (001) via relaxed Ge-VS.

Figure 10.8 Cross sectional schematic diagram of three samples (with different growth time) in which $Ge_{1-y}Sn_y$ and $Ge_{1-z}Sn_z$ epilayers have different Sn concentration ($y \neq z$) were grown on Si (001) via relaxed Ge-VS. Growth pressure and $SnCl_4$-H_2 gas flow were kept fixed at 500 Torr and 200 sccm, respectively. To achieve two different Sn concentrations, different growth temperatures were used, 280 °C for high Sn concentration $Ge_{1-y}Sn_y$ and 320 °C for low Sn concentration $Ge_{1-z}Sn_z$.

Growth pressure and $SnCl_4$-H_2 gas flow were kept fixed at 500 Torr and 200 sccm, respectively. To achieve two different Sn concentrations, different growth temperatures were used, 280 °C for high Sn concentration $Ge_{1-y}Sn_y$ and 320 °C for low Sn concentration $Ge_{1-z}Sn_z$.

ω-2θ coupled scan of fully-strained-$Ge_{0.89}Sn_{0.11}$\fully-strained-$Ge_{0.93}Sn_{0.07}$\Ge-VS\Si (001) heterostructure, is shown in Figure 10.9 (black). Successful RP-CVD growth was achieved by modifying the growth temperature from 320 ℃ for fully strained $Ge_{0.93}Sn_{0.07}$ to 280 ℃ for fully strained $Ge_{0.89}Sn_{0.11}$. All three fully strained $Ge_{0.89}Sn_{0.11}$ epilayer, fully strained $Ge_{0.93}Sn_{0.07}$ epilayer and relaxed Ge-VS have the same in-plane lattice constant. In addition, the effect of strain relaxation on Sn concentration of each layer on their Sn concentration was investigated by growing thicker $Ge_{1-y}Sn_y$\$Ge_{1-z}Sn_z$ epilayers. As shown in Figure 10.9, in the ω-2θ coupled scan of $Ge_{0.88}Sn_{0.12}$\$Ge_{0.92}Sn_{0.08}$\Ge-VS\Si (001) (red), the thickness fringes for the peak corresponding to the ~0.5 µm thick intermediate epilayer ($Ge_{0.92}Sn_{0.08}$) have disappeared due to strain relaxation. Also, since there is no shoulder on the left hand side of the Ge peak in ω-2θ coupled scans of grown heterostructures, which shows the suppression of Sn precipitation and segregation as discussed before. Moreover, the strain relaxation for both ~0.5 µm thick epilayers ($Ge_{0.87}Sn_{0.13}$ and $Ge_{0.92}Sn_{0.08}$) can be observed in the ω-2θ coupled scan of $Ge_{0.87}Sn_{0.13}$\$Ge_{0.92}Sn_{0.08}$\Ge-VS\Si (001) (blue) in Figure 10.9.

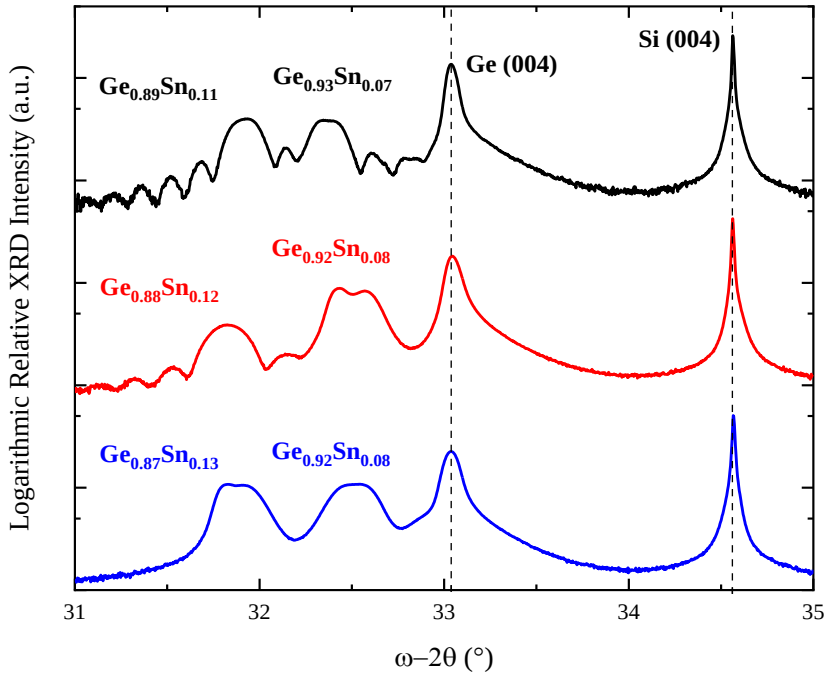

Figure 10.9 HR-XRD ω-2θ coupled scans of $Ge_{1-y}Sn_y$\$Ge_{1-z}Sn_z$\Ge-VS\Si (001) heterostructures, in which $y \neq z$. Their cross sectional schematic diagrams are shown in Figure 10.8. Black: $Ge_{0.89}Sn_{0.11}$\$Ge_{0.93}Sn_{0.07}$\Ge-VS\Si (001), Red: $Ge_{0.88}Sn_{0.12}$\$Ge_{0.92}Sn_{0.08}$\Ge-VS\Si (001), Blue: $Ge_{0.87}Sn_{0.13}$\ $Ge_{0.92}Sn_{0.08}$\Ge-VS\Si (001).

To investigate Sn concentration and strain relaxation, HR-XRD Symmetric and asymmetric RSMs for $Ge_{1-y}Sn_y$\$Ge_{1-z}Sn_z$\Ge-VS\Si (001) heterostructures were taken. As shown in Figure

10.10 (top RSMs), ~0.03 µm thick fully strained $Ge_{0.89}Sn_{0.11}$ was successfully grown on ~0.03 µm thick fully strained $Ge_{0.93}Sn_{0.07}$. It is clearly evident in the asymmetric RSM of $Ge_{0.89}Sn_{0.11}\backslash Ge_{0.93}Sn_{0.07}\backslash$Ge-VS\Si (001) that both $Ge_{0.89}Sn_{0.11}\backslash Ge_{0.93}Sn_{0.07}$ epilayers have the same in-plane lattice constant.

In addition, thicker intermediate $Ge_{1-z}Sn_z$, in which partial relaxation occurred, was grown to examine its effects on the quality of $Ge_{1-y}Sn_y$, which was grown above it. As shown in Figure 10.10 (middle RSMs), ~0.03 µm thick fully strained $Ge_{0.88}Sn_{0.12}$ was successfully grown on ~0.5 µm thick partially relaxed $Ge_{0.92}Sn_{0.08}$. It is important to bear in mind that, as can be seen in the asymmetric RSM of $Ge_{0.88}Sn_{0.12}\backslash Ge_{0.92}Sn_{0.08}\backslash$Ge-VS\Si (001), $Ge_{0.88}Sn_{0.12}$ epilayer is fully strained in relation to the partially relaxed $Ge_{0.92}Sn_{0.08}$ epilayer. This means that $Ge_{0.88}Sn_{0.12}$ has the same in-plane lattice constant as the partially relaxed $Ge_{0.92}Sn_{0.08}$, not the Ge buffer layer. This can also be confirmed in Figure 10.9 in the HR-XRD ω-2θ coupled scan of $Ge_{0.88}Sn_{0.12}\backslash Ge_{0.92}Sn_{0.08}\backslash$Ge-VS\Si (001), in which thickness fringes of $Ge_{0.88}Sn_{0.12}$ peak are visible. Comparing the Sn concentration of both epilayers with the previous heterostructure in which both $Ge_{1-y}Sn_y\backslash Ge_{1-z}Sn_z$ epilayers are fully strained, it can be realised that the strained relaxation in the intermediate $Ge_{1-z}Sn_z$ epilayer not only increased the Sn concentration in its epilayer, but also in the grown $Ge_{1-y}Sn_y$ epilayer by ~1 at.%.

Furthermore, thicker partially relaxed $Ge_{1-y}Sn_y\backslash Ge_{1-z}Sn_z$ epilayers were grown. The only difference between this heterostructure and the previous one is that the top $Ge_{1-y}Sn_y$ epilayer is also partially relaxed. This can be seen in the HR-XRD ω-2θ coupled scan of $Ge_{0.87}Sn_{0.13}\backslash Ge_{0.92}Sn_{0.08}\backslash$Ge-VS\Si in Figure 10.9, which shows both $Ge_{1-y}Sn_y\backslash Ge_{1-z}Sn_z$ epilayers have no thickness fringes. The characteristics of the intermediate $Ge_{1-z}Sn_z$, Ge-VS and Si (001) are all the same. However, the top $Ge_{1-y}Sn_y$ epilayer is partially relaxed concerning the intermediate $Ge_{1-z}Sn_z$ epilayer. As expected, the Sn concentration in the top epilayer is increased by approximately 1 at.% as a consequence of strain relaxation. This can be seen in the asymmetric RSM of $Ge_{0.87}Sn_{0.13}\backslash Ge_{0.92}Sn_{0.08}\backslash$Ge-VS\Si in Figure 10.10 (bottom RSMs). The Sn concentration of the top $Ge_{1-y}Sn_y$ epilayer in $Ge_{0.87}Sn_{0.13}\backslash Ge_{0.92}Sn_{0.08}\backslash$Ge-VS\Si is greater by ~2 at.% compared to that of $Ge_{0.89}Sn_{0.11}\backslash Ge_{0.93}Sn_{0.07}\backslash$Ge-VS\Si . This is due to the strain relaxation within the epilayer. The strain relaxation of the top $Ge_{1-y}Sn_y$ epilayer came not only from its own thickness, which passed h_c, but also from the strain relaxation of the intermediate $Ge_{1-z}Sn_z$ epilayer.

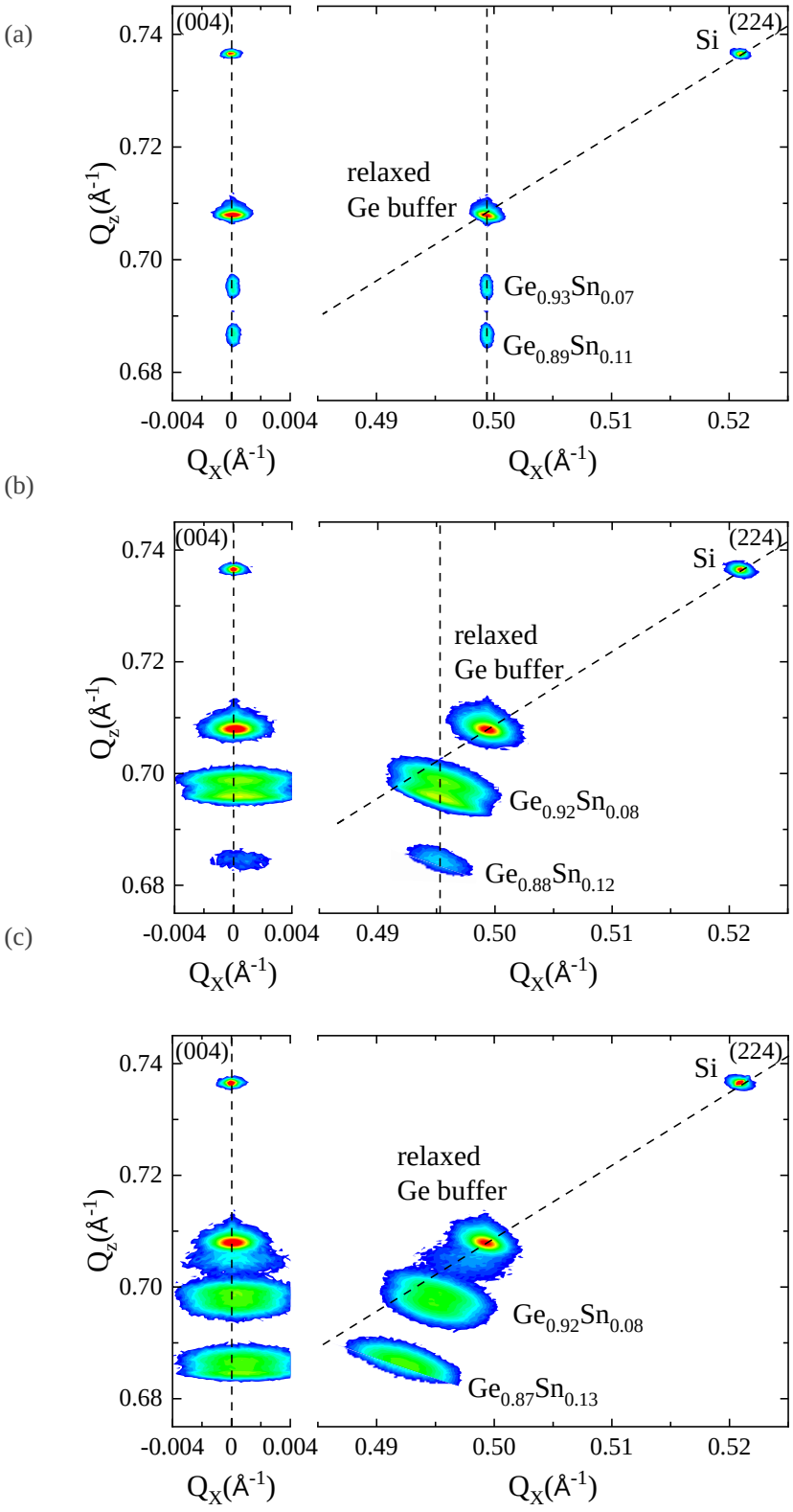

Figure 10.10 Symmetric and asymmetric RSMs for $Ge_{1-y}Sn_y$\$Ge_{1-z}Sn_z$ ($y \neq z$) heterostructures grown on Si (001) via relaxed Ge-VS. Their cross sectional schematic diagrams and respective HR-XRD ω-2θ coupled scans are shown in Figure 10.8 and Figure 10.9, respectively. Top: $Ge_{0.89}Sn_{0.11}$\$Ge_{0.93}Sn_{0.07}$\Ge-VS\Si (001). Middle: $Ge_{0.88}Sn_{0.12}$\$Ge_{0.92}Sn_{0.08}$\Ge-VS\Si (001). Bottom: $Ge_{0.87}Sn_{0.13}$\$Ge_{0.92}Sn_{0.08}$\Ge-VS\Si (001).

10.4.1 Surface Morphology of $Ge_{1-y}Sn_y\backslash Ge_{1-z}Sn_z$ ($y \neq z$) Multilayers

The surface morphology of grown $Ge_{1-y}Sn_y$ epilayers was investigated using AFM scans. The AFM scans with the corresponding surface roughness of three $Ge_{1-y}Sn_y$ epilayers grown with the same growth conditions but with different growth time are shown in Figure 10.11.

As explained in previous chapters, all fully compressive strained $Ge_{1-y}Sn_y$ epilayers grown by GeH_4 precursor, in which Sn segregation is controlled, had low surface roughness of ~1 nm. As shown in Figure 10.11 (top), the surface roughness of $Ge_{0.89}Sn_{0.11}\backslash Ge_{0.93}Sn_{0.07}\backslash$Ge-VS\Si, in which the top epilayer is fully strained, is ~1 nm.

However, when fully strained $Ge_{1-y}Sn_y$ is grown above a thicker intermediate $Ge_{1-z}Sn_z$ epilayer, which is partially relaxed, the surface roughness (RMS) increases. As shown in Figure 10.11 (middle), the surface roughness (RMS) of $Ge_{0.88}Sn_{0.12}\backslash Ge_{0.92}Sn_{0.08}\backslash$Ge-VS\Si is ~7 nm. It should be noted that, as can be seen in the asymmetric RSM of $Ge_{0.88}Sn_{0.12}\backslash Ge_{0.92}Sn_{0.08}\backslash$Ge-VS\Si (001) in Figure 10.10, $Ge_{0.88}Sn_{0.12}$ epilayer is fully strained in relation to the partially relaxed $Ge_{0.92}Sn_{0.08}$ epilayer. The $Ge_{0.88}Sn_{0.12}$ epilayer has the same in-plane lattice constant as the partially relaxed $Ge_{0.92}Sn_{0.08}$, not the Ge buffer layer. This can also be confirmed in Figure 10.9 in the HR-XRD ω-2θ coupled scan of $Ge_{0.88}Sn_{0.12}\backslash Ge_{0.92}Sn_{0.08}\backslash$Ge-VS\Si, in which thickness fringes of $Ge_{0.88}Sn_{0.12}$ peak are visible. Therefore, the increase in surface roughness is solely due to the greater thickness of the intermediate $Ge_{0.92}Sn_{0.08}$ epilayer, which is the reason for the increase in Sn concentration of $Ge_{0.88}Sn_{0.12}$ (by ~1 at.%) and its in-plane lattice constant.

Additionally, AFM scans of $Ge_{0.87}Sn_{0.13}\backslash Ge_{0.92}Sn_{0.08}\backslash$Ge-VS\Si (001) heterostructure, in which both $Ge_{0.87}Sn_{0.13}$ and $Ge_{0.92}Sn_{0.08}$ epilayers are partially relaxed, are shown in Figure 10.11. The HR-XRD ω-2θ coupled scan (Figure 10.9) and asymmetric RSM (Figure 10.10) of $Ge_{0.87}Sn_{0.13}\backslash Ge_{0.92}Sn_{0.08}\backslash$Ge-VS\Si (001) show both $Ge_{1-y}Sn_y\backslash Ge_{1-z}Sn_z$ epilayers are partially relaxed. As already explained, the Sn concentration in the top epilayer is increased by approximately 1 at.% as a consequence of strain relaxation. As shown in Figure 10.11, surface roughness (RMS) of $Ge_{0.87}Sn_{0.13}\backslash Ge_{0.92}Sn_{0.08}\backslash$Ge-VS\Si (001) is slightly higher, ~11 nm. Apart from the increase in Sn concentration and in-plane lattice constant due to strain relaxation, there are no other reasons why the surface roughness is higher and Sn segregation is controlled, similar to the other two heterostructures.

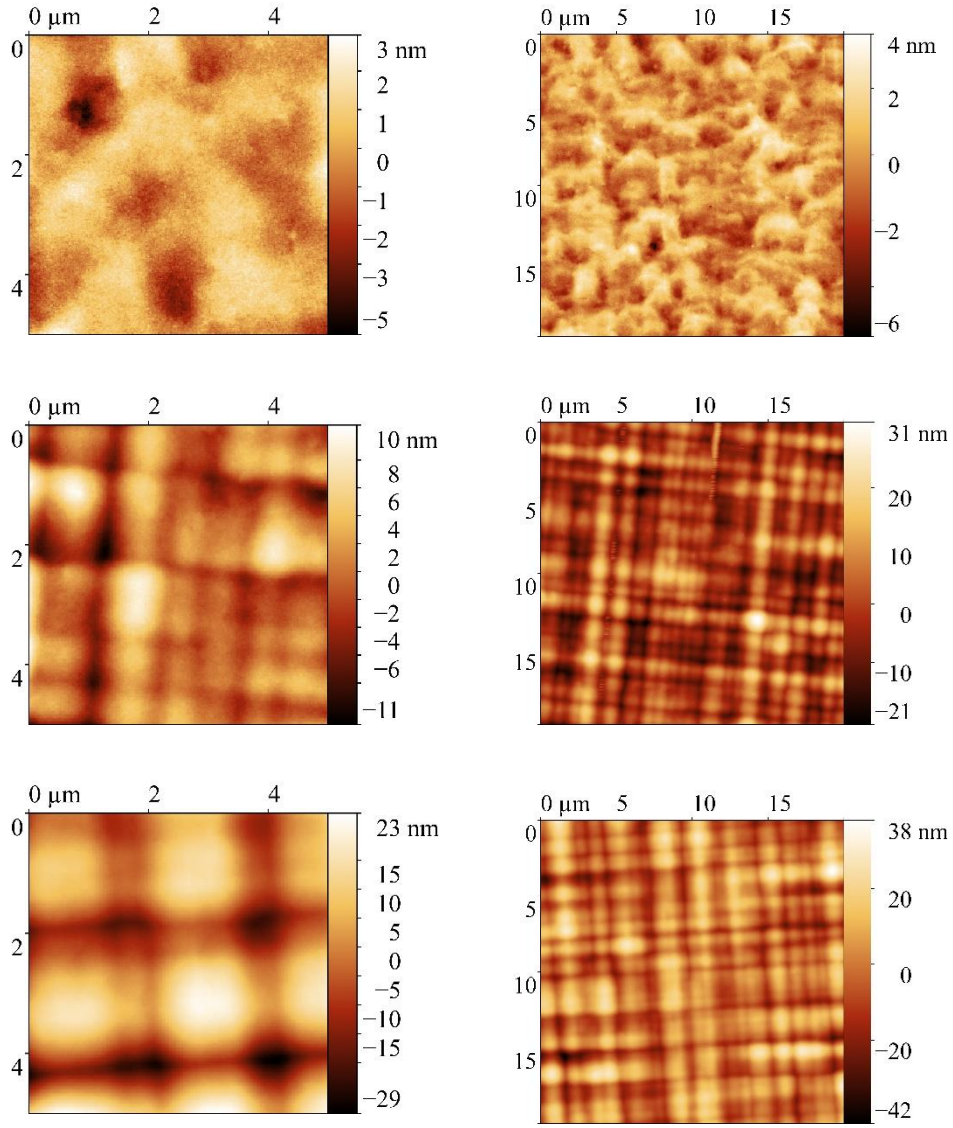

Figure 10.11 AFM scans of $Ge_{1-y}Sn_y\backslash Ge_{1-z}Sn_z$ ($y \neq z$) heterostructures grown on Si (001) via relaxed Ge in RP-CVD. Their cross sectional schematic diagrams, respective HR-XRD ω-2θ coupled scans, and symmetric/asymmetric RSMs are shown in Figure 10.8, Figure 10.9 and Figure 10.10, respectively. All these AFM scans are taken using tapping mode. Top: AFM scans of $Ge_{0.89}Sn_{0.11}\backslash Ge_{0.93}Sn_{0.07}\backslash$Ge-VS\Si (001) with RMS of ~1 nm. Middle: AFM scans of $Ge_{0.88}Sn_{0.12}\backslash\ Ge_{0.92}Sn_{0.08}\backslash$Ge-VS\Si (001) with RMS of ~7 nm. Bottom: AFM scans of $Ge_{0.87}Sn_{0.13}\backslash\ Ge_{0.92}Sn_{0.08}\backslash$Ge-VS\Si (001) with RMS of ~11 nm. As the thickness of the $Ge_{1-y}Sn_y$ epilayer increases, which means that more strain relaxation is achieved, the surface roughness in terms of RMS increases.

10.5 Conclusion

Growth of Ge-cap\$Ge_{1-y}Sn_y$\Ge-VS, $Ge_{1-y}Sn_y$\Ge multilayers, and $Ge_{1-y}Sn_y$\$Ge_{1-z}Sn_z$ ($y \neq z$) were all investigated. As already mentioned, Ge growth at low temperatures ($\leq$ 300 °C) is impossible, because Ge atoms cannot be produced without the presence of $SnCl_4$ when GeH_4 precursor is used at low growth temperatures. Similarly, since the Sn concentration in $Ge_{1-y}Sn_y$ closely depends on the growth temperature, it is not possible to grow $Ge_{1-y}Sn_y$ with very different Sn concentrations at the same growth temperature. Nevertheless, such Sn concentration variations are limited and may not be an appropriate technique. Therefore, changing growth temperature during CVD growth seems necessary to optimise the characteristics of each epilayer. Successful growth of the corresponding heterostructures, the investigation of the growth mechanism, and the impact of growth conditions on the quality of epilayers have been extensively carried out. Further research is necessary to develop and study the techniques mentioned in this chapter. Depending on the application, it is possible to epitaxy and engineer epilayers in the required manner.

Chapter 11

Conclusion

11.1 Achievements & Further Research

The heteroepitaxial growth of $Ge_{1-y}Sn_y$ on a Si (001) substrate via a relaxed Ge-VS was investigated with either of two commonly available commercial Ge precursors, GeH_4 and Ge_2H_6, in combination with $SnCl_4$ precursors, in RP-CVD. Since Ge_2H_6 is much more expensive, difficult to handle and store than GeH_4, it is of great interest to develop high quality $Ge_{1-y}Sn_y$ epilayers with high Sn concentration using the latter precursor. In chapter 4, the effects of CVD growth conditions, such as pressure, temperature and $SnCl_4/GeH_4$ ratio, were carefully studied experimentally when using GeH_4 over Ge_2H_6 as the Ge precursor. In addition, some explanations were given about Sn segregation and its role in the formation of Sn-rich micro-islands on the surface of the $Ge_{1-y}Sn_y$ epilayers. Surface morphology is important not only for device fabrication, but also for further epitaxial growth on the $Ge_{1-y}Sn_y$ epilayers. It was shown that the higher pressure ($\geq$ 500 Torr) is not only more advantageous to increase Sn concentration, but also to expand the allowed region for other CVD growth conditions, such as $SnCl_4/GeH_4$ ratio and growth temperature. In terms of growth temperature, lowering the temperature generally increases Sn concentration and reduces growth rate. The temperature can be used as a primary condition to adjust the Sn concentration in $Ge_{1-y}Sn_y$ during epitaxial growth. In chapter 5, it was demonstrated that both Ge precursors, GeH_4 and Ge_2H_6 can be used to achieve growth of strained and relaxed $Ge_{1-y}Sn_y$ epilayers, but incorporation of Sn into $Ge_{1-y}Sn_y$ was significantly higher when using the more reactive Ge precursor, Ge_2H_6. The main differences between the two precursors are based on process optimisation, which enables the growth of $Ge_{1-y}Sn_y$ binary alloys with sufficient Sn concentration at relatively lower cost. The results demonstrated that when using GeH_4, a lower $Ge_{1-y}Sn_y$ growth rate was achieved than when using Ge_2H_6 under very similar growth conditions. $Ge_{1-y}Sn_y$ epilayers grown with GeH_4 had lower surface roughness than epilayers grown with Ge_2H_6. This is because Sn segregation and precipitation could be controlled when

GeH_4 was used over Ge_2H_6. This could be crucial for achieving high quality metal contacts on the $Ge_{1-y}Sn_y$ epilayer, the growth of thick $Ge_{1-y}Sn_y$ epilayers for strain relaxation, and further heteroepitaxial growth of multilayers or quantum wells. The results of this investigation show that GeH_4 could be a viable Ge precursor preference for low cost epitaxial growth of $Ge_{1-y}Sn_y$ epilayers.

In addition, the growth of $Ge_{1-y}Sn_y$ at a very low temperature of 240 °C when using GeH_4 in combination with $SnCl_4$, which was previously assumed to be impossible, was successfully achieved. In chapter 6 it was shown that growth temperature is not the only factor that breaks GeH_4 molecules, but also the amount of $SnCl_4$ to GeH_4 should be taken into account. As growth temperature decreases, the allowed range of the $SnCl_4/GeH_4$ ratio, in which growth of $Ge_{1-y}Sn_y$ is possible, shrinks significantly. If the $SnCl_4/GeH_4$ ratio is too large, growth is stopped due to segregation due to the high amount of Sn atoms. On the other hand, if the $SnCl_4/GeH_4$ ratio is too low, growth is also stopped because there is not enough $SnCl_4$ to break an effective number of GeH_4 molecules to keep up the essential growth rate. Considering these, it is necessary to have the right $SnCl_4/GeH_4$ ratio as well as a high amount of GeH_4. While sacrificing growth rate at this temperature, it is easier to suppress precipitation and segregation in $Ge_{1-y}Sn_y$ epilayers. The lowest possible growth temperature at which epitaxial growth of $Ge_{1-y}Sn_y$ is allowed was estimated at ~231 °C, which is very close to the melting point of Sn. However, additional experiments are needed to experimentally determine such a minimum growth temperature. In addition, further studies are needed to investigate the growth of $Ge_{1-y}Sn_y$ at $SnCl_4/GeH_4$ ratio below 0.002, especially at growth temperatures of 270 °C and 280 °C. It should also be noted that more investigations should be done collect more experimental data to find the permitted $SnCl_4/GeH_4$ ratio regions more precisely.

In chapter 7, the effect of strain relaxation in compressive strained $Ge_{1-y}Sn_y$ on growth rate and Sn concentration of $Ge_{1-y}Sn_y$ epilayers, which were grown at 260 °C and 500 Torr with $SnCl_4/GeH_4$ ratio of 3.3×10^{-3}, was investigated. It is important to note that strain relaxation could be different in $Ge_{1-y}Sn_y$ epilayers with the same Sn concentration but grown under different CVD growth conditions. Further research should therefore be carried out to investigate strain relaxation for $Ge_{1-y}Sn_y$ epilayers grown under different CVD growth conditions. Moreover, since the strain relaxation in $Ge_{1-y}Sn_y$ epilayers affects the electrical, for example indirect-to-direct bandgap transition, and the physical properties of epilayers, it

is therefore essential to consider further investigations in order to fully understand the mechanism of strain relaxation of $Ge_{1-y}Sn_y$ epilayers.

Additionally, the grading technique, in which $SnCl_4$-H_2 (or $SnCl_4/GeH_4$ ratio) is tuned during the growth of $Ge_{1-y}Sn_y$, was performed at pressure of 500 Torr and two different temperatures of 280 °C and 260 °C. The effect of the grading technique on the quality of the graded $Ge_{1-y}Sn_y$ was investigated in chapter 8. It was shown how the grading technique enabled the growth of thick $Ge_{1-y}Sn_y$ by suppressing Sn segregation at a lower growth temperature of 260 °C. It should also be noted that the thickness of $Ge_{1-y}Sn_y$ was lower when using the grading technique than when fixed $SnCl_4$-H_2 was used. This is because not all values for the $SnCl_4/GeH_4$ ratio are allowed at a given growth temperature. This also means that during the growth of $Ge_{1-y}Sn_y$ using the grading technique, no growth was achieved, and all precursors were wasted when the $SnCl_4/GeH_4$ ratio was at unacceptable value during the growth. The effect of the graded $Ge_{1-y}Sn_y$ (as an intermediate layer) on the quality and growth of the following $Ge_{1-y}Sn_y$ grown above it was also examined. Higher quality $Ge_{1-y}Sn_y$ with a smoother surface (low surface roughness) was achieved with the grading technique than with fixed $SnCl_4$-H_2. Furthermore, the grading technique was not found useful to improve the quality of the interface between Ge-VS and $Ge_{1-y}Sn_y$. Further study is required to investigate the mechanism of grading technique when growing $Ge_{1-y}Sn_y$ epilayers in more detail. For example, how it supports suppressing segregation during the growth of $Ge_{1-y}Sn_y$, the effect of the technique at other growth temperatures and pressures, how its growth rate behaves and changes during the growth of $Ge_{1-y}Sn_y$, and how it influences the h_c in which strain relaxation begins.

Doping $Ge_{1-y}Sn_y$ binary alloys were studied and presented in chapter 9. Two precursors were used: B_2H_6 was used to achieve B doped $Ge_{1-y}Sn_y$, and PH_3 was used to achieve P doped $Ge_{1-y}Sn_y$ binary alloys. The incorporation of B and P into $Ge_{1-y}Sn_y$ epilayers did not affect the quality of epilayers. However, they slightly influenced the Sn concentration and growth rate of the epilayers. Since doped $Ge_{1-y}Sn_y$ epilayers could offer more flexibility to control physical, electrical, and optical properties over ordinary $Ge_{1-y}Sn_y$ binary alloys, it is crucial to understand mechanisms that can control the incorporation of dopant into $Ge_{1-y}Sn_y$ epilayers. Further research is proposed to understand the effects of B and P incorporation into $Ge_{1-y}Sn_y$ epilayers, including Sn concentration, growth rate of epilayers. Finally, explanations of chemical reactions in the CVD chamber could open up a new path to the development of high quality doped $Ge_{1-y}Sn_y$ epilayers. The incorporation of Si into $Ge_{1-y}Sn_y$ (as known as

$Ge_{1-x-y}Si_xSn_y$) was also investigated. The incorporation of Si up to ~3 at.% into $Ge_{1-x-y}Si_xSn_y$ with a Sn concentration of 9.5 at.% was successfully achieved. The effects of growth temperature on epitaxial growth of $Ge_{1-x-y}Si_xSn_y$ epilayers were studied. Since the presence of Si precursors and the incorporation of Si into $Ge_{1-x-y}Si_xSn_y$ influence the incorporation of Sn, it can be difficult to reconcile both the incorporation of Si and Sn simultaneously. Further research is needed to understand the mechanism of epitaxial growth of $Ge_{1-x-y}Si_xSn_y$ epilayers.

Growth of Ge-cap\$Ge_{1-y}Sn_y$\Ge-VS, $Ge_{1-y}Sn_y$\Ge multilayers, and $Ge_{1-y}Sn_y$\$Ge_{1-z}Sn_z$ ($y \neq z$) were also investigated in chapter 10. Ge growth at low temperatures (≤ 300 °C) is not possible, because Ge atoms cannot be produced without the presence of $SnCl_4$ when GeH_4 precursor is used at low growth temperatures. Similarly, since the Sn concentration in $Ge_{1-y}Sn_y$ closely depends on the growth temperature, it is not possible to grow $Ge_{1-y}Sn_y$ with very different Sn concentrations at the same growth temperature. Nevertheless, such Sn concentration variations are limited and may not be an appropriate technique. Therefore, changing growth temperature during CVD growth seems necessary to optimise the characteristics of each epilayer. Successful growth of the corresponding heterostructures, the investigation of the growth mechanism, and the impact of growth conditions on the quality of epilayers have been extensively carried out. Further studies are necessary to develop and study the techniques mentioned in this chapter. Depending on the application, it is possible to epitaxially grow and engineer epilayers in a required manner.

References

[1] E. R. Johnson and S. M. Christian, Physical Review **95**, 560 (1954).

[2] E. O. Göbel and K. Ploog, Progress in Quantum Electronics **14**, 289 (1990).

[3] B. A. Joyce, Advanced Materials **5**, 773 (1993).

[4] J. Kouvetakis, J. Menendez, and A. V. G. Chizmeshya, in *Annual Review of Materials Research* (Annual Reviews, Palo Alto, 2006), pp. 497.

[5] S. Zaima, Japanese Journal of Applied Physics **52**, 030001 (2013).

[6] S. Zaima, O. Nakatsuka, N. Taoka, M. Kurosawa, W. Takeuchi, and M. Sakashita, Science and Technology of Advanced Materials **16**, 22, 043502 (2015).

[7] C. D. Thurmond, F. A. Trumbore, and M. Kowalchik, The Journal of Chemical Physics **25**, 799 (1956).

[8] F. A. Trumbore, Journal of The Electrochemical Society **103**, 597 (1956).

[9] H. Stöhr and W. Klemm, Zeitschrift für anorganische und allgemeine Chemie **241**, 305 (1939).

[10] S. Wirths, D. Buca, and S. Mantl, Progress in Crystal Growth and Characterization of Materials **62**, 1 (2016).

[11] G. Busch, J. Wieland, and H. Zoller, HELVETICA PHYSICA ACTA **23**, 528 (1950).

[12] A. W. Ewald and O. N. Tufte, Journal of Applied Physics **29**, 1007 (1958).

[13] A. W. Ewald and O. N. Tufte, Journal of Physics and Chemistry of Solids **8**, 523 (1959).

[14] C. H. L. Goodman, Iee Proceedings-I Communications Speech and Vision **129**, 189 (1982).

[15] R. F. C. Farrow, D. S. Robertson, G. M. Williams, A. G. Cullis, G. R. Jones, I. M. Young, and P. N. J. Dennis, Journal of Crystal Growth **54**, 507 (1981).

[16] S. Oguz, W. Paul, T. F. Deutsch, B. Y. Tsaur, and D. V. Murphy, Applied Physics Letters **43**, 848 (1983).

[17] S. I. Shah, J. E. Greene, L. L. Abels, Q. Yao, and P. M. Raccah, Journal of Crystal Growth **83**, 3 (1987).

[18] E. A. Fitzgerald *et al.*, Journal of Electronic Materials **20**, 489 (1991).

[19] W. Wegscheider, J. Olajos, U. Menczigar, W. Dondl, and G. Abstreiter, Journal of Crystal Growth **123**, 75 (1992).

[20] M. T. Asom, E. A. Fitzgerald, A. R. Kortan, B. Spear, and L. C. Kimerling, Applied Physics Letters **55**, 578 (1989).

[21] P. R. Pukite, A. Harwit, and S. S. Iyer, Applied Physics Letters **54**, 2142 (1989).

[22] H. Höchst, M. A. Engelhardt, and I. Hernández-Calderón, Physical Review B **40**, 9703 (1989).

[23] J. Piao, R. Beresford, T. Licata, W. I. Wang, and H. Homma, Journal of Vacuum Science & Technology B: Microelectronics Processing and Phenomena **8**, 221 (1990).

[24] T. Maruyama, Journal of The Electrochemical Society **145**, 1303 (1998).

[25] H. P. L. d. Guevara, A. G. Rodríguez, H. Navarro-Contreras, and M. A. Vidal, Applied Physics Letters **83**, 4942 (2003).

[26] J. Zheng, L. Li, T. Zhou, Y. Zuo, C. Li, B. Cheng, and Q. Wang, ECS Solid State Letters **3**, P111 (2014).

[27] T. Tsukamoto, N. Hirose, A. Kasamatsu, T. Mimura, T. Matsui, and Y. Suda, Journal of Materials Science **50**, 4366 (2015).

[28] G. He and H. A. Atwater, Nuclear Instruments and Methods in Physics Research Section B: Beam Interactions with Materials and Atoms **106**, 126 (1995).

[29] G. He and H. A. Atwater, Applied Physics Letters **68**, 664 (1996).

[30] M. E. Taylor, G. He, C. Saipetch, H. A. Atwater, and T. J. Watson, MRS Proceedings **388**, 97, 97 (1995).

[31] M. E. Taylor, G. He, H. A. Atwater, and A. Polman, Journal of Applied Physics **80**, 4384 (1996).

[32] R. R. Lieten, J. W. Seo, S. Decoster, A. Vantomme, S. Peters, K. C. Bustillo, E. E. Haller, M. Menghini, and J.-P. Locquet, Applied Physics Letters **102**, 052106 (2013).

[33] H. Höchst, M. A. Engelhardt, and I. Hernández-Calderón, Physical Review B **40**, 9703 (1989).

[34] M. Rojas-López, H. Navarro-Contreras, P. Desjardins, O. Gurdal, N. Taylor, J. R. A. Carlsson, and J. E. Greene, Journal of Applied Physics **84**, 2219 (1998).

[35] E. Kasper, J. Werner, M. Oehme, S. Escoubas, N. Burle, and J. Schulze, Thin Solid Films **520**, 3195 (2012).

[36] M. Oehme, D. Buca, K. Kostecki, S. Wirths, B. Holländer, E. Kasper, and J. Schulze, Journal of Crystal Growth **384**, 71 (2013).

[37] M. Bauer, J. Taraci, J. Tolle, A. V. G. Chizmeshya, S. Zollner, D. J. Smith, J. Menendez, C. Hu, and J. Kouvetakis, Applied Physics Letters **81**, 2992 (2002).

[38] J. Tolle, R. Roucka, V. D'Costa, J. Menendez, A. Chizmeshya, and J. Kouvetakis, MRS Proceedings **891**, 0891, 0891-ee12-08 (2005).

[39] B. Vincent *et al.*, Applied Physics Letters **99**, 3, 152103 (2011).

[40] F. Gencarelli, B. Vincent, L. Souriau, O. Richard, W. Vandervorst, R. Loo, M. Caymax, and M. Heyns, Thin Solid Films **520**, 3211 (2012).

[41] F. Gencarelli *et al.*, Ecs Journal of Solid State Science and Technology **2**, P134 (2013).

[42] R. Chen, Y.-C. Huang, S. Gupta, A. C. Lin, E. Sanchez, Y. Kim, K. C. Saraswat, T. I. Kamins, and J. S. Harris, Journal of Crystal Growth **365**, 29 (2013).

[43] C. L. Senaratne, J. D. Gallagher, T. Aoki, J. Kouvetakis, and J. Menéndez, Chemistry of Materials **26**, 6033 (2014).

[44] N. von den Driesch *et al.*, Chemistry of Materials **27**, 4693 (2015).

[45] S. Wirths, D. Buca, G. Mussler, A. T. Tiedemann, B. Holländer, P. Bernardy, T. Stoica, D. Grützmacher, and S. Mantl, ECS Journal of Solid State Science and Technology **2**, N99 (2013).

[46] J. Taraci *et al.*, Journal of the American Chemical Society **123**, 10980 (2001).

[47] J. Taraci, J. Tolle, J. Kouvetakis, M. R. McCartney, D. J. Smith, J. Menendez, and M. A. Santana, Applied Physics Letters **78**, 3607 (2001).

[48] J. Q. Xie, A. V. G. Chizmeshya, J. Tolle, V. R. D'Costa, J. Menendez, and J. Kouvetakis, Chemistry of Materials **22**, 3779 (2010).

[49] J. Margetis *et al.*, Sige, Ge, and Related Compounds 6: Materials, Processing, and Devices **64**, 711 (2014).

[50] S. Gupta, B. Magyari-Kope, Y. Nishi, and K. C. Saraswat, Journal of Applied Physics **113**, 7, 073707 (2013).

[51] L. Ansari, G. Fagas, J.-P. Colinge, and J. C. Greer, Nano Letters **12**, 2222 (2012).

[52] H. Höchst and I. Hernández-Calderón, Surface Science **126**, 25 (1983).

[53] S. Groves and W. Paul, Physical Review Letters **11**, 194 (1963).

[54] P. Moontragoon, Z. Ikonic, and P. Harrison, Semiconductor Science and Technology **22**, 742 (2007).

[55] R. W. Olesinski and G. J. Abbaschian, Bulletin of Alloy Phase Diagrams **5**, 265 (1984).

[56] J. P. Fleurial and A. Borshchevsky, Journal of the Electrochemical Society **137**, 2928 (1990).

[57] R. R. Lieten, T. Maeda, W. Jevasuwan, H. Hattori, N. Uchida, S. Miura, M. Tanaka, and J. P. Locquet, Applied Physics Express **6**, 101301 (2013).

[58] P. F. Guo *et al.*, Journal of Applied Physics **114**, 044510 (2013).

[59] C. Eckhardt, K. Hummer, and G. Kresse, Physical Review B **89**, 165201 (2014).

[60] J. Zheng, Z. Liu, C. L. Xue, C. B. Li, Y. H. Zuo, B. W. Cheng, and Q. M. Wang, Journal of Semiconductors **39**, 6, 061006 (2018).

[61] R. A. Soref and L. Friedman, Superlattices and Microstructures **14**, 189 (1993).

[62] O. Gurdal, P. Desjardins, J. R. A. Carlsson, N. Taylor, H. H. Radamson, J.-E. Sundgren, and J. E. Greene, Journal of Applied Physics **83**, 162 (1998).

[63] S. Takeuchi, A. Sakai, K. Yamamoto, O. Nakatsuka, M. Ogawa, and S. Zaima, Semiconductor Science and Technology **22**, S231 (2006).

[64] S. Takeuchi, Y. Shimura, O. Nakatsuka, S. Zaima, M. Ogawa, and A. Sakai, Applied Physics Letters **92**, 231916 (2008).

[65] S. Takeuchi, A. Sakai, O. Nakatsuka, M. Ogawa, and S. Zaima, Thin Solid Films **517**, 159 (2008).

[66] S. Wirths *et al.*, Applied Physics Letters **102**, 192103 (2013).

[67] D. Weisshaupt, P. Jahandar, G. Colston, P. Allred, J. Schulze, and M. Myronov, 2017 40th International Convention on Information and Communication Technology, Electronics and Microelectronics (Mipro), 43 (2017).

[68] P. Jahandar, D. Weisshaupt, G. Colston, P. Allred, J. Schulze, and M. Myronov, Semiconductor Science and Technology **33**, 6, 034003 (2018).

[69] K. L. Low, Y. Yang, G. Q. Han, W. J. Fan, and Y. C. Yeo, Journal of Applied Physics **112**, 9, 103715 (2012).

[70] A. A. Tonkikh, C. Eisenschmidt, V. G. Talalaev, N. D. Zakharov, J. Schilling, G. Schmidt, and P. Werner, Applied Physics Letters **103**, 032106 (2013).

[71] B. Dutt, H. Lin, D. S. Sukhdeo, B. M. Vulovic, S. Gupta, D. Nam, K. C. Saraswat, and J. S. Harris, Ieee Journal of Selected Topics in Quantum Electronics **19**, 1502706 (2013).

[72] A. M. Ionescu and H. Riel, Nature **479**, 329 (2011).

[73] R. Kotlyar, U. E. Avci, S. Cea, R. Rios, T. D. Linton, K. J. Kuhn, and I. A. Young, Applied Physics Letters **102**, 113106 (2013).

[74] G. Sun and S. Q. Yu, Solid-State Electronics **83**, 76 (2013).

[75] L. Vivien, *Handbook of silicon photonics*, Series in optics and optoelectronics.

[76] V. V. Mitin, V. A. Kochelap, and M. A. Stroscio, *Introduction to Nanoelectronics: Science, Nanotechnology, Engineering, and Applications* (Cambridge University Press, Cambridge, 2007).

[77] F. Gencarelli, (2015).

[78] F. Frank and J. Van Der Merwe, Proc. Roy. Soc. London A **198**, 216 (1949).

[79] M. Volmer and A. Weber, Zeitschrift für Physikalische Chemie **119U**, 277 (1926).

[80] K. Kaiserl. Akademie der Wissenschaften in Wien. Mathematisch-Naturwissenschaftliche, *Sitzungsberichte der Mathematisch-Naturwissenschaftliche Classe* (K.-K. Hof- und StaatsDruckerei in Commission bei W. Braumüller, Wien :, 1848), Vol. Bd.1 (1848).

[81] J. A. Van Vechten and J. C. Phillips, Physical Review B **2**, 2160 (1970).

[82] Y. G. Sadofyev, V. P. Martovitsky, A. V. Klekovkin, V. V. Saraikin, and I. S. Vasil'evskii, Physics Procedia **72**, 411 (2015).

[83] W. Wang, Q. Zhou, Y. Dong, E. S. Tok, and Y. C. Yeo, Applied Physics Letters **106**, 4, 232106 (2015).

[84] G. Eneman, E. Simoen, R. Delhougne, P. Verheyen, R. Loo, and K. De Meyer, Applied Physics Letters **87**, 192112 (2005).

[85] L. M. Giovane, H. C. Luan, A. M. Agarwal, and L. C. Kimerling, Applied Physics Letters **78**, 541 (2001).

[86] K. A. Bratland, Y. L. Foo, T. Spila, H. S. Seo, R. T. Haasch, P. Desjardins, and J. E. Greene, Journal of Applied Physics **97**, 044904 (2005).

[87] H. Groiss, M. Glaser, M. Schatzl, M. Brehm, D. Gerthsen, D. Roth, P. Bauer, and F. Schäffler, Scientific Reports **7**, 16114 (2017).

[88] M. F. Fyhn, J. Chevallier, and A. N. Larsen, Journal of Vacuum Science & Technology B **16**, 1777 (1998).

[89] L. Vitos, A. V. Ruban, H. L. Skriver, and J. Kollar, Surface Science **411**, 186 (1998).

[90] R. J. Jaccodine, Journal of The Electrochemical Society **110**, 524 (1963).

[91] K. Kato, T. Asano, N. Taoka, M. Sakashita, W. Takeuchi, O. Nakatsuka, and S. Zaima, Japanese Journal of Applied Physics **53**, 72 (2014).

[92] N. Taoka *et al.*, Applied Physics Letters **106**, 061107 (2015).

[93] W. Wang, L. Z. Li, Q. Zhou, J. S. Pan, Z. Zhang, E. S. Tok, and Y. C. Yeo, Applied Surface Science **321**, 240 (2014).

[94] K. Kato, N. Taoka, T. Asano, T. Yoshida, M. Sakashita, O. Nakatsuka, and S. Zaima, Applied Physics Letters **105**, 122103 (2014).

[95] E. Kasper, M. Kittler, M. Oehme, and T. Arguirov, Photonics Research **1**, 69 (2013).

[96] N. Bhargava, M. Coppinger, J. P. Gupta, L. Wielunski, and J. Kolodzey, Applied Physics Letters **103**, 041908 (2013).

[97] Y. Inuzuka, S. Ike, T. Asano, W. Takeuchi, N. Taoka, O. Nakatsuka, and S. Zaima, Ecs Solid State Letters **4**, P59 (2015).

[98] P. C. Grant *et al.*, Journal of Vacuum Science & Technology B **35**, 061204 (2017).

[99] S. Wirths, D. Buca, A. T. Tiedemann, B. Hollander, P. Bernardy, T. Stoica, D. Grutzmacher, and S. Mantl, Sige, Ge, and Related Compounds 5: Materials, Processing, and Devices **50**, 885 (2012).

[100] G. Grzybowski, R. T. Beeler, L. Jiang, D. J. Smith, J. Kouvetakis, and J. Menendez, Applied Physics Letters **101**, 072105 (2012).

[101] D. Eres, D. H. Lowndes, J. Z. Tischler, J. W. Sharp, D. B. Geohegan, and S. J. Pennycook, Applied Physics Letters **55**, 858 (1989).

[102] J. Margetis, S. Q. Yu, B. H. Li, and J. Tolle, Journal of Vacuum Science & Technology A **37**, 8, 021508 (2019).

[103] R. Loo *et al.*, Semiconductor Science and Technology **33**, 114010 (2018).

[104] J. Taraci *et al.*, MRS Online Proceedings Library **692**, 1141 (2011).

[105] M. R. Bauer, C. S. Cook, P. Aella, J. Tolle, J. Kouvetakis, P. A. Crozier, A. V. G. Chizmeshya, D. J. Smith, and S. Zollner, Applied Physics Letters **83**, 3489 (2003).

[106] M. R. Bauer, J. Tolle, C. Bungay, A. V. G. Chizmeshya, D. J. Smith, J. Menendez, and J. Kouvetakis, Solid State Communications **127**, 355 (2003).

[107] S. J. Su, W. Wang, B. W. Cheng, G. Z. Zhang, W. X. Hu, C. L. Xue, Y. H. Zuo, and Q. M. Wang, Journal of Crystal Growth **317**, 43 (2011).

[108] R. Ragan, C. C. Ahn, and H. A. Atwater, Applied physics letters **82**, 3439 (2003).

[109] A. W. Searcy and R. D. Freeman, Journal of the American Chemical Society **76**, 5229 (1954).

[110] R. Loo, G. Wang, L. Souriau, J. C. Lin, S. Takeuchi, G. Brammertz, and M. Caymax, Ulsi Process Integration 6 **25**, 335 (2009).

[111] L. Colace, G. Masini, F. Galluzzi, G. Assanto, G. Capellini, L. Di Gaspare, E. Palange, and F. Evangelisti, Applied Physics Letters **72**, 3175 (1998).

[112] V. A. Shah, A. Dobbie, M. Myronov, and D. R. Leadley, Solid-State Electronics **62**, 189 (2011).

[113] C. Xu, R. T. Beeler, L. Y. Jiang, G. Grzybowski, A. V. G. Chizmeshya, J. Menendez, and J. Kouvetakis, Semiconductor Science and Technology **28**, 105001 (2013).

[114] J. M. Hartmann, H. Grampeix, and L. Clavelier, Sige, Ge, and Related Compounds 3: Materials, Processing, and Devices **16**, 583 (2008).

[115] C. L. Senaratne, J. D. Gallagher, L. Y. Jiang, T. Aoki, D. J. Smith, J. Menendez, and J. Kouvetakis, Journal of Applied Physics **116**, 133509 (2014).

[116] J. D. Gallagher, C. L. Senaratne, J. Kouvetakis, and J. Menendez, Applied Physics Letters **105**, 142102 (2014).

[117] F. Gencarelli *et al.*, Thin Solid Films **590**, 163 (2015).

[118] R. Beeler, R. Roucka, A. V. G. Chizmeshya, J. Kouvetakis, and J. Menendez, Physical Review B **84**, 035204 (2011).

[119] F. Gencarelli *et al.*, Journal of Applied Physics **117**, 095702 (2015).

[120] A. Mosleh, S. A. Ghetmiri, B. R. Conley, M. Hawkridge, M. Benamara, A. Nazzal, J. Tolle, S. Q. Yu, and H. A. Naseem, Journal of Electronic Materials **43**, 938 (2014).

[121] S. Wirths *et al.*, Applied Physics Letters **103**, 192110 (2013).

[122] S. Wirths *et al.*, Nature Photonics **9**, 88 (2015).

[123] J. P. Gupta, N. Bhargava, S. Kim, T. Adam, and J. Kolodzey, Applied Physics Letters **102**, 4, 251117 (2013).

[124] H. H. Tseng, K. Y. Wu, H. Li, V. Mashanov, H. H. Cheng, G. Sun, and R. A. Soref, Applied Physics Letters **102**, 4, 182106 (2013).

[125] M. Oehme *et al.*, Ieee Photonics Technology Letters **26**, 187 (2014).

[126] D. Stange *et al.*, Optics Express **24**, 1358 (2016).

[127] R. W. Millar, D. C. S. Dumas, K. F. Gallacher, P. Jahandar, C. MacGregor, M. Myronov, and D. J. Paul, Optics Express **25**, 25374 (2017).

[128] S. Al-Kabi *et al.*, Applied Physics Letters **109**, 4, 171105 (2016).

[129] D. Stange *et al.*, Acs Photonics **3**, 1279 (2016).

[130] S. J. Su *et al.*, Optics Express **19**, 6408 (2011).

[131] D. L. Zhang, C. L. Xue, B. W. Cheng, S. J. Su, Z. Liu, X. Zhang, G. Z. Zhang, C. B. Li, and Q. M. Wang, Applied Physics Letters **102**, 4, 141111 (2013).

[132] H. H. Tseng, H. Li, V. Mashanov, Y. J. Yang, H. H. Cheng, G. E. Chang, R. A. Soref, and G. Sun, Applied Physics Letters **103**, 5, 231907 (2013).

[133] Y. Dong *et al.*, Optics Express **23**, 18611 (2015).

[134] M. Oehme *et al.*, Optics Letters **39**, 4711 (2014).

[135] J. Zheng, S. Y. Wang, Z. Liu, H. Cong, C. L. Xue, C. B. Li, Y. H. Zuo, B. W. Cheng, and Q. M. Wang, Applied Physics Letters **108**, 4, 033503 (2016).

[136] B. R. Conley *et al.*, Optics Express **22**, 15639 (2014).

[137] B. R. Conley *et al.*, Applied Physics Letters **105**, 5, 221117 (2014).

[138] C. Chang, H. Li, S. H. Huang, H. H. Cheng, G. Sun, and R. A. Soref, Applied Physics Letters **108**, 4, 151101 (2016).

[139] S. De Cesari, A. Balocchi, E. Vitiello, P. Jahandar, E. Grilli, T. Amand, X. Marie, M. Myronov, and F. Pezzoli, Physical Review B **99**, 9, 035202 (2019).

[140] R. Soref, Nature Photonics **4**, 495 (2010).

[141] M. J. R. Heck and J. E. Bowers, IEEE Journal of Selected Topics in Quantum Electronics **20**, 332 (2014).

[142] P. Chaisakul, D. Marris-Morini, G. Isella, D. Chrastina, N. Izard, X. Le Roux, S. Edmond, J. R. Coudevylle, and L. Vivien, Applied Physics Letters **99**, 141106 (2011).

[143] Y. H. Chen, C. Li, Z. W. Zhou, H. K. Lai, S. Y. Chen, W. C. Ding, B. W. Cheng, and Y. D. Yu, Applied Physics Letters **94**, 141902 (2009).

[144] S.-L. Cheng, J. Lu, G. Shambat, H.-Y. Yu, K. Saraswat, J. Vuckovic, and Y. Nishi, Optics Express **17**, 10019 (2009).

[145] W. X. Hu, B. W. Cheng, C. L. Xue, H. Y. Xue, S. J. Su, A. Q. Bai, L. P. Luo, Y. D. Yu, and Q. M. Wang, Applied Physics Letters **95**, 092102 (2009).

[146] J. F. Liu, X. C. Sun, L. C. Kimerling, and J. Michel, Optics Letters **34**, 1738 (2009).

[147] X. C. Sun, J. F. Liu, L. C. Kimerling, and J. Michel, Optics Letters **34**, 1198 (2009).

[148] X. C. Sun, J. F. Liu, L. C. Kimerling, and J. Michel, Applied Physics Letters **95**, 011911 (2009).

[149] J. D. Sau and M. L. Cohen, Physical Review B **75**, 045208 (2007).

[150] K. H. Kao, A. S. Verhulst, W. G. Vandenberghe, B. Soree, G. Groeseneken, and K. De Meyer, Ieee Transactions on Electron Devices **59**, 292 (2012).

[151] C. Schulte-Braucks, D. Stange, N. von den Driesch, S. Blaeser, Z. Ikonic, J. M. Hartmann, S. Mantl, and D. Buca, Applied Physics Letters **107**, 042101 (2015).

[152] Y. Gul, M. Myronov, S. N. Holmes, and M. Pepper, Physical Review Applied **14**, 054064 (2020).

[153] Y. Gul, S. N. Holmes, C.-W. Cho, B. Piot, M. Myronov, and M. Pepper, Journal of Physics: Condensed Matter **34**, 485301 (2022).

[154] J. Mathews, R. Roucka, J. Q. Xie, S. Q. Yu, J. Menendez, and J. Kouvetakis, Applied Physics Letters **95**, 133506 (2009).

[155] J. Werner, M. Oehme, A. Schirmer, E. Kasper, and J. Schulze, Thin Solid Films **520**, 3361 (2012).

[156] A. Gassenq, F. Gencarelli, J. Van Campenhout, Y. Shimura, R. Loo, G. Narcy, B. Vincent, and G. Roelkens, Optics Express **20**, 27297 (2012).

[157] Y.-H. Zhu, Q. Xu, W.-J. Fan, and J.-W. Wang, Journal of Applied Physics **107**, 073108 (2010).

[158] G. Sun, H. H. Cheng, J. Menendez, J. B. Khurgin, and R. A. Soref, Applied physics letters **90**, 251105 (2007).

[159] S. Chang and S. L. Chuang, IEEE Journal of Quantum Electronics **43**, 249 (2007).

[160] G.-E. Chang, S.-W. Chang, and S. L. Chuang, Optics Express **17**, 11246 (2009).

[161] G. Sun, R. A. Soref, and H. H. Cheng, Journal of Applied Physics **108**, 033107 (2010).

[162] G. E. Chang, S. W. Chang, and S. L. Chuang, IEEE Journal of Quantum Electronics **46**, 1813 (2010).

[163] J. C. Sturm and K. H. Chung, Sige, Ge, and Related Compounds 3: Materials, Processing, and Devices **16**, 799 (2008).

[164] S. Wirths *et al.*, Thin Solid Films **557**, 183 (2014).

[165] C. Xu, R. T. Beeler, G. J. Grzybowski, A. V. G. Chizmeshya, D. J. Smith, J. Menendez, and J. Kouvetakis, Journal of the American Chemical Society **134**, 20756 (2012).

[166] L. Vivien and L. Pavesi, *Handbook of silicon photonics*, Series in optics and optoelectronics.

[167] J. Margetis *et al.*, Materials Science in Semiconductor Processing **70**, 38 (2017).

[168] J. Margetis *et al.*, Journal of Crystal Growth **463**, 128 (2017).

[169] C. L. Senaratne, P. M. Wallace, J. D. Gallagher, P. E. Sims, J. Kouvetakis, and J. Menendez, Journal of Applied Physics **120**, 025701 (2016).

[170] microbenotes.com/electron-microscope-principle-types-components-applications-advantages-limitations/, (Microbe Notes).

[171] K. D. Vernon-Parry, III-Vs Review **13**, 40 (2000).

[172] An Introduction to Surface Analysis by XPS and AES, 165 (2003).

[173] A. Gassenq *et al.*, Applied Physics Letters **109**, 242107 (2016).

[174] J. Aubin, J. M. Hartmann, J. P. Barnes, J. B. Pin, and M. Bauer, Sige, Ge, and Related Materials: Materials, Processing, and Devices 7 **75**, 387 (2016).

[175] S. Wirths *et al.*, Sige, Ge, and Related Compounds 6: Materials, Processing, and Devices **64**, 689 (2014).

[176] R. Soref, J. Kouvetakis, and J. Menendez, in *Symposium on Group 4 Semiconductor Nanostructures held at the 2006 MRS Fall Meeting* (Materials Research Soc, Boston, MA, 2006), pp. 13.

[177] V. R. D'Costa, Y. Y. Fang, J. Tolle, J. Kouvetakis, and J. Menendez, Thin Solid Films **518**, 2531 (2010).

[178] M. El Kurdi, G. Fishman, S. Sauvage, and P. Boucaud, Journal of Applied Physics **107**, 013710 (2010).

[179] Y. Y. Fang, J. Tolle, A. V. G. Chizmeshya, J. Kouvetakis, V. R. D'Costa, and J. Menendez, Applied Physics Letters **95**, 081113 (2009).

[180] J. Q. Xie, J. Tolle, V. R. D'Costa, A. V. G. Chizmeshya, J. Menendez, and J. Kouvetakis, Applied Physics Letters **95**, 181909 (2009).